IMPERIAL

Low-Order Non-Linear Spectroscopy of Chiral Molecules

Joshua David Thompson Vogwell

A thesis presented for the degree

of

Doctor of Philosophy

Department of Physics

Imperial College London

United Kingdom of Great Britain and Northern Ireland

May 7, 2026

Statement of Originality

I declare that the work contained in this Thesis is my own unless stated otherwise in the text.

Joshua David Thompson Vogwell

Copyright declaration

The copyright of this thesis rests with the author. Unless otherwise indicated, its contents are licensed under a Creative Commons Attribution-Non Commercial 4.0 International Licence (CC BY-NC).

Under this licence, you may copy and redistribute the material in any medium or format. You may also create and distribute modified versions of the work. This is on the condition that: you credit the author and do not use it, or any derivative works, for a commercial purpose.

When reusing or sharing this work, ensure you make the licence terms clear to others by naming the licence and linking to the licence text. Where a work has been adapted, you should indicate that the work has been changed and describe those changes.

Please seek permission from the copyright holder for uses of this work that are not included in this licence or permitted under UK Copyright Law.

Low-Order Non-Linear Spectroscopy of Chiral Molecules

Joshua David Thompson Vogwell

Abstract

We present a computational and theoretical study of low-order non-linear spectroscopy in chiral molecules. In particular, we present a novel technique for ultrafast sum-frequency generation spectroscopy in chiral molecules, and a discussion of the implications of molecular conformers upon our technique. First, we present the results of time-dependent density-functional-theory simulations of enantiosensitive sum-frequency generation in the chiral molecule propylene oxide, using the software package OCTOPUS combined with signal processing and propagation codes. Using these tools, we demonstrate how sum-frequency generation can be used in an ensemble of randomly oriented chiral molecules to produce a far-field signal which is enantiosensitive on the level of total intensity. This enantiosensitivity is much more efficient than older optical-activity based methods, since it eschews magnetic effects in favour of stronger electric-dipole interactions, whilst remaining fully controllable using the phases of input components. This technique presents exciting opportunities for ultrafast chiral measurement, using relatively low laser intensities which may be applicable to general laboratory settings. Secondly, we use a bespoke spectral Schrödinger-equation solver in a basis set of field-free states obtained using Density Functional Theory (DFT) to simulate the polarisation response of randomly oriented carvone to the driving field used in chiral sum-frequency generation. We repeat this for multiple sets of input frequencies and for the three most common conformers of carvone. In doing so, we demonstrate that our chiroptical technique is robust against conformational effects. We further demonstrate the existence of interconformer interferences, as well as enantiosensitive interference between conformers. This presents further opportunities to use solvents or companion molecules to generate reference signals for ultrafast heterodyne measurements of chirality, and to study conformational geometry itself in an ultrafast-optics setting.

Contents

List of Figures **17**

1 Chirality and Chiral Molecules **27**
1.1 Chirality in Chemistry and Biology 31
1.1.1 Introduction to Isomerism 31
1.1.2 Chiral Biochemistry 36

2 Chiroptical spectroscopy **41**
2.1 Light-Matter Interactions 41
2.1.1 Maxwell's Equations 42
2.1.2 Linear Optics 42
2.1.3 Non-linear Optics 44
2.1.4 Perturbative Phenomena 45
2.1.5 Non-perturbative Phenomena 48
2.2 Optical Activity 51
2.2.1 Circular Dichroism 52
2.2.2 Optical Rotation 54
2.2.3 Non-linear and Enhanced Optical Activity 57
2.3 Chirality of Reagents vs Observers 57
2.3.1 Photoelectron Circular Dichroism 59
2.3.2 Synthetic Chiral Light 61
2.4 Novel Chiroptical Approaches 64
2.4.1 Photo-excitation Circular Dichroism 65
2.4.2 Microwave Three-wave Mixing 66
2.4.3 Static Field Dichroism 67
2.4.4 Chiral High-Harmonic Generation 69
2.4.5 Coulomb Explosion Imaging 70

3 Computational Methods **73**
3.1 Solving the Time-Dependent Schrödinger equation 73
3.1.1 Spatial vs Spectral Methods 74
3.1.2 Perturbation Theory 76
3.2 Computational Methods in Quantum Chemistry 77
3.2.1 The Molecular Hamiltonian 78
3.2.2 The Born-Oppenheimer Approximation 79
3.2.3 Hartree-Fock Theory 80

3.2.4 Density Functional Theory 87
3.2.5 Time-Dependent Density Functional Theory 93
3.3 Orientational-averaging Schemes 99
3.3.1 Lebedev Quadrature 100

4 Chiral sum-frequency generation 103
4.1 Numerical Demonstration of our Approach 106
4.1.1 Modelling the Laser Field 107
4.1.2 Modelling the Response of Randomly Oriented Molecules . . . 109
4.1.3 Intensities in the Far Field 112
4.2 Results and Discussion 113
4.2.1 Conclusions and Prospectives 117

5 Conformational effects in SFG 119
5.1 Conformational Effects in Chiral Sum-frequency Generation 120
5.2 Modelling Conformational Effects in Chiral SFG 121
5.2.1 Solving the Time-dependent Schrödinger Equation 124
5.3 Results and Discussion 125
5.3.1 Conformational Averaging 125
5.3.2 Inter-conformer Interference 128
5.3.3 Investigating Alternative Emission Pathways 133
5.3.4 Alternate Processing 135
5.3.5 Conclusion 136

6 Conclusions and prospectives 139

Acknowledgements

I must acknowledge the people who have contributed to this work directly over the last few years;

- David, for his supervision, advice, and encouragement,
- Laura, for her invaluable coding help, mentoring in science, and penchant for animated figures in Matlab,
- Patricia, for contributing vital simulations,
- Rico, for infectious enthusiasm and eminently readable code,
- Peilin, with whom I have shared a desk and exchanged coding troubles,
- Misha and Olga, for valuable scientific conversations,
- Mary, for advice and encouragement,

I would now like to thank the people without whom the past years would have been much more difficult and much less fun;

- Jacob, for engaging conversations about the world, politics and (very occasionally) science,
- Felix, for free-willed discussions of fruit, planes and rodent control techniques,
- Rose and Hortense for good, clean humour, bakes, and organising group social occasions,
- The humour and antics of Tim and Joey,
- Belen and Nikolas for polite, good-natured, and even-mannered debate and, with Oliver and Miguel, for analysis of road markings, trade data, cunning wordplay and opaque surfaces, as well as all other members of the XLC and denizens of 6M02 past and present.

I would also like to thank my parents for help, advice, proof-reading and always being there for me. I am indebted to the inventions of Robert Stevenson and Isembard Kingdom Brunel for getting me to the office, and most of the way back, most of the time. I would finally like to wish good-luck to fellow chiralists Rose, Peilin, Mitchell, Ed and (other) Jacob.

Publications arising from this work

- J. D. T. Vogwell et al. "Ultrafast Control over Chiral Sum-frequency Generation". In: Science Advances 9.33 (2023), eadj1429
- O. Alexander et al. "Attosecond Impulsive Stimulated X-ray Raman Scattering in Liquid Water". In: Science Advances 10.39 (2024), eadp0841 (results not included in this thesis)

List of Abbreviations

ALDA Adiabatic local density approximation

ATI Above threshold ionisation

B3 Becke three parameter

BINOL 1,1'-Bi-2-naphthol

BOA Born-Oppenheimer approximation

CAM Coulomb attenuating method

CAMB3LYP Coulomb attenuating method Becke three parameter Lee-Yang-Parr

CB Circular birefringence

CD Circular dichroism

CEI Coulomb explosion imaging

CPL Circularly polarised light

DFT Density functional theory

DNA Deoxyribonucleic acid

E 'Entegen' or 'Opposing'

EDA Electric dipole approximation

GGA Generalised gradient approximation

HFT Hartree-Fock theory

HHG High harmonic generation

HK Hohenberg-Kohn

IR Infrared

KS Kohn-Sham

L Lab frame

LCAO Linear combination of atomic orbitals

LDA Local density approximation

LYP Lee-Yang-Parr

M Molecular frame

M3WM Microwave three-wave-mixing

MBI Max-Born Institute (Berlin)

MPI Multi photon ionisation

NL Non-linear

NN Nuclear-nuclear

NYU New York University

OA Optical activity

OR Optical rotation

PECD Photoelectron circular dichroism

PEXCD Photoelectron-photoexcitation circular dichroism

PXCD Photoexcitation circular dichroism

SD Slater determinant

SFG Sum-frequency generation

SHG Second harmonic generation

SHG-CD Second harmonic generation circular dichroism

TDDFT Time-dependent density functional theory

TDSE Time-dependent Schrödinger equation

THG Third-harmonic generation

UV Ultraviolet

XC Exchange-correlation

Z 'Zusammen' or 'Together'

bs Barrier suppression

eN Electron-nuclear

eV Electron-volt

ee Electron-electron

l Linear

nc Nuclear

nl Non-local

List of Figures

1.1 A diagram showing two opposite hands, and the impossibility of superimposing them. The fact that opposite hands are mirror-images of one-another, combined with the fact that they cannot be superimposed, makes hands chiral objects. Reproduced under creative commons from M. Karras [29]. 27

1.2 Examples of chirality in 2-dimensions, including (a) a Z shape, and (b) a rotating circle, which exhibit so-called *pseudo*-chirality in 2-D since they are non superimposable via direct isometries, but transform into one-another upon time reversal. Contrast a Z shape in 3-dimensions (c), which enables one figure to be transformed into the other by a rotation. (d) shows how tetrahedrons, when each side is distinct, exist as two non-superimposable reflected forms. (e) shows a helix, which is a chiral shape in 3-D. 29

1.3 A diagram showing the helical wavefront of an optical vortex, which is a chiral object analogously to circularly polarised light. Vortex beams, unlike circularly polarised light, can also have topological indices greater than one, corresponding to a wavefront consisting of double, triple or higher helices. The above figure corresponds to the right- and left-handed wavefronts of vortex light with topological index 1, -1, 3 and -3, and the axial intensity distribution of vortex light (bottom right). Reproduced under creative commons from A. Ambrosio [37]. 30

1.4 A key showing relationships between different forms of isomerism. Adapted from teaching materials by David Ayuso. 32

1.5 Carbon atoms can form covalent bonds with up to four other atoms, typically in a tetrahedral arrangement. If all four of these substituents are unique, then reflecting the carbon atom will result in mirror image that cannot be made to coincide with the original: such centres exhibit chirality. Reproduced from Wikipedia under creative commons [55]. 32

1.6 Since the two stereogenic centres of cis-1,2-dimethylcyclopropane are mirror images of each other, reversing the absolute configurations of both centres will transform one into the other, and so the molecule is not chiral but a 'meso-isomer'. 33

1.7 Examples of non-central chirality in molecules. (a) and (b) show opposite enantiomers of 1,1'-Bi-2-naphthol(BINOL), which exhibit axial chirality. (c) shows helicene, which is chiral by dint of its overall helical shape, while (d) shows trans-cyclooctene which has planar chirality. Reproduced from Wikipedia under creative commons [58–60]. 34

1.8 Chiral molecules may react differently with another chiral reagent, in this case a receptor site with a chiral shape. (a) Shows compatibility of a chiral ligand with a receptor while (b) shows incompatibility of the oppositely handed ligand with the same receptor. Reproduced under open access license from MDPI [64]. 35

1.9 Conformational isomers of butane, showing relative energy differences. Reproduced from Wikipedia under creative commons [77]. 36

1.10 Examples of chiral molecules relevant to biology. (a) shows the two enantiomers of the molecule carvone, which is *centrally* chiral: the carbon atom within the ring attached to the propenyl moiety is a stereogenic centre. *(R)*-carvone has a minty odour while the *(S)*-enantiomer smells closer to caraway or dill. (b) shows the structure of *(R,R,R)*-αtocopherol, also known as vitamin E, which has three stereogenic centers; two along the chain, one where the chain attaches to the ring. Reproduced from Wikipedia under creative commons [84, 85]. 37

1.11 Examples of chiral drugs. (a) shows the two enantiomers of ibuprofen. The right-enantiomer is converted into the left- within the body, so the drug's chirality is irrelevant to its usage. (b) shows the two enantiomers of thalidomide. *(R)*-thalidomide (top) is an effective sedative, *(S)*-thalidomide (bottom) is teratogenic. The molecule has a chiral centre on the glutamine ring (right) where it connects to the phthalimide moiety (left). Reproduced from Taylor & Francis Publishing and Wikipedia under creative commons [103, 104]. 38

2.1 A non-linear optics energy diagram showing resonant sum frequency generation (left), a second order process, and third harmonic generation (right), a third order process. Adapted under open access from American Association for the Advancement of Science [156]. 46

2.2 A simulated hydrogen HHG spectrum, showing a characteristic plateau of successively higher harmonic orders, up to a cutoff around the 31^{st} harmonic where the intensity of subsequent orders decreases exponentially. Reproduced under open access from IntechOpen [174]. . . . 48

2.3 A diagram showing the semi-classical three-step conceptualisation of HHG: starting from rest (a), tunnel ionisation (b), a free electron trajectory driven by the laser field(c), and finally recombination with the parent ion, releasing a burst of radiation (d). Reproduced with permission from Nature Publishing [176] 49

2.4 A diagram showing the helical figure drawn by the tip of the electric field vector of a circularly polarised light wave in space. Helices are chiral figures, but the length-scale of the helix of the light is much greater than that of the chiral molecule, and so the molecule hardly 'feels' the light as chiral, making CPL an inefficient chiral reagent. . . 52

2.5 A schematic of an optical rotation setup, with unpolarised light (2) from a source (1) linearly polarised (4) using a polariser (3), rotated (7) by a sample in a container (5,6), before being measured (8) using a second polarised plate (7). Reproduced from Wikipedia under creative commons [199]. 54

2.6 A diagram showing the behaviour of the chirality of molecule (L or R), the sense of the circular polarisation of incident light, and the resulting vector observable under various transformations: reflection in xy-plane ($\hat{\sigma}_z$), reflection in xz-plane ($\hat{\sigma}_y$), and rotation by π rad about the x-axis ($\hat{R}_x^\pi$). Reproduced with permission of APS Publishing [196]. 59

2.7 A diagram showing the photoelectron angular distribution from a chiral molecule illuminated by circularly polarised light. The chirality of the molecule creates a forward-backward asymmetry in the photoelectron angular distribution, while reversing either the chirality of the molecule or the handedness of the field will reverse the forward-backward asymmetry. Reproduced with permission from the Faraday division of the Royal Society of Chemistry [215]. 60

2.8 Diagrams showing CPL (a) vs SCL (b) in the electric dipole approximation. The figure for circularly polarised light is a planar circle, which is not chiral. By adding a longitudinal component, this makes the figure non-planar, which (when combined with the sense of the rotation of the field vector in time) makes the figure chiral, even within the dipole approximation [20]. Figure kindly provided by Andrés Ordoñez. 62

2.9 (a) Shows the evolution in time (red and blue), loci throughout space (yellow), and variation through space of the tip of the electric field vector in synthetic chiral light. (b) Lissajous figures traced by the tip of the electric field vector of synthetic chiral light at a single point in space over time. (c) Energy level diagram for enantiosensitive second-harmonic generation by synthetic chiral light. (d) Energy level diagram of enantiosensitive pump-probe absorption using synthetic chiral light. (e) Energy level diagram of HHG using synthetic chiral light. Reproduced with permission from Nature Publishing [20]. . . . 63

2.10 (a) An energy level diagram of absorption CD. Note: the enantiosensitivity of the technique relies on magnetic dipole interactions. (b) Energy level diagram of PXCD, with the enantiosensitivity deriving from transition dipoles from three transitions, $|0\rangle$ to $|2\rangle$, decay from $|2\rangle$ to $|1\rangle$, and $|1\rangle$ to $|0\rangle$. The right panel shows the tip of the dipole vector of a molecule in PXCD. (c) PEXCD, with the decay from state $|2\rangle$ to $|1\rangle$ replaced with a raman-type transition to and from continuum. (d) Energy level diagram of PECD in the chiral (left) and achiral (right) case. Reproduced with permission from AIP Publishing [231]. 66

4.1 (**A**) The proposed optical setup combines a linearly polarised beam with frequency ω and a second beam that carries cross-polarised ω and 2ω frequencies. The ω frequency components are polarised in the plane of propagation, and the 2ω component is polarised orthogonal to this plane. (**B**) Multiphoton pathways describing chiral SFG (left) and achiral THG (right). The induced polarisation associated with SFG has the same amplitude and opposite phase in opposite molecular enantiomers, $P^L_{SFG} = -P^R_{SFG}$, whereas the polarisation associated with THG is identical, $P^L_{THG} = P^R_{THG}$. (**C**) Multiphoton diagrams describing momentum conservation in SFG (left) and THG (right). Reproduced under open access licence from American Association for the Advancement of Science [156]. 106

4.2 A schematic showing the general procedure used in this work. In-group codes were used in combination with open-source software. . . 107

4.3 Optical amplitude (top), optical phase (middle), and argument of fifth order chiral correlation function (bottom) of the driving field in the interaction region along the $\hat{x}$ axis. Area under the argument of the chiral correlation function is shaded in black. 108

4.4 Time series of laser pulse of wavelength 361 nm and full-width-half-maximum of 3.27 fs, together with associated polarisation response. The electric field has been scaled so as to match the amplitude of the polarisation response, where the z direction refers to the longitudinal axis, while y is the transverse direction out-of-non-collinear-plane, and x is the transverse axis within the non-collinear plane. 110

4.5 Orientationally-averaged single-molecule polarisation response $D(\omega)$ of propylene oxide to a cross-polarised ω and 2ω flat-top Gaussian laser pulse of fundamental wavelength 361 nm and full-width-half-maximum of 3.27 fs. Figure includes harmonic intensity calculated from dipole response (solid) and acceleration (dotted). The achiral component in non-collinear plane is in blue, while chiral longitudinal component is in red. 111

4.6 Near-field polarisation response of propylene oxide in a chiral SFG setup, showing chiral (SFG) and achiral (THG) components of polarisation, and the associated phases in π radians. 113

4.7 (**A** and **B**) Intensity at angular frequency 3ω in the far field associated with chiral SFG (A) and achiral THG (B). (**C** to **F**) Total intensity emitted from left- (C) and (E) and right-handed (D) and (F) propylene oxide, resulting from adding the chiral SFG (A) and achiral THG (B) contributions, for $\phi_{2\omega} = 0.67\pi$ (C) and (D) and $\phi_{2\omega} = 1.67\pi$ (E) and (F). Laser parameters $I_\omega^{(1)} = I_\omega^{(2)} = 3 \times 10^{12}\,\mathrm{Wcm}^{-2}, I_{2\omega}^{(2)} = 7 \times 10^{11}\,\mathrm{Wcm}^{-2}$, pulse duration 7 fs and opening angle $2\alpha = 50°$, arb. u. is arbitrary units. Reproduced under open access licence from the American Association for the Advancement of Science [156]. 116

4.8 (**A** and **B**) Intensity at frequency 3ω emitted from left-handed (A) and right handed (B) propyleneoxide as a function of the divergence angle and the two-colour phase delay. (**C**) Dissymmetry factor $\gamma = 2(I_L - I_R)/(I_L + I_R)$. Grey colour indicates absence of emission. See caption of figure 4.7 for laser parameters. Reproduced under open access licence from the American Association for the Advancement of Science [156]. 117

4.9 Beamline schematic of a chiral SFG experiment based on our scheme. Figure kindly provided by Rose Picciuto, adapted from unpublished experimental work. 118

5.1 Diagram showing the shapes of the six most common conformers of carvone. Reproduced with permissions from AIP publishing [368]. . . 122

5.2 A schematic showing the general procedure used in this work. In-house codes available in-group were applied and adapted, and transition-dipole matrix elements were provided by our collaborator Patricia Vindel. 123

5.3 Intensity of emission (top), and three-way interconformational interference (bottom), for $\hat{x}$-polarised (left), and $\hat{z}$-polarised (right) emissions from a representative mixture of chiral molecule carvone, against fundamental input and output frequencies in electron-Volts. Horizontal green lines indicate electronic energy levels, whilst diagonal lines indicate even (yellow) and odd (blue) harmonics relative to the fundamental input. Energy-level transitions are marked as horizontal green lines in (dashed = eq-1, dotted and dashed = eq-2, dotted = eq-3). 127

5.4 Intensity of $\hat{z}$-polarised (5.4a) and $\hat{x}$-polarised (5.4b) emission from individual conformers divided by total emission from all conformers for conformer 1,2,3 (left, middle, right), against the fundamental input frequency (x-axis) and emission frequency (y). Horizontal green lines indicate energy levels and diagonal blue and yellow lines indicate odd and even harmonics respectively. 129

5.5 Intensity (top) and pairwise interconformational interference (bottom), for chiral emissions from individual conformers of chiral molecule carvone against fundamental input frequency (x-axis), and frequency of emission (y-axis). Horizontal lines (green) indicate electronic energy levels, whilst diagonal lines indicate even (yellow) and odd (blue) harmonics of input fundamental. 131

5.6 Intensity (top) and pairwise interconformational interference (bottom), for achiral emissions from individual conformers of chiral molecule carvone against fundamental input frequency (x-axis), and frequency of emission (y-axis). Horizontal lines (green) indicate electronic energy levels, whilst diagonal lines indicate even (yellow) and odd (blue) harmonics of input fundamental. 132
5.7 Intensity of emission from a randomly oriented ensemble of carvone, on a logarithmic scale, for a driving field with fundamental frequency $\omega = 1.9eV$, showing polarisation response along the $\hat{x}$ (blue), $\hat{y}$ (green) and $\hat{z}$ directions with emission calculated from polarisation (solid) and second time derivative of polarisation (dashed) using the Lamor formula. Simulation with: forty-five states included (a); the ground and second excited state (b); the ground, first excited, and second excited state (c); the ground and second excited state, with the permanent dipoles of these states removed (d); the ground, first, and second excited states, with enhanced transition dipoles (e). . . . 134
5.8 Intensity (top) and pairwise interconformational interference (bottom), for $\hat{z}$-polarised (chiral) emissions from individual conformers of chiral molecule carvone against fundamental input frequency (x-axis), and frequency of emission (y-axis), as processed with a filter that excludes the initial pulse. Horizontal lines (green) indicate electronic energy levels, whilst diagonal lines indicate even (yellow) and odd (blue) harmonics of input fundamental. 135
5.9 Intensity (top) and pairwise interconformational interference (bottom), for $\hat{x}$-polarised (achiral) emissions from individual conformers of chiral molecule carvone against fundamental input frequency (x-axis), and frequency of emission (y-axis), as processed with a filter that excludes the initial pulse. Horizontal lines (green) indicate electronic energy levels, whilst diagonal lines indicate even (yellow) and odd (blue) harmonics of input fundamental. 136

Introduction

Chirality is the property of geometric objects which are not the same as their mirror image [1]. Chiral objects range from hands [2], to snail shells and corkscrews. However, chirality is particularly important in chemistry, where opposite-handed mirror-images are known as enantiomers [3]. Mirror-image pairs of chiral objects (such as chiral odour molecules) react differently with other chiral objects (like olfactory receptor proteins) of opposite handedness [4], and in enantiomers this manifests in oppositely handed molecules reacting in distinct ways with other chiral objects [5, 6], particularly the highly chiral environment of biology [7].

Light has, for hundreds of years, been used as a means to study the physical world [8], including chirality [9]. In the early 19th century, Bunsen and Kirchoff harnessed light to study the chemical properties of matter, using emission and absorption spectra to discover new elements [10]. Since then, tools utilising light have been vital tools in studying molecules and their physical behaviour. Chiral media have been examined via their effects on light; how certain kinds of light are deflected or dimmed as they pass through a chiral crystal or a solution of chiral molecules [11, 12]. However, as optical technology has improved apace across the last 68 years since the invention of the optical laser, new frontiers have opened in the study of matter using light [13]. Specifically, the ability of scientists and engineers to produce bursts of light lasting femto- or even attoseconds allows the imaging of the internal dynamics of molecules as their electrons are moving [14–16]. Within this new world, the old chiral-optical toolkit has become increasingly constrained. Techniques such as optical rotation and circular dichroism are inefficient probes of chirality on the level of individual molecules, since they rely on weak magnetic interactions between the light and the electronic cloud. Such techniques therefore require large numbers of molecules to produce observable effects, and are not, without significant modifications, appropriate for ultra-fast measurements of chiral molecules [11, 17].

In this ultrafast era, the new task is to find methods of detecting molecular chirality which are compatible with the near-attosecond timescales of cutting edge optical and molecular physics. Such methods must move away from using magnetic interactions, as do older techniques, and instead generate a chiral response within the dominant electric-dipole interaction [18, 19]. One such technique is the generation of synthetic chiral light, where the Lissajous figure of the electric field follows a chiral trajectory in time [20]. This makes such light an effective chiral reagent even within the electric dipole regime.

Combining synthetic chiral light with extremely intense laser fields enables ultrafast chiral measurements using effects such as high-harmonic generation [21]. However, it is desirable to realise chiral methods that make use of synthetic chiral light in the context of more gentle laser intensities that are more applicable to standard laboratory settings. Chirality is of perhaps greatest import in biology and pharmacology, and this makes chiral measurements which are non-ionising, non-destructive, portable and work in liquid phase a goal of great interest.

The development of such novel techniques can be split into theoretical and experimental domains; understanding the mechanisms and viability of a technique and then realising it in a laboratory setting. The first of these, the theoretical conceptualisation and understanding, is greatly aided by the use of computational tools. Even fairly simple self-interacting quantum systems are fiendishly and notoriously difficult to simulate using a computer, and anything beyond helium atoms or H_2^+ ions presents an intractable technological challenge without making use of substantial simplifying assumptions [22]. The techniques described and used in the rest of this thesis, namely density functional theory [22–24], time-dependent density functional theory [25, 26], and the spectral propagation of electron wavefunctions, represent acceptable compromises between an accurate picture of physical processes and necessary simplifications and simplifying assumptions to make these problems tractable [24, 27, 28].

Outline

The broad aim of this work is to theoretically investigate the possibility of using low-order non-linear processes to realise chiral measurements using synthetic chiral light. This opens up the potential for ultrafast chiral techniques with the enantiosensitive efficiency of non-magnetic-dipole techniques without the need for extreme laser intensities.

In chapter 1, I shall explain the origins of chirality as a physical and mathematical property. I shall then go on to explain some of the ways in which chirality manifests within physical phenomena. Finally, I will explain the importance of chirality within chemistry and biology, as well as a broader introduction to the concept of isomerism in chemistry and examples of the real-world implications of chiral chemistry within medicine.

In chapter 2, I introduce the theory of light-matter interactions, from Maxwell's equations to non-linear optics. I shall then explore chiral techniques in optics, from optical activity to more modern methods. I will draw a distinction between methods which use light as a chiral reagent and those which construct a chiral measuring apparatus, making use of the concepts of chiral pseudoscalars and pseudovectors to characterise each technique.

In chapter 3, I will then go on to give a thorough explanation of some of the computational techniques used in the study of chiral light-matter interactions, with an introduction to Hartree-Fock theory as well as a particular emphasis on both time-dependent and time-independent density functional theory.

In chapter 4, I will present a novel technique using synthetic chiral light to achieve enantiosensitive measurement of chiral molecules within the perturbative regime. I will further explain the motivations for developing such a technique, before demonstrating its potential using time-dependent density functional theory. The results of these simulations will be presented and explained, before the implications are discussed.

Finally, in chapter 5, I shall present the results of investigations we have conducted into the potential effects and implications of conformational isomerism upon this technique. I will present the results of numerical simulations, as well as a discussion of the implications of this work on both the study of chirality and the study of conformers using low-order non-linear spectroscopy.

Chapter 1

Chirality and Chiral Molecules

Chirality is a property of geometric objects, wherein an object is said to be chiral if it is not possible to superimpose it with a mirror image [2]. More precisely, a chiral object cannot be mapped on to its mirror image by proper rotations and translations. Therefore a chiral object and its mirror image form a similar yet properly *distinct* pair, known most generally as *enantiomorphs* [1].

A classic example of a chiral pair are human hands (see Figure 1.1), where the left and right hands are (ideally) mirror images of one another, yet there is no way to physically overlap them. No matter which way you might turn either hand, the thumbs will be on opposite sides, the palms face in opposite directions, or the fingers point the wrong way. Indeed, coined by William Thompson 1st Baron Kelvin in 1893 [2], the word *'chirality'* is derived from the ancient Greek word for hand, '$\chi\varepsilon\iota\rho o\varsigma$'.

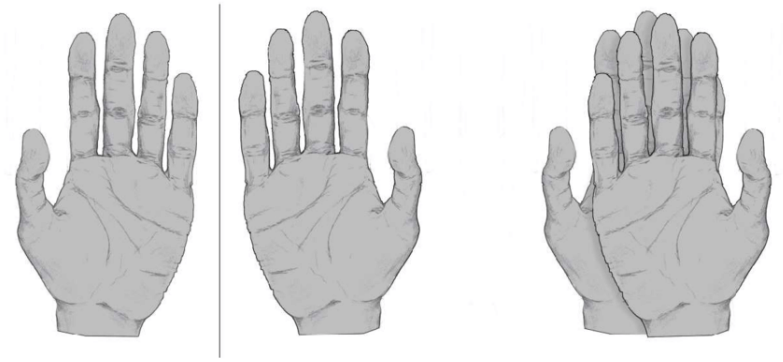


Figure 1.1: A diagram showing two opposite hands, and the impossibility of superimposing them. The fact that opposite hands are mirror-images of one-another, combined with the fact that they cannot be superimposed, makes hands chiral objects. Reproduced under creative commons from M. Karras [29].

Objects which are not chiral, said to be *achiral* or more rarely *amphichiral*, lack this property. The mirror reflection of an achiral object is perfectly identical to the original, and can always be rotated and translated such as to overlap with it.

Chiral Interactions

Oppositely-handed chiral objects are identical up to this non-superimposability with their reflection, and this means they have identical interactions with non-chiral objects [30]. For example, an achiral glove with nothing distinguishing the back- from the palm-side will be able to fit either hand just as well. Chirality reveals itself when a chiral object interacts with another chiral object. A chiral glove with a distinct back- and palm-side will only fit properly on one hand. If it is put on the wrong hand it will be upside down, the little finger of the hand will be in the thumb of the glove, and so on. Similarly, it is strange to shake a right hand with a left hand; either the palms will face the same way, or one will be upside down. This concept is very general: chiral objects are identical up to interactions with something that is either chiral [4] or that provides some chiral measurement [18]. This idea will be further developed in chapter 2.3.

Formal Definitions

Formal mathematical definitions of chirality arise from group theory. However, more casual descriptions of chirality, as eluded, are all that is needed to understand this work. Nevertheless, it may be interesting to dip in to this more 'fundamental' literature. Why exactly do reflections have this 'special' property of being able to transform one object into a different one?

The formal definition of chirality hinges upon the concept of an *isometry*; a geometric transformation which preserves the scale of an object on which it operates. We can classify isometries as either being 'direct' isometries, such as proper rotations and translations, or as 'indirect' isometries, which (in three dimensions) include planar reflections, improper rotations (composed of a planar reflection and a proper rotation) and both axial and point inversions [31]. Direct isometries are distinguished by the property that they can always be expressed as the square of another isometry. In other words, there exists some other isometric transformation that, when performed twice, gives the same final result as the isometry in question. For example, a matrix expressing a rotation about an axis of 180° can be expressed as the square of a matrix which expresses a rotation about the same axis by 90°, and both of these operations leave the total volume of the object rotated unchanged.

By contrast, a reflection is an indirect isometry, since there is no operation which, when performed twice in succession, can amount to a reflection. If we move each point of a three-dimensional object through a mirror plane as if we were about to reflect the object, but then stop half way, we flatten the object, and so the operation is singular and not an isometry. Formally, a chiral object is one which is not symmetric under *any* indirect isometries. For example, in three dimensions, a chiral object will be asymmetric under planar reflections, point inversions, axial inversions and improper rotations; all indirect isometries. Since a chiral object lacks inversion symmetries it must, by definition, also be non-centrosymmetric [32].

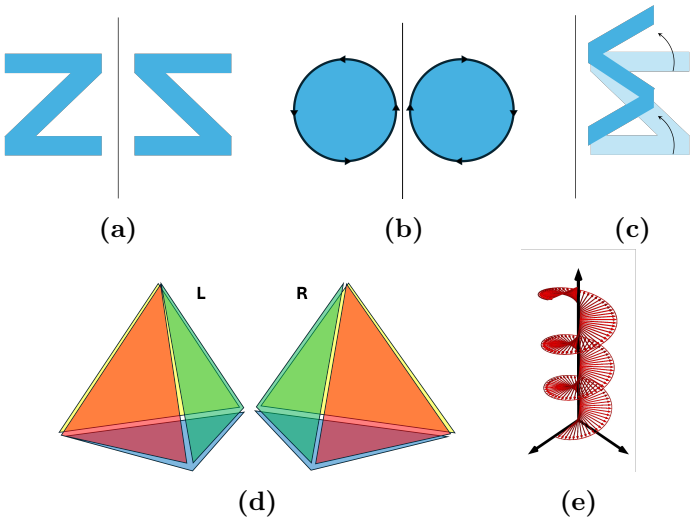


Figure 1.2: Examples of chirality in 2-dimensions, including (a) a Z shape, and (b) a rotating circle, which exhibit so-called *pseudo*-chirality in 2-D since they are non superimposable via direct isometries, but transform into one-another upon time reversal. Contrast a Z shape in 3-dimensions (c), which enables one figure to be transformed into the other by a rotation. (d) shows how tetrahedrons, when each side is distinct, exist as two non-superimposable reflected forms. (e) shows a helix, which is a chiral shape in 3-D.

Within Euclidean geometries, chirality exists in any number of dimensions greater than one. In 2-D space, chiral objects must be *bounded* (*i.e.* non-infinite) and lack an axis of symmetry. In 2-D, L and Z shapes are chiral (see figure 1.2), as are scalene triangles (but not isosceles or equilateral triangles, since these possess axial symmetry). None of these objects are chiral in three-dimensional space: in any N-D space, any object occupying fewer than N dimensions can not be chiral since it is symmetric under reflection in the $(N-1)$-dimensional hyperplane containing it. For a Z shape, for example, to be chiral in 3-D, the shape must have a defined orientation perpendicular to its plane: the bottom must be distinguishable from the top [5, 6]. More conventional 3-D chiral objects include helices, Möbius strips, hands, and tetrahedra with 4 distinguishable faces (see Figure.1.2).

Another way of understanding this is that isometries which are *indirect* in N-dimensions can always be expressed as a direct isometry in $(N+1)$-dimensional space. Line reflections in 2-D are equivalent to rotations about an axis in 3-D, and reflections through a plane are equivalent to a rotation about a plane in 4-D. Therefore, a chiral 2-D object which is not symmetric under any indirect isometry in 2-D, gains a path of direct isometries between its two 'enantiomorphs' in 3-D, becoming achiral. Perhaps more unsettlingly, 3-D enantiomorphs such as hands can also be connected via rotations through a fourth dimension.

Chiral Phenomena in Physics

Chiral effects arise in a multitude of contexts within physics. Fundamental particles have spins which, when combined with linear momentum, makes them chiral objects [33]. Storm systems will have reversed chirality in different hemispheres [34] thanks

to the distinguishability of their top and bottom side, and spiral galaxies can be said to be chiral when combined with their velocity as they move towards or away from us [35, 36].

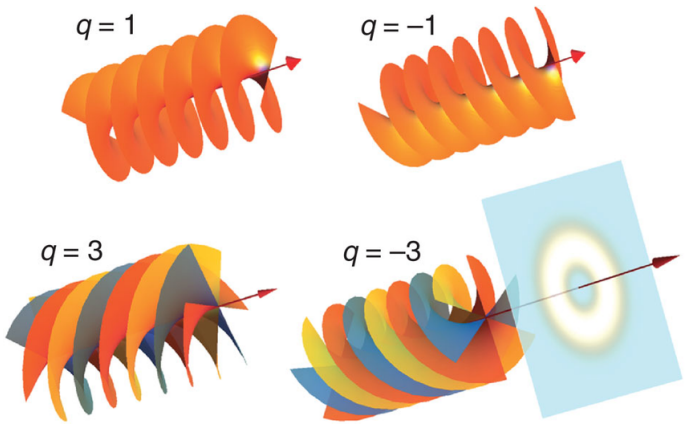


Figure 1.3: A diagram showing the helical wavefront of an optical vortex, which is a chiral object analogously to circularly polarised light. Vortex beams, unlike circularly polarised light, can also have topological indices greater than one, corresponding to a wavefront consisting of double, triple or higher helices. The above figure corresponds to the right- and left-handed wavefronts of vortex light with topological index 1, -1, 3 and -3, and the axial intensity distribution of vortex light (bottom right). Reproduced under creative commons from A. Ambrosio [37].

The spins of particles such as electrons and photons is, in and of itself, a chiral phenomenon only in 2-dimensions. When combined with a linear momentum to form a 'helicity', however, particles of opposite spin become oppositely chiral [33]. This, and the chirality of galaxies, illustrate the distinctions between chirality in 2- and 3-dimensions.

In the case of photons, photon momenta are forbidden from being zero, and so photons are always chiral in any frame of reference. Equivalently, in the classical electrodynamic picture, electromagnetic waves can be chiral [33]. In the simplest case, that of circularly-polarised light, the tips of the electric field vector at points along the direction of propagation draw a helix around the axis of propagation of the wave (see Figure 1.2 (e)). If you look down the axis of propagation of the wave, reflecting the wave in a plane containing the propagation axis will reverse the sense of this helix, turning left-handed circularly polarised light into right handed and vice-versa: circularly polarised light is chiral. This chirality manifests when circularly polarised light (or elliptically polarised light, which is also chiral for the same reasons) interacts with chiral media [38]. Absorption and phase-velocity of circularly polarised light in a chiral medium differs between left- and right-circularly polarised waves, leading to circular dichroism (CD) and circular birefringence respectively [11]. Such effects are known generally as 'optical activity' (see chapter 2.2.2).

As well as the helicity of the loci traced by field vectors in circularly polarised light, light can also be chiral by having a helical wavefront, as in the case of so-called 'vortex beams' [39] (see figure 1.3). Such beams can be thought of as possessing *or-*

bital angular momentum, in contrast to the *spin* angular momentum possessed by circularly polarised beams, and vortex beams can also be subject to chiral effects [40, 41]. An interesting thing to note is that, while elliptically polarised light can be only left- or right- handed, corresponding to the two values of spin angular-momentum accessible to a photon, vortex beams can have arbitrarily large topological indices, corresponding to arbitrarily large values of orbital angular momentum and associated separate helical wavefronts (see Figure1.3). Furthermore, the helical wavefront gives rise to a 'doughnut'-shaped intensity profile, since the phase-fronts intersect along the optical axis, and so the intensity of the beam must vanish lest the phase be multivalued [39].

1.1 Chirality in Chemistry and Biology

Molecules are discrete collections of atomic nuclei in physical space, bound together by clouds of electrons. As such, they are inherently geometric objects. The geometry of molecules and the spatial distributions of electrons are largely what determines how molecules interact. This means that not only *can* molecules be chiral but that oppositely handed chiral molecules interact differently with other chiral molecules [5, 6]. Twin enantiomorphs of a molecule are known in chemical terminology as *enantiomers* [3].

Opposite enantiomers have exactly the same mass, energetic structure (down to a vanishingly small correction due to parity violations [42–44]), and identical intermolecular interactions (among similarly handed molecules). This means that pure samples of opposite enantiomers have identical physical properties, such as melting and boiling points [45], will behave identically in achiral solvents, and will undergo the same reactions and have identical reactivities with achiral molecules.

This is of particular significance amongst organic molecules. The ability of carbon atoms to bond with (typically) four others allows for large, complex arrangements which are more likely to be chiral, which contrasts with inorganic molecules. Inorganic molecules are typically smaller, and their simple structures often preclude (with a few exceptions, such as transition metal complexes [46]) chiral chemistry.

1.1.1 Introduction to Isomerism

Chirality in chemistry forms a subcategory of the broader phenomenon of isomerism [47, 48].

Isomers refer to molecules which contain the same numbers of different types of atoms, but arranged differently. The most basic form of isomerism is *structural* isomerism, where structural isomers have the same atoms but different chemical connectivity; different bonds [49] (see fig 1.4). The concept of isomerism was discovered by Friedrich Wöhler when he found that the elemental composition of both silver fulminate and silver cyanate were identical, AgCNo [50]. The two compounds have different properties (silver fulminate is explosive, while silver cyanate is not), due to the different arrangement of the carbon, nitrogen and oxygen atoms within the fulminate and cyanate ions. Structural isomerism is very common among organic

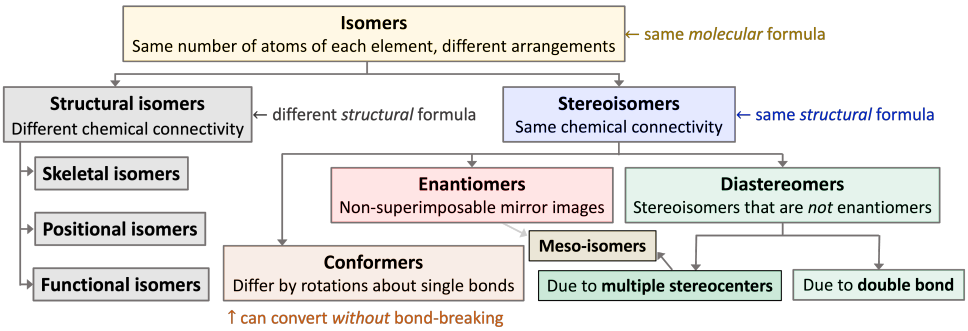


Figure 1.4: A key showing relationships between different forms of isomerism. Adapted from teaching materials by David Ayuso.

molecules, which contain many carbon atoms each bound to up to four others. This can be via alternative branching of carbon-carbon chains (skeletal isomers), different positions of particular functional groups (positional isomers), or arrangements of atoms giving rise to different functional groups (functional isomers) [49].

Another more subtle category of isomerism is stereoisomerism, where molecules share the same types of atoms and the same chemical connectivity, but a different arrangement of atoms in space [51]. Stereoisomerism comes in the form of enantiomers, which exist as non-superimposable mirror-image pairs, and diastereomers, which includes all other forms of stereoisomerism [52]. Stereoisomerism usually exists due to restricted rotation about bonds within the molecule, which prevents continuous deformation of one stereoisomer into another. For example, E and Z isomers correspond to arrangements of groups about planar double-bonds which cannot rotate [3].

Chiral Centres

In organic molecules chirality most commonly arises from the presence of a carbon atom attached to four distinct groups in a tetrahedral arrangement [53, 54]. Just like a tetrahedron with four differently coloured faces, this will have two different absolute configurations; two opposite enantiomorphs (see figures 1.2 and 1.5). Such a chiral carbon atom (or indeed any atom in an analogous position) is known as a stereocentre or *stereogenic* centre [3].

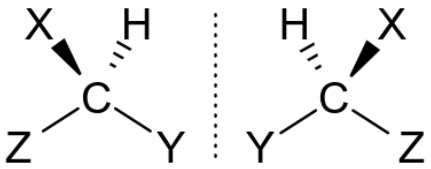


Figure 1.5: Carbon atoms can form covalent bonds with up to four other atoms, typically in a tetrahedral arrangement. If all four of these substituents are unique, then reflecting the carbon atom will result in mirror image that cannot be made to coincide with the original: such centres exhibit chirality. Reproduced from Wikipedia under creative commons [55].

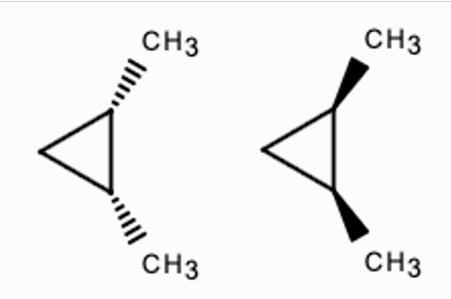


Figure 1.6: Since the two stereogenic centres of cis-1,2-dimethylcyclopropane are mirror images of each other, reversing the absolute configurations of both centres will transform one into the other, and so the molecule is not chiral but a 'meso-isomer'.

A molecule with one such stereogenic centre will have two enantiomers, but molecules can also have more than one stereocentre. In such cases, the absolute configurations about N stereocentres will give rise to a family of 2^N *stereoisomers*. Members of such a family of molecules with absolute configurations reversed at each stereogenic centre will be opposite enantiomers of one another, but other arrangements will be *diastereomers* which can have distinct physical properties (including melting/boiling points and densities) since they are not mirror images of one another [52]. However, molecules with an even number of stereogenic centres can still be achiral if two of the stereogenic centres can be transposed into one-another under a mirror reflection (combined with any other set of transformations) [56]. For instance cis-1,2-methylcyclopropane (figure 1.6) has two chiral carbon atoms which are mirror reflections of each-other. If you plane-reflect the entire molecule, it can always be rotated such that one chiral centre will take the place of the other, reproducing the original structure. Such a molecule is known as a 'meso-isomer', however the two other diastereomers within the 1,2-cyclopropane family (the trans isomers), are enantiomers since both chiral centres have the same absolute configuration [3].

Although chiral centres are most commonly carbon atoms in organic molecules, they do no have to be. Sulfoxides, which consist of a sulphur atom bonded to one oxygen and two carbon atoms, can be chiral about the sulphur atom thanks to their trigonal-pyramidal structure [57]. Beyond organic chemistry, transition metals can act as stereogenic centres of complexes with a chiral arrangement of ligands [46].

Non-Central Chirality

Aside from so-called *central* chirality, chirality can also arise in molecular structures due to chiral *axes* (eg. 1,1'-Bi-2-naphthol) [61], *planes* (eg. trans-cyclooctene), or due to inherent chiral curvature of the molecule (eg. helicenes) [52, 62, 63] (see figure 1.7):

For example, axial chirality arises from a non-planar arrangement of the molecule about a chiral axis, rather than a chiral centre. In BINOL the two biaryl moieties restrict rotation about the connecting carbon-carbon bond which, together with the

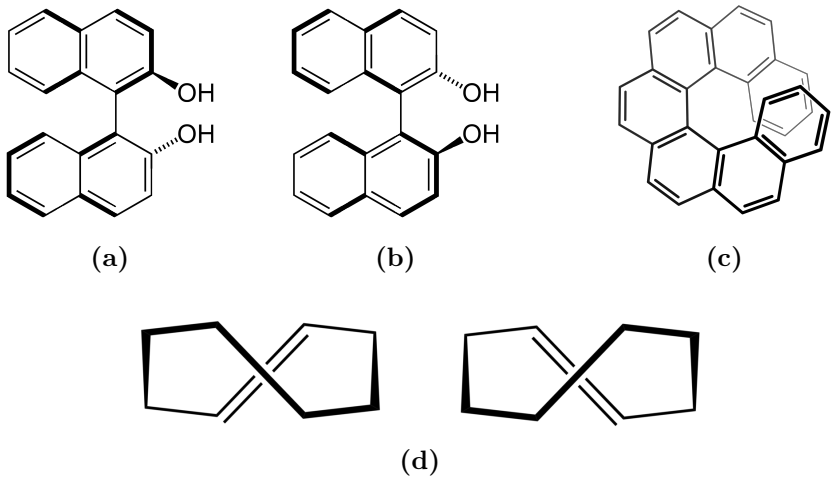


Figure 1.7: Examples of non-central chirality in molecules. (a) and (b) show opposite enantiomers of 1,1'-Bi-2-naphthol(BINOL), which exhibit axial chirality. (c) shows helicene, which is chiral by dint of its overall helical shape, while (d) shows trans-cyclooctene which has planar chirality. Reproduced from Wikipedia under creative commons [58–60].

molecules asymmetry about the axis of this bond, makes it chiral [3, 52]. Alternately, trans-cyclooctene is chiral by dint of its double bond restricting the twisting of either side of the molecule smoothly between two enantiomorphic conformers.

Chiral Chemical Interactions

Just as oppositely handed enantiomorphs interact differently with other chiral objects, chiral molecules are observed to behave differently when interacting with chiral reagents [65] (see figure 1.8), including other chiral molecules and chiral electric fields [20, 66].

This includes other molecules of the same chiral compound: Although intermolecular interactions between left- and left-handed molecules will be identical to those between right- and right-handed molecules, these will both differ from the interactions between left- and right-handed molecules. This means that mixtures of enantiomers will differ in density [67], melting points [68], boiling points and solubilities from enantiomerically pure samples, and that these properties will depend on the degree of abundance of enantiomers relative to one another (but not on the sense of the overabundance; a 60:40 mixture will behave the same as a 40:60 mixture, for example) [45, 69]. An exact one-to-one mixture of two opposite enantiomers is known as a *racemic* mixture, while if a mixture of enantiomers has more of one and less of the other it is known as a *scalemic* mixture [3]. With respect to one enantiomer, a solution which has an overabundance of a specific enantiomer is *enantioenriched*, and if there is only one enantiomer present then the sample is *enantiopure* [70].

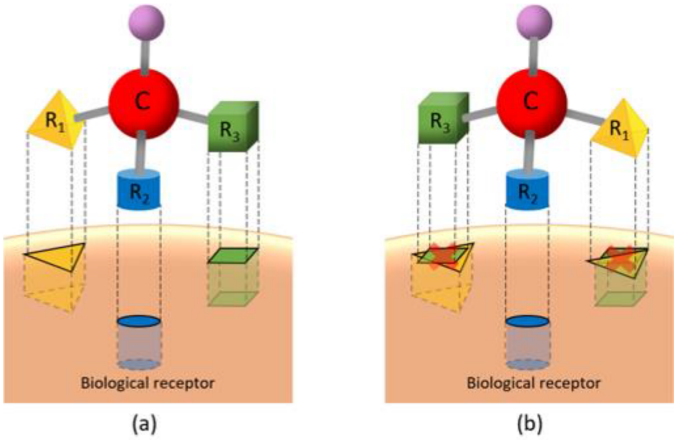


Figure 1.8: Chiral molecules may react differently with another chiral reagent, in this case a receptor site with a chiral shape. (a) Shows compatibility of a chiral ligand with a receptor while (b) shows incompatibility of the oppositely handed ligand with the same receptor. Reproduced under open access license from MDPI [64].

Conformational Isomerism

Most chiral molecules are large organic molecules, since large size and the chemical connectivity of carbon allows for there to be more chiral centres. These features also mean that many chiral molecules have several carbon-carbon single bonds formed by the overlap of sp-3 orbitals. These 'σ'-type bonding orbitals are azimuthally symmetric, and lack off-axis electron density, and this makes them free to rotate (unlike π-bonding orbitals which have off axis electron-density, which inhibits free rotation) [70].

Since these bonds can rotate freely, this can allow multiple arrangements whereby atoms in a molecule can be in different positions within space but retain the same chemical connectivity (*i.e.* bonding) [71, 72]. These arrangements are differentiated by the differences in potential energy caused by mutual repulsion of the electron clouds surrounding substituent groups of the carbons of the rotating bond. The potential energy surface of the molecule has local minima, which are stable or meta-stable conformations, conformers, as well as local maxima, which are the transitional states between these conformers [73, 74] (see figure 1.9).

Since the interactions driving these energy differences are relatively long-range and weak, the energy barriers between adjacent local minima are small, and so different conformers are able to readily interconvert, as the relevant single-bonds rotate about their axes [75]. This contrasts other stereoisomers where such inter-conversion requires bond-breaking. The intermediate case is that of 'atropisomers', which have bonds which, while very stiff, can still rotate without breaking [76]. At a sufficiently high temperature, the energy stored in the vibrations and rotations of the molecule are sufficient to rotate the bonds through the different conformers, and so a dynamic equilibrium is established whereby the different conformations coexist in proportions determined by the energetics of the different conformers [73]. Conformers can be opposing enantiomorphs, as in hydrogen peroxide, or diastereomers

as is more typically the case.

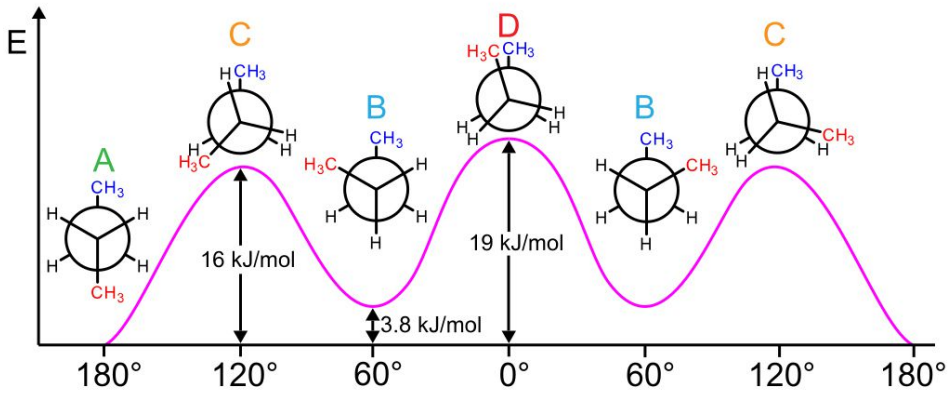


Figure 1.9: Conformational isomers of butane, showing relative energy differences. Reproduced from Wikipedia under creative commons [77].

1.1.2 Chiral Biochemistry

Perhaps chirality in chemistry would be merely an obscure quirk of geometry if it were not the case that most biological matter is chiral, being composed of large and complex organic molecules with often viciously convoluted stereochemistry [53, 78]. Most amino acids and sugars are chiral, and these molecules make up the various proteins and carbohydrates which form the greater body of biological matter [79]. Not only is the double-helix shape of DNA chiral, but the nucleobases and the ribose which makes up DNA strands are chiral *themselves*, such is the ubiquity of chirality within biochemistry. This is not coincidental, for achiral polymers to form from chiral monomers would require alternating pairs of opposite enantiomers, which would make things like DNA replication and protein synthesis much more complex [79]. The consequence of all of this is that biological systems are very much chiral environments, and so the behaviour of chiral molecules within biological environments can differ greatly between opposite enantiomers [7].

One classic, and illustrative, example of this in action is the fact that many odorous chiral compounds exhibit a different scent than their oppositely-handed twin. The human sense of smell is thought to arise from molecules binding to receptors in the nasal cavity, and this interaction depends on the geometry of both the molecule and receptor in question, like a key in a lock [80]. Both the molecule and the receptors are chiral, and this means that opposite enantiomers bind differently to scent receptors, and are thus perceived as having different odours [81]. For instance, opposite enantiomers of the chiral molecule carvone (see figure 1.10) can smell either of caraway seeds or of spearmint, while opposite enantiomers of

fenchone are responsible for the odours of fennel and some varieties of wormwood [82, 83].

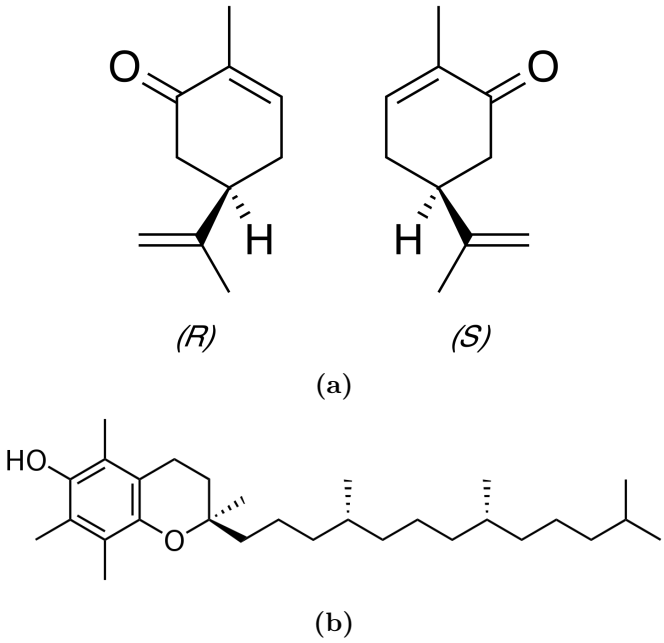


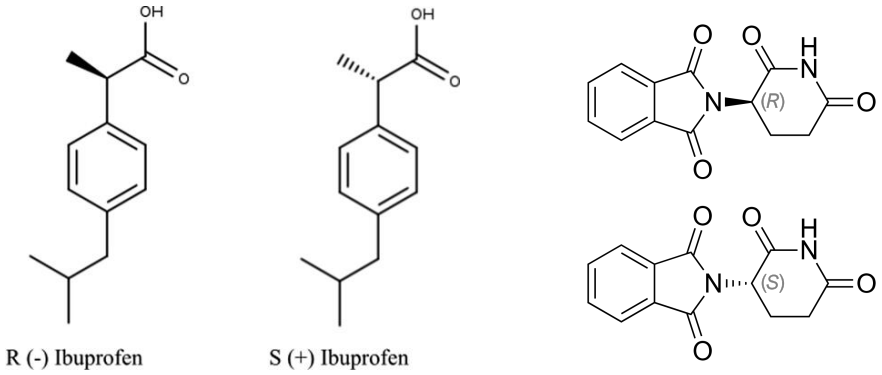
Figure 1.10: Examples of chiral molecules relevant to biology. (a) shows the two enantiomers of the molecule carvone, which is *centrally* chiral: the carbon atom within the ring attached to the propenyl moiety is a stereogenic centre. *(R)*-carvone has a minty odour while the *(S)*-enantiomer smells closer to caraway or dill. (b) shows the structure of *(R,R,R)*-αtocopherol, also known as vitamin E, which has three stereogenic centers; two along the chain, one where the chain attaches to the ring. Reproduced from Wikipedia under creative commons [84, 85].

Another interesting example of chiral effects in biochemistry is that of α-tocopherol, otherwise known as vitamin E [86]. This molecule has three chiral centres and thus has a family of eight stereoisomers, in four pairs of enantiomers (see figure 1.10). The most common form in nature, which is also the most effective, is the thrice-right-handed configuration, while its enantiomer (the thrice-left-handed configuration) is the least effective. Other intermediate configurations fall somewhere in between in their efficacy [87, 88]. Synthetic vitamin E is a racemic mixture of all isomers, and so is less effective than the naturally sourced (and thus enantiopure) version for the same dosage [89].

Chiral Pharmacology

The at-times radically divergent behaviour of different enantiomers in the strongly chiral environment of the human body has vital importance on the action of different medicinal compounds [90–94]. Opposite enantiomers can behave very differently to each other throughout the transportation and metabolism of the drug (pharmacokinetics), and have different effects upon the cells and tissues of the body (pharmacodynamics)[95–101]. Within the jargon of pharmacology, the enantiomer which has the desired effect is known as the eutomer, and the less desired enantiomer

is known as the dystomer, relative to the desired effect of the compound [102].



(a) (b)

Figure 1.11: Examples of chiral drugs. (a) shows the two enantiomers of ibuprofen. The right-enantiomer is converted into the left- within the body, so the drug's chirality is irrelevant to its usage. (b) shows the two enantiomers of thalidomide. *(R)*-thalidomide (top) is an effective sedative, *(S)*-thalidomide (bottom) is teratogenic. The molecule has a chiral centre on the glutamine ring (right) where it connects to the phthalimide moiety (left). Reproduced from Taylor & Francis Publishing and Wikipedia under creative commons [103, 104].

In many cases, the dystomer has largely benign effects. Right-handed salbutamol is a bronchodilator used to treat acute asthma attacks, while the dystomeric left-handed form of the drug is simply worse at doing the same thing [98]. The right-handed dystomer of the non-steroidal anti-inflammatory agent ibuprofen (see figure 1.11) is converted into the left-handed eutomer *in vivo*, and so the chiral nature of ibuprofen is irrelevant to its use [105].

Unfortunately, dystomers do no always have such benign effects [106–109]. Eutomeric ketamine is used as a dissociative anaesthetic, while eutomeric methamphetamine can be used as a nasal decongestant since it binds to neurotransmitter receptors in the synapses of the nose, resulting in vaso-constriction (narrowing of blood vessels) in soft tissue surrounding airways. Dystomeric ketamine can instead induce hallucinations and euphoria, whilst dystomeric methamphetamine binds much more strongly to receptors in the nervous system, making it a powerful and highly addictive stimulant [110, 111].

Perhaps most notorious is the case of the sedative thalidomide (see figure1.11), once prescribed to pregnant women to treat morning sickness. The dystomeric form is a *'teratogen'* that causes mutations and malformations in foetuses [90, 112]: infants born from mothers who took thalidomide are much more likely to have birth defects, most commonly malformed hands and limbs. Even if only the eutomer is given to a pregnant woman, the compound is 'racemized' [113, 114], becoming an even mixture of the two enantiomers, when dissolved in water. *Even enantiopure thalidomide is potentially extremely harmful to pregnant women and their unborn infants* [115].

Despite these tragic complications, thalidomide still finds use as a treatment for leprosy in many developing countries [116, 117], particularly in Latin America, and

also has potential in treating some cancers [118, 119]. This highlights the fact that which enantiomer is desirable and which is not depends entirely on the circumstances of the drug's use, and whether or not adverse effects of the dystomer are relevant or acceptable depending on the circumstances of use.

Conclusion

In this chapter, I have given an overview of the origins and importance of chirality throughout the natural sciences. Initially, I introduced chirality as a geometric property of objects, and explained the mathematical foundations of chirality as a general property in spaces of arbitrary dimensionality. Then, I gave an overview of how chirality as a geoemtric property manifests throughout physics, with a particular emphasis on chiral phenomena involving light and electromagnetism, which will become vital later.

Section 1.1 explored the ways in which chirality arises in chemistry and biology. This necessitated an explanation, in section 1.1.1, of the various kinds of isomerism in chemistry, from structural isomers to stereoisomers, and from enantiomers to conformers. This section describes in detail the ways in which molecules may exhibit chirality, from central chirality to axial and planar chirality, how chirality manifests in chemical interactions, and an exploration of situations in which molecules have multiple chiral centres. Finally, in section 1.1.2, we describe the manifestations of chirality in the sphere of perhaps the greatest importance to humans; biology and pharmacology. I illustrate how different enantiomers can behave distinctly within the highly chiral environments of biological systems, with the illustrative examples of opposite enantiomers with different odours and the differing efficacy of diastereomers of vitamin E. I then give a brief introduction into the fundamentals of chirality in pharmacology. Through the lens of eutomers and dystomers, we see how opposite enantiomers can behave differently throughout pharmacokinesis and pharmacodynamics from benign situations (such as salbutamol) where a dystomer is relatively harmless to the tragic example of thalidomide, where the dystomer is not only extremely harmful but the molecule is racemized in an aqueous solution. Nonetheless, our understanding of chiral pharmacology must be informed by the desired effects of any chiral drug and what side-effects are important in any given use-case. This all gives a vital motivation as to why chirality is an important area of study. In the next chapter, we turn towards methods by which we can study chirality in chemical substances using electromagnetism as a probe. This will require an overview into light-matter interactions, beginning with electrodynamics, before moving on to linear and non-linear optics, and then an exploration of chiroptical methods.

Chapter 2

Chiroptical spectroscopy

Chirality plays a crucial role in chemistry [65], medicine [90–94], and biology [7], with both beneficial applications and potential risks for human health [106–109]. However, telling apart substances with the same melting points, boiling points, solubilities and essentially the same energetic structure [45] can be challenging [7]. Indeed, chirality only reveals itself in interactions with other chiral objects [5, 6], and so techniques aiming to distinguish different enantiomers need to present either a chiral reagent [20, 66, 120] of some kind or a measuring setup which is itself overall chiral [18].

While there are non-optical techniques, such as chiral chromatography [121], for distinguishing enantiomers, methods that rely on electromagnetic radiation offer distinct advantages [122–124]. Notably, light-based techniques for chiroptical spectroscopy do not require chemical transformations or reactions of the sample molecules. These methods can provide highly versatile and sensitive measurements, with the added benefit of achieving temporal resolutions that would be unattainable through other means [18]. As a result, chiroptical spectroscopy stands out as a powerful approach for studying chirality and differentiating enantiomers without altering the samples themselves.

2.1 Light-Matter Interactions

To understand better how light might be used as a probe of molecular chirality, it may be useful to review some of the fundamentals of how light interacts with matter. Light can be thought of both as a collection of particles, photons [125, 126], and as being comprised of a wave [127] propagating through the electric and magnetic fields [128]. The dynamics of electric and magnetic fields are governed, in the classical regime, by Maxwell's equations of electrodynamics [128].

Relatively intense forms of light are typically best modelled as waves in the classical picture, while the particle nature of light becomes relatively more important when total intensity, and so the total number of photons, is low [129–133]. For our purposes we do not need to consider the quantum nature of the electromagnetic

field on the whole, since we will be considering forms of light sufficiently intense to be examined in the classical regime [134]. However, absorption and emission of individual photons is still relevant on the level of individual molecules [135]. We will be modelling molecular systems quantum-mechanically, but electric and magnetic fields classically [136]; a 'semi-classical' treatment.

2.1.1 Maxwell's Equations

The behaviour of electric and magnetic fields can be modelled in the 'classical', relativistic case using Maxwell's equations:

$$\nabla \cdot \vec{D} = \rho_f \tag{2.1}$$

$$\nabla \cdot \vec{B} = 0 \tag{2.2}$$

$$\nabla \times \vec{E} = -\frac{\partial}{\partial t}\vec{B} \tag{2.3}$$

$$\nabla \times \vec{H} = \vec{J_f} + \frac{\partial}{\partial t}\vec{D} \tag{2.4}$$

where ρ_f is the free charge density, $\vec{J_f}$ is the free current density, $\vec{E}$ is the electric field, $\vec{H}$ the magnetic field, $\vec{D} = \epsilon_0\vec{E} + \vec{P}$ is the electric displacement field including electric polarisation $\vec{P}$, and $\vec{B} = \mu_0(\vec{H} + \vec{M})$ is magnetic flux density including magnetisation $\vec{M}$ [137, 138].

If we assume a medium that is neutral and non conducting ($\rho_f, \vec{J_f} = 0$), and that the divergence of the electric field is zero, we can take the curl of the Faraday equation (2.3) to find the wave equation [128];

$$\nabla^2\vec{E} - \frac{1}{c^2}\frac{\partial^2}{\partial t^2}\vec{E} = \frac{1}{c^2}\left(\frac{\partial^2}{\partial t^2}\vec{P} + \frac{1}{\epsilon_0}\frac{\partial}{\partial t}\nabla \times \vec{M} + \frac{1}{\mu_0\epsilon_0^2}\nabla(\nabla \cdot \vec{P})\right) \tag{2.5}$$

and an equivalent wave equation can be derived using the curl of equation 2.4. Therefore, the optical properties of a medium depend on how a medium responds to an applied magnetic or electric field [134].

2.1.2 Linear Optics

In a classical picture, when circularly polarised light is incident upon a molecule (or solid), the electric-field component of the light exerts a force upon the electrons within the molecule, displacing them linearly from their equilibrium position and inducing an electric dipole. Concurrently, the magnetic field of the light causes the electrons to circulate, inducing a magnetic dipole. These induced electric and magnetic polarisations serve to retard the advancing wave, as well as attenuate the light by converting some of the wave-energy into electronic motion and then heat via nuclear motion. One simplifying assumption we can make is that the applied electric and magnetic fields $\vec{E}$ and $\vec{H}$ are mapped onto induced polarisation and magnetisations $\vec{P}$ and $\vec{M}$ by constant tensorial susceptibilities:

$$\vec{P} = \varepsilon_0\underline{\underline{\chi_e}}\vec{E} \tag{2.6}$$

$$\vec{M} = \underline{\underline{\chi_\nu}}\vec{H} \tag{2.7}$$

where the electric susceptibility $\underline{\underline{\chi_e}}$ and magnetic susceptibility $\underline{\underline{\chi_\nu}}$ are constant tensors of the second degree. This is the assumption of linearity; that is that there is a linear relationship between the external electric and magnetic fields and the polarisations and magnetisations induced in the optical medium [139].

We can substitute the instantaneous relations into the wave equation, assuming homogeneity and isotropy, to find the linear electromagnetic wave equation

$$\nabla^2 \vec{E} - \frac{n_\ell^2}{c^2} \frac{\partial^2}{\partial t^2} \vec{E} = 0 \tag{2.8}$$

Where $n_\ell^2 = (1 + \chi_\nu)(1 + \chi_e)$ is the linear refractive index of the material which encodes the optical properties of the medium, and does not change in response to radiation or applied fields. The solutions to this equation will be a linear sum of sinusoidal waves propagating with uniform phase velocity $v = c/n_\ell$, with refractive index n_ℓ encoding the degree to which a transmitted wave is retarded as it passes through the medium. The refractive index can also be used to determine changes in angle (refraction) and reflection at interfaces between media with different optical properties [134, 139].

Furthermore, we can consider complex susceptibilities which then give rise to a complex refractive index. The imaginary component of the refractive index is known as the extinction coefficient, and will lead to an attenuation of waves as they pass through the medium [139], while the real component constitutes our refractive index as introduced earlier.

The above derivations assume that the material reacts instantaneously to the application of an external electric or magnetic field, however this is not exactly true [140]. When a field is applied to a material, the distribution of charge and magnetic dipoles will change in response, but this will take place over a short time interval rather than instantaneously [140]. Therefore, we cannot just relate our medium's polarisation/magnetisation response to external fields by constant tensors. Instead, we can account for this non-instantaneous response by modelling magnetisation and polarisation via the convolution of a time-varying electric or magnetic field with a time-dependent tensorial susceptibility serving as a transfer function;

$$\vec{P}(t) = \varepsilon_0 \left(\underline{\underline{\chi_e}} * \vec{E} \right)(t) \tag{2.9}$$

$$\vec{M}(t) = \left(\underline{\underline{\chi_\nu}} * \vec{H} \right)(t) \tag{2.10}$$

where $*$ denotes convolution, and $\underline{\underline{\chi_e}}(t'), \underline{\underline{\chi_\nu}}(t') = \underline{\underline{0}}$ for $t' > t$ so as to obey causality. We can exploit the convolution theorem to find more convenient relations in the frequency domain

$$\vec{P}(\omega) = \varepsilon_0 \underline{\underline{\chi_e}}(\omega) \vec{E}(\omega) \tag{2.11}$$

$$\vec{M}(\omega) = \underline{\underline{\chi_\nu}}(\omega) \vec{H}(\omega) \tag{2.12}$$

Here we again make the assumption that the response of the medium is also linear, so if the electric field is oscillating at frequency ω with wave-vector $\vec{k}$, the polarisation and magnetisation will also oscillate with the same frequency and wave-vector, albeit with a different amplitude and phase. This means that the time and space derivatives of $\vec{E}(\omega)$,$\vec{H}(\omega)$,$\vec{P}(\omega)$,$\vec{M}(\omega)$ will differ only by some complex tensorial factor. We can insert our frequency dependent susceptibilities into our wave equation 2.5, and using plane-wave trial solutions recover the dispersion relation for light in a dispersive medium [140]:

$$k^2 = \frac{\omega^2 n^2(\omega)}{c^2} \tag{2.13}$$

where $n^2(\omega) = (1 + \chi_e(\omega))(1 + \chi_\nu(\omega))$ is a frequency dependent complex refractive index, assuming isotropy and homogeneity.

We can now see that the non-instantaneous response of polarisation and magnetisation to electric and magnetic fields gives rise to waves with a frequency dependent velocity, an effect known as dispersion [141]. The imaginary part of this refractive index also gives rise to frequency dependent extinction, allowing our material to be more opaque at certain frequencies while being transparent at others. When treated in this non-instantaneous manner, we can begin to find that both real and imaginary parts of the refractive index originate with the time-varying polarisation response of the material, and these two phenomena (refraction and extinction) can be linked mathematically by the Kramers-Kronig transform [142–144].

Finally, we can loosen our assumption of isotropy, which will lead to a tensorial refractive index, which will act differently on waves travelling in different directions, and with different polarisations (birefringence). These effects; refraction, reflection, extinction, dispersion and birefringence; constitute the domain of linear optics. In all of these cases, the optical properties of a medium do not change depending on the strength of electric or magnetic fields to which it is subjected. This means that waves passing through the medium cannot influence the transmission of other waves, even when they intersect. This property is known as the 'principle of superposition', and is characteristic of linear systems [145].

2.1.3 Non-linear Optics

The linear regime is not universal: for certain materials, and for sufficiently large field strengths, linearity breaks down [146, 147]. Non-linear effects in optics include optical solitons, where diffraction and non-linear self-focussing balance each other out to produce a stable propagating waveform [148], self focussing, where sufficiently intense lasers alter the refractive index of a medium such as to focus laser as it is transmitted [149], and wave-mixing, where multiple waves interact to generate signals of new frequencies [150, 151].

Wave-mixing phenomena are the effects we wish to focus on here. Once linearity no longer holds, the principle of superposition is also no longer valid. This allows optical processes involving more than two photons [150, 151], and so allows molecules to interact with optical fields with multiple propagation directions and frequency

components [152]. Therefore, in a non-linear wave-mixing process, the field can drive molecules through more than two transitions: not just up to one exited state and back (or not, as in the case of Raman scattering). This enables processes which are chiral within the electric dipole approximation [20, 153]. We will discuss this further in section 2.3.

Broadly, non-linear optical phenomena can be divided into perturbative or non-perturbative phenomena [145]. In a perturbative regime, the intensity of progressively higher-order processes decreases exponentially, and so higher order corrections can be treated as a converging series which can be truncated but retain accuracy. This can be rationalised as higher-order processes being ones requiring greater numbers of photons, and so being exponentially less probable [145]. Non-perturbative processes lack this property, and so can not be modelled with a perturbative series expansion.

2.1.4 Perturbative Phenomena

The crux of this work is to explore perturbative non-linear processes and how we might use them to study chiral molecules. As stated previously, in perturbative phenomena, non-linear effects are treated as higher-order corrections to a dominant linear response, and these higher order corrections must necessarily get progressively smaller so as the series will converge [145].

The usual treatment is to express the polarisation and magnetisation responses to electric and magnetic fields in terms of higher-order susceptibilities $\chi_e^{(n)}$ and $\chi_\nu^{(n)}$[145]. For brevity we will ignore magnetism, since magnetic fields in electromagnetic radiation tend to be much weaker and so non-linear effects which require high intensities tend to be dominated by electric-field-effects. Along with magnetism, we will also ignore terms involving electric multipoles of order two and beyond: we shall make the electric dipole approximation. Furthermore, we shall model the polarisation response as being instantaneous, since we will not be considering dispersion in our analysis.

Using these higher-order susceptibilities, we can model the non-linear polarisation response as:

$$\vec{P} = \varepsilon_0 \left(\underline{\underline{\underline{\underline{\chi_e^{(1)}}}}} \vec{E}(t) + \underline{\underline{\underline{\underline{\chi_e^{(2)}}}}} \vec{E}(t)\vec{E}(t) + \cdots + \underline{\underline{\underline{\underline{\chi_e^{(n)}}}}} \vec{E}(t)^n + \ldots \right) \tag{2.14}$$

where $\vec{E}(t)^n$ denotes the n-times tensor product of $\vec{E}(t)$, and n^{th} order susceptibility $\underline{\underline{\underline{\underline{\chi_e^{(n)}}}}}$ is a tensor of the $(n+1)^{th}$ degree.

Starting with Maxwell's equations, and assuming that electric field and polarisation divergence $\nabla \cdot \vec{E}, \nabla \cdot \vec{P} \approx 0$, we can derive the non-linear wave equation:

$$\nabla^2 \vec{E} - \frac{n_\ell^2}{c^2} \frac{\partial^2}{\partial t^2} \vec{E} = \frac{1}{\varepsilon_o c^2} \frac{\partial^2}{\partial t^2} \vec{P}_{NL} \tag{2.15}$$

where n_ℓ is the zeroth order refractive index of the material, and $\vec{P}_{NL}$ is the non-linear correction to the polarisation $\vec{P}$. If we compare to the linearised electromagnetic wave equation 2.8, we see that the left hand side of the non-linear wave

equation is the same as that of the linear wave-equation, which allows electromagnetic waves to propagate. However, the right hand side of the equation is unique to the non-linear regime, and can be interpreted as a 'source' term which can drive new oscillations [154, 155].

One illustrative example of effects which emerge from this perturbative analysis is wave-mixing. If we consider only the second order susceptibility $\chi_e^{(2)}$, and two incident waves with electric fields amplitudes $\vec{\mathcal{E}}_1$ and $\vec{\mathcal{E}}_2$ and angular frequencies ω_1 and ω_2, we find

$$\vec{P}_{NL} = \varepsilon_0 \underline{\underline{\chi_e^{(2)}}} \vec{E}(t)\vec{E}(t) \tag{2.16}$$

where (simplifying, for now, to the case of real fields and real-valued susceptibilities),

$$\vec{E}(t) = \vec{\mathcal{E}}_1 \cos(\omega_1 t) \ + \vec{\mathcal{E}}_2 \cos(\omega_2 t) \tag{2.17}$$

and so, applying some basic trigonometry,

$$\begin{aligned}\vec{P}_{NL} = \varepsilon_0 \chi_e^{(2)}((\vec{\mathcal{E}}_1^2 + \vec{\mathcal{E}}_2^2) + \frac{1}{2}\vec{\mathcal{E}}_1^2 \cos(2\omega_1) + \frac{1}{2}\vec{\mathcal{E}}_2^2 \cos(2\omega_2) + \\ \vec{\mathcal{E}}_1 \vec{\mathcal{E}}_2 \cos(\omega_1 + \omega_2) + \vec{\mathcal{E}}_1 \vec{\mathcal{E}}_2 \cos(\omega_1 - \omega_2))\end{aligned} \tag{2.18}$$

It can be seen above that the second order non-linearity allows two waves to mix, generating waves of different frequencies: the second harmonics of both waves, the sum-frequency signal (see fig 2.1), the difference-frequency signal, and a static field response (known as 'optical rectification').[145]

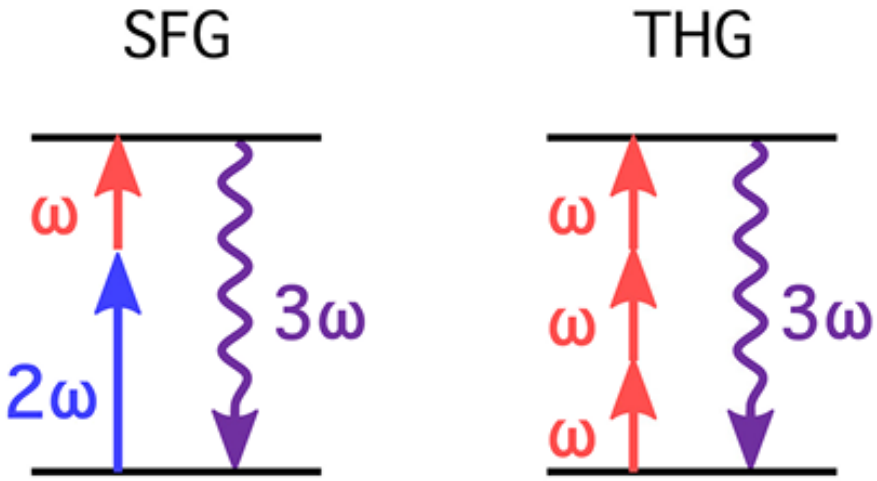


Figure 2.1: A non-linear optics energy diagram showing resonant sum frequency generation (left), a second order process, and third harmonic generation (right), a third order process. Adapted under open access from American Association for the Advancement of Science [156].

Higher-order perturbative wave-mixing, such as third-harmonic generation, can also occur, being governed by higher order susceptibility tensors $\chi_e^{(3)}$ and so on.

However within the perturbative regime progressively higher order processes reduce in strength exponentially: in order to achieve efficient emission of high-order harmonics a non-perturbative process is required.

Within both the perturbative and non-perturbative regimes, even-ordered processes are subject to symmetry constraints, which forbid them in many materials. For example, if we look again at our second-order non-linear process above,

$$\vec{P}_{NL} = \varepsilon_0 \chi_e^{(2)} \vec{E}(t) \vec{E}(t) \tag{2.19}$$

and we subject it to a parity transformation, such that all spatial features are inverted, we find

$$-\vec{P}_{NL} = \varepsilon_0 \mathcal{P}\left(\chi_e^{(2)}\right) \left(-\vec{E}(t)\right) \left(-\vec{E}(t)\right) = \mathcal{P}\left(\chi_e^{(2)}\right) \vec{P}_{NL}. \tag{2.20}$$

Thus we can see that, if the non-linear susceptibility tensor is symmetric under parity, as would be the case for a centrosymmetric medium (*i.e.* one that is symmetric under inversion), then the second-order non-linear polarisation response must vanish, necessarily along with the second-order susceptibility tensor itself. Therefore, sum-frequency generation (SFG), second-harmonic generation, difference-frequency generation and optical rectification are all parity-forbidden in centrosymmetric media [154]. This can be trivially generalised to all processes that rely on even-ordered non-linear susceptibilities, though higher-order processes (4th-order, 6th-order *etc.*) become progressively less efficient so long as the driving field remains within the perturbative regime [154]. These parity-forbidden modes are therefore observed only in non-centrosymmetric media, such as a chiral medium, or an anisotropic region of a non-chiral medium such as a boundary [157]. Note, however, that resonant SHG, and resonant SFG at surfaces are sensitive to molecular orientation (a form of anisotropy), and so molecules in a medium must be preferentially oriented along some axis for the effect to be observed [158, 159].

We can also see that when these modes are permitted due to the chirality of the medium, *i.e.* when $\mathcal{P}\left(\chi_e^{(2)}\right) = -\chi_e^{(2)}$, the non-linear emission will have opposite phase in opposite enantiomers. This makes sense intuitively: if we bring together two sets of oppositely handed molecules, the even-ordered processes of each will have opposite phase and cancel each other out, as we would expect for a racemic material.

It is also important to note that, even if an emission pathway is allowed microscopically, whether it can then be observed in the far field relies on the matching of the phase of emission from the points within a sample, or equivalently on momentum conservation from the driving beams to the emitted non-linear response.

2.1.5 Non-perturbative Phenomena

It is worth exploring some non-perturbative non-linear phenomena, as they are important to many of the recent developments in the study of chiroptical phenomena. These effects arise in the regime where the electric field of the incident light is sufficiently strong that they drive non-linear effects too large to be considered as a small perturbative correction [154]. In particular, this typically happens when electric fields associated with incoming light are of comparable strength to the internal electric fields of atoms and molecules, but not so high as to drive electrons to relativistic energies [154, 160]. These effects include above-threshold ionisation (ATI) [161], optical filamentation [162], and high-harmonic generation (HHG) [163, 164], which is perhaps the most relevant to the study of chiral molecules at this time [165, 166].

Consider a gas of atoms, struck by a high-intensity beam of light. If this should trigger various non-linear pathways, we would expect to measure a spectrum of emitted light that would correspond to the series of harmonics of the frequency of the incident laser. In a perturbative regime, we would expect to see the intensities of this emitted light to decay exponentially as the harmonic number increased, with each subsequent harmonic being some constant factor less intense than the previous. However, for a sufficiently intense laser, and for a judicious choice of target, this is not what we observe (see figure 2.2)[167–172].

Instead, we observe that successive harmonics decrease in intensity before reaching a 'plateau' (see fig 2.2), where each successive harmonic is roughly the same strength as the last, and then a cutoff where the exponential decrease resumes. This makes no sense when modelled using perturbations, and so a non-perturbative model is needed [173].

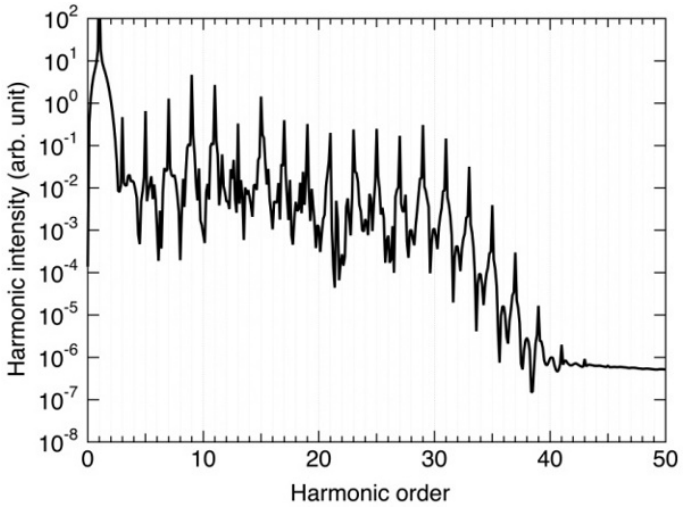


Figure 2.2: A simulated hydrogen HHG spectrum, showing a characteristic plateau of successively higher harmonic orders, up to a cutoff around the 31^{st} harmonic where the intensity of subsequent orders decreases exponentially. Reproduced under open access from IntechOpen [174].

This is typically understood in terms of the semi-classical 'three-stage model'

(see fig 2.3) [163, 175]. In sufficiently intense laser fields, the electric field of the light becomes of comparable strength to the intramolecular/intraatomic electric fields. This lowers the potential barrier keeping electrons bound to their parent nuclei, and decreases the potential of the adjacent continuum such that the electrons can 'tunnel-ionise', quantum-tunnelling into the continuum, which is step one.

Once the electron is in the continuum, it is accelerated by the driving field; first away from the parent ion but then back towards it: This is the step two. The subsequent re-collision, the third step, releases the gained kinetic energy of the electron as a short pulse of high frequency radiation. These pulses are emitted every half-cycle of the driving field, as the optical electric field changes direction.

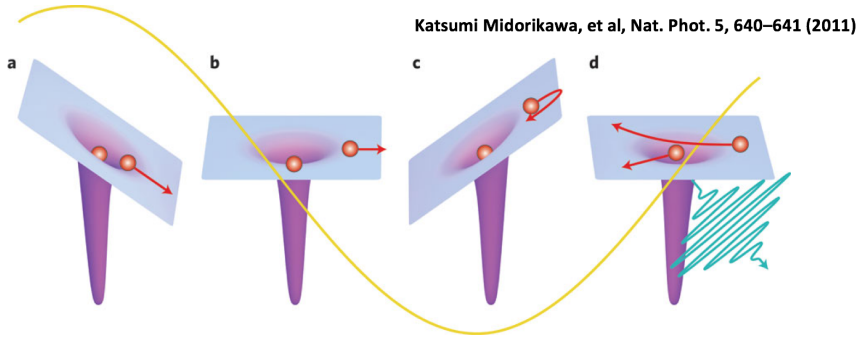


Figure 2.3: A diagram showing the semi-classical three-step conceptualisation of HHG: starting from rest (a), tunnel ionisation (b), a free electron trajectory driven by the laser field(c), and finally recombination with the parent ion, releasing a burst of radiation (d). Reproduced with permission from Nature Publishing [176]

The importance of this process lies both within the short timescale on which it occurs, and the synchronisation with the cycles of the driving field. The short timescale is useful for metrology and the study of the electronic evolution of samples with fine time resolution [177, 178]. Furthermore, since HHG causes each molecule to emit at the same point in the optical cycle, the relationship between the driving-field wavefront and the HHG emission is fixed, enabling coherent constructive addition of the HHG signal through the sample along the direction of propagation of the driving field. This process of constructive emission with a frequency comb up to very high harmonics results in a train of extremely short pulses, which can then be applied to other tasks [177, 178].

HHG is not the only important non-perturbative process, however, and it is useful to compare it specifically to multiphoton ionisation (MPI) and ATI. MPI refers to the process by which a bound electron will absorb multiple photons at once, gain energy and thereby escape the atomic potential well [163]. By contrast, ATI is when the electric field of the laser is so intense that it completely suppresses the potential barrier separating the bound electron from the continuum, and so the electron essentially 'falls-out' from its parent atom [161, 179, 180].

HHG relies on tunnel ionisation as the first step, and this restricts the laser amplitudes which can successfully drive it. ATI results in electrons ionised with more kinetic energy, spending more time in the continuum, and thus breaking the

fixed relationship with the phases of the driving field. The resulting interference with these ultra-long pathways drastically reduces the efficiency of emission [181, 182]. Meanwhile, even in strong fields, MPI behaves somewhat like a perturbative process, with the likelihood of ionisation via greater numbers of photons decreasing as a power-series [163]. This precludes the plateau seen in HHG spectra, and so MPI cannot drive HHG.

We can analyse these different regimes by considering the relationship between the amplitude of the driving field and the probability of tunnel ionisation within one quarter of a laser cycle. If the amplitude of the driving field is insufficient, then the height of the remaining potential barrier will make it unlikely that an electron will tunnel out before the field changes direction: MPI will be preferred. If the amplitude is too large, then the electric field of the laser will overwhelm that of the atom or molecule, and the electron will essentially 'fall' out of the potential well: ATI will dominate. It is only when the timescale of an electron tunnelling into the continuum is much less than half an oscillation of the driving field that tunnel ionisation, and thus HHG, is preferred; i.e. when the Keldysh parameter [183, 184]:

$$\gamma = \frac{|\tau_{tunnel}|}{\frac{1}{4\pi}\tau_{oscillation}} < 1 \tag{2.21}$$

where $\tau_{oscillation}$ is the period of the oscillations of the electric field. We can estimate the tunnelling time τ_{tunnel} by assuming that a bound electron with energy $-I_p$ tunnels through the potential barrier before emerging into the continuum where the potential of the driving field is level with the bottom of the atomic potential well, $x_0 = I_p/eE_0$ where E_0 is the amplitude of the electric field. This assumes that the Coulomb potential of the atom is small at that distance, and that the driving field is constant in space. As the electron tunnels under the barrier, it has kinetic energy $\frac{1}{2}m_e v^2 = -I_p$ and so velocity $v = i\sqrt{\frac{2I_p}{m_e}}$. Our velocity being imaginary indicates that the electron is passing through a classically forbidden region of space. We then get tunnel time:

$$\tau_{tunnel} = -i\frac{\sqrt{2m_e I_p}}{2eE_0} \tag{2.22}$$

yielding (if we ignore that our timescale is complex), the Keldysh parameter:

$$\gamma = \omega\frac{\sqrt{2m_e I_p}}{eE_0}, \tag{2.23}$$

where ω is the angular frequency of the driving field, or more commonly:

$$\gamma = \frac{I_p}{2\mathcal{U}_p}, \tag{2.24}$$

where $\mathcal{U}_p = e^2E_0^2/2m_e\omega^2$ is the 'ponderomotive' energy, which is a time average of the potential energy of an electron relative to the bottom of the potential field of passing light [185].

The Keldysh parameter defines the boundary between the multi-photon regime and the tunnel ionisation regime [186–188]; when $\gamma < 1$ tunnel ionisation is efficient

within the timescale of laser oscillations, and when $\gamma > 1$ tunnel ionisation will tend to occur too infrequently to dominate over multi-photon ionisation.

Meanwhile, when optical field amplitude E is greater than the barrier suppression threshold E_{bs},

$$E > E_{bs} = \frac{1}{4}\frac{4\pi\epsilon_0}{e^3} I_p^2, \tag{2.25}$$

the top of the potential barrier is moved beneath the ground state of the electron: this is known as 'barrier suppression'. Such a strong field will favour ATI rather than tunnel ionisation, and therefore will not produce high-harmonics as efficiently [179, 180].

2.2 Optical Activity

We return now to the domain of linear optics. Arguably, chirality as a property of chemicals was discovered via the effect chiral substances have on polarised light. In the early 19th century, François Arago [189] and Sir John Herschel [190] observed the rotation of the plane of polarised light in quartz crystals, while Jean-Baptiste Biôt observed the same happening in organic liquids, specifically turpentine [191]. This property, coined as 'optical rotation', found its use particularly in the sugar industry. Sucrose, a dimer and the primary component of refined sugar, rotates plane polarised light in the dextrorotatory (clockwise as seen looking towards the light source) direction, but when broken down in to its constituent monomers the resulting solution (known as inverted syrup) rotates plane polarised light anticlockwise (laevorotatory) [9].

The optical-rotatory technique exploits the interaction between light and chiral molecules within the linear regime. Light is not the only way one can distinguish oppositely-handed chiral molecules, but it has distinct advantages [122–124]. A common non-optical approach is to use chiral chromatography with a stationary phase with known handedness [192]. However this requires a chromatography column, it needs the molecules being studied to adsorb onto the stationary phase, it necessitates the sample to be dissolved in a fluid, and needs time for the chromatographic solution to progress through the column. Light-based methods can be faster, potentially simpler, can usually avoid having to chemically alter the sample, are not affected by the presence of achiral substances (like solvents) [124], and can be done over the course of time (e.g. to study reactions or photochemistry) [193].

The traditional all-optical methods for studying chirality make use of a group of phenomena, including optical rotation, known collectively as 'optical activity' [11, 12], whereby chiral media interact in subtly different ways with left- and right-handed circularly polarised light. Circularly polarised light is chiral, since the electric field vectors trace a helix through space (see fig 1.2). This means we can expect chiral molecules to interact differently with left- or right-handed circularly polarised light. However, on the scale of individual molecules, these differences are minute, since (unless the circularly polarised light is in the X-ray or beyond regions of the spectrum) the "pitch" of the helix of circularly polarised light is very much larger

than the scale of individual molecules (see fig 2.4), and so coupling between the chirality of individual molecules and the optical field are weak [17].

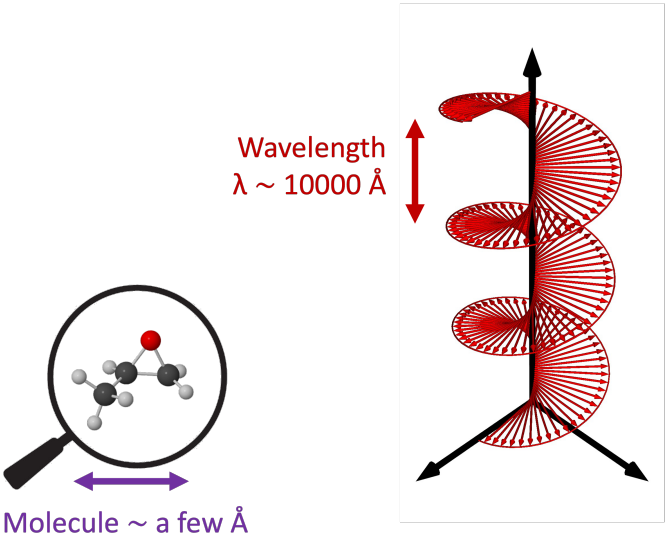


Figure 2.4: A diagram showing the helical figure drawn by the tip of the electric field vector of a circularly polarised light wave in space. Helices are chiral figures, but the length-scale of the helix of the light is much greater than that of the chiral molecule, and so the molecule hardly 'feels' the light as chiral, making CPL an inefficient chiral reagent.

Equivalently, under the electric dipole approximation (EDA), the shape drawn by the tip of a single electric field vector of circularly polarised light in space, or the Lissajous figure, is a flat circle. As we know, thanks to the nature of chirality in three-dimensions, no non-oriented two-dimensional object can be chiral since they always have reflection symmetry, and so circularly polarised light is *not* chiral within the EDA [17]. Instead, enantiosensitive interactions between the optical field and the molecules rely on magnetic interactions, as well as higher order electric field effects (quadrupole and so on). This means that the efficiency of traditional optical-activity-based methods is limited at $\sim 0.01\%$ for optical or near optical frequencies, since the samples can only 'feel' the chirality through the magnetic field of the radiation, which depends on the pitch of the helix of the light. For x-rays, more efficient enantiosensitivity is possible due to the shorter 'pitch' of the light, near the scale of the molecules themselves, such that the molecule can 'feel' the chirality more keenly [17].

Therefore optical activity within the visible or IR parts of the spectrum is most effective in samples which are either large, or highly concentrated [11], since on a molecule-by-molecule basis it is very weak.

2.2.1 Circular Dichroism

Perhaps the most straightforward expression of optical activity is 'Circular Dichroism', which is the differential absorption of left- and right-handed circularly polarised light by chiral media. This is particularly strong at frequencies close to the spectral

absorption bands of the medium. The phenomenon was first discovered and described in the early 19$^{\text{th}}$ century by Jean Baptiste Biôt, Augustin Fresnel and Aimé Cotton [191, 194].

As discussed in section 2.1.2, passing electromagnetic waves cause electrons in a substance to oscillate and circulate, inducing an electric polarisation and a magnetisation. This motion will be impeded by the electric and magnetic fields of the molecules or material involved, and this is why most substances slow and attenuate light as it passes through them. However, the combination of linear displacement and circulation caused by the combination of electric and magnetic forces acting on electrons results in a helical motion, and this helix will have opposite handedness if it is the result of left- versus right-handed circularly polarised light [195]. The molecular potential of a chiral molecule will impede left- or right-handed helical electron motion differently, and this will be reversed for the opposite enantiomer. This results in left- or right-handed circularly polarised light being impeded differently by chiral media, an effect known as 'circular birefringence' [194], and absorbed differently; 'circular dichroism' [191, 194].

Incorporating the quantum nature of the molecules, we might say the absorption of the light is due to the excitation of some transition $|g\rangle \rightarrow |n\rangle$, with excitation amplitude a_n given by:

$$a_n = -\langle n|\vec{d}|g\rangle \cdot \vec{\mathcal{E}} - \langle n|\vec{m}|g\rangle \cdot \vec{\mathcal{B}}, \tag{2.26}$$

where $\vec{d}$ and $\vec{m}$ are the electric and magnetic dipole operators respectively, while $\vec{\mathcal{E}}$ and $\vec{\mathcal{B}}$ are the time-independent components of the electric and magnetic fields respectively [11, 38].

We find the population of the excited state:

$$|a_n|^2 = a_n^* a_n = |\langle n|\vec{d}|g\rangle \cdot \vec{\mathcal{E}}|^2 + 2\Re\{\langle g|\vec{d}^*|n\rangle \cdot \langle n|\vec{m}|g\rangle\} + |\langle n|\vec{m}|g\rangle \cdot \vec{\mathcal{B}}|^2. \tag{2.27}$$

Taking the double magnetic field term $|\langle n|\vec{m}|g\rangle \cdot \vec{\mathcal{B}}|^2$ to be small, and writing electric and magnetic transition dipoles as $\vec{d}_{ng}$ and $\vec{m}_{ng}$ respectively, we average the excitation amplitude $|a_n|^2$ around unit sphere of element $\mathrm{d}\Omega$ to find orientation-averaged population, corresponding to an average over a large ensemble of randomly oriented molecules:

$$\int |a_n|^2 \, \mathrm{d}\Omega = \frac{1}{3}|\vec{d}_{ng}|^2|\vec{\mathcal{E}}|^2 + \frac{2}{3}\Re\{(\vec{d}^*_{ng} \cdot \vec{m}_{ng})(\vec{\mathcal{E}^*} \cdot \vec{\mathcal{B}})\}. \tag{2.28}$$

Here we encounter a *pseudoscalar* quantity in $\vec{d}^*_{ng} \cdot \vec{m}_{ng}$. Pseudoscalars are mathematical quantities which behave like scalars in most contexts, but are antisymmetric under operations such as inversions and reflections. This quantity is rotationally invariant and specific to a given molecule, essentially encoding the handedness of the molecule [196]. We also see a second pseudoscalar, $\vec{\mathcal{E}^*} \cdot \vec{\mathcal{B}}$, which encodes the handedness of the electromagnetic field instead of the molecule.

Since unperturbed states are pure and stationary, $|g\rangle, |n\rangle \in \Re$, $\vec{d}_{ng} \in \Re$ and $\vec{m}_{ng} \in \Im$, and rewriting $\vec{\mathcal{B}} = \hat{k} \times \vec{\mathcal{E}}/c$, we find:

$$\int |a_n|^2 \, \mathrm{d}\Omega = \frac{1}{3}|\vec{d}_{ng}|^2|\vec{\mathcal{E}}|^2 + \frac{2}{3c}(\vec{d}^{\,*}_{ng} \cdot \Im\{\vec{m}_{ng}\})(\hat{k} \cdot (i\vec{\mathcal{E}} \times \vec{\mathcal{E}}^*)) \tag{2.29}$$

where $\hat{k}$ is the unit vector in the propagation direction and $i\vec{\mathcal{E}} \times \vec{\mathcal{E}}^* \in \Re$ and is parallel to the spin of the photon, and so the triple product $(\hat{k} \cdot (i\vec{\mathcal{E}} \times \vec{\mathcal{E}}^*))$ encodes the helicity of the light [11]. The dominant, electric dipole term in the above equation does not depend on the handedness of either the field *or* the molecule. The comparatively small enantio-sensitive contribution to the absorption comes from the second term, which relies on magnetic dipole effects [197]. Within this term, we see two pseudoscalar quantities: $\vec{d}^{\,*}_{ng} \cdot \Im\{\vec{m}_{ng}\}$ which encodes the handedness of the molecule and $(\hat{k} \cdot (i\vec{\mathcal{E}} \times \vec{\mathcal{E}}^*))$ which encodes the handedness of light.

It is important to note that this chiral molecular pseudoscalar quantity $\vec{d}^{\,*}_{ng} \cdot \Im\{\vec{m}_{ng}\}$ will be different for each transition $\vec{d}_{ng}$, and so both the degree and the absolute sense of the dichroism will differ between molecules and for different wavelengths of light. It is due to this variation that using circular dichroism (and optical activity more generally) as an analytic tool relies on knowing, *a priori*, the sense and degree of dichroism to expect for a certain molecule at a certain wavelength in order to characterise a sample. It is not generally possible to determine the absolute configuration of a chiral sample using optical activity alone without first knowing the 'circular dichroism spectrum' to expect for a given molecule [198].

2.2.2 Optical Rotation

Perhaps the most widely known and widely used method to characterise chiral samples is optical rotation.

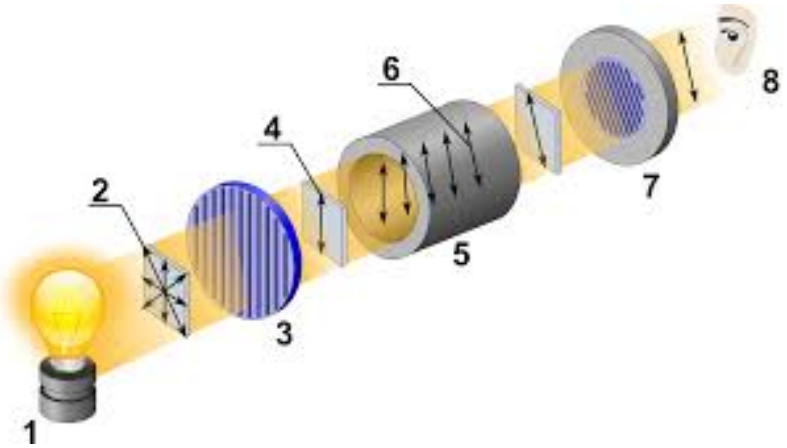


Figure 2.5: A schematic of an optical rotation setup, with unpolarised light (2) from a source (1) linearly polarised (4) using a polariser (3), rotated (7) by a sample in a container (5,6), before being measured (8) using a second polarised plate (7). Reproduced from Wikipedia under creative commons [199].

Optical rotation was discovered by François Arago in 1811, and denotes the rotation of the plane of polarisation of linearly polarised light as it passes through

a chiral medium [189]. The plane of the polarisation of this light can be seen to rotate either clockwise or anticlockwise when viewed towards the light source, and the medium is thus characterised as either 'dextro-' (right) or 'lævo-' (left) rotatory [70] (see fig 2.5).

Perhaps counterintuitively, this can be described as a consequence of 'circular birefringence'; the difference between phase velocities of left- or right-handed circularly polarised light through a chiral medium [194]. This is because linearly polarised light can be decomposed into two circularly polarised waves, one left- and one right-handed, with the phase delay between the two determining the polarisation plane of the linear wave:

$$\vec{\mathcal{E}}_{\vartheta_i} = \frac{1}{\sqrt{2}}(e^{-i\vartheta_i}\vec{\mathcal{E}}_L \ + e^{i\vartheta_i}\vec{\mathcal{E}}_R) \tag{2.30}$$

which, if $\vec{\mathcal{E}}_L = (\hat{x} + i\hat{y})/\sqrt{2}$ and $\vec{\mathcal{E}}_R = (\hat{x} - i\hat{y})/\sqrt{2}$, can be rewritten as:

$$\vec{\mathcal{E}}_{\vartheta_i} = \hat{x}\cos\vartheta_i + \hat{y}\sin\vartheta_i \tag{2.31}$$

where $\hat{x}$ and $\hat{y}$ define a basis for the plane orthogonal to the propagation direction of the linearly polarised wave, and ϑ_i is the angle of the plane of polarisation of incoming light relative to the $\hat{x}$ direction.

If we pass the wave through a medium wherein the right-circularly polarised component travels at phase speed $c^{(R)}$ and the left-circularly polarised component travels at phase speed $c^{(L)}$, after distance L the accumulated phase difference will be:

$$\Delta\phi = L\left(\frac{\omega}{c^{(R)}} - \frac{\omega}{c^{(L)}}\right) \tag{2.32}$$

$$= \frac{2\pi L}{\lambda}\Delta n \tag{2.33}$$

where $\Delta n = (\frac{c}{c^{(R)}} - \frac{c}{c^{(l)}})$ is the difference in the refractive index n of the material for right- vs left- circularly polarised light.

Therefore, as linearly polarised light with a plane of polarisation tilted by angle ϑ_i passes through the chiral medium, it will be tilted to angle ϑ_f where:

$$\vec{\mathcal{E}}_{\vartheta_f} = \frac{1}{\sqrt{2}}(e^{-i\vartheta_i}e^{-i\frac{\Delta\phi}{2}}\vec{\mathcal{E}}_R \ + e^{i\vartheta_i}e^{i\frac{\Delta\phi}{2}}\vec{\mathcal{E}}_L) \tag{2.34}$$

$$= \hat{x}\cos(\vartheta_i + \frac{\Delta\phi}{2}) + \hat{y}\sin(\vartheta_i + \frac{\Delta\phi}{2}) \tag{2.35}$$

$$\implies \vartheta_f = \vartheta_i + \frac{\Delta\phi}{2} \tag{2.36}$$

thereby rotating the plane of polarisation *anticlockwise* by $\Delta\phi/2$. The degree of differential retardation $\Delta\phi$, and thus angle of rotation, is proportional to the path length L and inversely proportional to wavelength λ, and so is stronger for light of shorter wavelength passing through larger samples.

On a microscopic scale, this can be thought of as acting via the magnetoelectric cross-susceptibilities of the material, that is the propensity for electric fields to magnetise the material and magnetic fields to polarise. These magnetoelectric elements will both give rise to different refractive indices for oppositely-handed CPL (birefringence), and will also convert electric field along one axis, via magnetisation, into polarisation along another, thereby tilting the plane of polarisation of the electric field as it propagates through the material. These processes are inherently tied to the microscopic processes underlying circular dichroism, linked by a Kramers-Kronig transform [142–144]: optical rotation can be said to be controlled by the real part of the refractive indices of the material, while circular dichroism is governed by the imaginary part (the extinction). Indeed, both processes are molecule specific and wavelength dependent, are strongest close to absorption peaks of the material, and so are often seen simultaneously [38].

Consequently, when linearly polarised light is shone through a chiral medium, it usually is not just rotated, but also becomes elliptically polarised as it passes through the material [134]. If we conceptualise linearly polarised light as a superposition of two oppositely-handed circularly polarised waves, and circular birefringence and dichroism are occurring simultaneously, one of these components will be retarded at the same time as one component will be attenuated. No longer an equal combination of oppositely handed waves, the resulting sum will be an elliptically polarised wave, with its major axis being rotated as it passes through the medium. Moreover, just as with circular dichroism, the sense of the rotation does not depend in any simple way upon the sense of the chirality of a sample. If a molecule is 'right-handed', which is in-and-of-itself an arbitrary label, this does not mean it will be dextrorotatory or vice-versa, and the same molecule can be dextro- or lævorotatory at different wavelengths [12, 200, 201].

In our discussion of optical rotation, unlike with circular dichroism, we have not discussed directly any chiral pseudoscalars. In the case of circular birefringence, we should expect to see two pseudoscalars; one encoding the handedness of the molecule, and the other encoding the handedness of the field [196]. Indeed, we would expect to use the same quantities: the imaginary components for CD and the real components for birefringence. However, although optical rotation can be understood in terms of birefringence, we cannot make sense of it using a chiral field pseudoscalar, since our electromagnetic field is linearly polarised: it is not chiral! So how can achiral light measure the chirality of molecules?

In fact, optical rotation exploits not the chirality of light but instead the chirality of the experimental setup [18]. If we consider a typical optical-rotation setup, consisting of a chiral sample held between two linear polarisers, the chirality of the setup is formed by the sense of rotation of one polariser relative to the other $\hat{e}_1 \times \hat{e}_2$ (a pseudovector), combined with the axis of propagation of light through the sample $\vec{k}$ (a vector). The combination of these two things realises a chiral pseudoscalar, but one which encodes the chirality of the experimental setup on the whole: $\vec{k} \cdot (\hat{e}_1 \times \hat{e}_2)$ (where $\hat{e}_i$ is the polarisation direction of polariser i). This 'chiral setup' pseudoscalar, together with a pseudoscalar encoding the handedness of the molecule (the same one as for circular dichroism), means we can expect our final measurement to be a scalar;

the total intensity of light transmitted by the second polariser at a given angle of rotation [202]. Twisting one polariser relative to the other so as to maximise the observed intensity measures the sense and degree of optical rotation, and thereby the chirality of the sample.

2.2.3 Non-linear and Enhanced Optical Activity

Non-linear analogues of optical activity also exist [203–206]. For example, second-harmonic generation circular-dichroism (SHG-CD) refers to a difference in the efficiency of SHG in chiral and anisotropic media when illuminated by a right- vs a left-handed circularly-polarised driving field [203, 204]. This arises due to an interference between a chiral SHG pathway, and an achiral SHG pathway that is enabled by the anisotropy of the sample. These pathways arise within the electric dipole approximation, and so can be several orders of magnitude stronger than traditional circular dichroism, being measurable even for thin films of molecules [205, 206].

Similarly, oppositely handed media will impart different phase shifts on the emitted second harmonics with left- or right- handed circular polarisation. When SHG in chiral media is driven by a linearly polarised driving field, the resulting second-harmonic signal will be rotated relative to the driver in opposite directions by an oppositely-handed non-linear medium, in a manner analogous to traditional optical rotation spectroscopy. This gives rise to so-called SHG optical rotation [203, 204].

Optical activity can also be enhanced in other ways, such as using nanophotonics and plasmon resonances to create 'superchiral' light [207–210]; circularly polarised light with tight 'twists' in the helix, which can dramatically boost the potential efficiency of optical activity.

2.3 Chirality of Reagents vs Observers

As mentioned previously, opposite enantiomers of chiral molecules behave identically unless they are interacting with some other chiral object. Therefore, all chiroptical techniques must have a chiral molecule interact with something chiral in order to realise a chiral measurement. There are two ways one might go about this; by using a chiral *reagent* which reacts differently with opposite enantiomers, or by using an experimental setup which realises a chiral *observer* [18, 19].

The first strategy is analogous to circular dichroism; the chiral reagent (circularly polarised light) interacts differently with opposite enantiomers of a chiral molecule, leading to a greater degree of absorption of circularly polarised light by one enantiomer versus the other. In this instance our observable is a scalar quantity, namely the degree of absorption.

The second strategy, using a chiral observer, is analogous to optical rotation. As explained in section 2.2.2, optical rotation features no chiral reagent, since the light is linearly polarised and thus achiral. Instead the sense of the rotation of the polarisation of the light, combined with the axis of propagation, forms a chiral setup

which can distinguish one enantiomer from the other. This is a chiral combination of achiral fields and achiral detectors [18, 196, 211, 212].

Another way of interpreting this distinction is as the identification of a molecule's chirality by scalar observables versus vectorial observables [18, 19]. When light is used as a chiral reagent, as in CD, the degree of reactivity between the enantiomer and the reagent constitutes a scalar enantiosensitive observable. By contrast, in the case of OR, the plane of polarisation of achiral linearly polarised light is rotated by the chiral medium, and the direction and magnitude of this rotation constitutes a vector observable. However, this can extend further to tensor observables, so long as we can measure them. For example, we can use an achiral two colour field which defines a non-oriented plane. The Lissajous figure of this field is a figure of eight, and our chiral observable consists of an in-plane polarisation component that breaks the symmetry of the Lissajous figure combined with an out-of-plane polarisation component and the phase between them; a quadrupole (tensor) observable [18].

These concepts can be understood in terms of the parity transformations of quantities which describe the system. The chirality of a molecular ensemble can be characterised by a pseudoscalar; this is a rotationally invariant quantity ψ that is *anti-symmetric* under parity operations:

$$\hat{\mathcal{P}}\psi \mapsto -\psi \tag{2.37}$$

In order to obtain a chiral observable, we can either have the chiral ensemble interact with another chiral reagent which will also be characterisable by a pseudovector, and the resulting observable will be a scalar: $\varsigma_{observable} = \psi_{sample} \times \psi_{reagent}$. Alternatively, to obtain a vector observable, we require an incident field to be characterisable by a 'pseudovector' $\vec{\Lambda}$, which transforms like a vector except under parity transformations where: $\hat{\mathcal{P}}\vec{\Lambda} \mapsto \vec{\Lambda}$. One example might be the normal to an oriented plane: $\vec{a} \times \vec{b}$ is normal to a plane defined by vectors $\vec{a}$ and $\vec{b}$, but if we transform $\vec{a}, \vec{b} \mapsto -\vec{a}, -\vec{b}$, we find the cross product remains unchanged. In physics, pseudovectors can include angular momentum, such as that of a photon. Therefore, we can realise this element of our chiral setup with circularly polarised light, which defines an oriented plane, normal to its helix, characterisable by a pseudoscalar, or alternatively two co-propagating beams with non-parallel planes of polarisation, which will do the same thing.

The multiplication of a pseudovector, characterising the 'chiral setup', and a pseudoscalar (characterising the incoming light) will yield a vector, which will have the opposite direction when *either* the chirality of the sample *or* the phase of the incident light are reversed. For instance, consider an interaction between a chiral ensemble and incident radiation, the polarisation of which can be defined by a pseudovector normal to the xy plane, such that an interaction between a *left*-handed ensemble and a field characterised by a psudovector pointing in the *positive* $\hat{z}$ direction yields a vectorial observable that also points in the positive $\hat{z}$ direction. A reflection in the xy plane will, while leaving the field pseudovector unchanged, transform the left -handed chiral ensemble to a *right*-handed one and reverse the sign of the vector observable (since vectors are antisymmetric under parity, see fig 2.6).

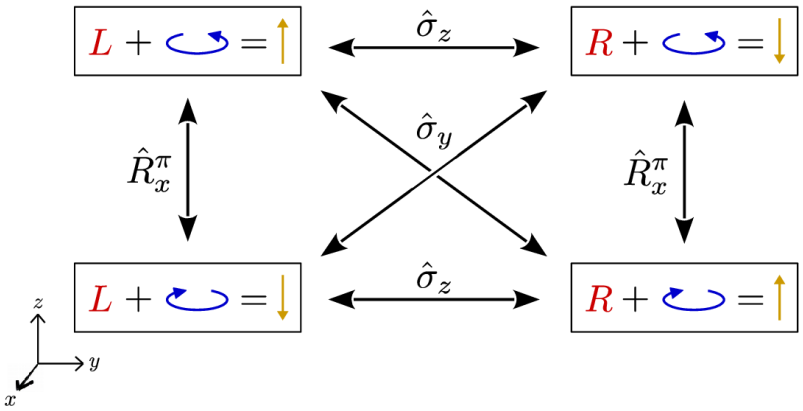


Figure 2.6: A diagram showing the behaviour of the chirality of molecule (L or R), the sense of the circular polarisation of incident light, and the resulting vector observable under various transformations: reflection in xy-plane ($\hat{\sigma}_z$), reflection in xz-plane ($\hat{\sigma}_y$), and rotation by π rad about the x-axis ($\hat{R}_x^\pi$). Reproduced with permission of APS Publishing [196].

Meanwhile, a rotation of π rad about the x axis will reverse the sign of the field pseudovector and the vector observable (since vectors and pseudovectors transform the same way under proper rotations), whilst leaving the chirality of the ensemble unchanged.

2.3.1 Photoelectron Circular Dichroism

Both CD and OR are limited in their efficiency by the fact that they rely on magnetic interactions between the molecule and the light to generate a chiral observable, and magnetic interactions are much weaker than electric interactions. In this and the following section we shall review two techniques which utilise a chiral observer and a chiral reagent respectively, but do so making use of interactions within the electric dipole approximation. The electric dipole term is the dominant term in the interaction between light and matter, and so chiroptical methods which interact with the chirality of molecules within this regime are able to be much more efficient [17].

Photoelectron circular dichroism (or PECD) is one chiral optical effect that provides chiral differentiation with high efficiencies by utilising purely electric dipole interactions [213, 214]. PECD is observed as a forward-backward asymmetry in the emission of photoelectrons from a scalemic (*i.e. not racemic*) ensemble of randomly oriented chiral molecules ionised by circularly polarised light, leading to a measurable net photoelectron current in a direction perpendicular to the plane of polarisation (see fig 2.7). In this instance, the 'chiral observer' is realised by the oriented plane defined by the spin of the circularly polarised photon (the pseudovector), together with a detector that can distinguish two opposite directions perpendicular to the plane of polarisation.

Traditionally, the asymmetry is usually described in terms of a decomposition of the angular dependence of the probability distribution of photoelectron momenta

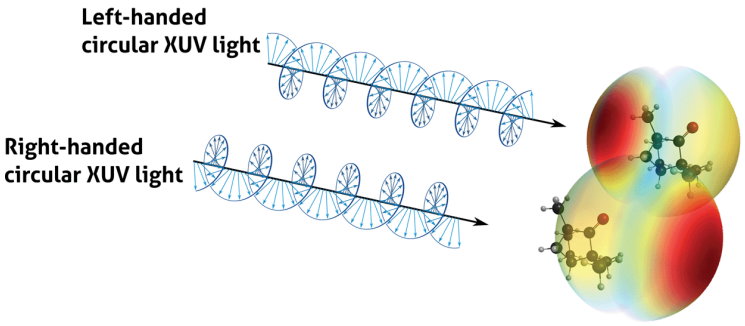


Figure 2.7: A diagram showing the photoelectron angular distribution from a chiral molecule illuminated by circularly polarised light. The chirality of the molecule creates a forward-backward asymmetry in the photoelectron angular distribution, while reversing either the chirality of the molecule or the handedness of the field will reverse the forward-backward asymmetry. Reproduced with permission from the Faraday division of the Royal Society of Chemistry [215].

as Legendre polynomials $\mathrm{P}_\ell(\cos\theta_k)$ [216]. Photoelectron current $\vec{j}(k)$ is given by:

$$\vec{j}(k) = \int \mathrm{d}\Omega_k \cdot (\vec{k} W(\vec{k})) \tag{2.38}$$

where $\int \mathrm{d}\Omega_k$ denotes integration over a solid angle and $W(\vec{k})$ is angular photoionisation probability distribution:

$$W(\vec{k}) = \sum_{\ell=0}^{2} \mathrm{b}_\ell(k)\, \mathrm{P}_\ell(\cos\theta_k) \tag{2.39}$$

$$= \mathrm{b}_0(k) \;+\; \mathrm{b}_1(k)\cos\theta_k \;+\; \frac{\mathrm{b}_2(k)}{2}(3\cos^2\theta_k - 1) \tag{2.40}$$

The resulting angular distribution has two lobes, one oriented forwards and one backwards along the axis of propagation.

If the incident radiation is linearly polarised, the sample molecules are achiral, or both, $\mathrm{b}_1(k) = 0$ (by symmetry) so the angular dependence is given by a sum of even-numbered Legendre polynomials. These are symmetrical about the plane orthogonal to the axis of propagation, so there will be no net photoelectron current along the axis of propagation. However, if the sample is chiral, and the incident light is circularly polarised, the odd-ordered Legendre polynomials are permitted. These orders are antisymmetric about the plane orthogonal to the axis of propagation, and this allows a forward-backward asymmetry in the emission of photoelectrons, and thereby a net photoelectron current along the axis of propagation [217].

In order to understand this process better at the molecular level, we can start by looking for a molecule-specific pseudoscalar ψ, which can arise either as the product of a vector $\vec{V}$ and pseudovector $\vec{\Lambda}$, or via a scalar triple product of three polar vectors in the molecular frame. Photoelectron current in the molecular frame can

be expressed as:

$$\vec{j}^{M}_{\vec{k}^{M}} = |a_{\vec{k}^{M}}|^2 \vec{k}^{M} \tag{2.41}$$

where superscripting by M or L denotes whether a value is for the molecular or lab frame respectively.

We calculate transition amplitude $a_{\vec{k}^{M}}$:

$$a_{\vec{k}^{M}} = i\tilde{\mathcal{E}} \langle \vec{k}^{M} | \vec{D}^{L} \cdot \hat{e}^{L}_{\sigma} | 0 \rangle = \frac{i\tilde{\mathcal{E}}}{\sqrt{2}} \left(\vec{d}^{L} \cdot \hat{x}^{L} + \sigma i \vec{d}^{L} \cdot \hat{y}^{L} \right) \tag{2.42}$$

where $\tilde{\mathcal{E}}$ is the Fourier Transform of the time dependent amplitude of the electric field at the transition frequency, $\vec{D}^{L}$ is the dipole operator in the lab frame, $\hat{e}^{L}_{\sigma}$ is the polarisation vector of the field with spin σ, and $\vec{d}^{L}$ is the matrix element of the transition dipole in the lab frame [196]. We can then multiply this by its complex conjugate to find:

$$|a_{\vec{k}^{M}}|^2 = \frac{|\tilde{\mathcal{E}}|^2}{2} \left[|\vec{D}^{L} \cdot \hat{x}^{L}|^2 + |\vec{D}^{L} \cdot \hat{y}^{L}|^2 + i\sigma \left(\vec{d}^{L*} \times \vec{D}^{L} \right) \cdot \hat{z}^{L} \right] \tag{2.43}$$

and then transform vectors to the molecular frame, and integrate over solid angle $\mathrm{d}\Omega^{M}_{k}$ to evaluate find photoelectron current:

$$\vec{j}^{L}(k) = \left(\frac{1}{6} \int \mathrm{d}\Omega^{M}_{k} \left[i(\vec{d}^{M*} \times \vec{d}^{M}) \cdot \vec{k}^{M} \right] \right) \left(\sigma |\tilde{\mathcal{E}}|^2 \hat{z}^{L} \right) \tag{2.44}$$

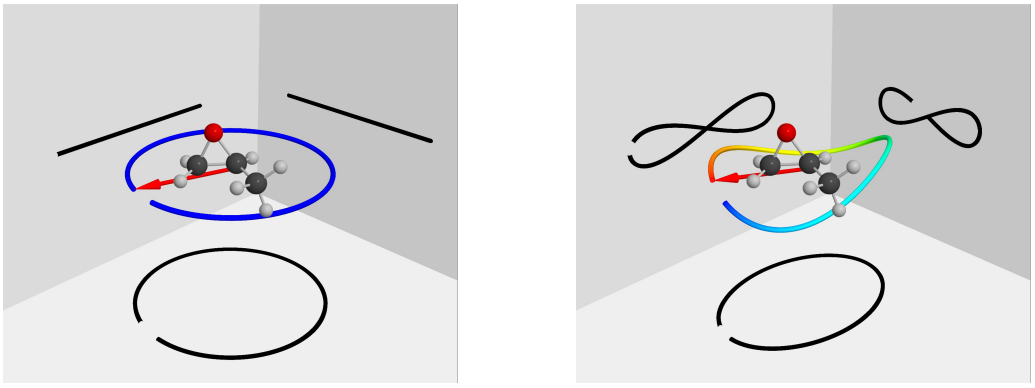
We then have a choice in construction of a chiral pseudovector, depending on whether we want to consider the phenomenon purely from the lab frame or purely from the molecular frame.

If we choose the lab frame, the chiral observer is realised by the triple product $(\vec{d}^{L*} \times \vec{d}^{L}) \cdot \sigma \hat{z}^{L}$ between the real and imaginary components of the dipole and the photon spin.

Alternatively, if we choose the molecule's frame of reference, the chiral observer is realised by the triple product $(\vec{d}^{M*} \times \vec{d}^{M}) \cdot \vec{k}^{M}$ between the real and imaginary parts of the dipole and the momentum of the photoelectron emission [218].

2.3.2 Synthetic Chiral Light

In the electric dipole approximation, if we take any point through which a circularly polarised electromagnetic wave passes, the electric field vector at that point spins through a circle. This figure can not be chiral since it possesses a plane of symmetry. As explained in section 2.2, in order for the charged particles in a molecule or substance to 'feel' the chirality of circularly- or elliptically-polarised light, we must consider the magnetic fields of the passing light. These are proportional to the rate of change of the electric field, and so rotate offset by 90° of phase from the electric field vector [134]. The magnetic and electric fields of the circularly polarised light, combined with the propagation direction of the light, form a chiral basis



(a) **(b)**

Figure 2.8: Diagrams showing CPL (a) vs SCL (b) in the electric dipole approximation. The figure for circularly polarised light is a planar circle, which is not chiral. By adding a longitudinal component, this makes the figure non-planar, which (when combined with the sense of the rotation of the field vector in time) makes the figure chiral, even within the dipole approximation [20]. Figure kindly provided by Andrés Ordoñez.

and make the oppositely-handed polarisations distinguishable. This dependence on magnetic interactions makes circularly polarised light an inefficient chiral reagent, since magnetic interactions are so much weaker than electric ones.

However, simple circularly polarised light is not the only option [20, 219]. We can tailor the electric field of the light such that the light exhibits chirality even when reduced to the electric dipole regime. For example, using a setup with an elliptical beam of frequency ω and a linearly polarised 2ω beam, and with the polarisation plane of the linearly polarised component perpendicular to the long axis of the ellipse, the Lissajous figure drawn by the tip of the electric field vector in the dipole approximation will draw out a bent-circle 'pringle' shape (see fig 2.8). This makes the figure non-planar and, combined with the sense of the rotation of the electric field vector (clockwise or anti-clockwise), will break the reflection-symmetry and make the figure chiral (or perhaps more properly 'pseudo'-chiral, since the handedness reverses with time-reversal).

This gives rise to a chiral pathway, wherein a chiral molecule absorbs 3 photons of frequency ω from the x component of the ω field, and then is stimulated to emit one photon into the y component, thereby recording the ellipticity of the ω field. In an isotropic ensemble of chiral molecules, this pathway gives rise to an induced polarisation along the $\hat{z}$ direction. There is also an achiral pathway, wherein the system absorbs one 2ω photon from the z component of the field, which thus also leads to an induced polarisation along the $\hat{z}$ direction. The induced polarisation thus gives rise to emission and absorption at the frequency ω, and since these polarisations are along the same axis they interfere, with the interference controlled by the two-colour phase delay (see fig 2.9).

By tuning this phase delay, along with the relative intensities and degrees of ellipticity of the incident fields, the interference between the two pathways can be

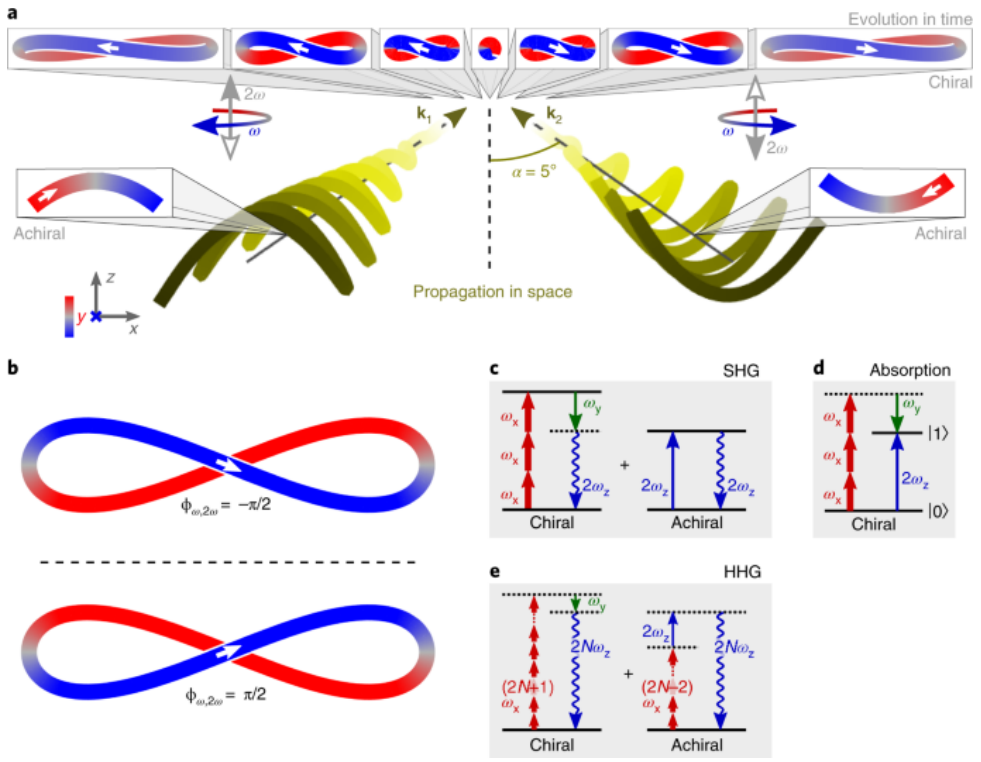


Figure 2.9: (a) Shows the evolution in time (red and blue), loci throughout space (yellow), and variation through space of the tip of the electric field vector in synthetic chiral light. (b) Lissajous figures traced by the tip of the electric field vector of synthetic chiral light at a single point in space over time. (c) Energy level diagram for enantiosensitive second-harmonic generation by synthetic chiral light. (d) Energy level diagram of enantiosensitive pump-probe absorption using synthetic chiral light. (e) Energy level diagram of HHG using synthetic chiral light. Reproduced with permission from Nature Publishing [20].

made to be completely destructive or maximally constructive, thereby maximally enhancing or fully suppressing the signal from either enantiomer. This explains the chiral signal in the second harmonic; chiral sensitivity in higher harmonics is explained by examining successively higher order chiral correlation functions. The chiral nature of the light field in the electronic dipole approximation makes synthetic chiral light an efficient chiral photonic reagent, both for interrogating the chirality of samples, but also in exciting specific chiral states in molecules, including imprinting chirality on otherwise non-chiral matter [220, 221].

Obtaining such enantiosensitive signals in the far field requires favourable phase-matching, and this in turn requires that the electric field have some non-zero longitudinal component [21]. This can be realised in multiple ways [156, 207, 219, 222–225]. One is to use a non-collinear setup [20, 21, 156]. Tight focussing can also be used [21, 219] close to the focus of a beam, due to Gauss' law requiring a longitudinal flux of electric field to balance the curvature of the wavefront [226, 227]. This enables one to achieve synthetic chiral light using a polychromatic but collinear setup. Alternatively, nanophotonic structures such as waveguides [228], nanotips [224, 225] or carefully engineered nanophotonic surfaces [207] can be used

in conjunction with lasers to sculpt the electric field and realise locally chiral light.

Synthetic chiral light can also make the free electron trajectory in HHG chiral. Since the enantio-sensitivity of the recombination between the electron and the parent ion is controlled by the trajectory of the electron prior to recollision, this should give rise to enantio-sensitive high harmonic emission using synthetic chiral light, with the specific harmonic orders that are made to express enantiosensitivity selected by appropriately tuning the parameters of the optical field [178]. Nonetheless, is it not entirely necessary to rely on intense laser fields and higher order processes, and recent developments have explored the use of more gentle synthetic chiral fields [156, 219]. For example, a synthetic chiral field can bring about an enantiosensitive Stark-shift in excited states of a chiral molecule. This in turn imparts an enantiosensitive phase shift on free-induction decay from that state, and this can then be measured [219].

It is also desirable for the light field's local chirality to be maintained across the sample region. If the local chirality should flip regularly over the sample region, the signals emitted will cancel out. The chiral field must be globally chiral, maintaining the same chirality over the entire sample region, or at least most of it. In the case of synthetic-chiral light from a co-planar non-collinear setup (with the fundamental components polarised in plane, and the harmonic polarised perpendicularly), the two overlapping fields form an interference pattern, in ellipticity for the ω field and in intensity for the 2ω field, so that the ellipticity reverses and the 'bend' in the trajectory reverses regularly. If these two interference patterns are aligned such that their nodes coincide, each time the chirality of the fields would flip, the overall phase of the field also flips, cancelling out and maintaining the same handedness. To achieve this, the differences in the two colour phase delays between each field should be *exactly* π. However, since the technique relies on perfectly interlaced sets of interference patterns to maintain its global chirality, it can be vulnerable to dispersive effects. In gaseous media, dispersion doesn't change the two colour phase delay in either beam enough across the interaction medium to ruin the chirality. However, dispersion does become a problem in the case of liquid and solid media with less favourable optical properties, thus limiting the maximum size of the interaction region to just a few microns in these cases [229, 230]. We can, in some circumstances, relax this requirement of stable global chirality [219, 222, 223]. Even if the chirality of the field reverses at some points in space, so long as there is some overall 'chirality dipole' (where chirality is asymmetrically distributed around the optical axis), this can be used to realise enantiosensitive measurements, such as enantiosensitive redirection of light [219, 222, 223].

2.4 Novel Chiroptical Approaches

Both PECD and synthetic chiral light exploit the strength of chiral effects which exist within the electric dipole approximation to realise much greater enantiosensitive efficiencies than methods that rely on the magnetic field of CPL [17, 19]. However, recent developments in chiroptical spectroscopy are not limited to just these few, and many exploit chiral effects within the electric dipole regime to realise efficient

enantiosensitive measurements compatible with small samples or fine time resolution [18].

2.4.1 Photo-excitation Circular Dichroism

Techniques which realise a chiral observer using circularly polarised light are not limited to those requiring photoionisation of the sample molecule. They can also be realised using bound-bound transitions, or a combination of bound-bound and bound-free transitions. One such technique is 'photo-excitation circular dichroism' or PXCD, which replaces using photoelectron current as a chiral vector observable with using the induced polarisation of the chiral molecules [231].

For a single excited state, the excitation dipole $\vec{d}^{M}_{0\to1}$ is real and so the triple product $(\vec{d}^{M*} \times \vec{d}^{M}) \cdot \vec{k}^{M}$, introduced previously, vanishes. A method involving a single excitation and then emission cannot realise a chiral sensitivity. However, coherently exciting two states $|1\rangle$ and $|2\rangle$ with non-parallel transition dipoles $\vec{d}^{M}_{0\to1} \times \vec{d}^{M}_{0\to2} \neq 0$ allows us to achieve a non-zero chiral triple-product:

$$(\vec{d}^{M}_{01} \times \vec{d}^{M*}_{20}) \cdot \vec{d}^{M}_{12} \tag{2.45}$$

or any permutations of the above.

For example, we can use a driving field with one component in resonance with one of the molecule's electronic transitions, alongside another component with a lower energy, resonant with a vibrational transition. The molecule is first excited from the ground state to an electronic and vibrational excited state, before it then decays to the vibrational ground of its electronic state, and then back to true ground.

In this case, the pseudoscalar is provided by a permutation of the triple product (see eq 2.45) of the transition dipoles of the initial excitation and subsequent decays, which will be of opposite sign in opposite enantiomers. If there are more than two excited levels in the system, the above analysis must be altered to sum over all potential states to which the molecule can excite.

The chiral response in PXCD is maximised in the case where the three transition dipoles are orthogonal, since this maximises the triple product of the transition dipoles, for example when using an ultrashort circularly polarised pulse both for the first excitation $|0\rangle \to |2\rangle$ and the stimulated decay $|1\rangle \to |0\rangle$. In this case, all of the initial excitation in the polarisation plane of incident light is converted into enantiosensitive motion along the axis of propagation.

As well as ionisation and bound-bound transitions, such chiral setups can also be achieved with Raman-type bound-continuum and continuum bound transitions; photo-electron-photo-excitation circular dichroism (PEXCD)[231]. This is very similar to PXCD, but with the decay from $|2\rangle \to |1\rangle$ replaced by a Raman-type ionisation from $|2\rangle \to |\vec{k}\rangle$ followed by a decay $|\vec{k}\rangle \to |1\rangle$, and then the electron decaying to ground state, as before (see fig 2.10). These Raman-type transitions via continuum can even be excited by a linearly polarised probe pulse.

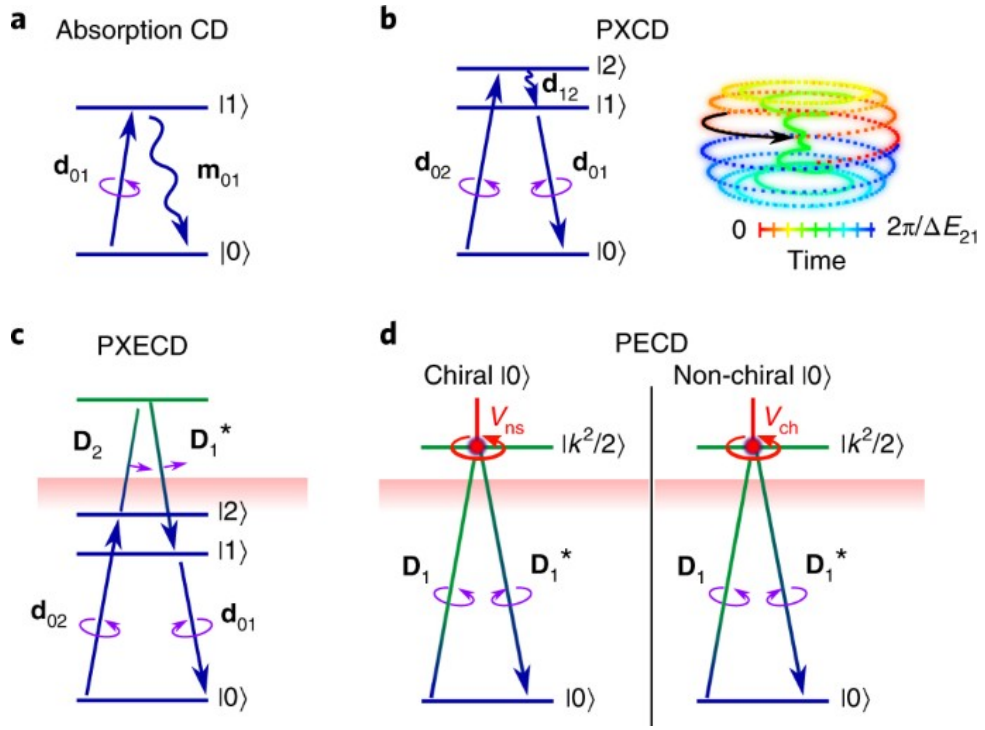


Figure 2.10: (a) An energy level diagram of absorption CD. Note: the enantiosensitivity of the technique relies on magnetic dipole interactions. (b) Energy level diagram of PXCD, with the enantiosensitivity deriving from transition dipoles from three transitions, $|0\rangle$ to $|2\rangle$, decay from $|2\rangle$ to $|1\rangle$, and $|1\rangle$ to $|0\rangle$. The right panel shows the tip of the dipole vector of a molecule in PXCD. (c) PEXCD, with the decay from state $|2\rangle$ to $|1\rangle$ replaced with a raman-type transition to and from continuum. (d) Energy level diagram of PECD in the chiral (left) and achiral (right) case. Reproduced with permission from AIP Publishing [231].

2.4.2 Microwave Three-wave Mixing

Another technique is 'microwave three-wave mixing' (M3WM), which uses three beams (called the 'drive', the 'twist', and the 'listener') propagating in three mutually orthogonal directions [232, 233], which drive the molecules of the sample in a closed three-step loop of rotational transitions. This is analogous to, for example, PXCD, but with electronic and vibrational transitions replaced with rotational ones, which have much lower energy [233].

The first two transitions, the *'drive'* and the *'twist'* are resonant excitations driven by linearly polarised pulses, which the third beam, the *'listen'*, is a reference signal which records the phase of the free induction decay of the molecules into the ground state, which differs by π between the enantiomers [234, 235].

Much like techniques such as PECD and PXCD, the mechanism for the resultant phase difference does not use any intrinsic chirality of incident light fields, but instead depends on a triple product of molecular dipole components. This technique is very sensitive even at very small changes in enantiomeric excess, but in order to interpret the phase of the FID one must compare the retrieved signal with that of a sample of the enantiomer with known handedness [153].

We can model the rotational dynamics of molecules by approximating them as asymmetric rigid rotors [236]. Rotational wavefunctions $|J, M\rangle$ are eigenstates of total angular momentum operator $\hat{J}^2$ and axial angular momentum operator $\hat{J}_z$, with eigenvalues

$$\hat{J}^2 |J, M\rangle = J(J+1) |J, M\rangle$$

and

$$\hat{J}_z |J, M\rangle = M |J, M\rangle ,$$

where $M \in \{-J, \ldots, +J\}$.

We calculate and sum over transition dipoles between the ground state, and two excited states in a similar way as previously:

$$\sum_{M_1,M_2,M_3} \langle \vec{d}^{\,L} \rangle_\chi = \sum_{M_1,M_2,M_3} \left[\vec{d}^{\,L}_{01} \cdot \tilde{\mathcal{E}}^{L*}(\omega_{10}) \right] \left[\vec{d}^{\,L}_{20} \cdot \tilde{\mathcal{E}}^{L*}(\omega_{20}) \right] \vec{d}^{\,L}_{12} e^{-i\omega_{21}t} + c.c. \tag{2.46}$$

$$= \sum_{M_1,M_2,M_3} \frac{1}{6} \left[(\vec{d}^{\,M}_{01} \times \vec{d}^{\,M}_{20}) \cdot \vec{d}^{\,M}_{12} \right] \left[\tilde{\mathcal{E}}^{L*}(\omega_{10}) \times \tilde{\mathcal{E}}^{L}(\omega_{20}) \right] e^{-i\omega_{21}t} + c.c. \tag{2.47}$$

where $+c.c.$ indicates the addition of complex conjugates. We see that the chiral molecular pseudoscalar in this case is given by the triple product of the transition dipoles associated with the 'drive' from ground to first excited state, 'twist' from first to second excited state, and the 'listen' from the second excited state back to the ground [19]: $(\vec{d}^{\,M}_{01} \times \vec{d}^{\,M}_{20}) \cdot \vec{d}^{\,M}_{12}$.

The signal thus depends on the relative phase between the drive and the twist, and is maximised when the three transition dipoles are orthogonal. Thus, a chiral signal is only reproducible when the phase delay between the drive and the twist is stable over time.

The techniques used in M3WM can further be extended to realise enantiosensitive population enhancement of specific rotational states, and this can be used to realise spectroscopic measurements targeting specific enantiomers even within mixed samples [237, 238].

2.4.3 Static Field Dichroism

Such enantiosensitive measurements can also make use of static field effects. Applying a static electric field to a collection of atoms will shift the energies of the electronic eigenstates of the molecules (Stark effect) [239]. We can excite the molecules into a static-field-shifted excited electronic state, before adiabatically withdrawing the static field and then allowing the molecules to first follow the excited state adiabatically back to the un-shifted excited state, and then decay back

to ground. This realises a three-transition setup analogous to PECD, PXCD and M3WM [19, 235].

The electronic eigenstates of bound electrons in an applied static electric field $\vec{E}_S$ are shifted from $|0\rangle, \ldots, |n\rangle$ to:

$$|n'\rangle = |n\rangle + \sum_{m \neq n} \frac{\vec{E}_S \cdot \vec{d}_{nm}}{\Delta E_{m,n}} |m\rangle , \tag{2.48}$$

where ΔE_{mn} is the energy difference between states $|m\rangle$ and $|n\rangle$ [19]. After applying the static field, an oscillating field resonant with the $|0\rangle \rightarrow |n\rangle$ transition is applied, producing oscillations of induced polarisation aligned with the static field:

$$a_{n'} = i \left[\vec{d}_{n'0} \cdot \vec{E}(\omega_{n'0}) \right] \tag{2.49}$$

$$= i \left(\left[\vec{d}_{n0} \cdot \vec{E}(\omega_{n'0}) \right] + \sum_{m \neq n} \frac{\vec{E}_S^L \cdot \vec{d}_{nm}}{\Delta E_{m,n}} \left[\vec{d}_{m0} \cdot \vec{E}^L(\omega_{n'0}) \right] \right) \tag{2.50}$$

so the expectation of the dipole has form:

$$\langle \vec{d} \rangle = \vec{d}_{00} + |a_{n'}|^2 \vec{d}^L_{n'n'} + \left(a_{n'} \vec{d}_{0,n'} e^{-i\omega_{n'0}t} + c.c. \right) \tag{2.51}$$

If we then average the oscillating term over possible orientations we find:

$$\int \mathrm{d}\varrho \left(a_{n'} \vec{d}^L_{0,n'} e^{-i\omega_{n'0}t} + c.c. \right) = \frac{i}{3} \left[\vec{d}_{n'0} \cdot \vec{d}_{0n'} \right] \vec{E}(\omega_{n'0}) e^{i\omega_{n'0}t} + c.c. \tag{2.52}$$

so the oscillations of the dipole are, on average, along the direction of the external field.

We then withdraw the static field adiabatically, causing the molecules to decay, first to the excited state $|n\rangle$, then to ground. The $|n'\rangle \rightarrow |n\rangle$ transition has dipole:

$$\langle \vec{d} \rangle = \vec{d}_{00} + |a_{n'}|^2 \vec{d}_{nn} + \left(a_{n'} \vec{d}_{0,n} e^{-i\omega_{n0}t + \varphi} + c.c. \right) \tag{2.53}$$

Where φ encodes the details of the removal of the field. The oscillating part can again be averaged to find:

$$\int \mathrm{d}\varrho \left(a_{n'} \vec{d}_{0,n} e^{-i\omega_{n0}t+\varphi} + c.c. \right) = i \Bigg(\frac{1}{3} \left[\vec{d}_{n0} \cdot \vec{d}_{0n} \right] \vec{\mathcal{E}}(\omega_{n'0})$$
$$+ \frac{1}{6} \sum_{m \neq n} \frac{1}{\Delta E_{m,n}} \left[(\vec{d}_{mn} \times \vec{d}_{m0}) \cdot \vec{d}^M_{0,n} \right] \left[\vec{E}_S \times \vec{E}(\omega_{n'0}) \right] \Bigg) e^{i\omega_{n0}t+\varphi} + c.c. \tag{2.54}$$

This features another enantiosensitive pseudoscalar $\left[(\vec{d}_{mn} \times \vec{d}_{m0}) \cdot \vec{d}_{0,n} \right]$, and so an enantiosensivive response which oscillates along an axis orthogonal to both the direction of the static field and the polarisation direction of the oscillating field.

Such an effect can be extended from the case of a static field, to the case of an oscillating field which changes much more slowly than the timescale of the oscillating pump pulse, for example a micro- or radio-wave field in the case of an infrared or optical pump. In a semi-quantum picture, the transition between perturbed excited state and excited state can be thought of as emission or absorption of a photon with arbitrarily low energy [235].

2.4.4 Chiral High-Harmonic Generation

Moving briefly to techniques utilising non-perturbative processes, chiral HHG creates an enantiosensitive vectorial signal using only electric-dipole-level interactions [21, 165, 240, 241].

The recombination stage in HHG, of the ionised electron with its parent ion, is the direct reverse of the photoionisation process in techniques such as PECD, and since the chiral triple product found in PECD should remain chiral even after reversing one of the steps, we should be able to construct a similar enantiosensitive pseudoscalar involving the real and imaginary parts of the recombination dipole:

$$\left[\Re\{\vec{D}_{rec}\} \times \Im\{\vec{D}_{rec}\}\right] \cdot i\sigma\hat{z} \tag{2.55}$$

This would lead the coherent dipole associated with recombination to have a chiral component which oscillates along the axis of propagation and is shifted by π in phase between opposite enantiomers.

This is analogous to the forward-backward asymmetry in PECD, but with the chiral trajectory of the electron before recombination taking the place of the enantiosensitive distribution of photoelectron emission [19, 215].

Since the chiral component of the oscillations is parallel to the axis of propagation of the incident laser, one would expect the chiral signal to be emitted perpendicular to the incoming beam. However, high harmonic generation usually benefits from coherent constructive addition of the light pulses emitted by each molecule along the direction of propagation due to its strict timing relative to the cycles of the driving field.

In this case, the direction of emission is perpendicular, not parallel, to the incident beam. This means that the phases of the emissions of different molecules along the axis of propagation of the incident beam cancel out, and so a coherent macroscopic signal is not generated [21, 241].

Therefore, methods to image molecular chirality using HHG require there to be some longitudinal component of the applied laser field, just as for synthetic chiral light. This allows a recombination dipole response along the propagation direction, and so a macroscopic signal can be generated that takes advantage of the coherent addition characteristic of HHG. This situation can be engineered by using, once again, very tightly focussed beams (which result in the laser field having a longitudinal component near the focus), using a non-collinear setup wherein the off-axis beams will have polarisation components along the overall axis of propagation [242], or using nanophotonics [207, 224, 225].

Since the timescales of HHG are so short, this technique has the advantage of being able to capture the electronic response of samples to intense laser fields with a sub-femtosecond temporal resolution [177, 243, 244], but still retains the drawbacks of using HHG as a technique in general, such as the large input intensities required [245]. Furthermore, in dispersive media, or optically thick media, the field may change too quickly across the sample region for chiral HHG to be practical for all but the smallest samples [229, 230].

2.4.5 Coulomb Explosion Imaging

The final technique we shall describe in this section is Coulomb explosion imaging. Molecules are collections of nuclei and electrons held together by electrostatic attraction [56]. If a molecule is ionised, this will leave a concentration of positive charge, as well as potentially emptying out the bonding orbitals which hold the positively charged parent nuclei together. If enough electrons are stripped from the molecule, the resulting concentration of positive charge and lack of bonding orbitals will result in the molecule breaking apart into charged ionic fragments, which repel each other and fly outwards [246]. This is known as a Coulomb explosion [247].

Coulomb explosion imaging, or CEI, utilises this to image the structure of molecules. The fragments that are expelled by the exploding molecular ions can be detected, and their masses, angles of emission and velocities can be used to characterise the shape of the molecule from which they were expelled [247–249]. In the case of chiral molecules, if the fragments are imaged coincidently, the chirality of the parent molecule can be inferred from the velocity map of the ion fragments [250].

In chiral CEI schemes, chiral molecules are aligned spatially using a moderately strong elliptically polarised laser field [250–252]. When this ellipse is rotated by a non-right-angle with respect to the normal to the detector plane, the momentum distributions of the ion fragments displays an asymmetry related to both the enantiomeric excess and the absolute configuration of the sample. The simplest case is that of a centrally chiral molecule, such as a chiral haloalkane, where the fragments are those substituents of the chiral carbon atom, where the distribution of different ions can be correlated directly to the absolute configuration of the chiral centre so long as the parent molecules were aligned initially [253, 254]. In the case of other forms of chirality, the technique is still applicable but subtly different. In the case of axial chirality, for instance, the absolute configuration can be determined using just two fragments connected through the axis of chirality, so long as the initial molecules were aligned along this axis [255].

In terms of a chiral triple product, the triple product of the velocities associated with three chiral ion fragments can be multiplied to extract a chiral pseudoscalar characterising the handedness of the molecule, but this requires knowledge of the full ion velocity map around the parent ion, and generally detectors measure these velocities within two-dimensional planes. Therefore, a simpler setup is to use an elliptical pulse to align the chiral molecules before they are ionised, and so a pseudoscalar can be constructed using two different ion momenta and the axis of alignment [253, 256, 257].

Conclusion

Throughout this chapter, we have given a brief introduction to the theory underpinning both light-matter interactions in general and *chiral* light-matter interactions in particular, as well as examples of recent developments in the field.

In section 2.1 we reiterated the theory of classical electrodynamics, beginning from Maxwell's equations and linear optics before expanding our understanding towards non-linear phenomena both of the perturbative and non-perturbative kinds. In doing so, we see the potential advantages of perturbative approaches over non-perturbative ones. Namely, a chiroptical method which utilises low-order perturbative effects will be realisable with much lower laser intensities than one which relies on higher-order or non-perturbative effects.

In section 2.2, we then explained the history and theory behind optical rotation, the oldest and still most widely utilised chiroptical phenomenon. Despite their simplicity and ubiquity, we explained how these techniques are hamstrung in certain circumstances by their reliance on magnetic effects which are, by their nature, much weaker than electric-dipole effects at sub-ionising frequencies. Thereby we identify a desire for chirality-sensitive optical effects that arise within the electric dipole approximation, and can therefore be much more efficient on a few-molecule basis. Such effects make use of the non-linear optical regime, wherein a molecule can 'see' the chirality of the electric field without the need for multipole or magnetic terms.

We explain, in section 2.3, the ways in which a chiral measurement can be made. A molecule can either 'react' with a chiral reagent, as in the case of synthetic chiral light, or the chirality of a molecule can be identified using some inherently chiral measurement setup, as in the illustrative example of PECD. These different schemes can be understood within the framework of chiral pseudoscalars, or pseudovectors which, when combined with a directionally-sensitive vectorial measurement, realise a chiral setup. This is a powerful analytical tool; the chirality of any object (a molecule, reagent, or measurement) can be characterised using a pseudoscalar, and so we can go about understanding nearly any chiral technique by constructing a chiral pseudoscalar triple-product.

We extended our understanding to various novel chiroptical approaches in section 2.4, going through various cutting-edge chiroptical techniques and deconstructing them in terms of the chiral pseudoscalar which characterises their measurement, from PXCD in section 2.4.1, to Coulomb explosion imaging in section 2.4.5. Now that we have an abstract theoretical understanding, it is necessary to turn to the computational tools we may need to model these effects.

Chapter 3

Computational Methods

In order to model how atoms and molecules respond to and emit light, we must first understand and be able to model the quantum mechanics of atoms and molecules. More specifically, we must be able to describe how the electrons in an atom or molecule evolve over time under the influence of electromagnetic fields; both those internal to the atom or molecule and external fields in the form of electromagnetic waves.

The time evolution of a quantum system, such as electrons within a molecule, is described by the time-dependent Schrödinger equation (TDSE) and any description of the interaction of molecules with light must begin by solving the TDSE, either directly or by some approximation.

In this work, it is assumed that the laser light being studied is sufficiently intense that its quantum nature can be safely ignored, and so the associated electric fields are continuous vector fields which can be described according to Maxwell's equations. Furthermore, since the magnetic fields associated with light are much weaker [258], at least in terms of forces exerted on electrons, than the electric fields (see section 2.2), we can neglect them in our investigations.

3.1 Solving the Time-Dependent Schrödinger equation

The time-dependent Schrödinger equation (TDSE) is an ordinary differential equation describing the time evolution of a quantum state $\Phi(t)$:

$$i\hbar\frac{d}{dt}\Phi(t) = \hat{H}(t)\Phi(t) \tag{3.1}$$

where $\hat{H}(t)$ is a Hermitian operator known as the *Hamiltonian*, which encapsulates the energetics of the system in question, and any dependence of either $\Phi(t)$ or $\hat{H}(t)$ on spatial or spin coordinates has been left implicit [33].

For a general multi-body system, comprised of N interacting particles each of

mass m_i and charge q_i the Hamiltonian will take the form:

$$\hat{H}(t) = \sum_{i=1}^{N} \left[\frac{\vec{p}_i^{\,2}}{2m_i} + \sum_{j=1, j\neq i}^{N} \frac{q_i q_j}{2|\vec{r}_i - \vec{r}_j|^2} \right] + \sum_{i=1}^{N} q_i \vec{r}_i \cdot \vec{E}(t) \tag{3.2}$$

where $\vec{p}_i$ is the momentum of the i^{th} body, and $\vec{E}$ is an externally applied field. In the above equation, the first term is a sum of the kinetic energies of each body and the electrostatic potential energy, and is known as the 'field-free' Hamiltonian $\hat{H}_0$. The second term is the potential energy of all elements due to external field $\vec{E}(t)$ [134], equivalent to external potential energy $V(t)$ [27].

The general solution to the TDSE takes the form:

$$\Phi(t) = \hat{\mathcal{U}}(t_0, t)\Phi(t_0) \tag{3.3}$$

where $\hat{\mathcal{U}}(t_0, t)$ is the 'time-evolution operator' which propagated the wavefunction Φ at time $t' = t_0$ to later time t, and is given formally by:

$$\hat{\mathcal{U}}(t_0, t) = e^{-\frac{i}{\hbar}\int_{t_0}^{t} \hat{H}(t')dt'}, \tag{3.4}$$

so long as $\hat{H}$ commutes with itself at later times. For the special case of a constant Hamiltonian, the TDSE can be solved exactly as:

$$\Phi(t) = e^{-\frac{i}{\hbar}(t-t_0)\hat{H}}\Phi(t_0) \tag{3.5}$$

which, setting the initial time $t_0 = 0$ and factoring the exponential procession into the wavefunction defines the wavefunction in the 'interaction picture' $\tilde{\Phi}$ [33, 259]. The interaction picture is a formulation of quantum mechanics wherein the undisturbed time evolution of a system is applied to operators, but time dependence due to external stimuli is carried by the wavefunction. This forms a sort of 'halfway-house' between the Schrödinger picture, wherein wavefunctions are time-dependent and operators constant, and the Heisenberg picture, where operators carry time dependence and wavefunctions do no change. The interaction picture is often used in the theory of light and light-matter interactions, since it is convenient to leave phase-procession of electron- or photon-wavefunctions implicit and only count time-variations due to interactions, hence the name.

Much as in Newtonian physics [260], the TDSE for a self-interacting system cannot be solved analytically for any number of bodies more than two [22], and so modelling any quantum system more complicated than a single hydrogen atom will necessitate either approximations or numerical methods to be used.

3.1.1 Spatial vs Spectral Methods

When formulating an approach to solving the TDSE for a multi-body system, the first decision to be made is whether to model the time evolution spatially or spectrally.

A spatial approach discretises physical space into grid-points, with the wavefunction expressed as an amplitude and phase at each grid-point [261, 262]. This

is the approach in, for example, time-dependent density functional theory. The drawback of this is the potentially large number of grid points needed to accurately model the quantum system can make these approaches prohibitively costly in terms of computer resources.

An alternative is to use a spectral approach, where the wavefunction is expressed as a linear combination of basis functions. This can be simpler to compute, but relies on a judicious choice of basis set which is well-defined and complete enough to capture the dynamics of the system.

One common spectral approach, and the one used in this work when determining the response of different conformers to laser fields (see section 5.2), is to use a basis consisting of a truncated series of the eigenstates of the field free hamiltonian $\hat{H}_0$ (or good approximations thereof):

$$\hat{H}_0\phi_m = E_m\phi_m \tag{3.6}$$

E_m being the energy of eigenstate ϕ_m, building up total wavefunction:

$$\Phi(t) = \sum_m \mathfrak{C}_m(t)\phi_m \tag{3.7}$$

thereby encoding the time-dependence of the system in spectral coefficients $\mathfrak{C}_m(t)$ which, due to the orthogonality of our basis set, is equivalent to $\langle\phi_i|\Phi(t)\rangle$.

If we insert this spectral expansion into the TDSE, we find:

$$i\hbar\frac{d}{dt}\sum_m \mathfrak{C}_m(t)\phi_m = \hat{H}(t)\sum_m \mathfrak{C}_m(t)\phi_m \tag{3.8}$$

$$= \sum_m \mathfrak{C}_m(t)\left(E_m + \hat{V}(t)\right)\phi_m. \tag{3.9}$$

If we contract over ϕ_m, bearing in mind our basis is orthogonal such that $\langle\phi_n|\phi_m\rangle = \delta_{nm}$, we find :

$$i\hbar\frac{d}{dt}\mathfrak{C}_n(t) = \mathfrak{C}_n(t)E_n + \sum_m \mathfrak{C}_m(t)\left\langle\phi_n\right|\hat{V}(t)\left|\phi_m\right\rangle \tag{3.10}$$

Here we see that, in the field free case $V(t) = 0$, we can solve to find the complex spectral coefficients merely precess in phase at an angular velocity determined by their energy, with constant amplitude:

$$\mathfrak{C}_n(t) = \mathfrak{C}_0 e^{-\frac{iE_n t}{\hbar}} \tag{3.11}$$

If we bring back our external potential $V(t)$, but his time work in the interaction picture $\tilde{\mathfrak{C}}_n(t) = \mathfrak{C}_n(t)e^{\frac{iE_nt}{\hbar}}$, we find:

$$i\hbar\frac{d}{dt}\tilde{\mathfrak{C}}_n(t) = \sum_m \tilde{\mathfrak{C}}_m(t)e^{\frac{i(E_n-E_m)t}{\hbar}}V_{nm}(t) \tag{3.12}$$

where $V_{nm}(t) = \langle\phi_n|\,\hat{V}(t)\,|\phi_m\rangle$ is the matrix element of the potential energy operator $\hat{V}(t)$. We can see that the coupling between different eigenstates of the field-free hamiltonian occurs via the external potential, which controls the relationships between different spectral coefficients. This is equivalent to the observation that, in order to move from one energy level to another, a quantum system much exchange the difference in energy with its surroundings.

The ordinary differential equation above, essentially a spectral decomposition of the TDSE, can be solved in the Schrödinger or interaction picture by breaking the time domain into small steps and solving by some iterative numerical scheme [259, 263]. Well known schemes such as the leapfrog method, Euler method, or various Runge-Kutta methods could all work, subject to the usual considerations around numerical stability and convergence [264]. Alternatively, if the external potential should be sufficiently weak, it may be more efficient to treat it as a perturbation [265], which we will discuss further in the following section.

3.1.2 Perturbation Theory

As seen in the previous section, if we choose to model our wavefunction within the 'interaction picture' , our TDSE in terms of spectral coefficients $\mathfrak{C}_n(t)$ is given by [33] equation 3.12. If our external potential $V(t)$ is sufficiently small that we are able to treat it as a small perturbation, we can express our TDSE in terms of a perturbative series [265]:

$$\tilde{\mathfrak{C}}_n(t) = \tilde{\mathfrak{C}}_n^{(0)}(t) + \lambda\tilde{\mathfrak{C}}_n^{(1)}(t) + \lambda^2\tilde{\mathfrak{C}}_n^{(2)}(t) + \dots \tag{3.13}$$

where λ denotes some small parameter encoding the strength of the perturbation, and the tilde indicates we are working in the interaction picture so field free procession is implicit. Since our time-dependent perturbation is small, we can set the zeroth order term to be equal to our starting condition $\tilde{\mathfrak{C}}_n^{(0)}(t) \approx \tilde{\mathfrak{C}}_n(0)$, in other words, since our $V(t)$ is small, the system will not change very much over time. If we then require that the perturbed state be an eigenvector of the perturbed interaction picture hamiltonian $\hat{H}_I = \hat{H}_0 + e^{\frac{i\hat{H}_0t}{\hbar}}\lambda\hat{V}(t)e^{\frac{-i\hat{H}_0t}{\hbar}}$ (where $\hat{H}_0$ represents the time-independent component of the Hamiltonian), we find:

$$\hat{H}_I\left(\tilde{\mathfrak{C}}_n(0) + \lambda\tilde{\mathfrak{C}}_n^{(1)}(t) + \dots\right) = \left(E_n^{(0)} + \lambda E_n^{(1)} + \dots\right)\left(\tilde{\mathfrak{C}}_n(0) + \lambda\tilde{\mathfrak{C}}_n^{(1)}(t) + \dots\right) \tag{3.14}$$

We can then equate powers of λ on both sides of the equation above to arrive at iterative series relation:

$$i\hbar\frac{d}{dt}\tilde{\mathfrak{C}}_n^{(r)}(t) = \sum_m \tilde{\mathfrak{C}}_m^{(r-1)}(t)e^{\frac{i(E_n-E_m)t}{\hbar}}\langle\phi_n|\hat{V}(t)|\phi_m\rangle \tag{3.15}$$

which, taken to first order, made such that the molecule is wholly in the ground state at $t = 0$, and assuming an adiabatic switch-on to remove the lower limit of our integrals, we find:

$$\tilde{\mathfrak{C}}_n^{(1)}(t) \approx \delta_{0n} - \frac{i}{\hbar}\int_0^t e^{\frac{i(E_n-E_0)t'}{\hbar}}\langle\phi_n|\hat{V}(t')|\phi_0\rangle\,dt' \tag{3.16}$$

$$\approx \delta_{0n} - \frac{i}{\hbar}\vec{d}_{n0}\cdot\int_0^t e^{\frac{i(E_n-E_0)t'}{\hbar}}\vec{E}(t')dt' \tag{3.17}$$

since $V(t) = \vec{d}\cdot\vec{E}(t)$ where $\vec{d}$ is the electric dipole operator, $\vec{E}(t)$ is the electric field vector, and $\vec{d}_{0n}$ is the electric transition-dipole matrix-element between the ground state and the n^{th} excited state. Once the perturbed interaction-picture spectral coefficients are found, the Schrödinger picture coefficients can be recovered by factoring back out static state procession.

Although perturbation theory is a convenient analytic means to approximate the time evolution of a system, it is limited in the sense that it is only valid for sufficiently small external potential. Nonetheless, it can be useful to test and calibrate other methods of solving the TDSE, such as the more complete spectral scheme outlined in the previous section.

3.2 Computational Methods in Quantum Chemistry

The methods described previously for solving the time-dependent Schrödinger equation still require some extra input; for the case of both spectral methods and perturbation theory, we need to have good values for the transition-dipole matrix elements before we can propagate the TDSE. In order to get these we must turn either to experimental data, or to so-called *ab initio* methods, which can simulate a quantum mechanical system using only physical constants and some initial geometry [266].

There are a wide variety of such methods, but the ones we shall be focussing on are Hartree-Fock theory, density functional theory, and time-dependent density functional theory. However, the first step in formulating any scheme to efficiently undertake quantum-chemical simulations is to form the Hamiltonian for the molecular system, undisturbed by any external forces. We can then simulate the quantum system, and, in the time-dependent case, introduce external driving fields.

3.2.1 The Molecular Hamiltonian

For an entire molecule, consisting of N_N nuclei and N_e electrons, the molecular Hamiltonian will consist of the sum of the kinetic energy operators $\hat{T}_e$ and $\hat{T}_N$ of the electrons and nuclei respectively, together with the potential energy from internuclear repulsion $\hat{V}_{NN}$, electron-electron repulsion $\hat{V}_{ee}$, and electron-nuclear attraction $\hat{V}_{eN}$ such that total molecular hamiltonian:

$$\hat{H} = \hat{T}_e + \hat{T}_N + \hat{V}_{NN} + \hat{V}_{ee} + \hat{V}_{eN} \tag{3.18}$$

Taking each term in turn, electron kinetic energy:

$$\hat{T}_e = -\frac{\hbar^2}{2m_e}\sum_{i=1}^{N_e}\nabla_i^2 \tag{3.19}$$

where ∇_i^2 indicates the Laplacian operator ∇^2 acting on the i^{th} electron [27]. Nuclear kinetic energy:

$$\hat{T}_N = -\frac{\hbar^2}{2}\sum_{r=1}^{N_N}\frac{1}{m_j}\nabla_j^2 \tag{3.20}$$

inter-electronic repulsion:

$$\hat{V}_{ee} = \sum_{i=1}^{N_e}\sum_{j>i}^{N_e}\frac{1}{4\pi\epsilon_0}\frac{e^2}{|\vec{r}_i - \vec{r}_j|} \tag{3.21}$$

where $\vec{r}_i$ indicates spatial position (excluding spin coordinates) of the i^{th} electron, electro-nuclear attraction:

$$\hat{V}_{eN} = -\sum_{i=1}^{N_e}\sum_{r=1}^{N_N}\frac{1}{4\pi\epsilon_0}\frac{Z_r e^2}{|\vec{r}_i - \vec{R}_r|} \tag{3.22}$$

where Z_r is the charge (relative to an electron) of the r^{th} nucleus, and R_r its position. Finally, nuclear repulsion:

$$\hat{V}_{NN} = \sum_{r=1}^{N_N}\sum_{s>r}^{N_N}\frac{1}{4\pi\epsilon_0}\frac{Z_r Z_s e^2}{|\vec{R}_r - \vec{R}_s|} \tag{3.23}$$

Here we see the core problem in quantum chemistry; that the wavefunction of the system depends on itself in a number of different ways, with nuclear wavefunctions depending on electronic wavefunctions and vice-versa, making it impossible to solve analytically, and dramatically increasing the complexity of solving numerically.

Most techniques take a 'self-consistent' approach, where an initial guess as to the wavefunction of the system is refined iteratively until the solution converges such that the charge distribution is consistent with the assumed electric field. However, the presence of many moving parts; multiple nuclei and electrons, all of which are interdependent quantum objects, increases the computational cost exponentially with each new object. This makes solving these equations naïvely intractable apart from for the smallest and simplest systems (eg. helium nuclei or H_2^+ ions). Valid approximations which reduce the number of degrees of freedom of the system must be found in order to make progress.

3.2.2 The Born-Oppenheimer Approximation

One such common approximation is the Born-Oppenheimer approximation (BOA) [267]. Since electrons and nuclei generally have comparable charges (especially in organic chemistry, where $Z_N \lesssim 20$), the extramolecular electromagnetic forces they are subjected to are generally similar. However, nuclei are very much heavier than electrons ($M_p/M_e \simeq 1836$), and so their velocities must be much less than those of electrons. Thus, nuclear motion will tend to occur on a much longer timescale than electronic motion ($\tau_{nuclear} \simeq 10^{-14}s$ vs $\tau_{electronic} \simeq 10^{-18}s$).

We can therefore consider splitting the molecular wavefunction into an electronic part and nuclear part [268]:

$$\Phi_{n\nu}(\vec{x}, \vec{R}) = \Psi_n(\vec{x}, \vec{R})\Theta_{n\nu}(\vec{R}) \tag{3.24}$$

where n and ν label electronic and nuclear stationary states respectively, $\vec{R}$ denotes a collection of all nuclear coordinates, and $\vec{x}$ denotes a bundle of all electronic spatial and spin coordinates. Thus the total eigenvalue equation:

$$(\hat{T}_e + \hat{T}_N + \hat{V}_{ee} + \hat{V}_{eN} + \hat{V}_{NN})\Phi_{n\nu}(\vec{x}, \vec{R}) = E_{n\nu}\Phi_{n\nu}(\vec{x}, \vec{R}) \tag{3.25}$$

can be split into separate nuclear and electronic eigenvalue equations:

$$(\hat{T}_e + \hat{V}_{ee} + \hat{V}_{eN} + \hat{V}_{NN})\Psi_n(\vec{x}, \vec{R}) = E_n(\vec{R})\Psi_n(\vec{x}, \vec{R}) \tag{3.26}$$

where $\vec{R}$ is in this case a parameter, and:

$$(\hat{T}_N + E_n(\vec{R}))\Theta_{n\nu}(\vec{R}) = E_{n\nu}\Theta_{n\nu}(\vec{R}) \tag{3.27}$$

Thereby, the energy of an electronic state E_n depends on the nuclear coordinates, but the energy of the nuclear state $E_{n\nu}$ depends on the electronic state but does not depend on the exact coordinates of the electron. From the perspective of an electron, nuclei move so slowly that their motion is irrelevant; electrons adjust so quickly to new nuclear coordinates that the quantum nature of the nuclei doesn't matter. Conversely, from the perspective of a nucleus, electrons move so quickly that their quantum state is felt as an effective potential energy field $E_n(\vec{R})$ through which nuclei move. In the electronic eigenvalue equation, above, internuclear repulsion is a constant value which simply shifts total energy $E_n(\vec{R})$, whilst this inter-nuclear potential energy is included in nuclear eigenvalue equation via effective potential $E_n(\vec{R})$.

This approximation further relies on the assumption that the variation of electronic wavefunction $\Phi_{n\nu}(\vec{x}, \vec{R})$ is very smooth with respect to $\vec{R}$, *i.e.* the electrons rearrange themselves instantaneously as nuclei move, and small changes in nuclear geometry produce small changes in electronic structure. This assumption holds so long as spacing between electronic states is sufficiently large *i.e.* small nuclear perturbations don't lead to large changes in the quantum state of the electrons. This is especially powerful for small-to-medium-sized molecules, where electronic energy levels will tend to be more sparse, and therefore timescales for electronic transitions will remain reasonably short.

In this way, the electronic eigenstates will define a smooth 'potential energy surface' along which the nuclear configuration can traverse. Here we can begin to see a potential self-consistent approach to molecular geometry: The electronic eigenstates can be calculated from an informed initial guess of the nuclear equilibrium geometry, and this eigenstate can serve as a potential energy surface for the nuclear geometry. The nuclei can be moved so as to minimise this potential energy, the electronic eigenstates can be recalculated according to this new geometry, and this can be repeated until the calculation converges and a self-consistent approximation to the nuclear geometry of the molecule is achieved.

A related concept is the fixed-nuclei approximation, where nuclei are assumed to be spatially fixed at $R = R_{eq}$, and so the electronic eigenvalue problem reduces further to:

$$(\hat{T}_e + \hat{V}_{ee} + \hat{V}_{eN} + \hat{V}_{NN})\Psi_n(\vec{x}, \overrightarrow{R_{eq}}) = E_n(\overrightarrow{R_{eq}})\Psi_n(\vec{x}, \overrightarrow{R_{eq}}) \tag{3.28}$$

with the nuclear state neglected entirely. This problem has even lower dimensionality and so the computational cost is commensurately lower still. This assumption is valid for rapid electronic processes operating on or close to the few-femtosecond regime, prior to the onset of nuclear motion [269–272]. Therefore, the fixed-nuclei approximation is valid for coherent processes, occurring before the onset of decoherence due to vibrational excitation. In this work, we assume the fixed nuclei approximation to be valid so as to make computational progress in spite of being at the edge of that regime.

3.2.3 Hartree-Fock Theory

Hartree-Fock theory (HFT) is one such computational scheme that can be used to provide a first-approximation to the 'exact' ground state solution of the Schrödinger equation for a molecule [27]. HFT was an early example of a so-called 'self-consistent field' (SCF) technique, where the electronic wavefunction and molecular potential are calculated from each-other iteratively until a desired degree of agreement between the two is achieved [273–276].

The HF method assumes that the exact wavefunction of a molecule can be approximated by a linear combination of basis elements known as a Slater determinant [277], and relies on the minimisation of an energy-functional to approximate the ground state solution [275]. In this way, HFT is implicitly a 'mean-field' approximation, reducing the interactions between electrons to an effective electric potential caused by the sum of the nuclear electric field and the averaged behaviour of the other electrons [27]. In so doing, mean-field approaches reduce the dimensionality of the system. This makes them easier to compute at the cost of poorly accounting for electron-correlation effects [24, 27, 28].

Slater Determinants and Slater-Condon Rules

Many computational schemes for quantum chemistry rely on using Slater determinants. These are expressions which build up, by linear combination of basis elements, the wavefunction of a system of multiple fermions so as to satisfy the requirement

that fermionic wavefunctions be anti-symmetric under parity operations [277, 278]. Each basis element includes both spatial and spin components, and so the general wavefunction for an N-body fermionic system (eg. electrons in a molecule) can be written as determinant:

$$\Psi_{SD}(\vec{x}_1, \vec{x}_2, \ldots, \vec{x}_N) = \frac{1}{\sqrt{N!}} \begin{vmatrix} \phi_1(\vec{x}_1) & \phi_2(\vec{x}_1) & \ldots & \phi_N(\vec{x}_1) \\ \phi_1(\vec{x}_2) & \phi_2(\vec{x}_2) & \ldots & \phi_N(\vec{x}_2) \\ \vdots & \vdots & \ddots & \vdots \\ \phi_1(\vec{x}_N) & \phi_2(\vec{x}_N) & \ldots & \phi_N(\vec{x}_N) \end{vmatrix} \tag{3.29}$$

which is conveniently anti-symmetric under electron exchange and vanishes if the basis is non-orthogonal, automatically satisfying the Pauli principle [277].

The Slater-Condon rules are rules which express how operators acting on different numbers of bodies within an N-body system expressed as a Slater determinant can be expressed in terms of sums of operators acting on basis vectors [27, 279, 280]. This is useful since, in the case of our molecular Hamiltonian, we have terms which act of one body at a time (such as electronic kinetic energy $\hat{T}_e$), as well as terms which act on pairs of bodies, such as electron-electron Coulomb repulsion $\hat{V}_{ee}$. For a one-body operator such as electron kinetic energy, where total energy can be expressed as a sum over individual energies $\hat{T} = \sum_{i=1}^{N} \hat{t}$, we find that the expectation value:

$$\langle \Psi_{SD} | \hat{T} | \Psi_{SD} \rangle = \sum_{i=1}^{N} \langle \phi_i | \hat{t} | \phi_i \rangle . \tag{3.30}$$

Meanwhile matrix elements for such an operator where one wavefunction $|\Psi_m^p\rangle$ differs by substitution of element $\phi_m(\vec{x}_m)$ for $\phi_p(\vec{x}_m)$ will be:

$$\langle \Psi_{SD} | \hat{T} | \Psi_{SD,m}^p \rangle = \langle \phi_m | \hat{t} | \phi_p \rangle \tag{3.31}$$

and the matrix element for two wavefunctions differing by more than one element will vanish.

For two-body operators, such as Coulomb repulsion $\hat{V}_{ee}$, which take the form

$$\hat{V} = \frac{1}{2} \sum_{i=1}^{N} \sum_{j=1, j \neq i}^{N} \hat{v}(i, j),$$

the expectation value will be of the form:

$$\langle \Psi_{SD} | \hat{V} | \Psi_{SD} \rangle = \frac{1}{2} \sum_{i=1}^{N} \sum_{j=1, j \neq i}^{N} \langle \phi_i \phi_j | \hat{v} | \phi_i \phi_j \rangle \tag{3.32}$$

while one-step-off-diagonal matrix elements:

$$\langle \Psi_{SD} | \hat{V} | \Psi_{SD,m}^p \rangle = \sum_{i=1}^{N} \left(\langle \phi_m \phi_i | \hat{v} | \phi_p \phi_i \rangle - \langle \phi_m \phi_i | \hat{v} | \phi_i \phi_p \rangle \right) \tag{3.33}$$

and two-steps-off-diagonal elements (where elements $\phi_m(\vec{x}_m)$ and $\phi_n(\vec{x}_n)$ are replaced by $\phi_p(\vec{x}_m)$ and $\phi_q(\vec{x}_n)$) become:

$$\langle \Psi_{SD} | \hat{V} | \Psi^{pq}_{SD,mn} \rangle = \langle \phi_m \phi_n | \hat{v} | \phi_p \phi_q \rangle - \langle \phi_m \phi_n | \hat{v} | \phi_q \phi_p \rangle \tag{3.34}$$

Matrix elements of a two body operator for wavefunctions differing by three components or more will vanish.

The Fock Operator

The mathematical basis of HFT begins with the following assumptions; static nuclei, non-relativistic electron velocities, and energy eigenfunctions that can be described by a single Slater determinant composed of a linear combination of orthogonal basis functions which are finite and complete. Since nuclei are static, without loss of generality we can write our molecular electronic Hamiltonian as $\hat{H}_e = \hat{T}_e + \hat{V}_{eN} + \hat{V}_{ee}$. So, making use of the Slater-Condon rules [279, 280], we can find expectation value for energy (switching now to atomic units):

$$\begin{aligned}
\langle \Psi | \hat{H}_e | \Psi \rangle = & \sum_{i=1}^{N} \langle \phi_i(\vec{x}_i) | \hat{T} + \hat{V}_{eN} | \phi_i(\vec{x}_i) \rangle \\
& + \frac{1}{2} \sum_{i=1}^{N} \sum_{\substack{j=1 \\ j \neq i}}^{N} \langle \phi_i(\vec{x}_i) \phi_j(\vec{x}_j) | \frac{1}{|\vec{x}_i - \vec{x}_j|} | \phi_i(\vec{x}_i) \phi_j(\vec{x}_j) \rangle \\
& - \frac{1}{2} \sum_{i=1}^{N} \sum_{\substack{j=1 \\ j \neq i}}^{N} \langle \phi_i(\vec{x}_i) \phi_j(\vec{x}_j) | \frac{1}{|\vec{x}_i - \vec{x}_j|} | \phi_i(\vec{x}_j) \phi_j(\vec{x}_i) \rangle \, .
\end{aligned} \tag{3.35}$$

This construction forms our energy-functional, which we seek to minimise subject to the constraint that the basis must be orthogonal [27].

We can perform this variation by first taking the functional derivative of our energy functional $\delta \langle \Psi | \hat{H}_e | \Psi \rangle$ with respect to some component ϕ^*_k. Doing this for the first term yields:

$$\delta \sum_{i=1}^{N} \langle \phi_i(\vec{x}_i) | \hat{T} + \hat{V}_{eN} | \phi_i(\vec{x}_i) \rangle = \int d\vec{x_k} \left(\hat{T}_k + \hat{V}_{eN} \right) \phi_k(\vec{x_k}) \delta \phi^*_k(\vec{x_k}) \tag{3.36}$$

making use of the fact that the basis functions are orthogonal. For the second term:

$$\delta\left(\frac{1}{2}\sum_{i=1}^{N}\sum_{\substack{j=1\\j\neq i}}^{N}\langle\phi_i(\vec{x}_i)\phi_j(\vec{x}_j)|\,\frac{1}{|\vec{x}_i-\vec{x}_j|}\,|\phi_i(\vec{x}_i)\phi_j(\vec{x}_j)\rangle\right) \tag{3.37}$$

$$=\frac{1}{2}\int d\vec{x_k}\int d\vec{x_j}\sum_{j=1}^{N}\phi_j^*(\vec{x}_j)\frac{1}{|\vec{x}_k-\vec{x}_j|}\phi_j(\vec{x}_j)\phi_k(\vec{x_k})\delta\phi_k^*(\vec{x_k})$$

$$+\frac{1}{2}\int d\vec{x_i}\int d\vec{x_k}\sum_{i=1}^{N}\phi_i^*(\vec{x}_i)\frac{1}{|\vec{x}_i-\vec{x}_k|}\phi_i(\vec{x}_i)\phi_k(\vec{x_k})\delta\phi_k^*(\vec{x_k}) \tag{3.38}$$

$$=\int d\vec{x_k}\int d\vec{x_j}\left[\sum_{j=1}^{N}\frac{\phi_j^*(\vec{x_j})\phi_j(\vec{x_j})}{|\vec{x}_k-\vec{x}_j|}\right]\phi_k(\vec{x_k})\delta\phi_k^*(\vec{x_k}) \tag{3.39}$$

where we have used the fact that the potential is symmetric upon swapping the particle positions. We can write the total local particle density $\rho_l(\vec{x_j})$ as:

$$\rho_l(\vec{x_j})=\sum_{j=1}^{N}\phi_j^*(\vec{x_j})\phi_j(\vec{x_j}) \tag{3.40}$$

and define the 'Hartree potential' $\hat{V_h}$ as:

$$\hat{V_h}(\vec{x_i})=\int d\vec{x_j}\frac{\rho_l(\vec{x_j})}{|\vec{x_i}-\vec{x_j}|} \tag{3.41}$$

such that the second term in the functional derivative of our energy-functional becomes:

$$\delta\left(\frac{1}{2}\sum_{i=1}^{N}\sum_{\substack{j=1\\j\neq i}}^{N}\langle\phi_i(\vec{x}_i)\phi_j(\vec{x}_j)|\,\frac{1}{|\vec{x}_i-\vec{x}_j|}\,|\phi_i(\vec{x}_i)\phi_j(\vec{x}_j)\rangle\right) \tag{3.42}$$

$$=\int\hat{V_h}(\vec{x_k})\phi_k(\vec{x_k})\delta\phi_k^*(\vec{x_k})d\vec{x_k} \tag{3.43}$$

This 'Hartree term' essentially contains the electrostatic repulsion felt by an electron as a result of the electric field of the entire electron cloud including, strangely, itself [273].

We can repeat the same process for the third term of our energy-functional, finding first that:

$$\delta\left(-\frac{1}{2}\sum_{i=1}^{N}\sum_{\substack{j=1\\j\neq i}}^{N}\langle\phi_i(\vec{x}_i)\phi_j(\vec{x}_j)|\,\frac{1}{|\vec{x}_i-\vec{x}_j|}\,|\phi_i(\vec{x}_i)\phi_j(\vec{x}_j)\rangle\right) \tag{3.44}$$

$$=-\int d\vec{x_k}\int d\vec{x_j}\left[\sum_{j=1}^{N}\frac{\phi_j^*(\vec{x_j})\phi_j(\vec{x_k})}{|\vec{x}_k-\vec{x}_j|}\right]\phi_k(\vec{x_k})\delta\phi_k^*(\vec{x_k}) \tag{3.45}$$

We can then, analogously, define non-local particle density:

$$\rho_{nl}(\vec{x_i}, \vec{x_j}) = \sum_{j=1}^{N} \phi_j^*(\vec{x_j})\phi_j(\vec{x_i}) \tag{3.46}$$

and then define 'Fock potential' $\hat{V_f}$ as:

$$\hat{V_f} = -\frac{\rho_{nl}(\vec{x_i}, \vec{x_j})}{|\vec{x}_i - \vec{x}_j|} \tag{3.47}$$

so this final term becomes:

$$\delta \left(-\frac{1}{2} \sum_{i=1}^{N} \sum_{\substack{j=1 \\ j\neq i}}^{N} \langle \phi_i(\vec{x}_i)\phi_j(\vec{x}_j)| \frac{1}{|\vec{x}_i - \vec{x}_j|} |\phi_i(\vec{x}_i)\phi_j(\vec{x}_j)\rangle \right) \tag{3.48}$$

$$= \int d\vec{x_k} \int d\vec{x_j}\ \hat{V_f}\phi_k(\vec{x_k})\delta\phi_k^*(\vec{x_k}) \tag{3.49}$$

The Fock potential is sometimes called the exchange potential [27]. Due to the anti-symmetry of electrons under exchange of their positions (and spins), the expectation value of the distance between them will be increased, partially reducing the potential energy caused by coulomb repulsion [281]. The Fock potential encapsulates this effect, which has no real classical analogue [275].

Returning to our variation, minimising subject to the condition of an orthonormal basis, we have:

$$\delta \langle \Psi | \hat{H}_e | \Psi \rangle - \delta \left(\sum_{i=1}^{N} \sum_{j=1, i\neq j}^{N} \lambda_{ij}(\langle \phi_i | \phi_j \rangle - \delta_{ij}) \right) = 0 \tag{3.50}$$

We can choose our basis set such that Lagrange-matrix λ_{ij} is diagonal $\lambda_{jk} = \delta_{jk}\epsilon_k$. Thus, this variation becomes:

$$\int d\vec{x_k} \left(-\frac{1}{2}\nabla_k^2 + \hat{V}_{eN} + \hat{V}_h + \frac{\int d\vec{x_j} \hat{V_f}\phi_k(\vec{x_j})}{\phi_k(\vec{x_k})}\phi_k(\vec{x_k})\delta\phi_k^*(\vec{x_k}) - \epsilon_k\phi_k(\vec{x_k})\delta\phi_k^*(\vec{x_k}) \right) = 0 \tag{3.51}$$

Since this variation should also be stationary with respect to small differences in $\delta\phi_k^*(\vec{x_k})$, the integrand vanishes, leaving us with Hartree-Fock equation [27, 282, 283]:

$$\left(-\frac{1}{2}\nabla_k^2 + \hat{V}_{eN} + \hat{V}_h + \frac{\int d\vec{x}_j \hat{V_f}\phi_k(\vec{x}_j)}{\phi_k(\vec{x}_k)} \right) \phi_k(\vec{x}_k) = \epsilon_k\phi_k(\vec{x}_k). \tag{3.52}$$

The operators on the left hand side can be bundled into the Fock operator

$$\hat{F}(\vec{x}_k) = -\frac{1}{2}\nabla_k^2 + \hat{V}_{eN} + \hat{V}_h + \frac{\int d\vec{x}_j \hat{V}_f \phi_k(\vec{x}_j)}{\phi_k(\vec{x}_k)} \tag{3.53}$$

so:

$$\hat{F}(\vec{x}_k)\phi_k(\vec{x}_k) = \epsilon_k \phi_k(\vec{x}_k). \tag{3.54}$$

Although this appears like a simple eigenvalue equation, it is not. The equation contains both differentials of ϕ_k (in the kinetic energy), and integrals (in the Fock potential), and this makes it generally not soluble analytically [28].

Furthermore, despite a passing resemblance to the time-independent Schrödinger equation, the eigenvalues of the Fock operator are not the same as the energy-eigenvalues and the sum over them is not equal to the total (Hartree-Fock) energy of the system. If we attack the Hartree-Fock equation, above, from the left with ϕ_k, then sum over k, we can find that:

$$\sum_{k=1}^{N} \epsilon_k = \sum_{k=1}^{N} \langle \phi_k | \hat{F}(\vec{x_k}) | \phi_k \rangle \tag{3.55}$$

$$\begin{aligned} &= \sum_{k=1}^{N} \langle \phi_k(\vec{x}_k) | -\frac{1}{2}\nabla_k^2 + \hat{V}_{eN} | \phi_k(\vec{x}_k) \rangle \\ &\quad + \sum_{k=1}^{N}\sum_{\substack{j=1 \\ j\neq k}}^{N} \langle \phi_k(\vec{x}_k)\phi_j(\vec{x}_j) | \frac{1}{|\vec{x}_k - \vec{x}_j|} | \phi_k(\vec{x}_k)\phi_j(\vec{x}_j) \rangle \\ &\quad - \sum_{k=1}^{N}\sum_{j=1, j\neq k}^{N} \langle \phi_k(\vec{x}_k)\phi_j(\vec{x}_j) | \frac{1}{|\vec{x}_k - \vec{x}_j|} | \phi_k(\vec{x}_j)\phi_j(\vec{x}_k) \rangle \end{aligned} \tag{3.56}$$

$$= \langle \Psi | \hat{H}_{ni} | \Psi \rangle + 2 \langle \Psi | \hat{V}_{ee} | \Psi \rangle \tag{3.57}$$

where $\hat{H}_{ni} = -\nabla_k^2/2 + \hat{V}_{eN}$ is the Hamiltonian for an electron excluding inter-electronic repulsion. Therefore the sum of the eigenvalues of the Fock operator does not equal the expectation value of the minimised energy functional [23], but rather the expectation of the energy plus the expectation value of the total potential energy from electron-electron repulsion:

$$\sum_{k=1}^{N} \epsilon_k = \langle \Psi | \hat{H}_e | \Psi \rangle + \langle \Psi | \hat{V}_{ee} | \Psi \rangle \tag{3.58}$$

where $\hat{H}_e = \hat{H}_{ni} + \hat{V}_{ee}$.

Self-consistent Field Method

As stated previously, the Hartree-Fock equation is not analytically soluble outside of a few special cases, since the Fock operator simultaneously involves a derivative and

an integral of the basis vectors ϕ_k. Instead, the HF equations are typically solved iteratively using a computer, until the system is self-consistent [24, 27, 28]. This type of strategy is known as a self-consistent field method, as mentioned previously, and includes these steps:

1. Make an initial guess for the basis functions $\{\phi_i\}_{i\in\{1,N\}}$.
2. Use the basis functions to build local and non-local density ρ_l and ρ_{nl}.
3. Use these densities, together with the basis functions, to compute the Hartree and Fock potentials $\hat{V_h}$ and $\hat{V_f}$, and so obtain the matrix-elements of the Fock operator.
4. Holding these matrix elements fixed, solve the eigenvalue equation $\hat{F}\phi_k = \epsilon_k\phi_k$, yielding new basis functions $\{\phi_k\}_{k\in\{1,N\}}$.
5. Use these new basis functions to recalculate the densities ρ_l and ρ_{nl}, and repeat the entire procedure, until successive iterations yield sufficiently similar functions ϕ_k at the end.

This is essentially equivalent to guessing the electronic orbitals of a molecule, before adjusting the orbitals in a way that reduces the energy, and repeating until the system settles to a minimum. There is, however, no guarantee that the iterations will converge, and so the first guess to the orbitals must be judicious. Even then, some numerical tricks (for example, mixing the electron densities with a portion of that from the previous iteration) may be needed to prevent the computation from diverging [24, 284].

The initial guess for the basis set is, in the canonical case, done using a linear combination of atomic orbitals (LCAO) [285]. Slater-type atomic orbitals centred on each atom in the molecule are added together to form molecular orbitals, which are then iterated upon using the self-consistent-field procedure to refine them. Although Slater type orbitals are the 'ideal' case, due to their good satisfaction of requirements such as the Kato cusp condition and good long-distance behaviour, more simple Gaussian orbitals are more typically used [286].

This is because the product of any two Gaussian orbitals can be formed of a finite sum of other Gaussian orbitals, reducing integrals over orbitals around four centres to integrals around two, and then one centre. Despite this having the drawback of requiring a larger basis set than for Slater-type orbitals, it is usually worth it so as to compute fewer integrals, and can speed up computations by a factor of four or more [286, 287].

Unfortunately, Hartree-Fock theory, as a mean-field scheme, has a poor accounting of electron-electron correlation (within the $\hat{V}_{ee}$ term of the molecular Hamiltonian), and the mean-field the electron is simulated as being subject to includes itself [27, 28]! The central task of other computational schemes for simulating electronic properties of matter is to account better for this electron correlation and exchange [288]. For medium to large molecular systems, density functional theory (DFT) is a common compromise, achieving better accuracy than HF mean-field techniques

while attempting to control the extra, often prohibitive, computational cost of more comprehensive schemes [22–24].

3.2.4 Density Functional Theory

Density functional theory (DFT), makes the central innovation of working in terms of an electron density functional $\rho(\vec{r})$ instead of multi-electron wavefunctions Ψ[22–24], where the single-electron densities are related to the wavefunctions by:

$$\rho_n(\vec{r_1}) = N_e \int d\vec{r_2} \ldots \int d\vec{r_N} \langle \psi_n | \psi_n \rangle \tag{3.59}$$

This reduces our multi-electron system to a single-electron system, which is much easier to solve, but this jump to using the density-functional in the place of a wavefunction relies on the Hohenberg-Kohn theorems [289]. In our investigations, we have used DFT and time-dependent (TD) DFT to model the electronic response of molecules to intense laser fields, since the balance of accuracy vs computational intensity was satisfactory to our requirements.

The Hohenberg-Kohn Theorems

Existence Theorem 1 *"Any observable of a stationary non-degenerate ground state can, exactly in theory, be calculated from the electron density of the ground state."*

Variation Theorem 1 *"The electron density of a non-degenerate ground state can, exactly in theory, be calculated by determining the density which minimises the energy of the ground state."*

What the existence theorem means, essentially, is that the ground state energy $E_0 = \langle \psi_0 | \hat{H} | \psi_0 \rangle$ can be expressed as a unique functional of ground state electron density $E_0 = E[\rho_0(\vec{r})]$, and that this relation is unique: there are no two ground states which have the same electron density [289]. We can prove the first theorem by a simple proof by contradiction.

The molecular electric potential V_n (the sum potential energy due to Coulomb forces from both the nucleii and the electrons) is both (to within a constant) a unique functional of ρ, and ρ and V_n together then fix Hamiltonian $\hat{H}$. If we consider two molecular potentials V_n and V_n' which differ by more than the addition of some constant, and assume that these both give rise to the same electron density, these molecular potentials will give rise to two distinct Hamiltonians $\hat{H} = \hat{T} + \hat{V_n}$ and $\hat{H}' = \hat{T} + \hat{V_n}'$, wavefunctions Ψ and Ψ', and ground state energies $E_0 \neq E_0'$.

If we use wavefunction Ψ' as a trial wavefunction for the opposite Hamiltonian $\hat{H}$, we find that:

$$\langle \Psi' | \hat{H} | \Psi' \rangle = \langle \Psi' | \hat{H}' | \Psi' \rangle + \langle \Psi' | \hat{H} - \hat{H}' | \Psi' \rangle > E_0 \tag{3.60}$$

or equivalently (since Hamiltonians differ only by their different potentials):

$$E_0' + \int \rho(\vec{r}) \, (V_n - V_n') \, d\vec{r} > E_0 \tag{3.61}$$

If we repeat the above procedure, but using Ψ as a trial wavefunction for Hamiltonian $\hat{H}'$, we find:

$$E_0 - \int \rho(\vec{r}) \, (V_n - V_n') \, d\vec{r} > E_0' \tag{3.62}$$

Adding these two equations together, we find contradiction $E_0 + E_0' > E_0 + E_0'$, thus proving that there are no two distinct sets of molecular potential, many-body Hamiltonian and wavefunction which correspond to the same density [289].

The second of the Hohenberg-Kohn theorems is what we can now utilise to find our ground-state electron density, similar to the case of Hartree-Fock theory, this time by choosing some candidate electron density $\tilde{\rho}$ which corresponds to wavefunction $\tilde{\Psi}$.

Using this as a trial wavefunction for Hamiltonian $\hat{H}$:

$$\langle \tilde{\Psi} | \, \hat{H} \, | \tilde{\Psi} \rangle = T[\tilde{\rho}] + E_{ee}[\tilde{\rho}] + \int \rho(\vec{r}) V_n d\vec{r} = E[\tilde{\rho}(\vec{r})] \geq E_0[\rho_0] = \langle \Psi_0 | \, \hat{H} \, | \Psi_0 \rangle \tag{3.63}$$

Meaning that the energy functional $E[\rho(\vec{r})] = \int \rho(\vec{r}) V_n d\vec{r} + T[\rho(\vec{r})] + E_{ee}[\rho(\vec{r})]$, where T is kinetic energy and E_{ee} is potential from electron-electron repulsion, is minimised for the density of the true ground state energy functional (the variance theorem). The first part of this energy functional is system specific, while the second part is a universal functional which does not depend on the molecular potential, and is often bundled as the Hohenberg-Kohn functional $F_{HK}[\rho(\vec{r})] = T[\rho(\vec{r})] + E_{ee}[\rho(\vec{r})]$. E_{ee} can be further decomposed into 'classical' Hartree-repulsion energy [273]

$$E_h[\rho(\vec{r})] = \int \frac{\rho(\vec{r}) \rho(\vec{r'})}{|\vec{r} - \vec{r'}|} d\vec{r'} \tag{3.64}$$

and some non-classical component $E_{nc}[\rho(\vec{r})]$ [289].

In principle, we could find the exact ground-state density and wavefunction by minimising the energy functional subject to the condition of orthonormality. However, in practise, the energy functional we wish to minimise is not known, and the non-classical component of the electron-electron potential energy can only be approximated [22, 24].

The Kohn-Sham equations

In order to minimise this energy functional and find the ground-state electron density of the system, we now follow the Kohn-Sham approach, as discovered by Walter Kohn and Lu Jeu Sham in 1965 [290]. Our main issue is that, of the terms in the Hohenberg-Kohn functional, the only one that we know is the Hartree-electron-repulsion E_h: The non-classical electron-electron interaction term is unknown, and the true kinetic energy term T is altered by the existence of multiple self-interacting electrons [24].

Our approach will be, instead, to construct some fictitious system of N non-interacting electrons moving in some effective potential [291]. The Hamiltonian of such a system will therefore be:

$$\hat{H}_s = \hat{T}_s + \sum_{i=1}^{N} \hat{V}_s(\vec{r_i}) \tag{3.65}$$

where subscript s indicates operators belonging to our non-interacting system, $\hat{V}_s$ being the effective potential of this fictional system, and $T_s = -\frac{1}{2}\sum_i^N \nabla_i^2$ is the kinetic energy as defined in the usual way.

We say that the exact ground state wavefunction of this non-interacting system is given by Slater determinant Ψ, and that component spin orbitals of this Slater determinant ϕ_i obey eigenvalue equation:

$$\hat{f}_{KS}\phi_i = \epsilon_i\phi_i \tag{3.66}$$

where

$$\hat{f}_{KS} = -\frac{1}{2}\nabla^2 + V_s(\vec{r}), \tag{3.67}$$

and ϕ_i are the Kohn-Sham orbitals. These orbitals have no real physical meaning, they just happen to add up to produce the same electron density as found in our real system. To this end, we want to choose effective potential V_s such that $\rho_s(\vec{r}) = \sum_{i=1}^{N} |\phi_i(\vec{r})|^2$ of the functional system is equal to pure real ground-state electron density $\rho_0(\vec{r})$.

We now define Kohn-Sham operator $\hat{F}[\rho] = T_s[\rho] + E_h[\rho] + E_{XC}[\rho]$. Despite being, as defined, dependent on wavefunctions $T_s = -\frac{1}{2}\langle\phi_i|\nabla^2|\phi_i\rangle$, the fictitious kinetic energy is still a valid functional of ρ since all other terms in this equation are functionals, and so T_s must be as well.

The exchange-correlation functional E_{XC} is a collection of all unknown functionals:

$$E_{XC}[\rho] = (T[\rho] - T_s[\rho]) + (E_{ee}[\rho] - E_h[\rho]) = T_{nc}[\rho] + E_{nc}[\rho], \tag{3.68}$$

combining the residual part of the kinetic energy due to electron-electron interactions with the part of electron-electron repulsion that is not described by the Hartree term.

Using now the total energy functional of our real system $E[\rho] = T_s[\rho] + E_h[\rho] + E_{XC}[\rho] + E_n[\rho]$, and minimising this energy with variations of density $\delta\rho$ under the condition of orthonormality, we arrive at the Kohn-Sham equation:

$$\left(-\frac{1}{2}\nabla^2 + \left(\int \frac{\rho(\vec{r'})}{|\vec{r} - \vec{r'}|} d\vec{r'} + V_{XC}(\vec{r}) + V_n(\vec{r})\right)\right)\phi_i = \left(-\frac{1}{2}\nabla^2 + V_s(\vec{r})\right)\phi_i = \epsilon_i\phi_i \tag{3.69}$$

where:

$$V_s = \int \frac{\rho(\vec{r'})}{|\vec{r} - \vec{r'}|} d\vec{r'} + V_{XC}(\vec{r}) + V_n(\vec{r}) = V_h + V_{XC} \tag{3.70}$$

and:

$$V_{XC} = \frac{\delta E_{XC}}{\delta\rho} \tag{3.71}$$

where ϵ_i are the Kohn-Sham energies of our fictitious non-interacting system of electrons, and E_{XC} is the exchange-correlation energy.

We cannow feel confident in defining the Kohn-Sham Hamiltonian:

$$\hat{H}^{KS} = \left(-\frac{1}{2}\hat{\nabla}^2 + \hat{V}_s(\vec{r})\right) \tag{3.72}$$

such that the Kohn-Sham equations become:

$$\hat{H}^{KS}\phi_i = \epsilon_i\phi_i \tag{3.73}$$

This equation once again can not, in general, be solved analytically, since the Kohn-Sham Hamiltonian depends on the Kohn-Sham orbitals themselves, via the electron density ρ [22, 24]. We must again turn to some self-consistent field scheme.

The computation of Kohn-Sham orbitals is done by expressing them as a linear sum of a number of atomic 'pseudo-wavefunctions' $\phi_i = \sum_{j=1}^{N} a_{ij}\chi_j$, where χ_j are typically either formed from hydrogen-type atomic orbitals, or Gaussian-type orbitals [286].

We can then determine coefficients a_{ij} which result in correct Kohn-Sham energies ϵ_i using secular equation:

$$\sum_{j=1}^{N} a_{ij}\left(H_{kj}^{KS} - \epsilon_j S_{kj}\right) = 0 \tag{3.74}$$

where $H_{kj}^{KS} = \langle\chi_k| H^{KS} |\chi_j\rangle$ are the matrix elements of the Kohn-Sham Hamiltonian while $S_{kj} = \langle\chi_k|\chi_j\rangle$ are overlap integrals. All of this can only be solved by some iterative method, until the resulting Kohn-Sham energy and electron density are self consistent.

This is done, similarly to Hartree-Fock theory, by guessing an initial set of orbitals and establishing an initial density $\rho_{initial}$, before using that initial density to find the effective potential $V_s[\rho_{initial}]$. The matrix elements of Kohn-Sham Hamiltonian H_{kj}^{KS} can be found and, along with overlap integrals S_{kj}, used to establish a new set of Kohn-Sham orbitals $\phi_i^{(1)}$, and thus a new density $\rho^{(1)}$. The process is then repeated until successive values of the density are consistent down to some chosen tolerance [24].

Approximating Exchange-correlation Functionals

As said previously, this technique could in principle converge on an exact solution but for the unknown exchange-correlation functional E_{XC} which must be approximated [24, 292, 293]. One common and relatively simple approach is the so-called local density approximation (LDA), which approximates the electron cloud as a non-interacting homogeneous electron gas of density ρ [290, 294]. The LDA approximates the exchange energy to be a function of the local electron density, equal to the exchange energy of a homogeneous non-interacting electron gas with a uniform density $\rho(\vec{r})$, with corresponding exchange energy density of the form $\varepsilon_X[\rho(\vec{r})] = A\int \rho(\vec{r})^{\frac{4}{3}} d\vec{r}$, where A is some constant. Therefore, the exchange-correlation functional becomes:

$$E_{XC}[\rho] = \int \rho(\vec{r})\varepsilon_{XC}(\rho(\vec{r}))d\vec{r} \tag{3.75}$$

where exchange-correlation energy density ε_{XC} can be broken down into exchange and correlation components:

$$\varepsilon_{XC}(\rho) = \varepsilon_X(\rho) + \varepsilon_C(\rho) \tag{3.76}$$

Exchange energy density for a uniform electron gas can be written as:

$$\varepsilon_X(\rho) = -\mathcal{C}\rho^{\frac{1}{3}}, \tag{3.77}$$

where $\mathcal{C}$ is a constant, to as to be consistent with total exchange energy above, but correlation energy density ε_C has no simple expression. Instead, it is typically calculated numerically using quantum-mechanical Monte-Carlo simulations [295].

The exchange and correlation energy densities in the LDA are not particularly accurate [296], but nonetheless the LDA is quite often very accurate in practice. There are several reasons for this. The first is that the LDA tends to underestimate exchange energy, while overestimating the energy density for electron correlation, and so these errors tend to cancel each other out [297, 298]. Another reason can be explained by considering the exchange-correlation 'hole' in the electron density that is dug by an electron at any given point in space. In reality these holes in the electron density tend to be asymmetrical, but it can be shown that the electron-electron repulsion energy only depends on the spherically-averaged depletion of density within the hole and so the LDA, which implicitly approximates the hole as being spherically symmetric, does not suffer any reduction in accuracy due to this [296, 297, 299].

Perhaps the 'next level' up of approximations are generalised gradient approximations, or GGAs. These are similar to the LDA, in that they use the local electron

density to estimate the exchange-correlation energy, but seek to include some of the inhomogeneity of the electron density within a real molecule by expanding exchange-correlation energy density ε_{XC} in terms of the spatial derivatives of ρ as a Taylor series. In so doing, they can achieve incremental improvements on the accuracy of the LDA at the cost of more computational resources [300–303].

Lastly, many of the most commonly utilised exchange-correlation functionals in use today come from the family of 'Hybrid-exchange' functionals [304–306]. The exchange energy of a non-interacting electronic system can be calculated, in principle exactly, using the Fock energy E_f. The correlation and exchange energies associated with electron-electron interactions can be calculated then, exactly in theory, by calculating the work done on the system when taking it from a non-interacting state and gradually turning on electron-electron interactions. If we parameterise the degree to which electron-electron interactions are 'on' by some value λ, we can integrate the work done in bringing in the interactions to find:

$$E_{XC}[\rho] = \frac{1}{2}\int\int\int_{\lambda=0}^{1} \frac{\lambda}{|\vec{r}-\vec{r'}|}\left[\langle\rho(\vec{r})\rho(\vec{r'})\rangle - \rho(\vec{r})\delta(\vec{r}-\vec{r'})\right] d\lambda d\vec{r} d\vec{r'} \quad (3.78)$$

where $\lambda = 0$ corresponds to a non-interacting system while $\lambda = 1$ corresponds to a fully interacting one. This technique is known as the adiabatic connection [307].

Unfortunately, this integral is not known as the exact functional reliance of the density on electron-interaction parameter λ is itself not known, so instead the integral is usually approximated by some weighted sum of its end points [306].

For example, the Becke exchange-correlation functional [304]:

$$E_{XC}^{B} = E_{XC}^{LDA} + 0.2(E_X^{Fock} - E_X^{LDA}) + 0.72\Delta E_X + 0.81\Delta E_C^{PW91} \quad (3.79)$$

uses as a base the local density approximation, replacing some of this contribution with non-interacting Fock exchange energy, together with GGA corrections to both exchange and correlation energies (marked by Δ). This is desirable since the exchange-correlation hole in the LDA in very localised, whereas in reality it tends to be delocalised, and so the non-local contributions from the Fock-exchange together with quasi-local GGA terms corrects this [297]. One very common exchange correlation functional is the Becke-3 Lee-Yang-Parr functional [305]:

$$E_{XC}^{B3LYP} = (1-a)E_{XC}^{LDA} + aE_X^{Fock} + bE_X^{B88} + cE_C^{LYP} + (1-c)E_C^{LDA} \quad (3.80)$$

where the Lee-Yang-Parr functional correction is another GGA functional, and coefficients a, b, c are obtained semi-empirically. It is important to note that the exact mathematical expressions for energy functionals change on the inclusion of electron spin, but the underlying physics remains the same.

In section 5, we present results obtained using DFT. In that instance, we have used a general exchange-correlation provided by the Lee-Yang-Parr expression on a base of the Becke-3-parameter hybrid functional (B3LYP), with long-range electron correlation accounted for using the Coulomb-attenuating method (CAM) [308].

3.2.5 Time-Dependent Density Functional Theory

Standard DFT can be very effective in describing a static system, but to model the dynamic response of a quantum system to a time-varying external field, this scheme must be extended to the time-dependent case. To be confident in the validity of using a Kohn-Sham-type scheme for a time-dependent system, we need a theorem analogous to the Hohenberg-Kohn theorems. Unfortunately, unlike standard DFT, where the ground state can be determined by minimising an energy functional, in a time-dependent situation total energy is not conserved because the molecular system can absorb and lose energy from an external field. Instead, we can use a quantum mechanical action functional [25]:

$$\mathcal{A}[\Psi] = \int_{t_0}^{t_1} \langle\Psi| \, i\frac{\partial}{\partial t} - \hat{H}(t) \, |\Psi\rangle \tag{3.81}$$

which can be used, along with a functional derivative with respect to $\langle\Psi|$, to derive the time-dependent Schrödinger equation. Finding a stationary point of the action gives us a variational principle we can use to obtain a solution to our time-dependent problem.

We now must prove the unique mapping of time-dependent density $\rho(\vec{r}, t)$ to all other system variables; the Runge-Gross theorem [309].

The Runge-Gross Theorems

This uniqueness is equivalent to showing that if two time-dependent potentials $V(\vec{r}, t)$ and $V'(\vec{r}, t)$ differ by more than some purely-time dependent function $C(t)$, then they cannot reproduce the same total density. As in the proof of the Hohenberg-Kohn theorem, all other system variables depend on this; the system-specific potential defines the Hamiltonian, thus the wavefunction, and thus the density.

This proof only works if we restrict ourselves to potentials which are Taylor expandable about $t = t_0$ such that

$$V(\vec{r}, t) = \sum_{k=0}^{\infty} \frac{1}{k!} \left| \left(\frac{d^k}{dt^k} V(\vec{r}, t) \right) \right|_{t=t_0} (t - t_0)^k. \tag{3.82}$$

It will further be helpful to define some quantity $U_k(\vec{r})$ such that

$$U_k(\vec{r}) = \frac{\partial^k}{\partial t^k} \left| (V(\vec{r}, t) - V'(\vec{r}, t)) \right|_{t=t_0} \tag{3.83}$$

which will be constant if the two functions only differ by a simple function of time, but will vary if they differ by a function of both space and time.

For our proof, we must use probability-current density defined as:

$$\vec{j} = -\frac{1}{2i} \left(\nabla\Psi^*\Psi - \Psi^*\nabla\Psi \right). \tag{3.84}$$

Using Ehrenfest's theorem [310], we find that the time evolution of this current density follows:

$$i\frac{d}{dt}\vec{j} = \langle\Psi|\left[\vec{j}, \hat{H}(t)\right]|\Psi\rangle \tag{3.85}$$

whilst for the alternate potential V', we get:

$$i\frac{d}{dt}\vec{j'} = \langle\Psi'|\left[\vec{j}, \hat{H'}(t)\right]|\Psi'\rangle \tag{3.86}$$

Our two systems must start in the same state, such that $|\Psi(t_0)\rangle = |\Psi'(t_0)\rangle = |\Psi_0\rangle$, $\vec{j}(\vec{r}, t_0) = \vec{j'}(\vec{r}, t_0) = \vec{j_0}(\vec{r})$ and $\rho(\vec{r}, t_0) = \rho'(\vec{r}, t_0) = \rho_0(\vec{r})$.

By taking the difference between these two equations of motion at $t = t_0$, we find:

$$\begin{aligned} i\frac{d}{dt}\left|\left(\vec{j} - \vec{j'}\right)\right|_{t=t_0} &= \langle\Psi_0|\left[\hat{j}, \left(\hat{H}(t_0) - \hat{H'}(t_0)\right)\right]|\Psi_0\rangle & (3.87)\\ &= \langle\Psi_0|\left[\hat{j}, \left(\hat{V}(t_0) - \hat{V'}(t_0)\right)\right]|\Psi_0\rangle & (3.88)\\ &= i\rho_0(\vec{r})\nabla\left(V(\vec{r}, t_0) - V'(\vec{r}, t_0)\right) & (3.89)\end{aligned}$$

If we then force V and V' to differ at time $t = t_0$, then we find there will be a difference between the rates of change of the current densities

$$\frac{d}{dt}\vec{j} \neq \frac{d}{dt}\vec{j'}. \tag{3.90}$$

If we now time-differentiate the equations of motion recursively $k+1$ times, we find:

$$\left|\frac{d^{k+1}}{dt^{k+1}}\left(\vec{j} - \vec{j'}\right)\right|_{t=t_0} = \rho_0(\vec{r})\nabla U_k(\vec{r}) \neq 0 \tag{3.91}$$

so further time derivatives of currents $\vec{j}$ and $\vec{j'}$ will also diverge, and so we conclude that the current densities must change differently over time if the potentials V and V' differ by a function of space.

We need now only to demonstrate that if the current densities are different, this will result in a different electron density. We can make use of continuity:

$$\frac{\partial}{\partial t}\rho(\vec{r}, t) = -\nabla\cdot\vec{j}(\vec{r}, t) \tag{3.92}$$

For each case, taking the $k+1^{th}$ time derivative and finding the difference at $t = t_0$:

$$\begin{aligned} \frac{\partial^{k+2}}{\partial t^{k+2}}\left[\rho(\vec{r}, t) - \rho'(\vec{r}, t)\right]_{t=t_0} &= -\nabla\cdot\frac{\partial^{k+1}}{\partial t^{k+1}}\left[\vec{j}(\vec{r}, t) - \vec{j'}(\vec{r}, t)\right]_{t=t_0} & (3.93)\\ &= -\nabla\cdot\left[\rho_0(\vec{r})\nabla U_k(\vec{r})\right] & (3.94)\end{aligned}$$

If this quantity is not equal to zero, then the two densities must diverge over time. If we assume that $\nabla U_k \neq 0$ and use Green's theorem:

$$\int_V \rho_0(\vec{r})(\nabla U_k(\vec{r}))^2 d^3\vec{r} = \int_\Sigma \rho_0(\vec{r}) U_k(\vec{r}) \nabla U_k(\vec{r}) \cdot d\vec{\Sigma} - \int_V U_k(\vec{r}) \nabla \cdot [\rho_0(\vec{r}) \nabla U_k(\vec{r})]\, d^3\vec{r} \tag{3.95}$$

where V and Σ are arbitrary bounding surfaces. The left-hand side cannot be zero, since the integrand is always positive. However, the integrand in the second term on the right-hand side is zero, while the first term will vanish if either ρ or U_k are compact in space (which they are for molecules). This is a contradiction, proving the uniqueness of the mapping between electronic density and all other variables for time dependent systems holds, just as for time-independent systems.

The Time-dependent Kohn-Sham Equations

Thanks to the uniqueness property we have just proven, we can again use a Kohn-Sham-type procedure to model our (now time-dependent) molecular system [25, 26].

As before, we replace our real interacting system, which we cannot simulate directly, with a fictitious system of non-interacting electrons which replicates the same electron density. Since the electron density uniquely corresponds to all other physical variables, our fictitious system has the same properties as the real one.

By taking the functional derivative of the quantum-mechanical action with respect to wavefunction ϕ_i we find the time-dependent Kohn-Sham equations:

$$i\frac{\partial}{\partial t}\phi_i(\vec{r}, t) = \left[-\frac{1}{2}\nabla^2 + \hat{V}_{KS}(\vec{r}, t)\right] \phi_i(\vec{r}, t) \tag{3.96}$$

where electron density can be found by a sum over *occupied* orbitals:

$$\rho(\vec{r}, t) = \sum_{i=1}^{N_{occupied}} \langle \phi_i(\vec{r}, t) | \phi_i(\vec{r}, t) \rangle \tag{3.97}$$

and $\hat{V}_{KS}$ is the time-dependent effective potential which replicates in our fictitious system the same density as found in our real system:

$$\hat{V}_{KS}(\vec{r}, t) = \hat{V}_n(\vec{r}) + \hat{V}_{applied}(\vec{r}, t) + \hat{V}_h(\vec{r}) + \hat{V}_{XC}(\vec{r}) \tag{3.98}$$

where $\hat{V}_h$ is the Hartree coulomb-repulsion:

$$\hat{V}_h = \int \frac{\rho}{|\vec{r} - \vec{r'}|} \tag{3.99}$$

as before, $\hat{V}_{applied}$ is the externally applied time-varying electric field (eg. a laser beam), and $\hat{V}_{XC}$ is the exchange-correlation potential.

Although the exchange-correlation potential arises from the same physics as in the time-independent case, its particular mathematics differ. Whereas before it came about from a variation with respect to density ρ of the exchange-correlation energy functional, this is no longer possible since energy now varies with time [311]. The derivation via functional derivative of an action is, in the naïve sense, forbidden due to an issue with the flow of causality. This problem was solved by Robert van Leeuwen using the Keldysh formulation of complex time-path-integration to define via a new action [312]:

$$\hat{V}_{XC} = \left| \frac{\delta \tilde{\mathcal{A}}_{\mathcal{XC}}}{\delta \rho(\vec{r}, \tau)} \right|_{\rho(\vec{r},t)} \tag{3.100}$$

where τ is the Keldysh 'pesudo-time' and action $\tilde{\mathcal{A}}_{\mathcal{XC}}$ is, like the exchange-correlation energy, a functional which needs to be approximated [312].

These approximations are often analogues of those used in time-independent DFT. One of the most common types are the 'adiabatic' approximations. Just as the local density approximation uses a function of the density at a specific point in space to estimate the exchange-correlation energy at that point, adiabatic exchange-correlation potentials are 'local' in time, using the density at a point in time to estimate the exchange and correlation at that specific point in time [313, 314]. This is as opposed to an exchange-correlation potential which exhibits some hysteresis with respect to the changes of the density [315–317]; an adiabatic approximation $\hat{V}^{A}_{XC}[\rho(\vec{r}, t)]$ has no dependence on the time-derivatives of density $\partial\rho/\partial t$, or densities at any time other than time t, nor does the functional dependence of exchange-correlation potential on density ρ change with time.

The most common example of such an exchange-correlation potential is the adiabatic local-density approximation (ALDA) [318], which assumes that the exchange and correlation energies at any point within a molecule at any point in time are roughly equal to those in a static and homogeneous electron gas of equivalent density. This approximation behaves similarly to the time-independent LDA, being likewise accurate in practice despite theoretical shortcomings: errors in the exchange and correlation parts tend to cancel out, as do errors from not including non-local contributions, and errors from the imperfect representation of the shape of the exchange-correlation hole [296, 318]. Just as in the time-independent case, the ALDA is often supplemented with other exchange-correlation functions, such as the Fock energy and GGA-like approaches, to further refine its accuracy [25, 318, 319].

Propagation

As before, the time-dependent Kohn-Sham equations must be solved self-consistently. Now, however, they must also be propagated forward in time. There are various schemes for doing this, and many different codes. We have used the open-source TDDFT code OCTOPUS.

After having generated an initial state for time $t = t_0$, the state at time t_f

(expressed in terms of Kohn-Sham orbitals ϕ_i) can be expressed as:

$$\phi_i(\vec{r}, t_f) = \hat{\mathcal{U}}(t_f, t_0)\phi_i(\vec{r}, t_0) \tag{3.101}$$

where time-propagation operator $\hat{\mathcal{U}}$ can be expressed as:

$$\hat{\mathcal{U}}(t_f, t_0) = \mathcal{T} e^{-i\int_{t_0}^{t_f} \hat{H}_{KS}(t')dt'} \tag{3.102}$$

where $\mathcal{T}$ is the time-ordering operator and $\hat{H}_{KS}$ is the Kohn-Sham hamiltonian:

$$\hat{H}_{KS}(t) = -\frac{1}{2}\nabla^2 + \hat{V}_{KS}(\vec{r}, t). \tag{3.103}$$

The spatial and temporal domains are, in reality, continuous, but in order to solve the Kohn-Sham equations numerically both must be discretised. For the spatial domain, this means representing system variables such as the electron density, wavefunction, and effective potential by their values at points in a three-dimensional uniform grid within some simulation region. The time-domain must be discretised by dividing the time domain into a series of time-steps Δt such that time $t_{n+1} = t_n + \Delta t$, with:

$$\phi_i(\vec{r}, t_{n+1}) = \hat{\mathcal{U}}(t_{n+1}, t_n)\phi_i(\vec{r}, t_n) \tag{3.104}$$

Furthermore, since the state of the molecule at any time depends on the state at previous points in time, the propagation should begin from a point in time when applied fields are static so that calculations from then on are accurate [320]. The difficulty comes in evaluating the propagator $\hat{\mathcal{U}}$, specifically in finding an appropriate approximation of the time integral of the Hamiltonian. The Kohn-Sham Hamiltonian varies continuously with time, and so the correct value at the beginning of any given time-step may not necessarily be valid for all times within the time-step. Thus, for any technique, the time-step used must be sufficiently small lest the simulation diverge from the correct behaviour over time.

The naïve approach would be to use the value of the Hamiltonian at the beginning of a time-step to propagate over the rest of the time-step:

$$\hat{\mathcal{U}}(t + \Delta t, t) = \mathcal{T} e^{-i\hat{H}_{KS}(t)\Delta t} \tag{3.105}$$

However, we should expect our propagation to have time-reversal symmetry, which this lacks, since the time-reversed propagation would use the Hamiltonian as evaluated at the opposite end of the time-step.

The solution is to somehow force the propagation to have time-reversal symmetry. This can be done by splitting the time-step in half, and imposing that the states $\phi_i(t + \Delta t/2)$ halfway-through the step can be obtained both by propagating the initial state $\phi_i(t)$ forwards by a half-step $\Delta t/2$ or the final state $\phi_i(t + \Delta t)$ backwards by $\Delta t/2$. This can be done by propagating the initial state forwards one half-step using the Hamiltonian from the beginning of the step, and the rest of the way using the Hamiltonian from the end [261, 321, 322].

This is equivalent to approximating the time-integral of the Hamiltonian in the propagator by an average of its end points:

$$\phi_i(\vec{r}, t + \Delta t) = \hat{\mathcal{U}}^{-1}(t + \Delta t, t + \Delta t/2)\hat{\mathcal{U}}(t + \Delta t/2, t)\phi_i(\vec{r}, t) \tag{3.106}$$

$$= e^{-\frac{i}{2}(\hat{H}_{KS}(t)+\hat{H}_{KS}(t+\Delta t))\Delta t}\phi_i(\vec{r}, t) \tag{3.107}$$

where reverse propagator $\hat{\mathcal{U}}^{-1}(t + \Delta t, t) = \hat{\mathcal{U}}(t - \Delta t, t)$.

Specifics of OCTOPUS

The issue with doing this split propagation is obviously that you can not know the Hamiltonian from time t_{n+1} before you have evaluated the state of the system at that time!

One could propagate the state approximately first by a whole time step using the Hamiltonian from the beginning of the interval, before using the approximate Hamiltonian from the end of the interval for the split propagation scheme outlined above. This, however, entails a degree of redundant computation. Therefore, in order to save resources, we can truncate the Taylor series of the exponential within the approximate propagator. In OCTOPUS, this truncation is done at the fourth order in Δt, and this enables a very stable split propagation, given a judicious choice of time interval Δt [261, 322].

Another specific feature of how OCTOPUS tackles solving TDDFT is the inclusion of an absorption potential at the edge of a spatial domain [261]. A full solution to the time-dependent Kohn-Sham equations would require calculating for the entire spatial domain, but this is obviously not feasible. Computational resources are not unlimited, so the spatial domain of the problem must be truncated somewhere. If our solutions are well behaved, they should decrease exponentially towards $R \to \infty$, so our solutions should still converge given we have a large enough domain.

However, truncating the domain in this way may add unwanted artefacts to the simulation, such as electron density being reflected by the edge of the space. In order to prevent this, and reduce the size of the domain needed for the simulations to behave correctly, OCTOPUS adds an absorption potential $-iV_{abs}(\vec{r})$ to the Kohn-Sham potential V_{KS}, which is zero throughout most of the domain but rises continuously towards the edge of the spatial domain. For a judicious choice of both the height and width of this potential, it can be configured such that most of the electron density that is absorbed is that of electrons with momenta that would allow them to escape the molecule's potential well (photo-electrons), whilst minimising the amount of reflection and similar unwanted artefacts from the boundary.

The radius from the centre of the molecule where from which this potential starts to 'kick in' must also be set such that the potential does not disturb the electrons within the molecule as it lies in either the ground or relatively lowly excited states, and so the boundary must be at least several Ångstroms from the molecule itself [261].

Overall, TDDFT in general, and OCTOPUS in particular, have provided us with a satisfactory technique to model the electronic response of matter with sufficient

accuracy with an acceptable investment of computational resources. As such, the simulations conducted in section 4 were done using TDDFT in the software package OCTOPUS.

3.3 Orientational-averaging Schemes

After having simulated the electronic response of a single molecule to a passing laser pulse, the next task is how to convert that into a model of the emission of light. For this task, the pertinent variable is the time-series of the polarisation of the molecule:

$$\vec{P}(t) = \int \rho_d(\vec{r}, t) d^3\vec{r} \propto \sum_{i=1}^{N} \langle \phi_i(t) | \, \hat{d}(t) \, | \phi_i(t) \rangle \tag{3.108}$$

where $\hat{d}$ denotes the dipole operator and ρ_d is the electric dipole density at a given point in space. For TD-DFT conducted using a discrete spatial grid, this integral is evaluated at the grid-points $\vec{r}_i$ [323]. However, for spectral methods, the above integral can be evaluated as:

$$\vec{P}(t) = \sum_{i=1}^{N} |\mathcal{C}_i|^2 \vec{d}_{ii} \tag{3.109}$$

where $\vec{d}_{ij}$ is the matrix element of dipole operator $\langle \phi_i | \, \vec{d} \, | \phi_j \rangle$.

After simulating the polarisation response of a single molecule to an incoming laser field, our next task is to estimate the total polarisation response across an ensemble of many molecules. These molecules can be oriented in any way, but for the purposes of this work they shall be oriented randomly, and so we must average simulated polarisation responses from the same molecule in multiple orientations relative to the incident laser.

This is equivalent to an integral over a spherical surface:

$$I[\vec{P}] = \oint_{\mathcal{S}^2} \vec{P}(\varphi, \vartheta) d\Omega \tag{3.110}$$

which must be approximately discretised as:

$$\oint_{\mathcal{S}^2} \vec{P}(\varphi, \vartheta) d\Omega = \sum_{i=1}^{N} w_i \vec{P}(\vec{r_i}) = Q[\vec{P}] \tag{3.111}$$

where Ω denotes solid angle and weights w_i which all must sum to unity $\sum_{i=1}^{N} w_i = 1$. This kind of discretised integration scheme is known as a quadrature [324].

The quadrature we have chosen to use in this work is called the Lebedev quadrature [325]. Whereas some schemes, such as a Gaussian product, sum over grid points and weights indexed by two labels $\{i, j\}$, the Lebedev scheme involves a single sum over grid points indexed once, which makes it more efficient, requiring potentially fewer grid points [326].

3.3.1 Lebedev Quadrature

The Lebedev quadrature (as used on page 4.1.2) uses grid points distributed across the surface of a sphere so as to have octahedral rotational symmetry, and be symmetric under inversion, meaning that for any point on the sphere, there are either 5 (as with vertices of an octahedron), 7 (faces), 11 (midpoints of edges), 23 or 47 points which are equivalent under the symmetry. All these equivalent points must share the same weights, and we can build up our quadrature by adding combinations of these different equivalent points [325, 326].

For example, the smallest possible Lebedev quadrature is composed of the six vertices of a regular octahedron:

$$Q_6[P] = \frac{1}{6}\sum_{i=1}^{6} P(\vec{a}_i^{(1)}) \tag{3.112}$$

where grid points $\vec{a}_i^{(1)}$ are the six permutations of some basis element $\{\pm 1, 0, 0\}\,\vec{a}^{(1)}$. The next quadratures involve the faces $\frac{1}{\sqrt{3}}(\pm 1, \pm 1, \pm 1)\,\vec{a}^{(2)}$ and centres of edges with permutations of $\frac{1}{\sqrt{2}}\{\pm 1, \pm 1, 0\}\,\vec{a}^{(3)}$ of an octahedron, which we can add in to find quadratures for 14 or 26 points:

$$Q_{26}[P] = A_1\sum_{i=1}^{6} P(\vec{a}_i^{(1)}) + A_2\sum_{i=1}^{8} P(\vec{a}_i^{(2)}) + A_3\sum_{i=1}^{12} P(\vec{a}_i^{(3)}) \tag{3.113}$$

where $6A_1 + 8A_2 + 12A_3 = 1$.

There are three more sets of grid points $\vec{b}^{(k)}$, $\vec{c}^{(k)}$, $\vec{d}^{(k)}$ leading to generalised Lebedev quadrature:

$$\begin{aligned} Q_N[P] =& A_1\sum_{i=1}^{6} P(\vec{a}_i^{(1)}) + A_2\sum_{i=1}^{8} P(\vec{a}_i^{(2)}) + A_3\sum_{i=1}^{12} P(\vec{a}_i^{(3)}) \\ &+ \sum_{k=1}^{N_1} B_k \sum_{i=1}^{24} P(\vec{b}_i^{(k)}) + \sum_{k=1}^{N_2} C_k \sum_{i=1}^{24} P(\vec{c}_i^{(k)}) \\ &+ \sum_{k=1}^{N_3} D_k \sum_{i=1}^{48} P(\vec{d}_i^{(k)}) \end{aligned} \tag{3.114}$$

where B_k, C_k, and D_k are weighting coefficients for sets of points $\vec{b}^{(k)}$, $\vec{c}^{(k)}$, and $\vec{d}^{(k)}$.

Determining which of these later points and weights to use is more complicated, and is generally done by forcing the Quadrature to integrate exactly the spherical harmonics up to a given order [325, 326]. In our investigations, we opted to use a Lebedev quadrature with 26 points, as this offered the most appealing tradeoff between cost and accuracy for our purposes.

Conclusion

After motivating our interest in chirality in chapter 1, and giving an overview of chiral light-matter interactions in chapter 2, in this chapter we have explained some of the methods we might need to put these physical principles into action in order to understand chiral-molecular processes. These techniques are generally approaches to solving the time dependent Schrödinger equation. In section 3.1.1, I explained how such approaches can generally be split into two categories; those which solve the TDSE at different points in space, and those which use some kind of spectral decomposition. However, for multi-body systems, it becomes necessary to make simplifying assumptions in order to make progress. One such assumption, as outlined in section 3.1.2, is that time-dependent behaviour of a system can be approximated by assuming any external stimulus is sufficiently small that it can be modelled as a perturbation.

These methods of solving the TDSE still require extra input in the form of accurate transition dipoles. To fully model the dynamics of quantum systems, we turn to *ab initio* methods in section 3.2. These methods simulate the dynamics of quantum systems using just physical constants and some initial geometry. As explained in sections 3.2.1 and 3.2.2, these methods rely on a good understanding of the energetics of a molecule. Nonetheless simplifying assumptions, such as the Born-Oppenheimer and fixed-nuclei approximations, are necessary to make progress. Section 3.2.3 explains one such fundamental *ab initio* method in the form of Hartree-Fock theory. HFT provides a first-approximation to the 'exact' solution to the Schrödinger equation in a way which epitomises a family of 'mean-field' and 'self-consistent-field' techniques. A mean-field scheme reduces the dimensionality of a multi-electron system by modelling the interaction of any given electron with an effective potential, while a self-consistent scheme iteratively corrects the wavefunction and the electric field until the two converge upon a consistent answer. HFT in particular optimises the wavefunction of the electrons by minimising some energy functional, before recalculating the associated electric field and repeating until convergence is reached. In section 3.2.4, we move on to DFT. DFT switches from modelling the electrons in terms of wavefunctions to modelling electrons in terms of an electron-density-functional, before minimising the energy. This innovation relies on the Hohenberg-Kohn theorems, and enables the use of a Kohn-Sham technique where the interacting multi-electron system is replaced with a non-interacting system that reproduces the same density. This technique is then further expanded in section 3.2.5 by adding time-dependence, now making use of a quantum-mechanical action functional in place of energy. In the following chapters, we make use of DFT, TDDFT, and the orientational averaging method outlined in section 3.3.1 to model the behaviour of ensembles of chiral molecules in a tailored electric field.

Chapter 4

Chiral sum-frequency generation

The work done in this chapter has been published in reference J. D. T. Vogwell et al. "Ultrafast Control over Chiral Sum-frequency Generation". In: *Science Advances* 9.33 (2023), eadj1429.

As discussed previously, perturbative processes of even-numbered order are allowed only in non-centrosymmetric media. For the case of chiral media, these even-ordered processes will result in signals with opposite phases for opposite enantiomers. One such process is sum-frequency generation (SFG) [157, 327–332]. SFG is a second-order non-linear process which involves three photons; two absorbed and one emitted. This is appealing since, at least in a perturbative regime, the more photons are required for any given non-linear process the more unfavourable it is at any given driving field intensity [154], and so a relatively low-order process should be drivable using relatively lower-intensity fields than a higher-order process. The thrust of this work is to demonstrate that ultrafast enantiosensitive measurements are possible exploiting perturbative processes, and do not necessitate high-order nonlinearities [20, 21, 223, 242, 333–335].

In particular, SFG entails the (virtual) absorption of two photons of two different angular frequencies ω_1 and ω_2, with polarisations $\hat{e}_1$ and $\hat{e}_2$ and wave vectors $\vec{k}_1$ and $\vec{k}_2$, followed by the emission of a single photon with the sum-frequency $\omega_3 = \omega_1 + \omega_2$, polarisation $\hat{e}_3 = \hat{e}_1 \times \hat{e}_2$ and wave vector $\vec{k}_3 = \vec{k}_1 + \vec{k}_2$. SFG is most efficient when the sum-frequency is close to a resonance within the molecule [157], and has been successfully applied to biologically relevant systems at interfaces [336], from achiral organic molecules [337] and chiral amino acids [338] to larger biological structures [336] including peptides, proteins [339–346] and DNA [347–349]. This, as explained previously, is an effect that is allowed by symmetry in the bulk of an isotropic medium only if that medium is chiral, and will be emitted with opposite phase from oppositely-handed media. This inherent link to chirality is important, but so long as the sense of the handedness of the medium remains encoded within the phase of the signal, SFG allows us only to ascertain whether a sample is chiral or not. SFG will only be observed given we have some degree of enantio-enrichment within our sample, but standard SFG can not tell us which handedness predominates.

Due to the orientation of the polarisation of the sum-frequency response ($\hat{e}_3 = \hat{e}_1 \times \hat{e}_2$), our sum-frequency conversion is most efficient when our input beams are cross-polarised. However, if our input beams are cross-polarised and co-linear, the resultant SFG response will be longitudinally polarised. This fact, combined with the conservation of momentum $\vec{k}_3 = \vec{k}_1 + \vec{k}_2$, means that no SFG can be observed in the far field since longitudinal electromagnetic excitations cannot propagate, and off-axis propagation will be forbidden by momentum conservation (or equivalently, phase-matching). Thus we turn to the techniques described in section 2.3.2. We could utilise the longitudinal component acquired by light as it passes through a very tight focus, or use some nanophotonic structure. Instead, we opt to use two different-coloured non-collinear beams with orthogonal polarisation. This creates a SFG response in the molecules which is transverse relative to the wave vector of SFG emission, allowing the resulting signal to propagate.

However, the handedness of the sample remains concealed within the phase of the far-field signal. Instead, to be able to observe the handedness of a sample as an intensity, we have to use some kind of heterodyne detection method: we must have a reference signal, the phase of which is not chirality-sensitive, that will interfere with the enantio-sensitive sum-frequency signal and allow us to determine its phase. There are several potential ways one might go about achieving this. One could, for instance, use a three-colour setup, with a component frequencies of ω_1 and ω_2 to drive the SFG together with a reference beam $\omega_3 = \omega_1 + \omega_2$, leading to an enantio-sensitive interference between emitted SFG and the reference signal. One advantage of this setup would be the relative achievability of controlling the phase of the reference with respect to the other input frequencies, allowing full control over the interference (see figure 4.1).

An alternative method would be to generate the reference signal from the sample itself [350]. For example, applying an external electric field [351] would break the isotropy of the medium, allowing an achiral sum-frequency generation signal which could be used as a reference. One could also use low frequency radiation (eg. radio waves or microwaves), a reflected SFG signal generated at a boundary [157], or a sample adsorbed onto the surface of some nanophotonic material which can allow achiral SFG to occur [207, 224, 225]. All of these methods have the drawback that they limit the opportunities to control the phase of the reference signal. In the example of using the medium boundary to enable achiral SFG, one would have reflected SFG signals, internally reflected SFG signals and transmitted signals generated at the boundary which might all have different and potentially unpredictable phase relationships to each other and to the chiral sum-frequency signal, none of which is easily controlled.

Our solution is to use third-harmonic generation (THG), which is a third-order non-linear frequency up-conversion process wherein a molecule virtually absorbs three photons of frequency ω and emits one photon with frequency 3ω. As a process controlled by third-order susceptibility $\chi_e^{(3)}$, it is not forbidden in centrosymmetric media, it is emitted with the same phase in opposite enantiomers, and is emitted with the same polarisation as the total field at the fundamental frequency. If we set the frequency of our input beams such that $\omega_2 = 2\omega_1$, then our sum-frequency

signal will be generated with frequency $3\omega_1$. From now on, for convenience, I will omit any subscripts and refer to these frequencies as simply ω and multiples thereof. We will, with this set up, also have third harmonics generated at 3ω and 6ω. This means we have SFG and THG active at the same frequency of 3ω.

Notwithstanding dispersion, if our ω component of the input field travels along $\vec{k}_1 = k\sin\alpha\hat{x} + k\cos\alpha\hat{z}$ polarised in the non-collinear plane along $\hat{e}_1 = \hat{x}\cos\alpha - \hat{z}\sin\alpha$, and the 2ω component travels along $\vec{k}_2 = -2k\sin\alpha\hat{x} + 2k\cos\alpha\hat{z}$ and is polarised orthogonally along $\hat{e}_2 = \hat{y}$, then this would lead to a chiral polarisation response along the mutually orthogonal direction $\hat{e}_3 = \hat{x}\sin\alpha + \hat{z}\cos\alpha$, and an achiral response along $\hat{x}\cos\alpha + \hat{z}\sin\alpha$. These polarisations both have transverse components relative to the emission directions $\vec{k}_{SFG} = \vec{k_1}+\vec{k_2} = -k\sin\alpha\hat{x}+3k\cos\alpha$ for SFG and $\vec{k}_{THG} = 3\vec{k_1}$, and so SFG and THG signals will be observable in the far-field, but will not interfere, since they are emitted along different directions (see figure 4.1).

Again, there are several possible solutions. If we were to use very tightly focussed beams, then they would diverge more in the far field, and so if there might be some area of overlap between the THG and SFG peaks where interference might be observed. Another, perhaps naive, approach might be to use a mirror or a lens to reflect or refract one or other signal such as to coincide with the other. This would also give rise to an interference, however introducing a (potentially chromatic) mirror or lens introduces another source of error in the phase shift imparted on the signal.

Our solution was instead to add another component to our beam setup; another input beam with frequency ω collinear with the 2ω beam, but polarised in the same plane as our ω component (see figure 4.1). The addition of this beam realises synthetic chiral light [20] (see section 2.3.2), opening up three new pathways through which THG can occur: A molecule can undergo THG by absorbing three photons from the right-most beam, three from the left-most beam, or a mixture of two from one beam and another from the other. The resulting THG signal will then be emitted along either $\vec{k}_{LLL} = 3k\sin\alpha\hat{x} + 3k\cos\alpha\hat{z}, \vec{k}_{RRR} = -3k\sin\alpha\hat{x} + 3k\cos\alpha\hat{z}$, $\vec{k}_{LLR} = k\sin\alpha\hat{x} + 3k\cos\alpha\hat{z}$, and $\vec{k}_{RRL} = -k\sin\alpha\hat{x} + 3k\cos\alpha\hat{z} = \vec{k}_{SFG}$. From this setup we should observe, therefore, intensity peaks in the far field emitted at angles $\pm\alpha$ and $\pm\tan^{-1}(\sin(\alpha)/3) \approx \pm\alpha/3$. Thus we have one THG pathway which emits along the same wave-vector as our chiral SFG signal, and so will overlap in the far field, creating our entantiosensitive interference. The interference between SFG and THG is tunable by adjusting the relative intensities and relative phase delay of the ω and 2ω input components. Due to the combinatorics of a molecule taking photons from one or other input beam, the two 'mixed'-middle pathways should result in emission at four-times the intensity of the two 'pure'-outer pathways, since these pathways will emit with twice the amplitude.

So, for a judicious choice of intensities and phase, the SFG and THG should interfere such that they are fully destructive in one enantiomer whilst being fully constructive in the other, a situation which can be reversed by shifting either input frequency component through π radians of phase delay. Additionally, the existence of other peaks, particularly at an emission angle of $\approx \alpha/3$, is convenient for use as

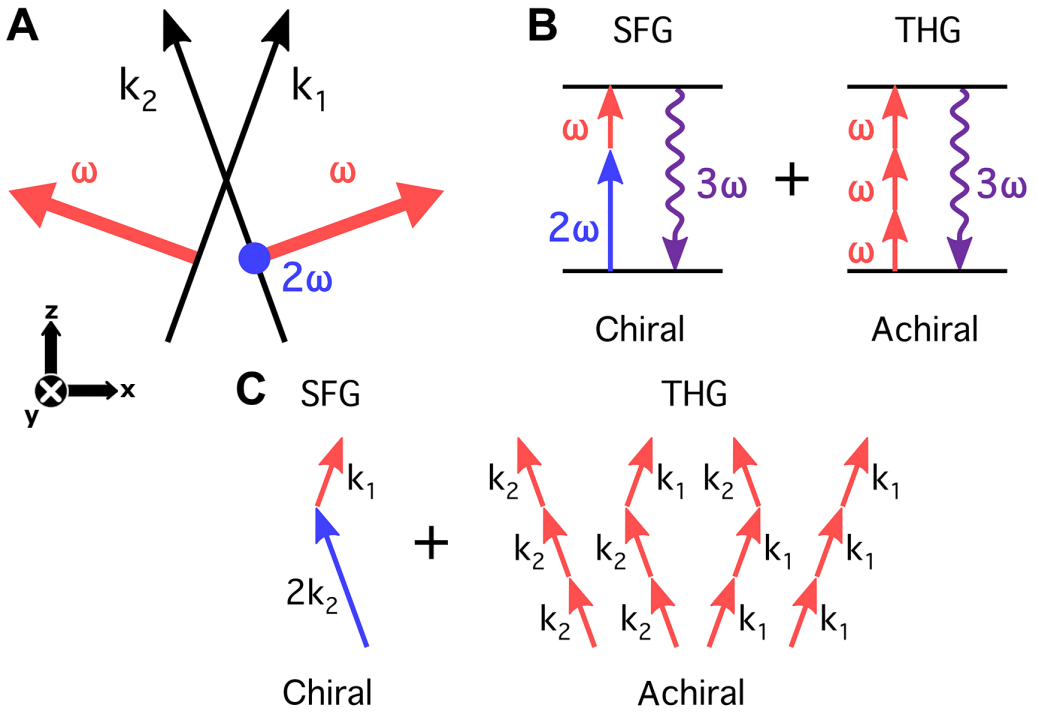


Figure 4.1: (**A**) The proposed optical setup combines a linearly polarised beam with frequency ω and a second beam that carries cross-polarised ω and 2ω frequencies. The ω frequency components are polarised in the plane of propagation, and the 2ω component is polarised orthogonal to this plane. (**B**) Multiphoton pathways describing chiral SFG (left) and achiral THG (right). The induced polarisation associated with SFG has the same amplitude and opposite phase in opposite molecular enantiomers, $P^L_{SFG} = -P^R_{SFG}$, whereas the polarisation associated with THG is identical, $P^L_{THG} = P^R_{THG}$. (**C**) Multiphoton diagrams describing momentum conservation in SFG (left) and THG (right). Reproduced under open access licence from American Association for the Advancement of Science [156].

a calibration tool. For perfect constructive interference, our enantiosensitive peak should have four-times the intensity of this reference peak, and the reference peak should not change in intensity as the two-colour phase-delay is varied.

4.1 Numerical Demonstration of our Approach

With the motivations and concept of the work established, the next tasks to be undertaken were numerical simulations to verify the potential efficacy of using this enantiosensitive SFG scheme to differentiate between enantiomers. This task can be broken down into four main parts (see fig 4.2);

1. Calculate the electric field of the laser in our interaction region.

2. Calculate the overall polarisation response of an ensemble of randomly oriented chiral molecules to our tailored driving field.

3. Use this orientationally-averaged polarisation response to estimate the re-

sponse of a gas of chiral molecules to the electric field throughout space in the near field.

4. Use this near field polarisation to work out the observable emission from the sample molecules in the far field, to assess if an observable enantiosensitive signal can be generated by a gas of chiral molecules using our method.

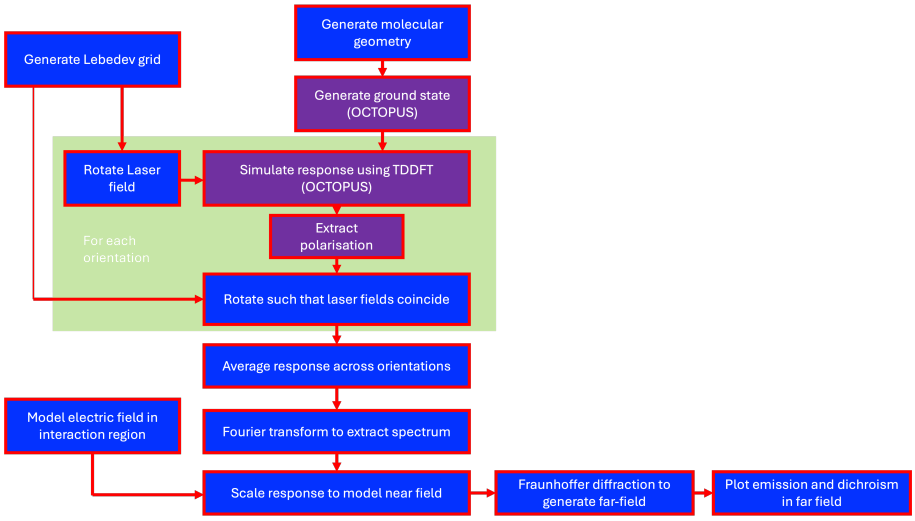


Figure 4.2: A schematic showing the general procedure used in this work. In-group codes were used in combination with open-source software.

4.1.1 Modelling the Laser Field

The first task was to model the driving field to which the molecules would respond. We first make the electric-dipole approximation, since the effects we wish to observe exist within the electric-dipole regime, while magnetic and multipole terms should be small at the frequencies we are studying.

Our setup comprised two non-collinear laser beams separated by angle 2α which crossed slightly down-beam of their foci, with one beam containing a component with frequency ω polarised within the plane of the two crossed beams, and the other containing both an in-plane ω component, and a perpendicular component with a frequency of 2ω (see figure 4.1). We chose a position down-beam of the focus of both lasers. All of our sample region had to be on one side of the focal point or the other. Being down-beam of the focus also had the advantage that light emitted by SFG and THG did not pass through a focus after being generated. We further assume that our sample medium is optically thin and non-dispersive, such that the properties of our applied field, such as beam waist and amplitude, remain constant along the propagation direction $\hat{z}$, and we neglect the curvature of the wavefront. We set $z = 0$ to be the position of our sample, such that the grating of the field in

the sample region is given by:

$$E_x(x,t) = 2E_{\omega,0}a(t)e^{\frac{-x^2}{w(\alpha)^2}}\cos(\alpha)\cos(k\sin(\alpha)x + \phi(x)) \tag{4.1}$$

$$E_y(x,t) = E_{2\omega,0}a(t)e^{\frac{-x^2}{w(\alpha)^2}} \tag{4.2}$$

$$E_z(x,t) = 2E_{\omega,0}a(t)e^{\frac{-x^2}{w(\alpha)^2}}\sin(\alpha)\sin(k\sin(\alpha)x) + \phi(x) \tag{4.3}$$

$$\phi(x) = \phi_{2\omega} + 2k\sin(\alpha)x \tag{4.4}$$

where $a(t)$ is the Gaussian temporal envelope of the field, $E_(\omega,0)$ and $E_(2\omega,0)$ are amplitudes of the electric fields, ω is the central angular frequency of the two ω beams, $\phi_{\omega,\ell}$, $\phi_{\omega,r}$ and $\phi_{2\omega}$ are the phases of the left and right ω components and the 2ω components respectively, while $w(\alpha)$ is the beam waist accounting for the angle of the beams relative to the $\hat{x}$-axis.

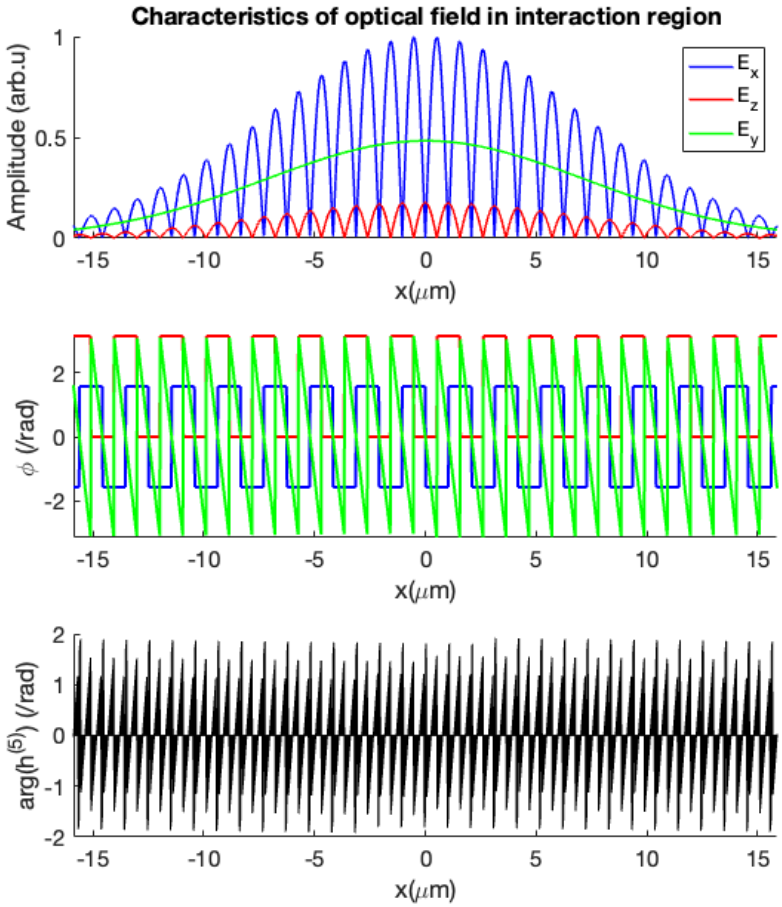


Figure 4.3: Optical amplitude (top), optical phase (middle), and argument of fifth order chiral correlation function (bottom) of the driving field in the interaction region along the $\hat{x}$ axis. Area under the argument of the chiral correlation function is shaded in black.

Figure 4.3 shows the characteristics of the driving field in the interaction region. The beam has a Gaussian profile, with an interference pattern in the $\hat{x}$ and

$\hat{y}$ components between the two non-collinear beams. The ω component of the field is elliptical, with the ellipticity flipping regularly through the interaction region. We can quantify the chirality of the driving filed using fifth-order chiral correlation function [20]:

$$h^{(5)}(-2\omega, -\omega, \omega, \omega, \omega) = \left\{ \vec{E}^*(2\omega) \cdot \left[\vec{E}^*(\omega) \times \vec{E}(\omega) \right] \right\} \left[\vec{E}(\omega) \cdot \vec{E}(\omega) \right] \tag{4.5}$$

where $E(\omega)$ is the Fourier-transform of the total electric field defined above, and $h^{(5)}$ flips sign as the ellipticity of the field flips. Although the local chirality of the field is not constant, its integral across the interaction region is non-zero, and we can therefore say that the field is globally chiral.

The polarisation response (in the electric-dipole approximation) of an isotropic chiral medium to this driving field is a vector

$$\vec{P}(x,t) = P_x(x,t)\hat{x} + P_y(x,t)\hat{y} + P_z(x,t)\hat{z} \tag{4.6}$$

The non-linear response of gaseous propylene oxide is evaluated as a function of transverse coordinate x, since the phase structure of the field is uniform in y, and z is fixed to be zero.

4.1.2 Modelling the Response of Randomly Oriented Molecules

The electronic response of the chiral molecule propylene oxide to the proposed driving field has been evaluated using time-dependent density functional theory (TD-DFT), using the software *Octopus* [262, 293, 319, 322, 352]. Several approximations and shortcuts needed to be used to prevent excessive computational intensity. The choice of molecule, in this case, was decided by the small size and relative simplicity of propyleneoxide, making calculations take less time and resources. Furthermore, an ensemble of molecules has been approximated by the average of one single molecule over multiple orientations, which neglects any potential effects of intermolecular interactions.

The simulations were conducted using TD-DFT with the local density approximation to account for electronic exchange and correlation effects [281, 293, 353]. We have used the averaged density self-interaction correction [354] to ensure an adequate description of the part of the electronic wavefuntction driven to a large distance from the molecule by the laser field. The 1s orbitals of carbon and oxygen atoms are described using pseudopotentials, since they play no part in the physical processes of interest. Despite the approximations we have made, the enantio-sensitive signal relies on the interference between two completely general multiphoton pathways which arise in isotropic chiral media.

Octopus extends the Kohn-Sham orbitals and electron densities into a uniform real-space grid, allowing the control of the quality of the discretisation by manipulating the spacing between adjacent points Δx (see sections 3.2.5-3.2.5). We have used a spherical basis set of radius $R = 41.9\,\text{au}$ and $\Delta x = 0.4\,\text{au}$ to reach convergence, with absorbing boundary conditions to avoid unphysical reflection of the electronic

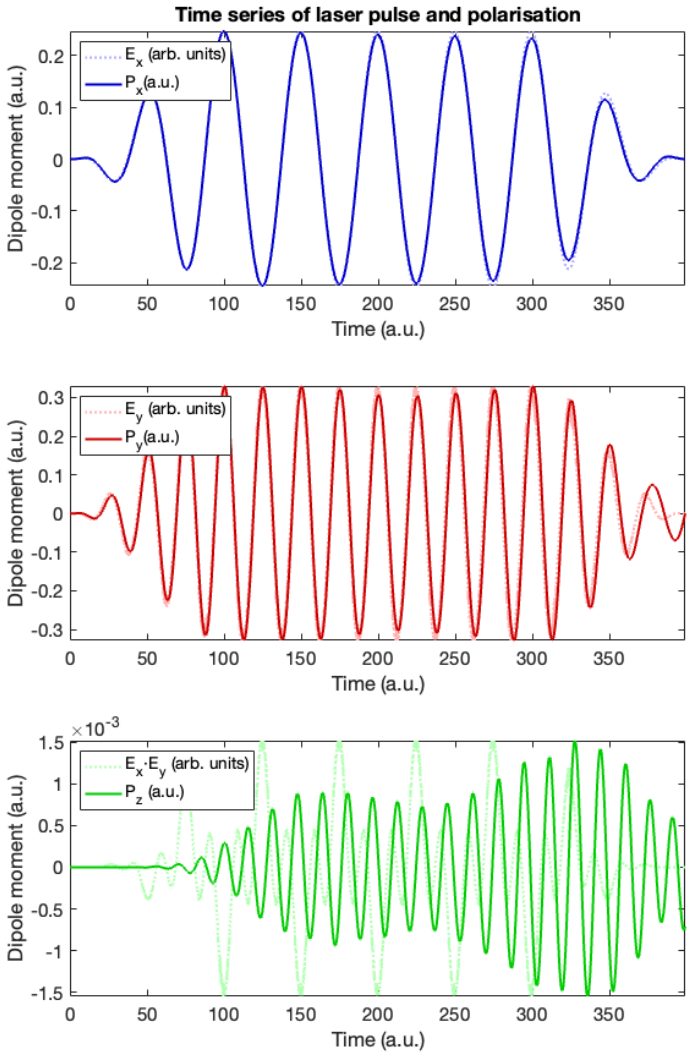


Figure 4.4: Time series of laser pulse of wavelength 361 nm and full-width-half-maximum of 3.27 fs, together with associated polarisation response. The electric field has been scaled so as to match the amplitude of the polarisation response, where the z direction refers to the longitudinal axis, while y is the transverse direction out-of-non-collinear-plane, and x is the transverse axis within the non-collinear plane.

wavefunction. The complex absorbing potential we used has width 20 au and height 0.2 au. We performed calculations for 208 different molecular orientations in an attempt to describe accurately the physics of randomly oriented molecules. The total polarisation is the result of the coherent addition of the contribution from all possible orientations:

$$\vec{P}(x,t) = \int \mathrm{d}\Omega \int \mathrm{d}\chi \vec{P}_{\Omega,\chi}(x,t) \tag{4.7}$$

where χ denotes angle of rotation of the molecule about the axis of propagation,

while Ω is a solid angle encoding rotation about its other Euler axes.

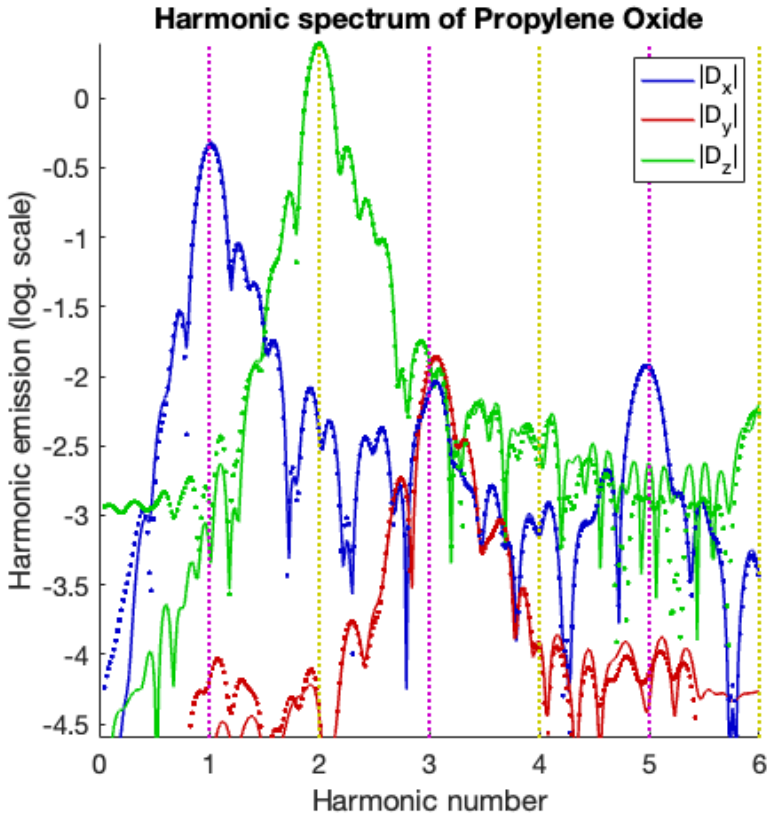


Figure 4.5: Orientationally-averaged single-molecule polarisation response $D(\omega)$ of propylene oxide to a cross-polarised ω and 2ω flat-top Gaussian laser pulse of fundamental wavelength 361 nm and full-width-half-maximum of 3.27 fs. Figure includes harmonic intensity calculated from dipole response (solid) and acceleration (dotted). The achiral component in non-collinear plane is in blue, while chiral longitudinal component is in red.

We approximate the integral over solid angle Ω using a Lebedev quadrature [325], wherein the integral is discretised into a weighted sum over Lebedev points:

$$\vec{P}_{average} = \frac{1}{N_{points}} \sum_{i=1}^{N_{points}} w_i \vec{P}_i \tag{4.8}$$

where N_{points} is the number of Lebedev points covering polar and azimuthal angular space, and w_i is a weighting for each point. In our case, we have used a Lebedev quadrature of degree 26 ($N_{points} = 26$), and eight different values of our axial rotation angle α (see section 3.3.1).

The procedure described above was applied to evaluate the electronic polarisation response (see figures 4.4 and 4.5) of randomly oriented propylene oxide to intersecting linearly polarised laser fields, with intensity of the fundamental field $I = 6 \times 10^{12}\,\mathrm{W\,cm^{-2}}$, and a carrier envelope phase of zero. The simulated laser pulse was trapezoidal, with amplitude increasing linearly for two cycles, remaining constant for four, before decreasing linearly for another two cycles. Although the field

we are simulating in *Octopus* is not exactly the chiral field described elsewhere, since it lacks a longitudinal component, we can still measure the chiral response since our simulation gives us direct access to the polarisation-response of the molecule along all axes [18]. This can be used to calculate the chiral response in the full scheme so long as we assume the longitudinal component of the field is small relative to the transverse component, which is valid in our setup. Therefore, the chirality of our setup is provided by the Lissajous figure drawn by the electric field in the interaction region combined with the wavevectors of the ω and 2ω field components. Simulations were run for the right handed enantiomer of propylene oxide, while results for the left handed enantiomer were obtained by using symmetry arguments.

Near-field Response

Once we have obtained a polarisation response of our randomly-oriented ensemble to our driving field, we can estimate the polarisation response from a gas (or thin liquid) of molecules in the interaction region (see figure 4.6). With this computational scheme, we used perturbative scaling rules to calculate the response of a molecule would be at any point given field intensities and a generalised single-molecule response. Since SFG and THG are both perturbative phenomena, their intensities follow a power-law relationship with intensities of the driving fields. We therefore made the assumption that the resulting polarisation $\vec{P}(x)$ would be proportional to the product of the field amplitudes of the incident beams raised to the power of the number of photons in the interaction taken from each beam:

$$P_{SFG} \propto I_{2\omega}^{\frac{1}{2}} I_{\omega}^{\frac{1}{2}} \tag{4.9}$$

$$P_{THG} \propto I_{\omega}^{\frac{3}{2}} \tag{4.10}$$

up to some phase factor.

This interaction is modelled in a thin, non-dispersive medium, and this situation is realisable using, for example, a thin liquid microjet [355–357], or a thick but optically non-dispersive gas.

4.1.3 Intensities in the Far Field

Having generated a map of near field polarisation response through space, we could then work out how the resulting emission would propagate and generate a pattern of intensity in the far field. In our analysis, we have separated the chiral (SFG) and achiral (THG) components of the emitted signal within the near field, and then we use the pattern of phase and intensity of the near-field response to calculate the response in the far field. For our purposes, using the Fraunhoffer method was sufficient. The far-field achiral (F_a) and chiral (F_c) components of the emitted third-harmonic and sum-frequency signals were evaluated using the Fraunhoffer equation:

$$F_a(\vartheta, t, N) \propto \int_{-\infty}^{\infty} \frac{\mathrm{d}^2}{\mathrm{d}t^2} P_{a\perp}(x, t, N) e^{-iKx} \mathrm{d}x, \tag{4.11}$$

$$F_c(\vartheta, t, N) \propto \int_{-\infty}^{\infty} \frac{\mathrm{d}^2}{\mathrm{d}t^2} P_{c\perp}(x, t, N) e^{-iKx} \mathrm{d}x, \tag{4.12}$$

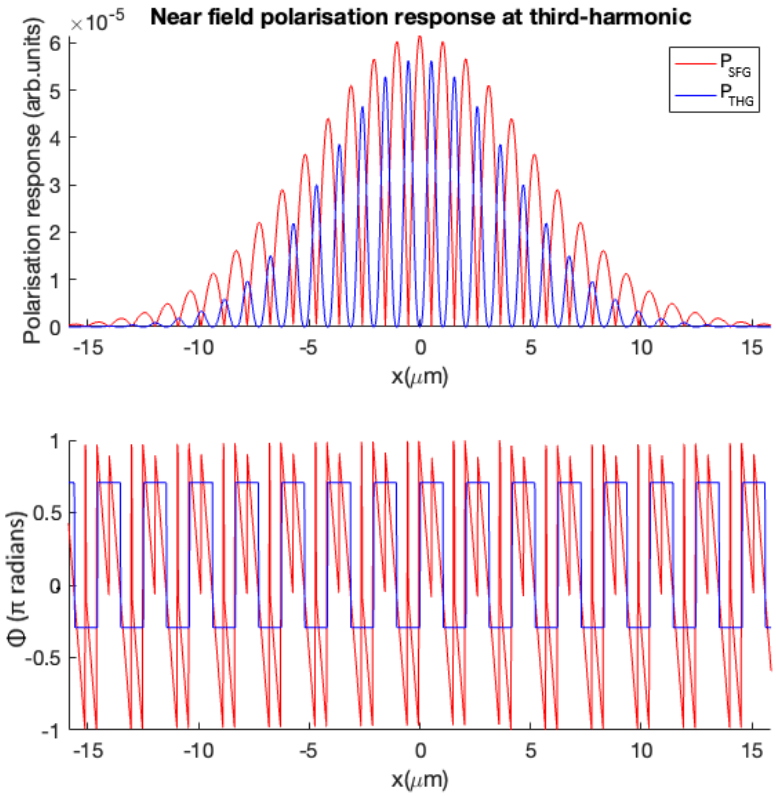


Figure 4.6: Near-field polarisation response of propylene oxide in a chiral SFG setup, showing chiral (SFG) and achiral (THG) components of polarisation, and the associated phases in π radians.

where $P_{a\perp}$ and $P_{c\perp}$ are the achiral (THG, $\hat{x}$) and chiral (SFG, $\hat{z}$) molecular polarisation components in the frequency domain which are perpendicular to the axis between the near-field sample region and the point being evaluated in the far-field, while N is the harmonic number (used here as a proxy for generalised output angular frequency ω_{out}), ϑ is the far-field divergence angle, and spatial frequency $K = (N\omega/c)\vartheta$. The results can be seen in figure 4.7. In this case we are interested only in the response at angular frequency 3ω corresponding to SFG and THG, and so N is fixed $N = 3$.

4.2 Results and Discussion

Our proposed setup for driving chiral SFG combines a linearly polarised beam with angular frequency ω and a second beam which carries cross polarised ω and 2ω angular frequencies, with the ω components polarised within the plane of propagation of the two non-collinear beams, whereas the 2ω component is polarised perpendicular to this plane.

This gives rise to a laser field in the sample region

$$\vec{E} = \mathcal{R}\{\vec{E}^{(1)} + \vec{E}^{(2)}\} \tag{4.13}$$

where

$$\vec{E}^{(1)} = E_{\omega}^{(1)} e^{-i\omega t + i\vec{k_1}\cdot\vec{r}} \hat{e_1} \tag{4.14}$$

and

$$\vec{E}^{(2)} = E_{\omega}^{(2)} e^{-i\omega t + i\vec{k_2}\cdot\vec{r}} \hat{e_2} + E_{2\omega}^{(2)} e^{-2i\omega t - i\phi_{2\omega} + 2i\vec{k_2}\cdot\vec{r}} \hat{y} \tag{4.15}$$

with $E_{\omega}^{(1)}$, $E_{\omega}^{(2)}$, and $E_{2\omega}^{(2)}$ are electric field amplitudes which include temporal and spatial envelopes, and $\phi_{2\omega}$ is the two-colour phase delay within the second beam. We hold the phase between the two ω beams constant.

To emphasise the differences between this setup and more traditional configurations for SFG;

- We have set the ratio between the input frequencies to $\omega_2/\omega_1 = 2$, such that we achieve spectral overlap between emission from sum-frequency and third-harmonic pathways,
- We add a component with the fundamental frequency ω to the second beam, such that we can achieve spatial overlap between one of the third-harmonic pathways and the chiral sum-frequency emission,

and these two features constitute a fundamental difference in the properties of the field generated. The SFG pathway works just as it would in any other implementation. However, the addition of a component with frequency ω to the second beam, we open three new pathways for THG, allowing the medium to absorb three photons from the same beam, or to absorb two from one and one from the other, giving rise to an achiral THG signal along four different directions. The one of these pathways which involves the absorption of one photon from the first beam and two from the second, leads to an achiral third-harmonic emission along exactly the same direction as the chiral sum-frequency signal, allowing these two contributions to interfere, thusly making the intensity of emission (along this axis) very strongly enantiosensitive. In traditional SFG setups, the polarisation of the electric field vector is confined to a plane, and is therefore achiral within the electric dipole approximation. Therefore, any measurement of a molecule's chirality must be via some chiral observer. In our setup, the combination of these two beams creates a field that is locally chiral within the electric dipole approximation, with the tip of the electric field vector following a chiral-trajectory through time, allowing us to use the driving field as a chiral reagent. This locally chiral field can then enable us to drive a strongly enantiosensitive response in a medium consisting of randomly oriented chiral molecules, via this interference between SFG and THG.

To demonstrate this proposal, we performed (as outlined above) state-of-the-art numerical simulations of randomly-oriented molecules of propyleneOxide, using the following laser parameters:

- The intensity of the ω component in both beams $I_{\omega}^{(1)} = I_{\omega}^{(2)} = 3 \times 10^{12}\,\mathrm{Wcm}^{-2}$
- The intensity of the 2ω component in the second beam $I_{2\omega}^{(2)} = 7 \times 10^{11}\,\mathrm{Wcm}^{-2}$

- A flat-top Gaussian pulse of FWHM duration 3.27fs,
- A total opening angle between the beams of $2\alpha = 50°$.

The flat top pulse is chosen over a Gaussian pulse as the extra time spent at full intensity allows for stronger non-linear effects with less total simulation time.

Figure 4.7 shows the intensity of these two contributions to emission at angular frequency 3ω in the far field and, as anticipated, the chiral sum-frequency contribution is emitted at a divergence angle of $-\tan^{-1}(\sin(\alpha)/3) = -8.1°$, whereas the achiral third-harmonic emission profile shows four peaks at angles; $-25.0°$, $-8.1°$, $8.1°$, and $25.0°$, corresponding to the four possible combinations of momenta from the incident beams (see figure 4.1). The intensity profiles of sum-frequency and third-harmonic contributions are, individually, not enantiosensitive, but since the SFG contribution is of opposite phase in opposite enantiomers, the total intensity of emission is strongly enantiosensitive due to either constructive or destructive interference between the two contributions. We have tuned the amplitude of the 2ω component of the driving field such that the sum-frequency and third-harmonic contributions at an emission angle of $-8.1°$ have equal amplitude. We can then adjust the two-colour phase delay in the driving field and thereby control the phase of sum-frequency generation, achieving full control over the enantiosensitive interference and, therefore, over the intensity of emission at frequency 3ω.

For $\phi_{2\omega} = 0.67\pi$, the SFG and THG contributions interfere constructively in the left handed molecules, and destructively in the right handed ones. Shifting this phase by π, i.e. setting $\phi_{2\omega} = 1.67\pi$, shifts the phase of SFG emission by π leading to a reversal of the interference. Figure 4.8 shows how we can, in this way, control the intensity of emission in a highly enantiosensitive manner. Since the polarisation associated with the SFG is out of phase in opposite enantiomers, the values of the two-colour phase delay $\phi_{2\omega}$ that maximise or quench emission at a divergence angle of $-8.1°$ from the left- or right- handed enantiomers are shifted by π. It is important to note that the specific values of this two-colour phase delay that optimise the enantiosensitive interference depend on the relative phase between the contributions to optically-induced polarisation via SFG and THG. These quantities record the anisotropy of the molecular potential and are specific to each molecule. Therefore, in principle, by adjusting the laser parameters (such as input frequencies, intensities, and phase delay) we can bring about an equally strong enantiosensitive response in any chiral molecule.

In order to quantify the extent of the enantiosensitivity of the non-linear optical response, we use a standard dissymetry factor

$$\gamma = \frac{I_L - I_R}{\frac{1}{2}(I_L + I_R)} \tag{4.16}$$

where $I_{L,R}$ are intensities of emission from the left- and right-handed enantiomers respectively.

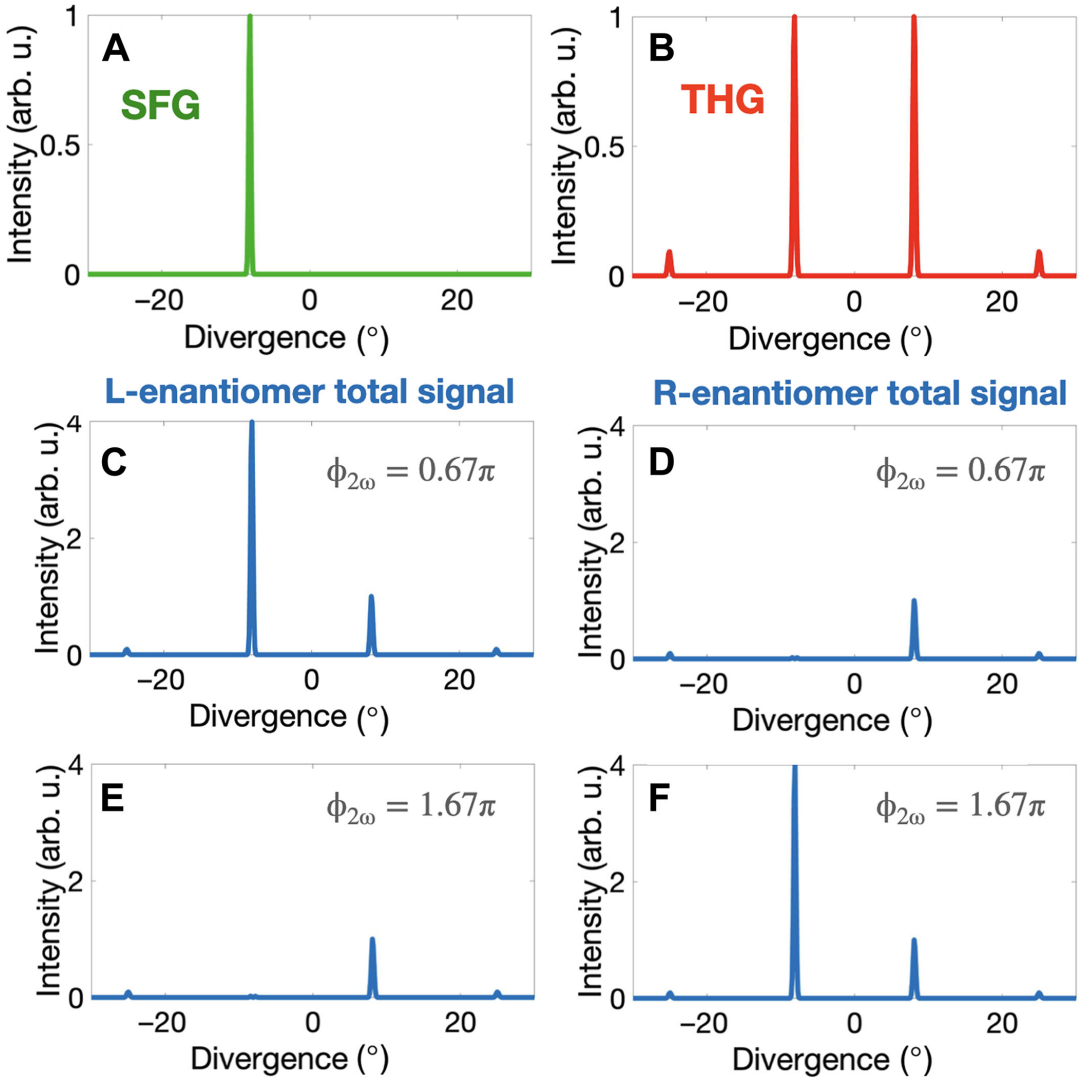


Figure 4.7: (**A** and **B**) Intensity at angular frequency 3ω in the far field associated with chiral SFG (A) and achiral THG (B). (**C** to **F**) Total intensity emitted from left- (C) and (E) and right-handed (D) and (F) propylene oxide, resulting from adding the chiral SFG (A) and achiral THG (B) contributions, for $\phi_{2\omega} = 0.67\pi$ (C) and (D) and $\phi_{2\omega} = 1.67\pi$ (E) and (F). Laser parameters $I_\omega^{(1)} = I_\omega^{(2)} = 3 \times 10^{12}\,\mathrm{Wcm}^{-2}, I_{2\omega}^{(2)} = 7 \times 10^{11}\,\mathrm{Wcm}^{-2}$, pulse duration 7 fs and opening angle $2\alpha = 50°$, arb. u. is arbitrary units. Reproduced under open access licence from the American Association for the Advancement of Science [156].

As shown in figure 4.8, γ reaches the limits of $\pm 200\%$; i.e. we can maximise emission via total constructive interference in the left-handed molecules and fully quenching the emission via total destructive interference in the right-handed molecules ($\gamma = 200\%$), or vice-versa ($\gamma = -200\%$), by adjusting the two colour phase delay $\phi_{2\omega}$ in the second beam.

This can be thought of either as controlling constructive vs destructive interference via the phase of SFG, or as using the two-colour phase delay to define the local handedness of the chiral electric field, and thereby controlling the enantiosensitive response of the chiral molecules.

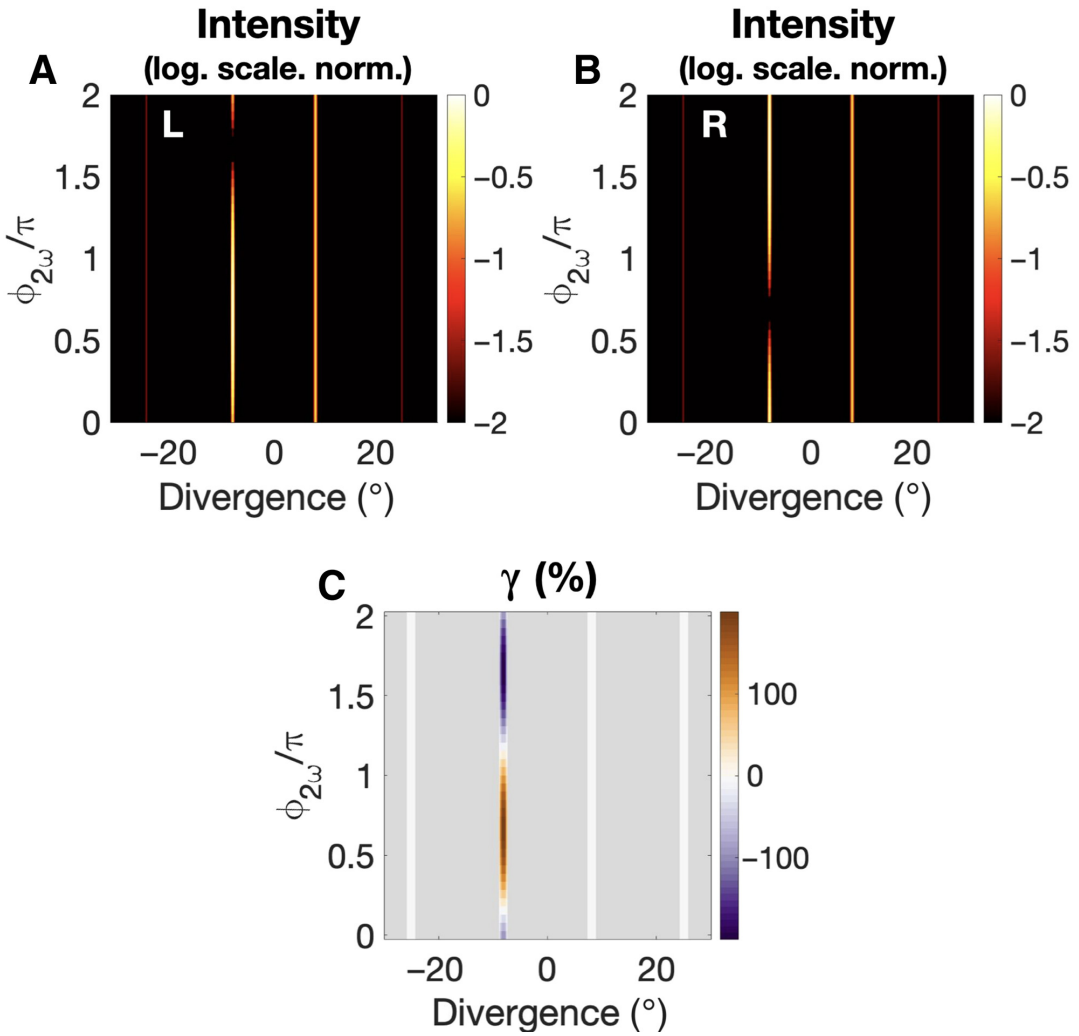


Figure 4.8: (**A** and **B**) Intensity at frequency 3ω emitted from left-handed (A) and right handed (B) propyleneoxide as a function of the divergence angle and the two-colour phase delay. (**C**) Dissymmetry factor $\gamma = 2(I_L - I_R)/(I_L + I_R)$. Grey colour indicates absence of emission. See caption of figure 4.7 for laser parameters. Reproduced under open access licence from the American Association for the Advancement of Science [156].

One important and useful feature of this setup is that, while the intensity of emission at an angle of $-8.1°$ is strongly enantiosensitive and fully controllable, the peak at $8.1°$ is completely independent both of the molecular handedness and the two-colour-phase delay. Due to the different phase matching conditions for SFG and THG, equivalent to considerations involving the conservation of momentum, the peak at $8.1°$ is purely due to THG, and can therefore be used as a reference for calibration and noise-reduction purposes in an experimental context.

4.2.1 Conclusions and Prospectives

Our proposal constitutes a simple, yet highly efficient, all-optical approach for chiral discrimination that relies on the interference between low-order nonlinear phenomena (SFG and THG) that are ubiquitous in nonlinear optics. They have both been

widely recorded in chiral and achiral media, in isotropic and anisotropic samples, and in the liquid, and solid phases of matter. However, despite the general importance of chiral molecules, to the best of our knowledge, these two phenomena had not been combined to achieve efficient chiral discrimination.

This takes advantage of the tremendous capabilities of modern optical technology for sculpting the polarisation of light with sub-optical-cycle temporal resolution. By controlling the two-colour phase delay in the proposed optical setup, we can tailor the chirality of the driving field, via its phase, to maximize the nonlinear response of a selected molecular enantiomer while suppressing it in its mirror twin. The possibility of driving strongly enantiosensitive interactions via low-order nonlinear processes creates tremendous opportunities for imaging and controlling molecular chirality on ultrafast time scales using laser fields with relatively gentle intensities, as well as for developing enantiosensitive optical traps and tweezers. Indeed, experimental work seeking to realise this proposal is ongoing at time of writing: an example schematic of a potential experimental setup is included in figure 4.9.

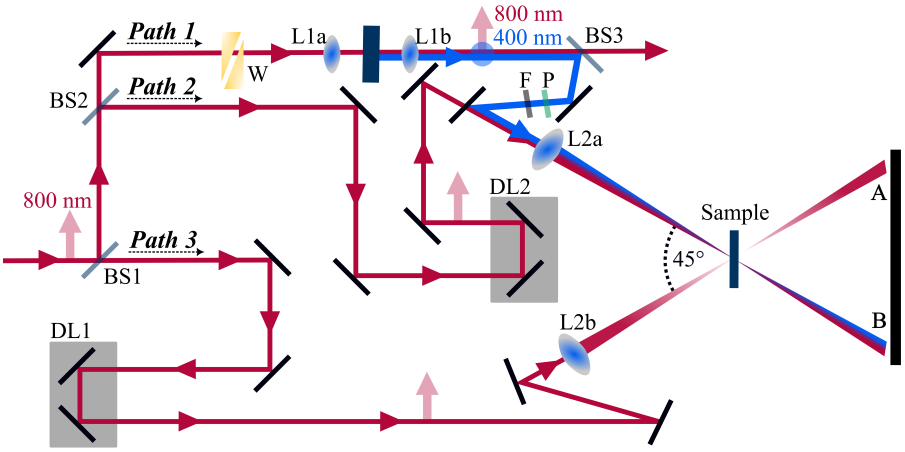


Figure 4.9: Beamline schematic of a chiral SFG experiment based on our scheme. Figure kindly provided by Rose Picciuto, adapted from unpublished experimental work.

Chapter 5

Conformational effects in SFG

The sensitivity of SFG to molecular geometry may open up opportunities for studying ultrafast chiral nonlinear effects with conformer specificity. As described in section 1.1.1, conformers are 'versions' of a molecule which share the same chemical bonding but different placement of atoms throughout space, and can interconvert without bond breaking [71, 72]. Conformers are of particular importance to the study of chiral molecules since many chiral molecules are large organic molecules. Due to the abundance of sp-3 derived σ-bonds which lack off-axis electron-density, moieties within large organic molecules typically have a large degree of rotational freedom. Conformers that differ by rotations around formally single bonds can interconvert without the need for bond-breaking, existing at local minima within the potential-energy surface within the conformational space defined by the angles of rotation about the molecule's bonds [70, 73, 74]. This means that energetic barriers between conformers tend to be relatively small [75], and so conformers can interconvert due to thermal excitations under standard conditions. Therefore different conformers of complex molecules usually coexist in laboratory settings with relative abundances that follow a Boltzmannian distribution due to the relative energies of the different conformers [73].

Conformational geometry can be important when considering chemical reactions, since the differently shaped molecular potentials of different conformers can change long-range intermolecular forces. Furthermore, differing orientations of groups within a molecule can often lead to different steric shielding of reactive groups within the molecule. Both of these effects combined mean that different conformers can vary substantially in their chemical reactivity, the types of reactions they are prone to undergo, and the ensuing products formed by such reactions [358, 359].

Although the electronic energy levels of different conformers are often similar, the coupling of the molecule to the field can vary much more profoundly. Different conformers have the same atoms and the same bonding, and so largely share molecular orbitals that can be thought of as emerging from the overlap of the same atomic orbitals. These molecular orbitals will therefore usually share similar energies, with differences caused by proximity to other groups within the molecule [360]. However, since the moieties which comprise the different conformers may be rotated

relative to one another, the shape of the molecular potential and distribution of electron density will be quite different. This will reveal itself in the transition-dipole matrix-elements of the different conformers. Thus, the energetics of the system will be quite similar between conformers, but the distribution of electron density and thus magnitude and direction of dipole moments will vary more. Transitions that are strong in one conformer may be weak in another, or the transition dipoles may be oriented differently relative to one-another, giving rise to differently favoured non-linear pathways from one conformer to the next [361].

Both SFG and THG emerge from the virtual excitation and subsequent decay of chiral molecules, and are thus quite sensitive to the shape of the molecular potential and the values of transition-dipole matrix-elements. This will affect both the efficiency of these processes at specific frequencies and the relative phase of the emitted radiation. It was therefore desirable to simulate the aforementioned chiral-SFG scheme (see chapter 4) for multiple conformers of a conformationally complex chiral molecule. Since the relationship between dipole matrix-elements of different conformers is unpredictable and varies depending on the transition in question, it was also desirable to scan through a number of different input frequencies, so as to excite chiral SFG via multiple different energetic pathways involving different dipole-elements.

5.1 Conformational Effects in Chiral Sum-frequency Generation

The feature of different conformers of most interest to us here is the effect that the different geometries of the molecular potential have on the phase imparted to emitted radiation via SFG and THG, as well as different conformers coupling to the electromagnetic field in distinct ways. This raises a few areas of interest that warrant further investigation.

Contrasting with conformational effects arising in different schemes, this scheme exhibits interference due to *coherent* addition of signals from multiple conformations. PECD, for example, is also highly sensitive to conformational geometry due to a differently shaped molecular potential passed through by the photoelectron as it escapes [362]. The photoelectron emission from different conformers may consequently have a distinctive photoelectron angular distribution. Conformational effects can play a larger role in specific instances where conformational geometry alters the ionisation energy [363]. However, these photoelectron currents will add on the level of total electron count, rather than the coherent addition and interference of individual wavefunctions. If we observe, in chiral SFG, inter-conformational interference, what is the character of this interference and how does it change throughout frequency space?

Finally, we must think about the implication of coherent inter-conformational interference more broadly. Conformationally sensitive spectroscopic techniques, such as hole-burning spectroscopy [364, 365] and supersonic non-collisional cold gas jets [366, 367], are sensitive to the small differences between electronic, vibrational, and

rotational transition energies of different conformers. By either using a sufficiently cold sample, or by 'burning' a hole in the molecular velocity distribution using a pump-laser, these techniques limit or sidestep the limitations on spectroscopic resolution due to thermal broadening. This allows tiny differences in transition energy to be resolved. Our technique would be sensitive to molecular conformational geometry not just by the electronic transition energies of different conformers, but at the level of the magnitude and relative orientations of the multiple transition-dipole matrix-elements involved in the non-linear pathways under investigation. Is there scope to exploit this sensitivity to use chiral SFG not just as a tool for studying chirality, but also as a tool for studying conformation?

Another implication of inter-conformer interference could be inter-molecular interference. Can we, by analogy, extend the concept of inter-conformational interference to inter-molecular interference? This could be used in chiral spectroscopy, by obtaining the reference signal either from the solvent or some achiral companion molecule, if they were to have a resonant transition at a similar energy to one in the chiral molecule being studied. This may make it much easier to match the intensity of emitted SFG with a reference signal, by varying the concentration of the sample rather than the intensity of the lasers used, since the relative laser intensities may be difficult to change depending on how the components are generated.

5.2 Modelling Conformational Effects in Chiral SFG

To simulate the effects of molecular conformations on chiral SFG, we had to change our approach compared to that used in chapter 4. In the previous simulations, the chiral molecule propylene oxide was used to demonstrate our setup, since it is very small (for a chiral molecule) and thus relatively inexpensive to simulate using TD-DFT. Propylene oxide is too small to exhibit any complex conformational geometry, since it lacks any freely rotating single bonds. Therefore, it was necessary to use a larger chiral molecule, one which does exhibit varied conformational geometry, to investigate these effects.

The molecule chosen was carvone, a cyclic chiral organic compound which has multiple stable conformers. Carvone consists of a cyclohexene ring with a substituted ketone group and an allyl group attached via a single bond. The conformers of carvone vary by the orientation of the allyl group relative to the plane of the central ring [368], and the rotation of the allyl group about the bond connecting it to the rest of the molecule. These rotations give rise to six distinct meta-stable conformations (see figure 5.1). Of these, three have the bond connecting the cyclohexene and allyl moieties roughly in plane with the ring, while the other three have the bond roughly perpendicular. These are referred to as equatorial and axial conformers respectively. The equatorial conformers are overwhelmingly more common, and so we omitted the three axial conformers from our analysis.

Whereas previously we desired to demonstrate the viability of chiral SFG in itself, we now investigate the effect of different conformers on the polarisation re-

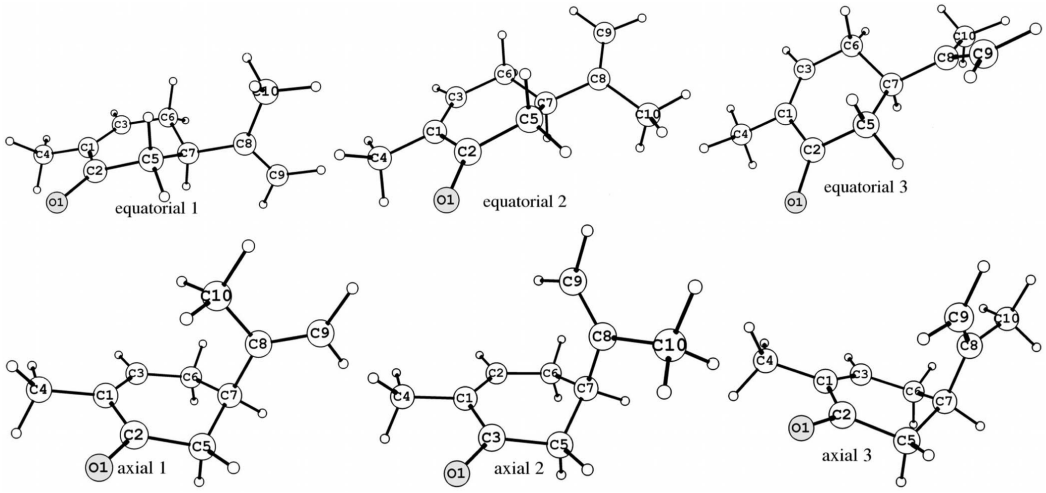


Figure 5.1: Diagram showing the shapes of the six most common conformers of carvone. Reproduced with permissions from AIP publishing [368].

sponse of a mixed ensemble of randomly oriented molecules. As such, we focus on the single-molecule response of the conformers. The relationship between the emission from different conformers is subtle and frequency-dependent; at different frequencies, achiral and chiral pathways within and between conformers can interfere constructively or destructively. Therefore, we needed to run simulations for a range of different input frequencies to 'map out' these relationships across frequency space; we turned to multi-dimensional spectroscopy.

This required us to simulate the single-molecule polarisation response for a much larger molecule and for many more different situations than before. We needed to simulate three different conformers of carvone, each for 208 different orientations and at 27 different input frequencies. Due to the increased computational demands it was therefore necessary to find a more efficient way of simulating the polarisation response. Carvone is bigger and therefore more computationally intensive to simulate than propylene oxide.

Instead of using TD-DFT to simulate the full polarisation response, as was done for propylene oxide, we decided to create a bespoke solver of the time-dependent Schrödinger equation for the applied field using spectral methods (see section 3.1.1). Our program would express the quantum-mechanical state of a molecule of carvone as a linear combination of the pure electronic states of the molecule, and solve the TDSE for a given applied electric field in terms of the complex occupancies of these states. This process requires three general steps:

1. Start by calculating the energies of the electronic states of the molecule and the dipole-matrix elements of the transitions between these states in a field free situation.

2. Using the above information to calculate, in terms of amplitudes of states, the time-dependent response of the molecule to our applied external field by solving the TDSE for a basis consisting of eigenstates of the field-free system.

3. Using the complex occupations of the states, calculate the variation in time of the polarisation of the molecule, and from that infer the frequencies at which the molecule would emit radiation.

The first step was completed modelling the conformers of carvone using density-functional theory (DFT) in the software package Gaussian [369]. For this work, we used the Coulomb attenuating method (CAM) to account for long-range electron correlation [308], with general non-local correlation provided by the Lee-Yang-Parr expression (LYP), with the base being the Becke-3-parameter hybrid functional (CAM-B3LYP) (see section 3.2.4, and figure 5.2). This was done in collaboration with Patricia Vindel (NYU).

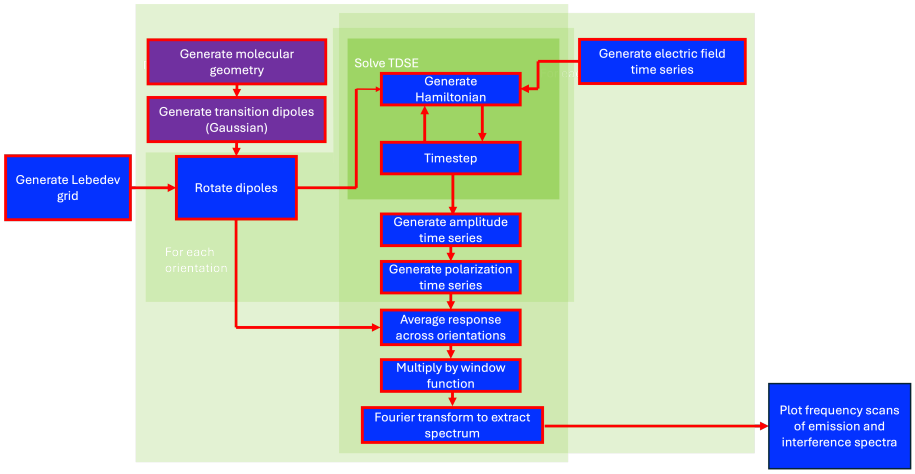


Figure 5.2: A schematic showing the general procedure used in this work. In-house codes available in-group were applied and adapted, and transition-dipole matrix elements were provided by our collaborator Patricia Vindel.

The last step is to retrieve the polarisation based on changes in complex amplitudes of states. The wave-function of our molecule can be represented by a sum of pure electronic states:

$$|\Psi_t\rangle = \sum_{i=0}^{N_s} \mathfrak{C}_i(t)\,|i\rangle \tag{5.1}$$

where N_s is the number of simulated states, then the polarisation can be found by contracting over the dipole operator $\vec{d}$ to get

$$\langle\Psi_t|\,\vec{d}\,|\Psi_t\rangle = \sum_{i=0}^{N_s}\sum_{j=0}^{N_s} \langle j|\,\mathfrak{C}_j^*(t)\,\vec{d}\,\mathfrak{C}_i(t)\,|i\rangle \tag{5.2}$$

$$= \sum_{i=0}^{N_s}\sum_{j=0}^{N_s} \mathfrak{C}_j^*(t)\mathfrak{C}_i(t)\,\vec{d}_{ij} \tag{5.3}$$

In other words, given we know the dipole matrix elements $\vec{d}_{ij}$, and we have a time series of complex occupancies $\mathfrak{C}_i(t)$, we can extract a time series of polarisation using equation 5.3.

5.2.1 Solving the Time-dependent Schrödinger Equation

Once we have the transition matrix elements for the dipole operator for each conformer of carvone, we can solve the time-dependent Schrödinger equation using a spectral method. As outlined in section 3.1, starting from time-dependent Schrödinger equation (equation 3.1) we can express our wavefunction as a linear sum of time-invariant states ψ_i corresponding to energy levels i of our molecule:

$$\Psi(t) = \sum_{j=0}^{N_s} \mathfrak{C}_j(t)\psi_j. \tag{5.4}$$

We find

$$\frac{d}{dt}\Psi(t) = -\frac{i}{\hbar}\hat{\mathcal{H}}(t)\Psi(t) \tag{5.5}$$

$$\implies \frac{d}{dt}\sum_{j=0}^{N_s} \mathfrak{C}_j(t)\psi_j = -\frac{i}{\hbar}\hat{\mathcal{H}}(t)\left(\sum_{j=0}^{N_s} \mathfrak{C}_i(t)\psi_j\right) \tag{5.6}$$

which, multiplying by complex conjugate ψ_i^* and expressing Hamiltonian matrix elements as $\mathcal{H}_{ij}$ while exploiting the orthogonality of our basis, reduces to

$$\frac{d\mathfrak{C}_i}{dt} = -\frac{i}{\hbar}\sum_{j=0}^{N_s} \mathcal{H}_{ij}(t)\mathfrak{C}_j(t) \tag{5.7}$$

This is an ordinary differential equation, which we can solve numerically using standard methods. In this case, we opted to use the fourth-order Runge-Kutta method.

In order to solve our differential equation, we need to evaluate $\mathcal{H}_{ij}$ at each time-step. In our spectral representation, we can split our hamiltonian matrix into two elements. Since the transition dipoles from one state to itself can be neglected due to the oscillation of the field, the diagonal elements $\mathcal{H}_{ii}$ will simply be the energy levels of each of our basis states. The off-diagonal elements $\mathcal{H}_{ij}, i \neq j$ will encapsulate the coupling of our molecule to an applied external field $\vec{E}(t)$, giving rise to an interaction component $V_{ij}(t) = \langle i|\, V(t)\, |j\rangle = \langle i|\, -\vec{d}\cdot\vec{E}(t)\, |j\rangle = -\vec{d}_{ij}\cdot\vec{E}(t)$, so our full Hamiltonian matrix element becomes:

$$\mathcal{H}_{ij}(t) = \delta_{ij}\mathcal{H}_{ij}^{(0)} - \vec{d}_{ij}\cdot\vec{E}(t) \tag{5.8}$$

where $\mathcal{H}_{ij}^{(0)}$ are matrix elements of our field-free Hamiltonian. This procedure allows us to find a time-series for the complex probability amplitudes $\mathfrak{C}_i$ of our basis states, given we have dipole matrix elements, field-free energy levels of our hamiltonian and a time series of our electric field. This was done in collaboration with Rico Heilemann (MBI).

Along with the ability to run a frequency scan, and ability to run simulations for multiple conformers, the gained efficiency of this TDSE solver compared to the TD-DFT used previously allows us to stimulate both a Gaussian pulse, but also a period after the pulse has finished, when the molecule would undergo free-induction decay. Since we are considering weak laser intensities, and dynamics which don't involve the electronic continuum, this approach is valid.

After running the simulations for 208 different orientations, chosen using the Lebedev-quadrature scheme outlined in section 3.3.1, the polarisation time-series for each is extracted. These are then orientationally averaged to estimate the polarisation response for an ensemble of non-interacting randomly oriented chiral molecules (see section 3.3.1) to an electric field of the same form as in the previous chapter (see chapter 4.1.1). The orientationally-averaged polarisation time-series was then processed by multiplying by a window function. In a physical context, the free-induction decay period would be limited by the process of nuclear decoherence, as the electronic excitation energy of the molecule is converted into nuclear motion causing a loss of the coherence of the emission. Furthermore, because our model is semi-classical, with the electric field being treated classically instead of being second-quantised, there is no mechanism *within* the simulation itself to describe the de-excitation of the molecule via emission of a photon (since that would require a quantum-mechanical description of the electromagnetic field), however this occurs on longer timescales than those we are considering. Our window function is used to roughly emulate these processes, with a smooth cutoff at around $40fs$ after the end of the pulse serving the dual purposes of removing the noise inherent to the abrupt end of the simulation (in the Fourier domain), and approximating the diminution of the polarisation response due to nuclear decoherence. Finally, the processed time series is then Fourier-transformed into a frequency-spectrum, providing us with a map of the non-linear emission of the molecule in frequency space.

5.3 Results and Discussion

To explore the questions posed, we reuse our setup from section 4.1.1. We combine a linearly polarised beam with angular frequency ω and a non-collinear second beam containing cross-polarised ω and 2ω angular frequencies, with the 2ω component polarised perpendicular to the non-collinear plane.

As explained in chapter 4, this setup generates an electric field within the interaction region that is locally chiral within the electric-dipole approximation, and the non-collinear setup enables an interference between the resultant chiral sum-frequency and achiral third-harmonic signals which are overlapped in both frequency and angular space. This setup thereby generates an enantiosensitive lower-order response from a field which is chiral within the electric-dipole approximation.

5.3.1 Conformational Averaging

Our first question is whether the fully-controllable enantiosensitive interference survives the coherent addition of emissions from multiple different molecular conformers coexisting within a sample. To answer this, we run simulations using a setup like the one outlined in chapter 4, with a Gaussian pulse, for the three most common conformers (i.e. the equatorial conformers) of carvone in 208 different orientations each, before averaging over all orientations and performing a weighted average of the polarisation response of the three conformers. We scan over multiple fundamental input frequencies ω, from $\hbar\omega = 0.77\,\text{eV}$ to $\hbar\omega = 2.51\,\text{eV}$ in steps of $0.064\,\text{eV}$, so as to build up a picture of different pathways and resonances, and thereby the variation

of the inter-conformational interference across the frequency space.

We wished to investigate both the total emission from all three conformers, but also the interference between the conformers, and so we define an interference parameter as follows; The total emission of an ensemble of chiral molecules belonging to three different conformers is going to be proportional to the squared magnitude of the sum of polarisations:

$$
\begin{aligned}
I &\propto |\overrightarrow{P_1} + \overrightarrow{P_2} + \overrightarrow{P_3}|^2 && (5.9)\\
&= (\overrightarrow{P_1} + \overrightarrow{P_2} + \overrightarrow{P_3}) \cdot (\overrightarrow{P_1} + \overrightarrow{P_2} + \overrightarrow{P_3})^* && (5.10)\\
&= (|\overrightarrow{P_1}|^2 + |\overrightarrow{P_2}|^2 + |\overrightarrow{P_3}|^2) \\
&+ \overrightarrow{P_1} \cdot (\overrightarrow{P_2} + \overrightarrow{P_3})^* + \overrightarrow{P_2} \cdot (\overrightarrow{P_1} + \overrightarrow{P_3})^* + \overrightarrow{P_3} \cdot (\overrightarrow{P_2} + \overrightarrow{P_1})^* && (5.11)
\end{aligned}
$$

where the last three terms correspond to the interference between the three polarisations. If all three polarisations interfere constructively, the last terms will add up to a positive value, while for destructive interference this will be negative. We can repeat the above analysis for different numbers of polarisations, and for different planes of polarisation, to find interference between THG or SFG from each of two or all three conformers at once, so generally we can quantify the interference between N signals polarised along $\hat{e}$ as:

$$
Y = \frac{\sum_{i,j=0,i\neq j}^{N} P_{\hat{e}}^{(i)} P_{\hat{e}}^{(j)*}}{\sum_{i=0}^{N} P_{\hat{e}}^{(i)} P_{\hat{e}}^{(i)*}} \tag{5.12}
$$

The results can be seen in figure 5.3., with the polarisation response along the $\hat{x}$ direction used as a proxy for achiral emission, and the response along the $\hat{z}$ direction used as a proxy for chiral emission. This is the same scheme used in chapter 4.

We can see that the driving field generates mostly achiral non-resonant emission along the odd-numbered harmonics, with peaks of resonant emission when odd harmonics intersect with energies of ground-to-excited-state transitions. One particular point of interest is the lack of resonant emission from the first-excited state transition, and the relatively large degree of emission resonant with the second excited state transition. As we demonstrate in section 5.3.3, this is due to the relatively small magnitude of the transition-dipole from ground to first excited state; this transition simply couples poorly to the electric field.

Another point of interest is the variation of the interconformational interference, particularly for chiral emission where linear and non-resonant processes are weaker. We see a band of destructive interconformational interference just above the ground-to-third-excited-state transition for chiral emission but no such band for achiral emission, while there are bands of constructive interconformational interference in the chiral emission near higher-energy transitions. It is also important to note that most of the energy-level transitions are very close together in different conformers, so differences in amplitude and phase of emission are due to the differences in relative orientation of transition-dipoles of different conformers, not the energy levels themselves.

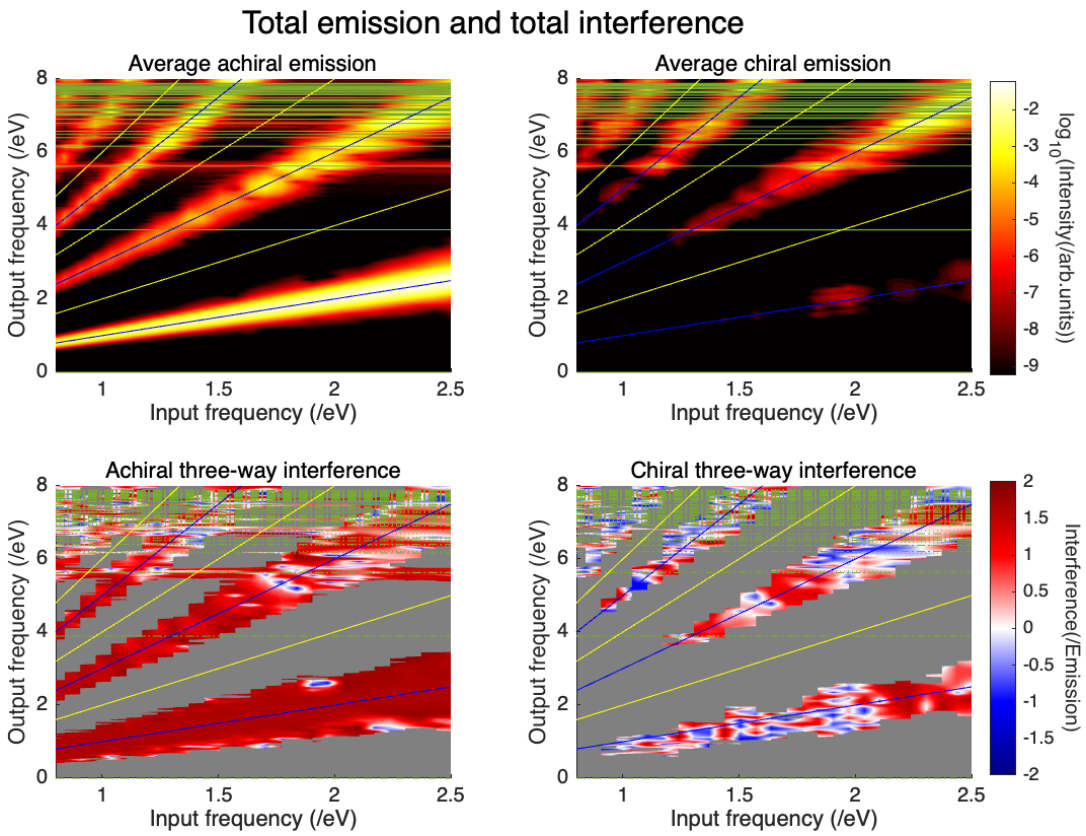


Figure 5.3: Intensity of emission (top), and three-way interconformational interference (bottom), for $\hat{x}$-polarised (left), and $\hat{z}$-polarised (right) emissions from a representative mixture of chiral molecule carvone, against fundamental input and output frequencies in electron-Volts. Horizontal green lines indicate electronic energy levels, whilst diagonal lines indicate even (yellow) and odd (blue) harmonics relative to the fundamental input. Energy-level transitions are marked as horizontal green lines in (dashed = eq-1, dotted and dashed = eq-2, dotted = eq-3).

Therefore, while the emissions from different conformers *do* destructively interfere at some points, it interferes constructively at others, and so it is possible, by choice of input frequency, to generate simultaneously light from both chiral and achiral pathways which survives conformational averaging, and this will give rise to a fully controllable enantiosensitive signal for the following reason:

If we combine three sinusoidal waves with identical frequencies but different phases, the resulting combined wave can always be written as another sine wave of the same frequency, but with amplitude and phase which depend on the interference due to relative phase between the emissions:

$$A\sin(3\omega t+\phi_a)+B\sin(3\omega t+\phi_b)+C\sin(3\omega t+\phi_c)=T\sin(3\omega t+\phi_t) \tag{5.13}$$

where

$$T=\sqrt{A^2+B^2+C^2+2AB\cos(\phi_a-\phi_b)+2AC\cos(\phi_a-\phi_c)+2BC\cos(\phi_b-\phi_c)} \tag{5.14}$$

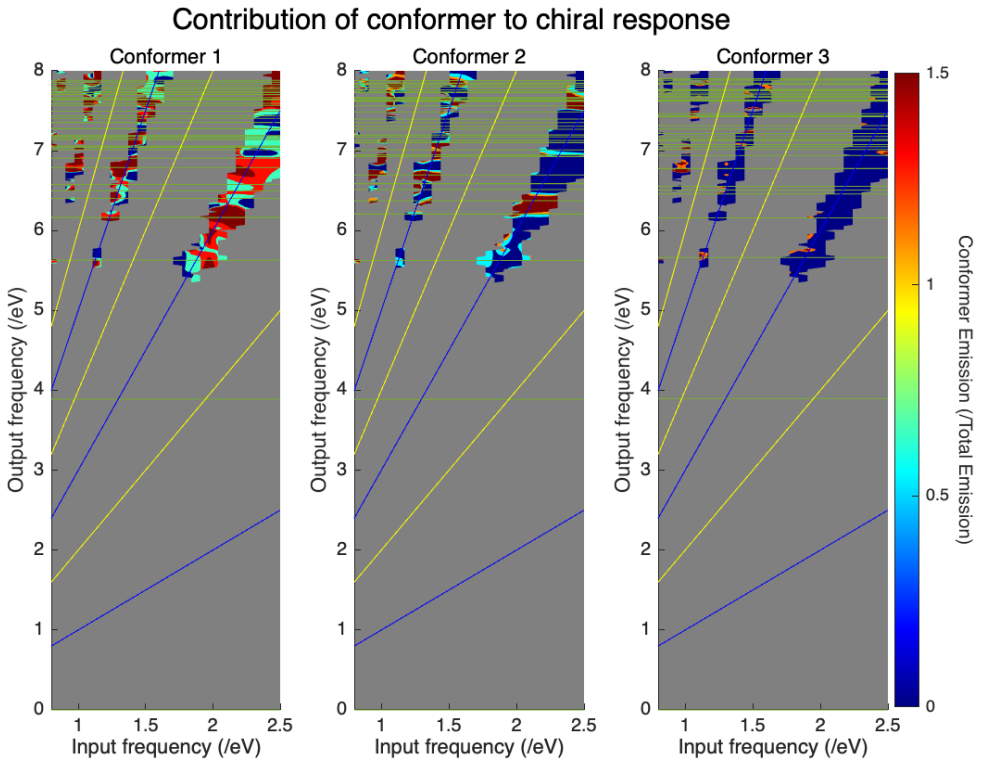
and

$$\phi_t=\tan^{-1}\left(\frac{A\cos(\phi_a)+B\cos(\phi_b)+C\cos(\phi_c)}{A\sin(\phi_a)+B\sin(\phi_b)+C\sin(\phi_c)}\right) \tag{5.15}$$

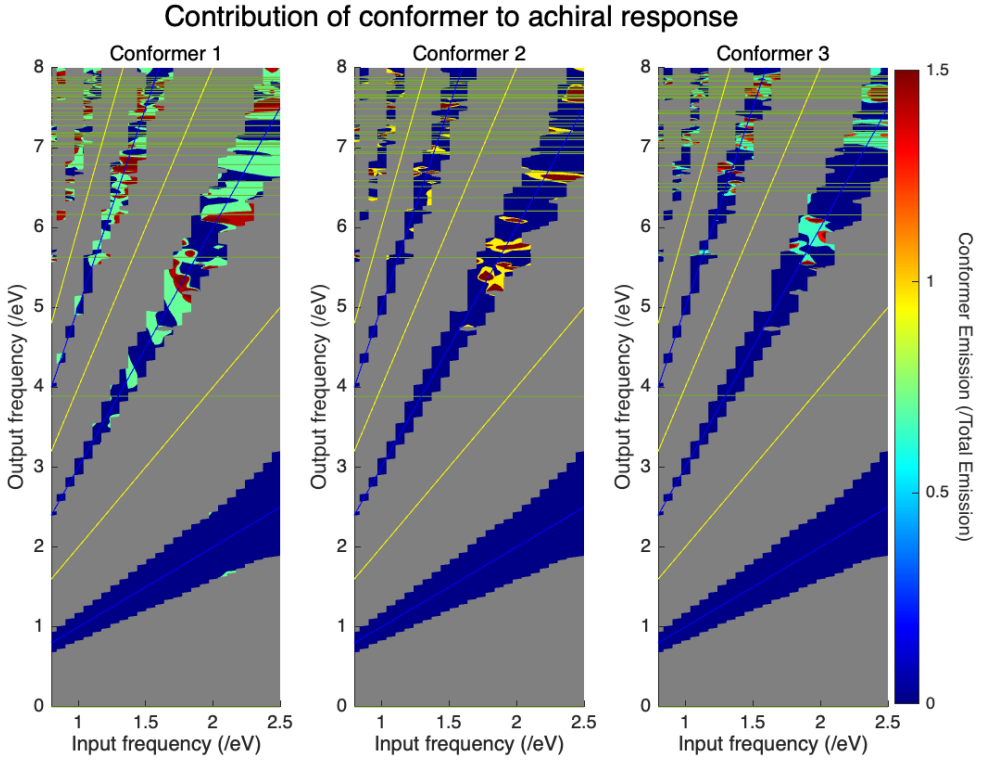
Therefore, we can say that, even as emissions from different conformers add coherently, the resulting combined emission will share the same frequency and will have one well-defined phase, with an entirely consistent relationship to the phases of the incident beams. We can say with confidence, then, that so long as there is not total destructive interference between emissions from different conformers, there will be a combined SFG signal which is entirely controllable via the two-colour phase delay. The same is also true of the achiral THG emissions, and so if emission from these two pathways survives conformational averaging, then there is a fully controllable enantiosensitive interference as outlined previously.

5.3.2 Inter-conformer Interference

Further questions we may ask are to quantify the character of interconformational interference, how this changes with frequency, and can we use this to identify a 'signature' of different conformers and use this method as an analytical technique to that end?



(a)



(b)

Figure 5.4: Intensity of $\hat{z}$-polarised (5.4a) and $\hat{x}$-polarised (5.4b) emission from individual conformers divided by total emission from all conformers for conformer 1,2,3 (left, middle, right), against the fundamental input frequency (x-axis) and emission frequency (y). Horizontal green lines indicate energy levels and diagonal blue and yellow lines indicate odd and even harmonics respectively.

To investigate, we break down our results by emissions from individual conformers. Figures 5.4a and 5.4b map the contribution of different conformers to the average emission across different points in frequency space:

$$\aleph_i \propto \frac{|\vec{P}_i|^2}{|\sum_{j=1}^{N} \vec{P}_j|^2} \tag{5.16}$$

with an end to identify regions where specific conformers may dominate over others on the level of total emission. Higher values (in red) indicate that the sum of the magnitudes of the individual conformational emissions is larger than the total emission from all three together, and so there must be some degree of destructive interference. Low values (blue) indicate that the specific conformer contributes little to total emission at the specific frequency, while low-to-intermediate values (green) indicate significant contribution to emission in concert with other conformers (implying constructive interference), and a ratio close to one (yellow) imply that the emission of a particular conformer is likely dominant at a given frequency. In figure 5.4a, showing emission from polarisation response along the $\hat{z}$ direction, the first and most abundant conformer largely dominates emission (likely due to its relative abundance) but is subject to destructive interference with the second most abundant conformer at the point where the third-harmonic intersects the third-excited-state transition, and subject to constructive interference, mostly with the second conformer, at other points. Meanwhile, figure 5.4b shows emission from polarisation response along the $\hat{x}$ direction. This picture is more complicated, with regions just below the second excited state transition having emission dominated uniquely by the second conformer, and between the second and third excited state dominated by the third conformer. Within non-resonant regions, conformers all constructively interfere and contribute evenly, which is expected as the linear response far from resonance will be in phase relative to the driving field generating it.

Interestingly, there are regions at around an input frequency of 2.1 eV and an output frequency of 6.3 eV where the achiral emission is dominated by conformer 1 whilst the chiral emission is dominated by conformer 2, giving an example of an enantiosensitive *interconformational* interference, with a final enantiosensitive signal having the chiral signal provided by one conformer and the reference provided by a different conformer. There is no reason why this concept of inter-conformational enantiosensitive interference cannot be extended, by analogy, to an enantiosensitive intermolecular interference. If THG from a different conformer of the same compound can serve as a reference for chiral SFG, so could a signal from a different molecule entirely, such as a solvent or companion molecule. Figures 5.5 and 5.6 show emission and pairwise interferences between specific conformers. These allow us to confirm our inferences about regions of constructive and destructive interferences from figures 5.4a and 5.4b.

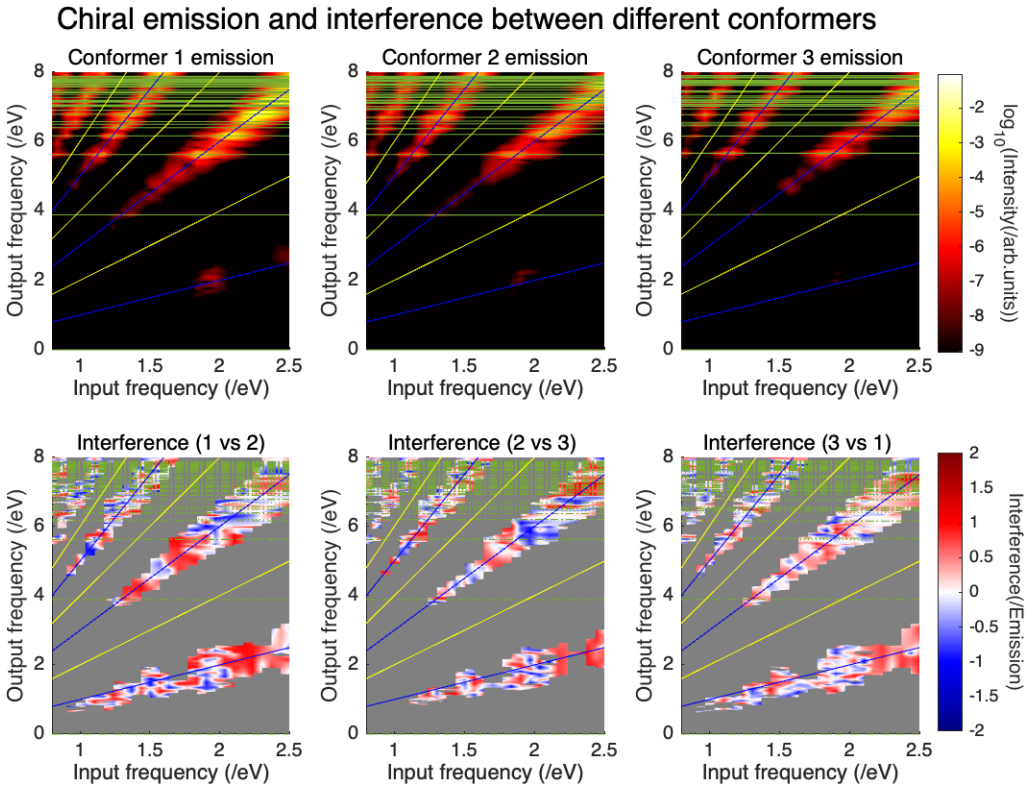


Figure 5.5: Intensity (top) and pairwise interconformational interference (bottom), for chiral emissions from individual conformers of chiral molecule carvone against fundamental input frequency (x-axis), and frequency of emission (y-axis). Horizontal lines (green) indicate electronic energy levels, whilst diagonal lines indicate even (yellow) and odd (blue) harmonics of input fundamental.

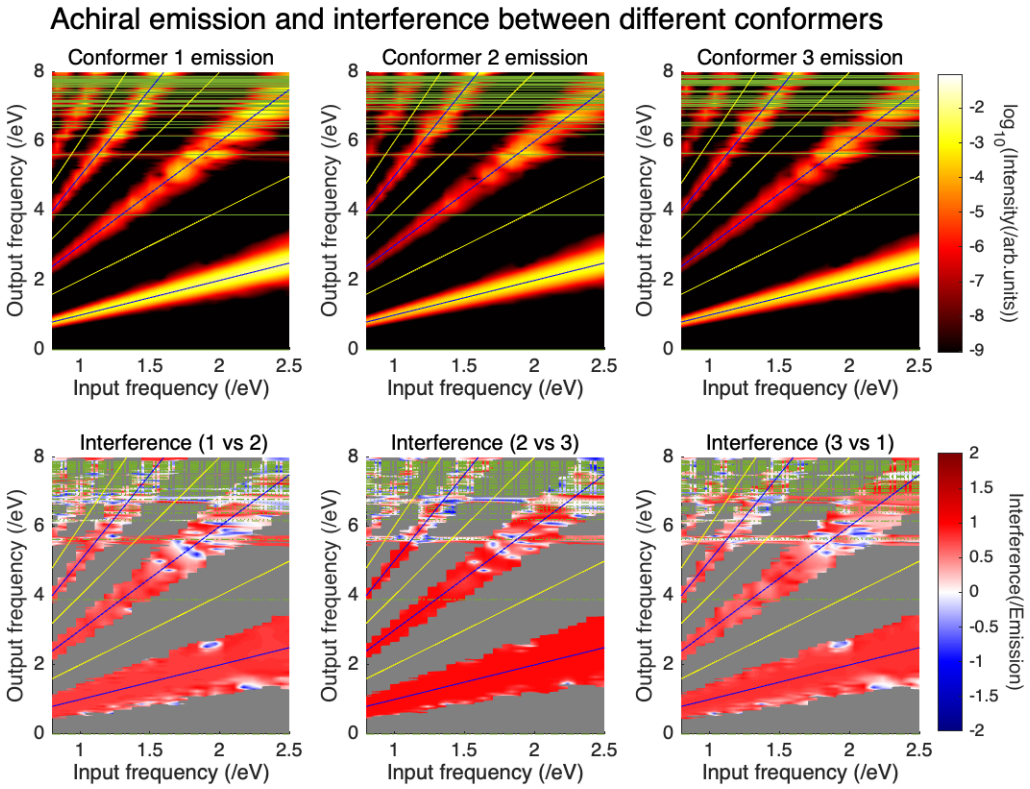


Figure 5.6: Intensity (top) and pairwise interconformational interference (bottom), for achiral emissions from individual conformers of chiral molecule carvone against fundamental input frequency (x-axis), and frequency of emission (y-axis). Horizontal lines (green) indicate electronic energy levels, whilst diagonal lines indicate even (yellow) and odd (blue) harmonics of input fundamental.

5.3.3 Investigating Alternative Emission Pathways

We can further investigate the different emission pathways for these emission peaks by examining the polarisation response of an individual conformer when we have 'turned off' certain transitions or excluded specific energy levels from our simulations. Figures 5.7a-5.7e use a fundamental frequency of 1.88 eV, targeting a resonance with the second excited state. This is appealing because the intermediate first excited state is located at almost exactly 2ω above ground, and so should provide a 'ladder resonance' for the sum-frequency generation pathway whereby the molecule first absorbs a photon of 2ω and then ω to access the second excited state.

Figure 5.7a shows the emission from conformer 1 of carvone, illuminated by our chiral SFG setup with fundamental angular frequency $\hbar\omega = 1.9\,\text{eV}$ so as to be resonant with the transition from ground to second excited state. This simulation was done with 45 states included in the calculations, which is the number of states needed for the simulations to converge, and shows a strong peak at the third harmonic in both $\hat{x}$ and $\hat{z}$ directions, as well as resonant peaks corresponding to the transition energies within the molecule. We want to investigate the different pathways that may be generating these emissions, most especially the peaks at the third harmonic, and to do this we can 'turn off' and exclude various transitions and states from the simulations.

In figure 5.7b we exclude all states but the ground state and second excited state and block them by setting all transition dipoles (except between ground and second-excited-state) to zero. This shows peaks along all three axes at the third harmonic, resonant with the one still-available transition. The chiral pathway, shown in red, is reduced the most, as this relies on there being three different transitions available in order to generate a polarisation response; most obviously, the pathway from ground to first excited state and then second excited state, absorbing one 2ω photon and one ω photon. Without this intermediate state available, the chiral pathway is greatly diminished, with any residual emission being enabled by Stark shift. We can turn this off by removing the permanent dipoles from the simulations, as in figure 5.7d, where the polarisation response along the $\hat{z}$ direction can be seen reduced to numerical zero.

Reintroducing the intermediate state yields the results seen in figure 5.7c, with both linear excitation along the $\hat{y}$ direction and SHG along the $\hat{z}$ direction increased greatly relative to a situation in which the intermediate state is excluded.

Finally, figure 5.7e shows the results when the transition dipole from ground to first excited state is made both very large and orthogonal to both the transition dipoles from ground and first excited state to second excited state. This enhances the SFG pathway, as well as other pathways which result in emission at the second harmonic ($\overrightarrow{d_{01}}$), fundamental ($\overrightarrow{d_{21}}$), and optical rectification. These investigations thus allow us to state that the SFG signal at input frequency 1.88 eV relies on the existence of the intermediate state. The lack of a strong enantiosensitive signal resonant with the first-excited state transition is thus most likely due to the lack of any intermediate state, combined with the weakness of the coupling of that transition to the electric field.

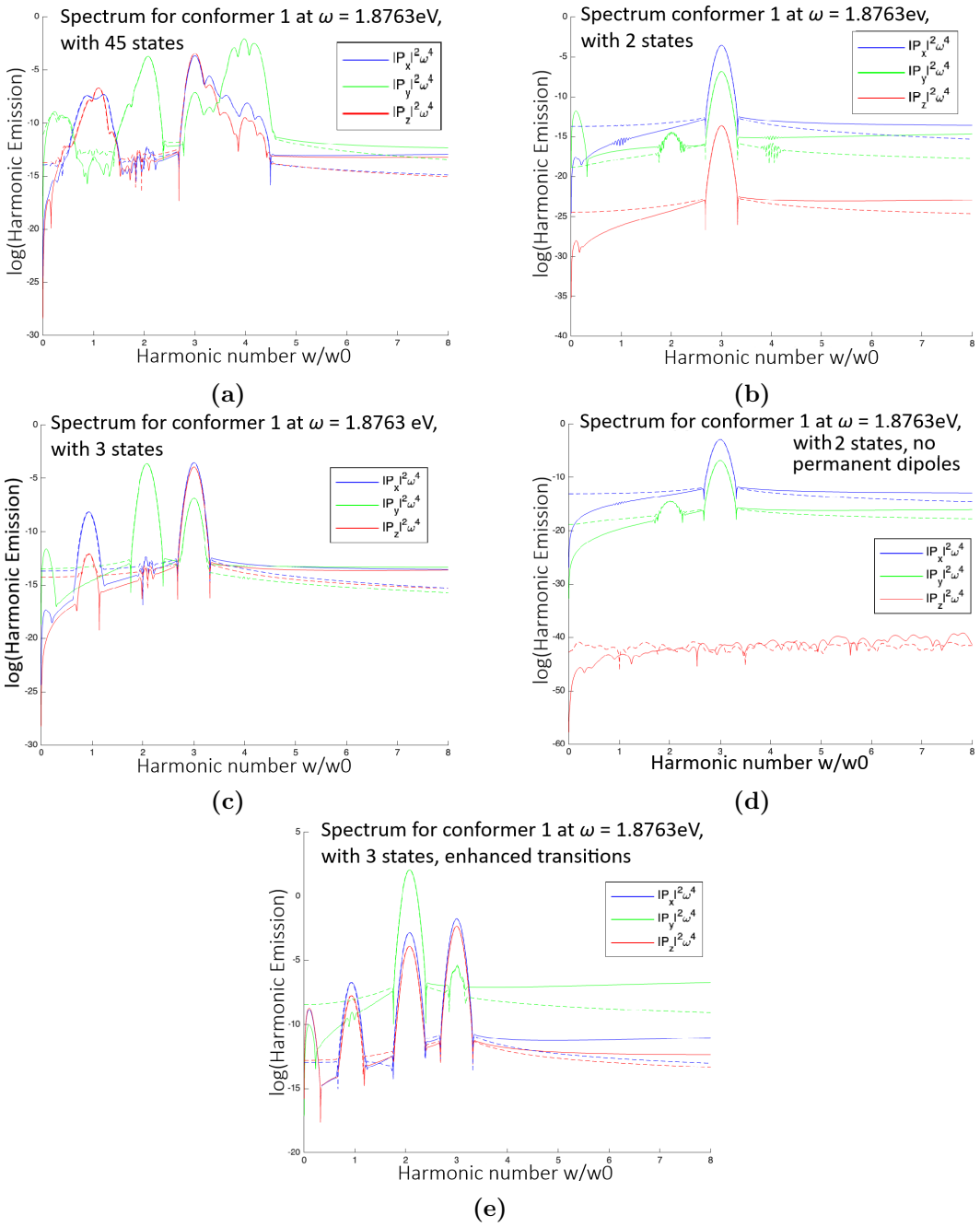


Figure 5.7: Intensity of emission from a randomly oriented ensemble of carvone, on a logarithmic scale, for a driving field with fundamental frequency $\omega = 1.9eV$, showing polarisation response along the $\hat{x}$ (blue), $\hat{y}$ (green) and $\hat{z}$ directions with emission calculated from polarisation (solid) and second time derivative of polarisation (dashed) using the Lamor formula. Simulation with: forty-five states included (a); the ground and second excited state (b); the ground, first excited, and second excited state (c); the ground and second excited state, with the permanent dipoles of these states removed (d); the ground, first, and second excited states, with enhanced transition dipoles (e).

5.3.4 Alternate Processing

Figures 5.3-5.6 are all generated using a filter which includes the polarisation response both during the pulse of the driving field and a period just after, smoothly decreasing so as to approximate the effect of nuclear decoherence. However, we can also use a filter which completely excludes the response of the molecules while the laser pulse is passing, and includes only the free-induction decay of the molecule after the pulse has receded. This will largely exclude any non-resonant emission driven by the laser pulse, showing only resonant pathways.

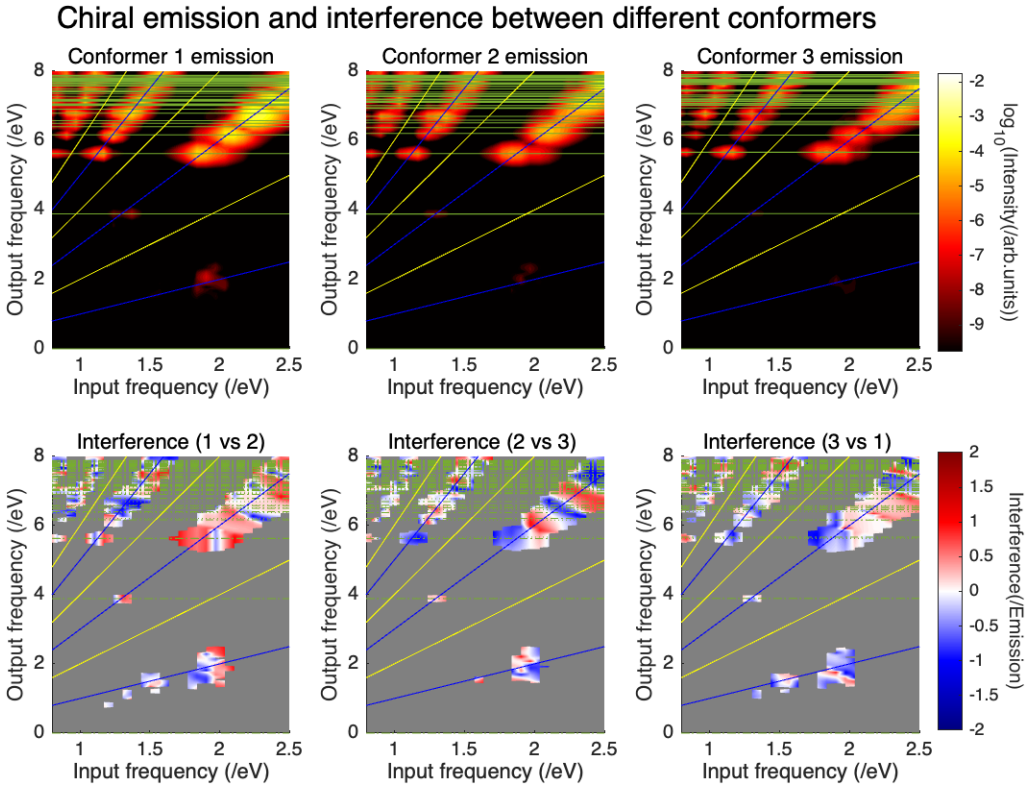


Figure 5.8: Intensity (top) and pairwise interconformational interference (bottom), for $\hat{z}$-polarised (chiral) emissions from individual conformers of chiral molecule carvone against fundamental input frequency (x-axis), and frequency of emission (y-axis), as processed with a filter that excludes the initial pulse. Horizontal lines (green) indicate electronic energy levels, whilst diagonal lines indicate even (yellow) and odd (blue) harmonics of input fundamental.

Figures 5.8 and 5.9 have been processed in this way, and make the resonant peaks more distinct by removing off-resonant signals. We can more easily see now that, for example, the peak corresponding to the transition between the ground state and first-excited state is relatively much weaker than many of those corresponding to the higher excited state transitions. The linear response to the pulse, as well as non-resonant emission along the harmonics, is much weaker within the free-electron decay than in the initial response of the molecules to the pulse, and the bulk of emission is found at or near points where odd-numbered harmonics intersect with ground-to-excited state transitions. Note the presence of emission along the fundamental for an input frequency of 1.9 eV. This is due to the transition between the second and first excited state, from a pathway whereby the molecule is excited to the second excited

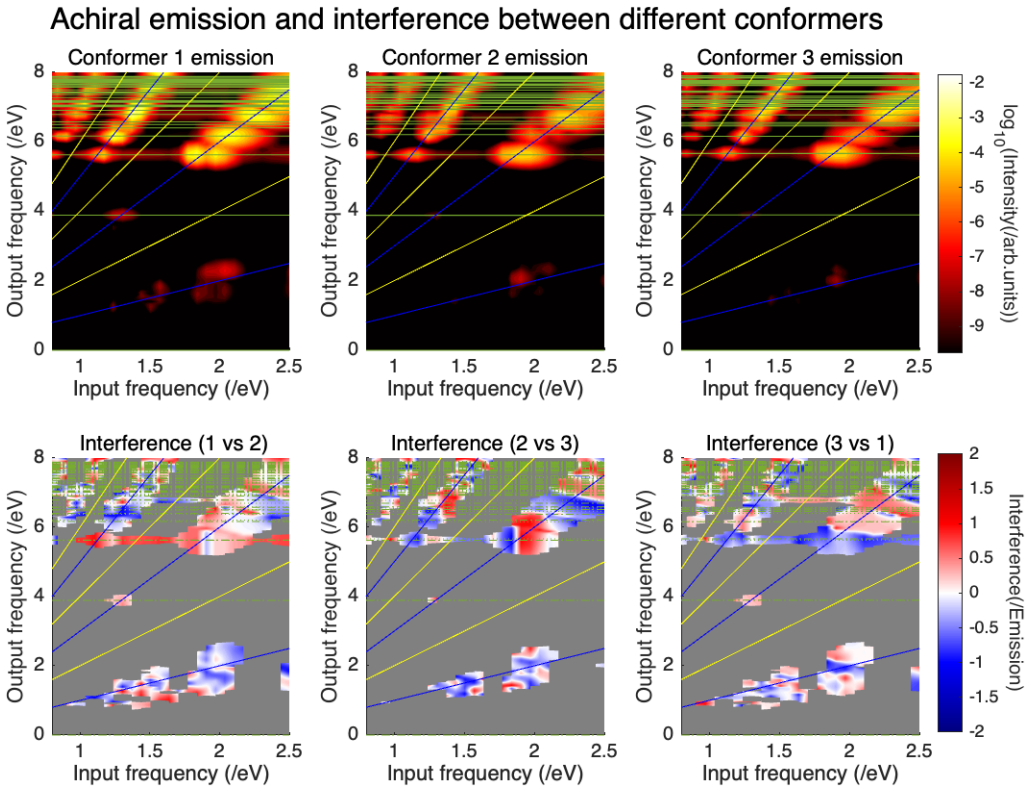


Figure 5.9: Intensity (top) and pairwise interconformational interference (bottom), for $\hat{x}$-polarised (achiral) emissions from individual conformers of chiral molecule carvone against fundamental input frequency (x-axis), and frequency of emission (y-axis), as processed with a filter that excludes the initial pulse. Horizontal lines (green) indicate electronic energy levels, whilst diagonal lines indicate even (yellow) and odd (blue) harmonics of input fundamental.

state, before falling back to the first exited state and emitting a photon with the fundamental frequency of the input ω. It is also interesting to see, by comparison with figures 5.5 and 5.6, that the linear response and non-resonant emission from during the initial pulse is largely in-phase from different conformers. Meanwhile, emission near-resonance, which is present both during the initial pulse and the subsequent free-induction decay, sees a much more complicated phase relationship between different conformers. For example, emission near the second-excited state energy is in-phase between conformers 1 and 2, but both of these conformers are out of phase with emission from conformer 3.

5.3.5 Conclusion

In summation of all of these results, we can conclude that a fully controllable enantiosensitive response can be generated from a chiral sample using our setup which could be used to differentiate between opposing enantiomers on the level of total intensity, and that this response both survives and remains fully controllable even with multiple conformers present within a sample. As a chiroptical tool, chiral SFG is most potentially useful in situations where sample molecules may also have varied conformational geometry. By judicious choice of input frequency, the existence of

multiple stable conformers within a sample need not scupper the potential for using SFG as a chiroptical tool.

Furthermore, these simulations identify the instance of fully coherent interconformational interferences, and this could be used as an analytical tool. Such experiments would require both robust computational and theoretical support, but analysis of varying conformational ratios could be calibrated by using environmental factors, specifically temperature, to vary conformational abundances and the consequent variation of inter-conformational interferences. This could then be used, for example, to study the change of conformational abundances during a chemical reaction.

Finally, we also demonstrate the existence of an inter-conformational enantiosensitive interference, with chiral signal and achiral reference generated in different conformers at certain frequencies. By analogy, this could also be extended to different isomers or even different compounds entirely; for example the generation of an enantiosensitive response in a solution with a chiral signal generated in a sample molecule while the reference could be generated in the solvent or a companion molecule. This could be very useful. By choosing a solvent or companion molecule resonant at a similar frequency to the chiral subject molecule, an enantiosensitive SFG signal could be generated using this inter-molecular interference. While the interference between SFG and THG in the same molecule can be tuned by varying input frequency and intensities of the laser setup, due to how beams of multiple frequencies are generated, there may be limited freedom in how the intensities of the fundamental and 2ω components differ relative to one-another. Using a solvent of companion molecule to generate the reference signal gives an extra controllable variable within the experimental setup, in the form of the relative concentrations of the chiral subject molecule and the reference. This allows the output intensities of chiral and achiral signals to be better matched even if it is not possible to use input beams of the correct relative intensities.

Chapter 6

Conclusions and prospectives

Throughout this work, we have given an overview of chirality as it arises mathematically and manifests throughout the domains of physics, chemistry and biochemistry. With the help of the physics of light-matter interactions and optics, we have explored some of the cutting edge methods of chiral sensing using light. We have also examined some of the theoretical tools necessary for us to simulate the physical processes of which we are interested.

In chapter 4, we introduced a novel technique which utilised synthetic chiral light to realise an efficient chiral measurement with low-order nonlinear processes, namely sum-frequency and third-harmonic generation. Using an interference between these processes, we showed with cutting-edge TDDFT simulations in propylene oxide that it should be possible to generate an enantiosensitive intensity in the far field. By tweaking the laser parameters, it should be possible in principle to generate a signal which is maximised for one enantiomer whilst being entirely suppressed for the opposite enantiomer. The exact setup we have presented is just one way of realising such a proposal. Although we chose to use THG to generate the reference signal, it should also be possible to produce the signal externally to the sample, such as with an optical-parametric amplifier, or internally to the sample, using (for instance) an electric or magnetic field to enable achiral SFG. The first proposal may or may not be practical depending on the specifics of any given laboratory, while the second will only be practical if the phase of the resulting reference is controllable, and this will require a very stable applied field. Similarly, different approaches to making the reference overlap with the chiral signal could also be tried, including mirrors and tightly focussed optics, so long as the phase imparted on the signals are stable and well characterised. Indeed, the non collinear setup presented could be replaced with an analogous setup using a tightly focussed beam.

In chapter 5, we presented our investigations into conformational effects in chiral SFG. In doing so we wanted to answer several questions; does the enantiosensitive interference survive conformational averaging? Can we observe a coherent interconformational interference? If so, how does this interference vary with frequency? Can we find a further application for this interconformational interference?

Using a combination of DFT and a spectral expansion of the TDSE, we simulated our chiral SFG setup for the three most common conformers of the chiral molecule carvone. We did this by scanning through a range of input frequencies, before averaging the response from the different conformers and characterising the interference between them. In doing so, we identified that the character of the interference is heavily frequency dependent, so even if conformational averaging quashes the enantiosensitivity at one frequency it is very unlikely to do so for all frequencies. Furthermore, the different conformers each have specific regions of a multi-dimensional spectrum where they dominate the response. This holds for both achiral and chiral pathways. Therefore, we can identify regions where we might expect interconformational interference, and even an enantiosensitive interconformational interference where an achiral and chiral response emerge from different conformers.

By analogy, this means that it should be possible to realise an enantiosensitve intermolecular interference at the right frequency and with the right molecule. For example, one could realise the chiral SFG setup but with the reference signal generated either by the sample or some achiral dye molecule. Furthermore, the existence of an interconformational interference could be used to realise ultrafast measurements with conformational specificity, providing that the response is sufficiently well-calibrated using either high-fidelity theoretical simulation or by varying conformational ratios via temperature.

Finally, by investigating the response with certain transitions blocked, we demonstrated that the lack of non-linear response resonant with the first-excited-state transition is due to the lack of an orthogonal transition to provide an intermediate resonance, combined with the weakness of the transition dipole itself, since the resonant SFG signal can be entirely suppressed by eliminating all intermediate states.

We should now turn briefly to the potential future avenues of research that emerge from the work described here. The investigations conducted in section 5 could be expanded theoretically by performing more simulations. Specifically, the concept of inter-molecular enantiosensitive interference, introduced here by analogy, could be tested explicitly in simulations by repeating the same steps for two different molecules which have similar transition energies. Such intermolecular interferences could then be tested in a laboratory setting, using the setup described in 4 with an achiral companion molecule or solvent combined with a chiral subject molecule. Furthermore, the concept of interconformer interference in itself warrants further study. This could be done theoretically, by modelling the expected output of a chiral SFG setup as conformational abundances are varied. Experimentally, conformational abundances could be varied by changing the temperature, since more energetic conformers will be more common at higher temperatures. Enantiosensitive SFG with conformer specificity could also prove useful if experiments can be realised which have the sample undergo a chemical reaction while being studied. Different conformers are subject to different degrees of steric shielding during chemical reactions, and so one may be able to observe different conformers undergoing reactions at different rates.

Bibliography

[1] V. Prelog. "Chirality in Chemistry". In: *Science* 193.4247 (1976), pp. 17–24.

[2] W. Thompson Baron Kelvin. *The Molecular Tactics of a Crystal*. Clarendon Press, 1894.

[3] A. D. McNaught, A. Wilkinson, et al. *Compendium of Chemical Terminology*. Vol. 1669. Blackwell Science Oxford, 1997.

[4] L. A. Paquette. *Chiral Reagents for Asymmetric Synthesis*. Vol. 2. John Wiley & Sons, 2003.

[5] F. A. Cotton. *Chemical Applications of Group Theory*. John Wiley & Sons, 1991.

[6] M. Hargittai and I. Hargittai. *Symmetry through the Eyes of a Chemist*. Springer Science & Business Media, 2009.

[7] A. Berthod. *Chiral Recognition Mechanisms*. 2006.

[8] N. C. Thomas. "The Early History of Spectroscopy". In: *Journal of chemical education* 68.8 (1991), p. 631.

[9] J. Moreno and R. Peinado. *Enological Chemistry*. Academic Press, 2012.

[10] G. Kirchhoff and R. Bunsen. *Chemische Analyse Durch Spectralbeobachtungen*. 72. Engelmann, 1895.

[11] L. D Barron. *Molecular Light Scattering and Optical Activity*. Cambridge University Press, 2009.

[12] H. Eyring, H.-C. Liu, and D. Caldwell. "Optical Rotatory Dispersion and Circular Dichroism". In: *Chemical Reviews* 68.5 (1968), pp. 525–540.

[13] J. Hecht. "Short History of Laser Development". In: *Optical engineering* 49.9 (2010), pp. 091002–091002.

[14] P. M. Kraus et al. "Measurement and Laser Control of Attosecond Charge Migration in Ionized Iodoacetylene". In: *Science* 350.6262 (2015), pp. 790–795.

[15] F. Krausz and M. Ivanov. "Attosecond Physics". In: *Reviews of modern physics* 81.1 (2009), p. 163.

[16] P. B. Corkum and F. Krausz. "Attosecond Science". In: *Nature physics* 3.6 (2007), pp. 381–387.

[17] N. Berova et al. *Comprehensive Chiroptical Spectroscopy, Volume 1: Instrumentation, Methodologies, and Theoretical Simulations*. Vol. 1. John Wiley & Sons, 2012.

[18] D. Ayuso, A. F. Ordonez, and O. Smirnova. "Ultrafast Chirality: the Road to Efficient Chiral Measurements". In: *Physical Chemistry Chemical Physics* 24.44 (2022), pp. 26962–26991.

[19] A. F. Ordonez and O. Smirnova. "Generalized Perspective on Chiral Measurements without Magnetic Interactions". In: *Phys. Rev. A* 98 (6 Dec. 2018), p. 063428. DOI: 10.1103/PhysRevA.98.063428.
[20] D. Ayuso et al. "Synthetic Chiral Light for Efficient Control of Chiral Light–Matter Interaction". In: *Nature Photonics* 13.12 (2019), pp. 866–871.
[21] D. Ayuso et al. "Strong Chiral Response in Non-collinear High Harmonic Generation Driven by Purely Electric-dipole Interactions". In: *Optics Express* 30.4 (2022), pp. 4659–4667.
[22] R. M. Dreizler and E. K. U. Gross. *Density Functional Theory: An Approach to the Quantum Many-Body Problem*. Springer Science & Business Media, 2012.
[23] I. N. Levine, D. H. Busch, and H. Shull. *Quantum Chemistry*. Vol. 6. Pearson Prentice Hall Upper Saddle River, NJ, 2009.
[24] C. J Cramer. *Essentials of Computational Chemistry: Theories and Models*. John Wiley & Sons, 2013.
[25] M. Stener, G. Fronzoni, and P. Decleva. "Time-dependent Density-Functional Theory for Molecular Photoionization with Noniterative Algorithm and Multicenter B-spline Basis Set: CS2 and C6H6 Case Studies". In: *The Journal of chemical physics* 122.23 (2005).
[26] M. A. L. Marques et al. *Time-dependent Density Functional Theory*. Vol. 706. Springer, 2006.
[27] A. Szabo and N. S. Ostlund. *Modern Quantum Chemistry: Introduction to Advanced Electronic Structure Theory*. Courier Corporation, 1996.
[28] A. Hinchliffe. *Modelling Molecular Structures*. Vol. 2. Wiley New York, 1996.
[29] M. Karras. "Synthesis of Enantiomerically Pure Helical Aromatics such as NHC Ligands and their Use in Asymmetric Catalysis". PhD thesis. Jan. 2018.
[30] H. Yamamoto and E. M. Carreira. *Comprehensive Chirality*. Vol. 1. Newnes, 2012.
[31] G. E. Martin. *Transformation Geometry: An Introduction to Symmetry*. Springer Science & Business Media, 2012.
[32] M. Petitjean. "Chirality in Metric Spaces". In: *Symmetry, Culture and Science* 21 (2010), pp. 27–36.
[33] L. D. Landau and E. M. Lifshitz. *Quantum Mechanics: Non-relativistic Theory*. Vol. 3. Elsevier, 2013.
[34] G. Kutzbach. *The Thermal Theory of Cyclones: A History of Meteorological Thought in the Nineteenth Century*. Springer, 2016.
[35] D. K. Kondepudi and D. J. Durand. "Chiral Asymmetry in Spiral Galaxies?" In: *Chirality: The Pharmacological, Biological, and Chemical Consequences of Molecular Asymmetry* 13.7 (2001), pp. 351–356.
[36] A. Slosar et al. "Galaxy Zoo: chiral correlation function of galaxy spins". In: *Monthly Notices of the Royal Astronomical Society* 392.3 (2009), pp. 1225–1232.
[37] A. Ambrosio et al. "Light-induced Spiral Mass Transport in Azo-polymer Films under Vortex-Beam Illumination". In: *Nature communications* 3.1 (2012), p. 989.
[38] T. Martin Lowry. "Optical Rotatory Power". In: *Journal of the Society of Chemical Industry* 54.20 (1935), pp. 477–483.

[39] P. Coullet, L. Gil, and F. Rocca. "Optical Vortices". In: *Optics Communications* 73.5 (Nov. 1989), pp. 403–408. DOI: 10.1016/0030-4018(89)90180-6.
[40] K. A. Forbes and D. Green. "Customized Optical Chirality of Vortex Structured Light through State and Degree-of-Polarization Control". In: *Phys. Rev. A* 107 (6 June 2023), p. 063504. DOI: 10.1103/PhysRevA.107.063504.
[41] N. Mayer et al. "Chiral Topological Light for Detection of Robust Enantiosensitive Observables". In: *Nature Photonics* 18.11 (2024), pp. 1155–1160.
[42] M. Quack, G. Seyfang, and G. Wichmann. "Perspectives on Parity Violation in Chiral Molecules: Theory, Spectroscopic Experiment and Biomolecular Homochirality". In: *Chemical Science* 13.36 (2022), pp. 10598–10643.
[43] M. Quack, Jürgen Stohner, and M. Willeke. "High-Resolution Spectroscopic Studies and Theory of Parity Violation in Chiral Molecules". In: *Annu. Rev. Phys. Chem.* 59.1 (2008), pp. 741–769.
[44] M. Quack. "How Important is Parity Violation for Molecular and Biomolecular Chirality?" In: *Angewandte Chemie International Edition* 41.24 (2002), pp. 4618–4630.
[45] Y. Corvis et al. "Insights into the Crystal Structure, Polymorphism and Thermal Behavior of Menthol Optical Isomers and Racemates". In: *CrystEngComm* 14.20 (2012), pp. 7055–7064.
[46] H. Amouri and M. Gruselle. *Chirality in Transition Metal Chemistry: Molecules, Supramolecular Assemblies and Materials*. John Wiley & Sons, 2008.
[47] R. H. Petrucci. "General Chemistry: Principles and Modern Applications". In: *(No Title)* (1993).
[48] T. W. G. Solomons and C. B. Fryhle. *Organic Chemistry*. John Wiley & Sons, 2008.
[49] R. Chang and J. Overby. *General Chemistry*. Random House New York, 1986.
[50] F. Kurzer. "Fulminic Acid in the History of Organic Chemistry". In: *Journal of chemical education* 77.7 (2000), p. 851.
[51] M. B. Smith. *March's Advanced Organic Chemistry: Reactions, Mechanisms, and Structure*. John Wiley & Sons, 2020.
[52] E. L. Eliel and S. H. Wilen. *Stereochemistry of Organic Compounds*. John Wiley & Sons, 1994.
[53] J. H. van't Hoff. "A Suggestion Looking to the Extension into Space of the Structural Formulas at Present used in Chemistry, and a Note upon the Relation between the Optical Activity and the Chemical Constitution of Organic Compounds". In: *Arch. Neerl. Sci. Exactes Nat* 9 (1874), pp. 445–454.
[54] J. A. Le Bel. "Sur les Lelations qui Existent Entre les Formules Atomiques des Corps Organiques et le Pouvoir Rotatoire de leurs Dissolutions". In: *Bull. Soc. Chim. Fr* 22 (1874), pp. 337–347.
[55] 'Innerstream'. "Chemical Diagram Showing a Chiral Center as Two Non-superimposable Mirror Images". In: *Wikimedia Commons* (2022).
[56] L. G. Wade. *Organic Chemistry*. Prentice-Hall, 2003.
[57] I. Fernández and N. Khiar. "Recent Developments in the Synthesis and Utilization of Chiral Sulfoxides". In: *Chemical reviews* 103.9 (2003), pp. 3651–3706.

[58] 'Benja-bmm27'. "Skeletal formula of R/S-BINOL". In: *Wikimedia Commons* (2007).
[59] 'Sponk'. "(P)-Heptahelicen". In: *Wikimedia Commons* (2010).
[60] 'Smokefoot'. "Chemical Structure of trans-cyclooctene". In: *Wikimedia Commons* (2017).
[61] L. C. Cross and W. Klyne. *Rules for the Nomenclature of Organic Chemistry: Section E: Stereochemistry (Recommendations 1974)*. Elsevier, 2013.
[62] B. Tan. *Axially Chiral Compounds: Asymmetric Synthesis and Applications*. John Wiley & Sons, 2021.
[63] T. Schmiermund. *Introduction to Stereochemistry*. Springer, 2021.
[64] R Santos, K. V. Pontes, and I. B. R. Nogueira. "Enantiomers and Their Resolution". In: *Encyclopedia* 2.1 (2022), pp. 151–188. ISSN: 2673-8392. DOI: 10.3390/encyclopedia2010011.
[65] E. M. Carreira and L. Kvaerno. *Classics in Stereoselective Synthesis*. John Wiley & Sons, 2009.
[66] J. L. Greenfield et al. "Pathways to Increase the Dissymmetry in the Interaction of Chiral Light and Chiral Molecules". In: *Chemical Science* 12.25 (2021), pp. 8589–8602.
[67] O. Wallach. "Zur Kenntniss der Terpene und der Ätherischen Oele". In: *Justus Liebigs Annalen der Chemie* 286.1 (1895), pp. 90–118.
[68] A. G. Mitchell. "Racemic Drugs: Racemic Mixture, Racemic Compound, or Pseudoracemate". In: *J Pharm Pharm Sci* 1.1 (1998), pp. 8–12.
[69] K. Klika. "Suggested New Terms for Describing Chiral States and the State-Dependent Behavior of Chiral Systems". In: *International Journal of Organic Chemistry* 02 (Jan. 2012), pp. 224–232. DOI: 10.4236/ijoc.2012.23031.
[70] G. P. Moss. "Basic Terminology of Stereochemistry (IUPAC Recommendations 1996)". In: *Pure and applied chemistry* 68.12 (1996), pp. 2193–2222.
[71] J. E. McMurry and C. Learning. *Organic Chemistry, Hybrid Edition*. Brooks/Cole, 2012.
[72] F. A. Carey and R. J. Sundberg. *Advanced Organic Chemistry: Part A: Structure and Mechanisms*. Springer Science & Business Media, 2007.
[73] E. V. Anslyn and D. A. Dougherty. *Modern Physical Organic Chemistry*. University science books, 2006.
[74] D. H. R. Barton. "The principles of Conformational Analysis". In: *Science* 169.3945 (1970), pp. 539–544.
[75] S. Liu. "Origin and Nature of Bond Rotation Barriers: A Unified View". In: *The Journal of Physical Chemistry A* 117.5 (2013), pp. 962–965.
[76] R. Kuhn. *Molekulare Asymmetrie*. 1933.
[77] 'Keministi'. "Butane Conformations and Relative Energies". In: *Wikimedia Commons* (2018).
[78] J. Gal. "Molecular Chirality: Language, History, and Significance". In: *Differentiation of enantiomers I* (2013), pp. 1–20.
[79] J. E. Hein and D. G. Blackmond. "On the Origin of Single Chirality of Amino Acids and Sugars in Biogenesis". In: *Accounts of chemical research* 45.12 (2012), pp. 2045–2054.

[80] D. E. Koshland Jr. “The Key–lock Theory and the Induced Fit Theory”. In: *Angewandte Chemie International Edition in English* 33.23-24 (1995), pp. 2375–2378.
[81] R. Bentley. “The Nose as a Stereochemist. Enantiomers and Odor”. In: *Chemical reviews* 106.9 (2006), pp. 4099–4112.
[82] T. J. Leitereg et al. “Chemical and Sensory Data Supporting the Difference between the Odors of the Enantiomeric Carvones”. In: *Journal of Agricultural and Food Chemistry* 19.4 (1971), pp. 785–787.
[83] T. J. Leitereg et al. “Evidence for the Difference between the Odours of the Optical Isomers (+)-and (-)-Carvone”. In: *Nature* 230.5294 (1971), pp. 455–456.
[84] Karlhahn’ ‘Walkerma. “Carvone”. In: *Wikimedia Commons* (2005).
[85] ‘Calvero with ChemDraw’. “Chemical Structure of α-tocopherol, aka Vitamin E.” In: *Wikimedia Commons* (2007).
[86] S. K. Jensen and C. Lauridsen. “α-Tocopherol Stereoisomers”. In: *Vitamins & Hormones* 76 (2007), pp. 281–308.
[87] M. G Traber and J. Atkinson. “Vitamin E, Antioxidant and Nothing More”. In: *Free radical biology and medicine* 43.1 (2007), pp. 4–15.
[88] L. J. Machlin. *Vitamin E. A Comprehensive Treatise.* 1980.
[89] R. Brigelius-Flohé and M. G. Traber. “Vitamin E: Function and Metabolism”. In: *The FASEB journal* 13.10 (1999), pp. 1145–1155.
[90] W. H. De Camp. “The FDA Perspective on the Development of Stereoisomers”. In: *Chirality* 1.1 (1989), pp. 2–6.
[91] A. Calcaterra and I. D’Acquarica. “The Market of Chiral Drugs: Chiral Switches versus De Novo Enantiomerically Pure Compounds”. In: *Journal of pharmaceutical and biomedical analysis* 147 (2018), pp. 323–340.
[92] I. Agranat, S. R. Wainschtein, and E. Z Zusman. “The Predicated Demise of Racemic New Molecular Entities is an Exaggeration”. In: *Nature Reviews Drug Discovery* 11.12 (2012), pp. 972–973.
[93] I. W. Wainer. “Three-Dimensional View of Pharmacology”. In: *American Journal of Hospital Pharmacy* 49.9_Suppl (1992), S4–S8.
[94] L. H. Easson and E. Stedman. “Studies on the Relationship between Chemical Constitution and Physiological Action: Molecular Dissymmetry and Physiological Activity”. In: *Biochemical Journal* 27.4 (1933), p. 1257.
[95] I. K. Reddy and R. Mehvar. *Chirality in Drug Design and Development.* CRC Press, 2004.
[96] W. H Brooks, W. C Guida, and K. G Daniel. “The significance of chirality in drug design and development”. In: *Current Topics in Medicinal Chemistry* 11.7 (2011), pp. 760–770.
[97] G.-Q. Lin, Q.-D. You, and J.-F. Cheng. *Chiral drugs: chemistry and biological action.* John Wiley & Sons, 2011.
[98] F. Jamali, R. Mehvar, and F. M. Pasutto. “Enantioselective Aspects of Drug Action and Disposition: Therapeutic Pitfalls”. In: *Journal of pharmaceutical sciences* 78.9 (1989), pp. 695–715.
[99] K. M. Williams. “Molecular Asymmetry and its Pharmacological Consequences”. In: *Advances in Pharmacology* 22 (1991), pp. 57–135.

[100] R. Crossley. “The Relevance of Chirality to the Study of Biological Activity”. In: *Tetrahedron* 48.38 (1992), pp. 8155–8178.
[101] M. Gross. “Significance of Drug Stereochemistry in Modern Pharmaceutical Research and Development”. In: *Annual reports in medicinal chemistry*. Vol. 25. Elsevier, 1990, pp. 323–331.
[102] E. J. Ariëns, E. W. Wuis, and E. J. Veringa. “Stereoselectivity of Bioactive Xenobiotics: a Pre-Pasteur Attitude in Medicinal Chemistry, Pharmacokinetics and Clinical Pharmacology”. In: *Biochemical Pharmacology* 37.1 (1988), pp. 9–18.
[103] C. M. Clemente et al. “An in Silico Analysis of Ibuprofen Enantiomers in High Concentrations of Sodium Chloride with SARS-CoV-2 Main Protease”. In: *Journal of Biomolecular Structure and Dynamics* 40.12 (2022), pp. 5653–5664.
[104] ‘Vaccinationist’. “Thalidomide Enantiomers”. In: *Wikimedia Commons* (2016).
[105] K. M. Williams. “Metabolic Chiral Inversion”. In: *“Problems and Wonders of Chiral Molecules”*. Akademiai Kiado Budapest, 1990, pp. 181–204.
[106] A. K. Scott. “Stereoisomers and Drug Toxicity: the Value of Single Stereoisomer Therapy”. In: *Drug safety* 8.2 (1993), pp. 149–159.
[107] J. R. Powell, I. W. Waimer, and D. E. Drayer. “Drug Stereochemistry Analytical Methods and Pharmacology”. In: *New York: Marcel Dekker, Inc* (1988), pp. 245–70.
[108] J. R. Powell. “The Efficacy and Toxicity of Drug Stereoisomerism”. In: *Drug stereochemistry* (1988), pp. 245–270.
[109] M. R. Wright and F. Jamali. “Methods for the Analysis of Enantiomers of Racemic Drugs Application to Pharmacological and Pharmacokinetic Studies”. In: *Journal of pharmacological and toxicological methods* 29.1 (1993), pp. 1–9.
[110] P. F. White et al. “Pharmacology of Ketamine Isomers in Surgical Patients”. In: *The Journal of the American Society of Anesthesiologists*. Vol. 52. 3. The American Society of Anesthesiologists. 1980, pp. 231–239.
[111] R. A. Kohrs and M. E. Durieux. “Ketamine: Teaching an Old Drug New Tricks”. In: *Anesthesia & Analgesia* 87.5 (1998), pp. 1186–1193.
[112] G. W. Mellin and M. Katzenstein. “The Saga of Thalidomide: Neuropathy to Embryopathy, with Case Reports of Congenital Anomalies”. In: *New England Journal of Medicine* 267.23 (1962), pp. 1184–1193.
[113] T. Eriksson et al. “Stereospecific Determination, Chiral Inversion in vitro and Pharmacokinetics in Humans of the Enantiomers of Thalidomide”. In: *Chirality* 7.1 (1995), pp. 44–52.
[114] T. Eriksson, S. Björkman, and P. Höglund. “Clinical Pharmacology of Thalidomide”. In: *European journal of clinical pharmacology* 57 (2001), pp. 365–376.
[115] M. Eichelbaum and A. S. Gross. “Stereochemical Aspects of Drug Action and Disposition”. In: *Advances in drug research*. Vol. 28. Elsevier, 1996, pp. 1–64.
[116] E. E. Castilla et al. “Thalidomide, a Current Teratogen in South America”. In: *Teratology* 54.6 (1996), pp. 273–277.
[117] W. A. Silverman. “The Schizophrenic Career of a “Monster Drug””. In: *Pediatrics* 110.2 (2002), pp. 404–406.

[118] D. R. Bielenberg and P. A. D'Amore. "Judah Folkman's Contribution to the Inhibition of Angiogenesis". In: *Lymphatic research and biology* 6.3-4 (2008), pp. 203–207.
[119] Cochrane Haematology Group et al. "Multiple drug Combinations of Bortezomib, Lenalidomide, and Thalidomide for First-Line Treatment in Adults with Transplant-Ineligible Multiple Myeloma: a Network Meta-Analysis". In: *Cochrane Database of Systematic Reviews* 2020.8 (1996).
[120] T. S. Metzger et al. "The Electron Spin as a Chiral Reagent". In: *Angewandte Chemie* 132.4 (2020), pp. 1670–1675.
[121] K. Robards and D. Ryan. *Principles and Practice of Modern Chromatographic Methods*. Academic Press, 2021.
[122] K. W. Busch and M. A. Busch. *Chiral Analysis*. Elsevier, 2011.
[123] P. Schreier, A. Bernreuther, and M. Huffer. *Analysis of Chiral Organic Molecules: Methodology and Applications*. Walter de Gruyter, 1995.
[124] A. Gergely. "A Review of the Application of Chiroptical Methods to Analytical Chemistry". In: *Journal of pharmaceutical and biomedical analysis* 7.5 (1989), pp. 523–541.
[125] A. Einstein. *Über einen die Erzeugung und Verwandlung des Lichtes Betreffenden Heuristischen Gesichtspunkt*. 1905.
[126] M. Planck. *Über das Gesetz der Energieverteilung im Normalspektrum*. Springer, 1978.
[127] T. Young. "VII. Outlines of Experiments and Inquiries Respecting Sound and Light. By Thomas Young, MDFRS In a Letter to Edward Whitaker Gray, MD Sec. R. S". In: *Philosophical Transactions of the Royal Society of London* 90 (1800), pp. 106–150.
[128] J. C. Maxwell. "VIII. A Dynamical Theory of the Electromagnetic Field". In: *Philosophical transactions of the Royal Society of London* 155 (1865), pp. 459–512.
[129] J. M. Fink et al. "Quantum-to-Classical Transition in Cavity Quantum Electrodynamics". In: *Physical review letters* 105.16 (2010), p. 163601.
[130] R. Loetzsch et al. "Testing Quantum Electrodynamics in Extreme Fields using Helium-like Uranium". In: *Nature* 625.7996 (2024), pp. 673–678.
[131] L. Morel et al. "Determination of the Fine-Structure Constant with an Accuracy of 81 Parts per Trillion". In: *Nature* 588.7836 (2020), pp. 61–65.
[132] T. Aoyama et al. "Tenth-Order QED Contribution to the Electron g-2 and an Improved Value of the Fine Structure Constant". In: *Physical Review Letters* 109.11 (2012), p. 111807.
[133] D. Hanneke, S. Fogwell, and G. Gabrielse. "New Measurement of the Electron Magnetic Moment and the Fine Structure Constant". In: *Physical review letters* 100.12 (2008), p. 120801.
[134] J. D. Jackson. *Classical Electrodynamics*. John Wiley & Sons, 1998.
[135] R. Gutzler et al. "Light–matter Interaction at Atomic Scales". In: *Nature Reviews Physics* 3.6 (2021), pp. 441–453.
[136] J. Weiner and P.-T. Ho. *Light-matter Interaction: Fundamentals and Applications*. Vol. 1. John Wiley & Sons, 2008.
[137] O. Heaviside. "IV. The General Solution of Maxwell's Electromagnetic Equations in a Homogeneous Isotropic Medium, Especially in Regard to the Deriva-

tion of Special Solutions, and the Formulæ for Plane Waves". In: *The London, Edinburgh, and Dublin Philosophical Magazine and Journal of Science* 27.164 (1889), pp. 29–50.
[138] M. Faraday. "V. Experimental Researches in Electricity". In: *Philosophical transactions of the Royal Society of London* 122 (1832), pp. 125–162.
[139] F. L. Pedrotti, L. M. Pedrotti, and L. S. Pedrotti. *Introduction to Optics*. Cambridge university press, 2017.
[140] J. Peatross and M. Ware. "Physics of Light and Optics". In: (2015).
[141] S. A. Korff and G. Breit. "Optical dispersion". In: *Reviews of Modern Physics* 4.3 (1932), p. 471.
[142] R De L. Kronig. "On the Theory of Dispersion of X-rays". In: *Journal of the Optical Society of America* 12.6 (1926), pp. 547–557.
[143] H. A. Kramers. *La Diffusion de la Lumiere par les Atomes*. 1928.
[144] J. S. Toll. "Causality and the Dispersion Relation: Logical Foundations". In: *Physical review* 104.6 (1956), p. 1760.
[145] R. W Boyd. *Nonlinear Optics*. Academic press, 2020.
[146] W. G. C. G. Kaiser and C. G. B. Garrett. "Two-photon Excitation in Ca F 2: Eu 2+". In: *Physical review letters* 7.6 (1961), p. 229.
[147] N Bloembergen. *Nonlinear Optics, 1965*.
[148] J. R. Taylor. *Optical Solitons: Theory and Experiment*. 10. Cambridge University Press, 1992.
[149] K. Konno and H. Suzuki. "Self-focussing of Laser Beam in Nonlinear Media". In: *Physica Scripta* 20.3-4 (1979), p. 382.
[150] P. A. Franken et al. "Generation of Optical Harmonics". In: *Physical review letters* 7.4 (1961), p. 118.
[151] P. A. Franken and J. F. Ward. "Optical Harmonics and Nonlinear Phenomena". In: *Reviews of Modern Physics* 35.1 (1963), p. 23.
[152] J. B. Bertrand et al. "Ultrahigh-order Wave Mixing in Noncollinear High Harmonic Generation". In: *Physical review letters* 106.2 (2011), p. 023001.
[153] D. Patterson and J. M. Doyle. "Sensitive Chiral Analysis via Microwave Three-Wave Mixing". In: *Physical review letters* 111.2 (2013), p. 023008.
[154] R. W. Boyd, A. L. Gaeta, and E. Giese. "Nonlinear Optics". In: *Springer Handbook of Atomic, Molecular, and Optical Physics*. Springer, 2008, pp. 1097–1110.
[155] J.-M. Liu. *Nonlinear Photonics*. Cambridge University Press, 2022.
[156] J. D. T. Vogwell et al. "Ultrafast Control over Chiral Sum-frequency Generation". In: *Science Advances* 9.33 (2023), eadj1429.
[157] M. A. Belkin et al. "Sum-frequency Generation in Chiral Liquids near Electronic Resonance". In: *Physical review letters* 87.11 (2001), p. 113001.
[158] H. Rangwalla and A. Dhinojwala. "Probing Hidden Polymeric Interfaces Usingir–Visible Sum-Frequency Generation Spectroscopy". In: *The Journal of Adhesion* 80.1-2 (2004), pp. 37–59.
[159] P. Guyot-Sionnest, W. Chen, and Y. R. Shen. "General Considerations on Optical Second-Harmonic Generation from Surfaces and Interfaces". In: *Physical Review B* 33.12 (1986), p. 8254.
[160] T. Brabec and H. Kapteyn. *Strong Field Laser Physics*. Vol. 1. Springer, 2008.

[161] P. Agostini and L. F. DiMauro. "Atoms in High Intensity Mid-Infrared Pulses". In: *Contemporary Physics* 49.3 (2008), pp. 179–197.
[162] H. M. Milchberg et al. "The Extreme Nonlinear Optics of Gases and Femtosecond Optical Filamentation". In: *Physics of Plasmas* 21.10 (2014).
[163] P. B. Corkum. "Plasma Perspective on Strong Field Multiphoton Ionization". In: *Physical review letters* 71.13 (1993), p. 1994.
[164] M. Lewenstein et al. "Theory of High-harmonic Generation by Low-frequency Laser Fields". In: *Physical Review A* 49.3 (1994), p. 2117.
[165] O. Smirnova, Y. Mairesse, and S. Patchkovskii. "Opportunities for Chiral Discrimination Using High Harmonic Generation in Tailored Laser Fields". In: *Journal of Physics B: Atomic, Molecular and Optical Physics* 48.23 (2015), p. 234005.
[166] O. Neufeld and O. Cohen. "Optical Chirality in Nonlinear Optics: Application to High Harmonic Generation". In: *Physical Review Letters* 120.13 (2018), p. 133206.
[167] G. Vampa et al. "Theoretical Analysis of High-harmonic Generation in Solids". In: *Physical review letters* 113.7 (2014), p. 073901.
[168] S. Ghimire et al. "Strong-field and Attosecond Physics in Solids". In: *Journal of Physics B: Atomic, Molecular and Optical Physics* 47.20 (2014), p. 204030.
[169] Ó. Zurrón-Cifuentes et al. "Optical Anisotropy of Non-perturbative High-order Harmonic Generation in Gapless Graphene". In: *Optics express* 27.5 (2019), pp. 7776–7786.
[170] T. T. Luu and H. J. Wörner. "Measurement of the Berry Curvature of Solids using High-harmonic Spectroscopy". In: *Nature communications* 9.1 (2018), p. 916.
[171] N. Yoshikawa, T. Tamaya, and K. Tanaka. "High-harmonic Generation in Graphene Enhanced by Elliptically Polarized Light Excitation". In: *Science* 356.6339 (2017), pp. 736–738.
[172] J. R. Sutherland et al. "High Harmonic Generation in a Semi-Infinite Gas Cell". In: *Optics Express* 12.19 (2004), pp. 4430–4436.
[173] XF Li et al. "Multiple-harmonic Generation in Rare Gases at High Laser Intensity". In: *Physical Review A* 39.11 (1989), p. 5751.
[174] K. L. Ishikawa. "High-harmonic generation". In: *Advances in Solid State Lasers Development and Applications* (2010), pp. 439–465.
[175] K. J. Schafer et al. "Above Threshold Ionization Beyond the High Harmonic Cutoff". In: *Physical review letters* 70.11 (1993), p. 1599.
[176] K. L. Midorikawa. "Ultrafast Dynamic Imaging". In: *Nature Photon* 5 (2011), pp. 640–641.
[177] O. Smirnova et al. "High Harmonic Interferometry of Multi-Electron Dynamics in Molecules". In: *Nature* 460.7258 (2009), pp. 972–977.
[178] O. Smirnova and M. Ivanov. "Multielectron High Harmonic Generation: Simple Man on a Complex Plane". In: *arXiv preprint arXiv:1304.2413* (2013).
[179] P. A. Moreno et al. "Influence of Barrier Suppression in High-order Harmonic Generation". In: *Physical Review A* 51.6 (1995), p. 4746.
[180] X. M. Tong and C. D. Lin. "Empirical Formula for Static Field Ionization Rates of Atoms and Molecules by Lasers in the Barrier-Suppression

Regime". In: *Journal of Physics B: Atomic, Molecular and Optical Physics* 38.15 (2005), p. 2593.
[181] S. Augst et al. "Laser Ionization of Noble Gases by Coulomb-barrier Suppression". In: *JOSA B* 8.4 (1991), pp. 858–867.
[182] A Becker et al. "Total Ionization Rates and Ion Yields of Atoms at Nonperturbative Laser Intensities". In: *Physical Review A* 64.2 (2001), p. 023408.
[183] S. L. Chin. "From multiphoton to tunnel ionization". In: *Advances in Multi-Photon Processes and Spectroscopy*. World Scientific, 2004, pp. 249–271.
[184] S. L. Chin. *Multiphoton Ionization of Atoms*. Elsevier, 2012.
[185] G. Malka and J. L. Miquel. "Experimental Confirmation of Ponderomotive-force Electrons Produced by an Ultrarelativistic Laser Pulse on a Solid Target". In: *Physical review letters* 77.1 (1996), p. 75.
[186] S. V. Popruzhenko. "Keldysh Theory of Strong Field Ionization: History, Applications, Difficulties and Perspectives". In: *Journal of Physics B: Atomic, Molecular and Optical Physics* 47.20 (2014), p. 204001.
[187] A. M. Zheltikov. "Keldysh Parameter, Photoionization Adiabaticity, and the Tunneling Time". In: *Physical Review A* 94.4 (2016), p. 043412.
[188] A. M. Zheltikov. "Keldysh Photoionization Theory: Through the Barriers". In: *Physics-Uspekhi* 60.11 (2017), p. 1087.
[189] D. F. J. Arago. "Memoir on a remarkable modification experienced by light rays in their passage through certain diaphanous bodies, and on some other new optical phenomena". In: *Mémoires de la Classe des Sciences Mathématiques et Physiques de l'Institut Impérial de France. 1st part. Paris* 93 (1811), p. 134.
[190] J. F. W. Herschel. "IV. On the Action of Crystallized Bodies on Homogeneous Light, and on the Causes of the Deviation from Newton's Scale in the Tints which Many of them Develope on Exposure to a Polarised Ray". In: *Philosophical Transactions of the Royal Society of London* 110 (1820), pp. 45–100.
[191] JB Biot. "Phenomenon of Successive Polarization, Observed in Homogeneous Fluids". In: *Bulletin des Sciences* (1815), pp. 190–192.
[192] T. E. Beesley and R. P. W. Scott. *Chiral Chromatography*. John Wiley & Sons, 1999.
[193] R. M. Esquerra et al. "Fast Time-resolved Magnetic Optical Rotatory Dispersion Measurements. 1. Mueller Analysis of Optical and Photoselection-induced Artifacts". In: *The Journal of Physical Chemistry A* 102.45 (1998), pp. 8740–8748.
[194] A. Fresnel. "Extrait du Second Mémoire sur la Double Réfraction". In: *Bulletin de la Société philomatique. Also in OCF* 2 (1822), pp. 465–478.
[195] S. S. Andrews and J. Tretton. "Physical Principles of Circular Dichroism". In: *Journal of Chemical Education* 97.12 (2020), pp. 4370–4376.
[196] A. F. Ordonez and O. Smirnova. "Generalized Perspective on Chiral Measurements without Magnetic Interactions". In: *Physical Review A* 98.6 (2018), p. 063428.
[197] N. Berova, K. Nakanishi, and R. W Woody. *Circular Dichroism: Principles and Applications*. John Wiley & Sons, 2000.

[198] A. L. Thompson and D. J. Watkin. "X-ray Crystallography and Chirality: Understanding the Limitations". In: *Tetrahedron: Asymmetry* 20.6-8 (2009), pp. 712–717.
[199] 'Kaidor'. "Polarimiter (Optical Rotation)". In: *Wikimedia Commons* (2013).
[200] W. Moffitt. "Optical Rotatory Dispersion of Helical Polymers". In: *The Journal of Chemical Physics* 25.3 (1956), pp. 467–478.
[201] G. Snatzke. "Circular Dichroism and Optical Rotatory Dispersion—Principles and Application to the Investigation of the Stereochemistry of Natural Products". In: *Angewandte Chemie International Edition in English* 7.1 (1968), pp. 14–25.
[202] J. A. Schellman. "Circular Dichroism and Optical Rotation". In: *Chemical Reviews* 75.3 (1975), pp. 323–331.
[203] J. D. Byers et al. "Second-harmonic Generation Circular-Dichroism Spectroscopy from Chiral Monolayers". In: *Physical Review B* 49.20 (1994), p. 14643.
[204] J. T. Collins et al. "Second-harmonic Generation Optical Rotation Solely Attributable to Chirality in Plasmonic Metasurfaces". In: *ACS nano* 12.6 (2018), pp. 5445–5451.
[205] T. Petralli-Mallow et al. "Circular Dichroism Spectroscopy at Interfaces: a Surface Second Harmonic Generation Study". In: *The Journal of Physical Chemistry* 97.7 (1993), pp. 1383–1388.
[206] G. J. Simpson. "Structural Origins of Circular Dichroism in Surface Second Harmonic Generation". In: *The Journal of chemical physics* 117.7 (2002), pp. 3398–3410.
[207] L. A. Warning et al. "Nanophotonic Approaches for Chirality Sensing". In: *ACS nano* 15.10 (2021), pp. 15538–15566.
[208] Y. Tang and A. E. Cohen. "Enhanced Enantioselectivity in Excitation of Chiral Molecules by Superchiral Light". In: *Science* 332.6027 (2011), pp. 333–336.
[209] A. Vázquez-Guardado and D. Chanda. "Superchiral Light Generation on Degenerate Achiral Surfaces". In: *Physical Review Letters* 120.13 (2018), p. 137601.
[210] A. Biswas et al. "Tunable Plasmonic Superchiral Light for Ultrasensitive Detection of Chiral Molecules". In: *Science advances* 10.8 (2024), eadk2560.
[211] N. L. Manakov, S. I. Marmo, and A. V. Meremianin. "A New Technique in the Theory of Angular Distributions in Atomic Processes: the Angular Distribution of Photoelectrons in Single and Double Photoionization". In: *Journal of Physics B: Atomic, Molecular and Optical Physics* 29.13 (1996), p. 2711.
[212] M. Y. Agre. "Theory of Spin Polarization Phenomena in Atomic and Molecular Photoeffects". In: *Optics and Spectroscopy* 101 (2006), pp. 356–370.
[213] N Böwering et al. "Asymmetry in Photoelectron Emission from Chiral Molecules Induced by Circularly Polarized Light". In: *Physical review letters* 86.7 (2001), p. 1187.
[214] I. Powis. "Photoelectron Circular Dichroism of the Randomly Oriented Chiral Molecules Glyceraldehyde and Lactic Acid". In: *The Journal of Chemical Physics* 112.1 (2000), pp. 301–310.

[215] S. Beaulieu et al. “Probing Ultrafast Dynamics of Chiral Molecules Using Time-resolved Photoelectron Circular Dichroism”. In: *Faraday discussions* 194 (2016), pp. 325–348.
[216] B. Ritchie. “Theory of the Angular Distribution of Photoelectrons Ejected from Optically Active Molecules and Molecular Negative Ions”. In: *Physical Review A* 13.4 (1976), p. 1411.
[217] N. A. Cherepkov. “Circular Dichroism of Molecules in the Continuous Absorption Region”. In: *Chemical Physics Letters* 87.4 (1982), pp. 344–348.
[218] R. E. Goetz et al. “Theoretical Description of Circular Dichroism in Photoelectron Angular Distributions of Randomly Oriented Chiral Molecules after Multi-Photon Photoionization”. In: *The Journal of chemical physics* 146.2 (2017), p. 024306.
[219] M. Khokhlova et al. “Enantiosensitive Steering of Free-Induction Decay”. In: *Science Advances* 8.24 (2022), eabq1962.
[220] A. F. Ordonez and O. Smirnova. “Propensity Rules in Photoelectron Circular Dichroism in Chiral Molecules. I. Chiral Hydrogen”. In: *Physical Review A* 99.4 (2019), p. 043416.
[221] A. Owens et al. “Climbing the Rotational Ladder to Chirality”. In: *Physical review letters* 121.19 (2018), p. 193201.
[222] Y-Y. Chen et al. “Enantio-discrimination via Light Deflection Effect”. In: *The Journal of Chemical Physics* 152.20 (2020).
[223] D. Ayuso et al. “Enantio-sensitive Unidirectional Light Bending”. In: *Nature Communications* 12.1 (2021), p. 3951.
[224] T. Brixner et al. “Quantum Control by Ultrafast Polarization Shaping”. In: *Physical review letters* 92.20 (2004), p. 208301.
[225] M. Krüger, M. Schenk, and P. Hommelhoff. “Attosecond Control of Electrons Emitted from a Nanoscale Metal Tip”. In: *Nature* 475.7354 (2011), pp. 78–81.
[226] D. Maluenda et al. “Experimental Estimation of the Longitudinal Component of a Highly Focused Electromagnetic Field”. In: *Scientific Reports* 11.1 (2021), p. 17992.
[227] T. M. Jeong et al. “Analysis on the Longitudinal Field Strength formed by Tightly-focused Radially-polarized Femtosecond Petawatt Laser Pulse”. In: *Optics Express* 26.25 (2018), pp. 33091–33107.
[228] J. E. Vázquez-Lozano and A. Martínez. “Toward Chiral Sensing and Spectroscopy Enabled by All-Dielectric Integrated Photonic Waveguides”. In: *Laser & Photonics Reviews* 14.9 (2020), p. 1900422.
[229] O. Pedatzur et al. “Attosecond Tunnelling Interferometry”. In: *Nature Physics* 11.10 (2015), pp. 815–819.
[230] D. Shafir et al. “Resolving the Time when an Electron Exits a Tunnelling Barrier”. In: *Nature* 485.7398 (2012), pp. 343–346.
[231] S. Beaulieu et al. “Photoexcitation Circular Dichroism in Chiral Molecules”. In: *Nature Physics* 14.5 (2018), pp. 484–489.
[232] V. A. Shubert et al. “Rotational Spectroscopy and Three-Wave Mixing of 4-Carvomenthenol: A Technical Guide to Measuring Chirality in the Microwave Regime”. In: *The Journal of chemical physics* 142.21 (2015), p. 214201.

[233] K. K. Lehmann and J. Lane. *Frontiers and Advances in Molecular Spectroscopy*. Elsevier, 2018.
[234] K. K. Lehmann. "Influence of Spatial Degeneracy on Rotational Spectroscopy: Three-wave Mixing and Enantiomeric State Separation of Chiral Molecules". In: *The Journal of Chemical Physics* 149.9 (2018), p. 094201.
[235] D. Patterson, M. Schnell, and J. M. Doyle. "Enantiomer-Specific Detection of Chiral Molecules via Microwave Spectroscopy". In: *Nature* 497.7450 (2013), pp. 475–477.
[236] H. W. Kroto. *Molecular Rotation Spectra*. Dover, 1992.
[237] S. Eibenberger, J. Doyle, and D. Patterson. "Enantiomer-Specific State Transfer of Chiral Molecules". In: *Physical review letters* 118.12 (2017), p. 123002.
[238] J. H. Lee et al. "Quantitative Study of Enantiomer-specific State Transfer". In: *Physical Review Letters* 128.17 (2022), p. 173001.
[239] D. A. Harmin. "Theory of the Stark Effect". In: *Physical review A* 26.5 (1982), p. 2656.
[240] R. Cireasa et al. "Probing Molecular Chirality on a Sub-femtosecond Timescale". In: *Nature Physics* 11.8 (2015), pp. 654–658.
[241] D. Ayuso et al. "Strong-field Control and Enhancement of Chiral Response in Bi-elliptical High-order Harmonic Generation: an Analytical Model". In: *Journal of Physics B: Atomic, Molecular and Optical Physics* 51.12 (2018), p. 124002.
[242] D. Ayuso et al. "Ultrafast Optical Rotation in Chiral Molecules with Ultrashort and Tightly Focused Beams". In: *Optica* 8.10 (2021), pp. 1243–1246.
[243] M. Lein. "Attosecond Probing of Vibrational Dynamics with High-harmonic Generation". In: *Physical review letters* 94.5 (2005), p. 053004.
[244] S. Baker et al. "Probing Proton Dynamics in Molecules on an Attosecond Time Scale". In: *Science* 312.5772 (2006), pp. 424–427.
[245] R. Weissenbilder et al. "How to Optimize High-Order Harmonic Generation in Gases". In: *Nature Reviews Physics* 4.11 (2022), pp. 713–722.
[246] B. Siegmann, U. Werner, and H. O. Lutz. "Multiple Ionisation and Fragmentation of Molecules". In: *Australian journal of physics* 52.3 (1999), pp. 545–554.
[247] F. Légaré et al. "Laser Coulomb-explosion Imaging of Small Molecules". In: *Physical Review A—Atomic, Molecular, and Optical Physics* 71.1 (2005), p. 013415.
[248] J. L. Miller. "Coulomb-explosion Imaging Tackles an 11-atom Molecule". In: *Physics Today* 75.5 (2022), pp. 12–14.
[249] R. Boll et al. "X-ray Multiphoton-induced Coulomb Explosion Images of Complex Single Molecules". In: *Nature Physics* 18.4 (2022), pp. 423–428.
[250] C. Saribal et al. "Detecting Handedness of Spatially Oriented Molecules by Coulomb Explosion Imaging". In: *The Journal of Chemical Physics* 154.7 (2021).
[251] J. Gagnon et al. "Coincidence Imaging of Polyatomic Molecules via Laser-induced Coulomb Explosion". In: *Journal of Physics B: Atomic, Molecular and Optical Physics* 41.21 (2008), p. 215104.

[252] M. Burt et al. “Communication: Gas-phase Structural Isomer Identification by Coulomb Explosion of Aligned Molecules”. In: *The Journal of Chemical Physics* 148.9 (2018).
[253] M. Pitzer et al. “Direct Determination of Absolute Molecular Stereochemistry in Gas Phase by Coulomb Explosion Imaging”. In: *Science* 341.6150 (2013), pp. 1096–1100.
[254] P. Herwig et al. “Metastable States of D 2- Observed by Foil-induced Coulomb Explosion Imaging”. In: *Physical Review A—Atomic, Molecular, and Optical Physics* 87.6 (2013), p. 062513.
[255] L. Christensen et al. “Using Laser-induced Coulomb Explosion of Aligned Chiral Molecules to Determine their Absolute Configuration”. In: *Physical Review A* 92.3 (2015), p. 033411.
[256] M. Pitzer. “How to Determine the Handedness of Single Molecules Using Coulomb Explosion Imaging”. In: *Journal of Physics B: Atomic, Molecular and Optical Physics* 50.15 (2017), p. 153001.
[257] P. Herwig et al. “Absolute Configuration Assignment of a Chiral Molecule in the Gas Phase Using Foil-induced Coulomb Explosion Imaging”. In: *Physical Review A* 90.5 (2014), p. 052503.
[258] L. D. Landau and E. M. Lífshíts. *Electrodynamics of Continuous Media*. Vol. 2. Pergamon Press Oxford, 1884.
[259] A. D Bandrauk and H. Lu. “Exponential Propagators (Integrators) for the Time-dependent Schrödinger Equation”. In: *Journal of Theoretical and Computational Chemistry* 12.06 (2013), p. 1340001.
[260] M. J. Valtonen and H. Karttunen. *The Three-body Problem*. Cambridge University Press, 2006.
[261] M. A. L. Marques et al. “Octopus: a First-principles Tool for Excited Electron–ion Dynamics”. In: *Computer Physics Communications* 151.1 (2003), pp. 60–78.
[262] N. Tancogne-Dejean et al. “Octopus, a Computational Framework for Exploring Light-Driven Phenomena and Quantum Dynamics in Extended and Finite Systems”. In: *The Journal of chemical physics* 152.12 (2020), p. 124119.
[263] C. J. Joachain, N. J Kylstra, and R. M. Potvliege. *Atoms in Intense Laser Fields*. Cambridge University Press, 2012.
[264] C. Leforestier et al. “A Comparison of Different Propagation Schemes for the Time Dependent Schrödinger Equation”. In: *Journal of Computational Physics* 94.1 (1991), pp. 59–80.
[265] P. W. Langhoff, S. T. Epstein, and M. Karplus. “Aspects of Time-dependent Perturbation Theory”. In: *Reviews of Modern Physics* 44.3 (1972), p. 602.
[266] A. R. Leach. *Molecular Modelling: Principles and Applications*. Pearson education, 2001.
[267] M. Born. “Born-Oppenheimer Approximation”. In: *Ann. Phys* 84 (1927), pp. 457–484.
[268] M. Born and R. Oppenheimer. “On the Quantum Theory of Molecules”. In: *Quantum Chemistry: Classic Scientific Papers*. World Scientific, 2000, pp. 1–24.

[269] A. I. Kuleff, J. Breidbach, and L. S. Cederbaum. "Multielectron Wave-packet Propagation: General Theory and Application". In: *The Journal of chemical physics* 123.4 (2005).

[270] A. I. Kuleff and L. S. Cederbaum. "Charge Migration in Different Conformers of Glycine: The Role of Nuclear Geometry". In: *Chemical Physics* 338.2-3 (2007), pp. 320–328.

[271] F. Remacle and R. D. Levine. "An Electronic Time Scale in Chemistry". In: *Proceedings of the National Academy of Sciences* 103.18 (2006), pp. 6793–6798.

[272] B. Mignolet, R. D. Levine, and F. Remacle. "Charge Migration in the Bifunctional PENNA Cation Induced and Probed by Ultrafast Ionization: a Dynamical Study". In: *Journal of Physics B: Atomic, Molecular and Optical Physics* 47.12 (2014), p. 124011.

[273] D. R. Hartree. "The Wave Mechanics of an Atom with a Non-Coulomb Central Field. Part I. Theory and Methods". In: *Mathematical Proceedings of the Cambridge Philosophical Society*. Vol. 24. 1. Cambridge university press. 1928, pp. 89–110.

[274] J. C. Slater. "The Self Consistent Field and the Structure of Atoms". In: *Physical Review* 32.3 (1928), p. 339.

[275] V. A. Fock. "An Approximate Method for Solving the Quantum Many-body Problem". In: *Zeitschrift fur Physik* 61.1-2 (1930), pp. 126–148.

[276] J. A. Gaunt. "A Theory of Hartree's Atomic Fields". In: *Mathematical Proceedings of the Cambridge Philosophical Society*. Vol. 24. 2. Cambridge University Press. 1928, pp. 328–342.

[277] J. C. Slater. "Note on Hartree's Method". In: *Physical Review* 35.2 (1930), p. 210.

[278] W. Pauli. "Über den Zusammenhang des Abschlusses der Elektronengruppen im Atom mit der Komplexstruktur der Spektren". In: *Zeitschrift für Physik* 31.1 (1925), pp. 765–783.

[279] J. C Slater. "The Theory of Complex Spectra". In: *Physical review* 34.10 (1929), p. 1293.

[280] E. U. Condon. "The Theory of Complex Spectra". In: *Physical Review* 36.7 (1930), p. 1121.

[281] P. A. M. Dirac. "Note on Exchange Phenomena in the Thomas Atom". In: *Mathematical Proceedings of the Cambridge Philosophical Society*. Vol. 26. 3. Cambridge University Press. 1930, pp. 376–385.

[282] P. Fulde. *Electron Correlations in Molecules and Solids*. Vol. 100. Springer Science & Business Media, 1995.

[283] R. McWeeny. "An Overview of Molecular Quantum Mechanics". In: *Methods in Computational Molecular Physics* (1992), pp. 3–17.

[284] A. B. Rocha. "Potential Curves for Inner-Shell States of CO Calculated at Multiconfigurational Self-Consistent Field Level". In: *The Journal of Chemical Physics* 134.2 (2011).

[285] J. E. Huheey et al. *Anorganische Chemie*. de Gruyter, 2014.

[286] I. I. Guseinov. "New Complete Orthonormal Sets of Exponential-Type Orbitals and Their Application to Translation of Slater Orbitals". In: *International Journal of Quantum Chemistry* 90.1 (2002), pp. 114–118.

[287] A. D Becke. “A Multicenter Numerical Integration Scheme for Polyatomic Molecules”. In: *The Journal of chemical physics* 88.4 (1988), pp. 2547–2553.
[288] R. McWeeny. “The Electron Correlation Problem”. In: *Methods in Computational Molecular Physics* (1992), pp. 47–56.
[289] P. Hohenberg and W. Kohn. “Inhomogeneous Electron Gas”. In: *Physical review* 136.3B (1964), B864.
[290] W. Kohn and L. J. Sham. “Quantum Density Oscillations in an Inhomogeneous Electron Gas”. In: *Physical Review* 137.6A (1965), A1697.
[291] W. Kohn and L. J. Sham. “Self-consistent Equations Including Exchange and Correlation Effects”. In: *Physical review* 140.4A (1965), A1133.
[292] J. P. Perdew et al. “Prescription for the Design and Selection of Density Functional Approximations: More Constraint Satisfaction with Fewer Fits”. In: *The Journal of chemical physics* 123.6 (2005).
[293] J. P. Perdew and A. Zunger. “Self-Interaction Correction to Density-Functional Approximations for Many-Electron Systems”. In: *Physical Review B* 23.10 (1981), p. 5048.
[294] J. P. Perdew and Y. Wang. “Accurate and Simple Analytic Representation of the Electron-Gas Correlation Energy”. In: *Physical review B* 45.23 (1992), p. 13244.
[295] D. M. Ceperley and B. J. Alder. “Ground State of the Electron Gas by a Stochastic Method”. In: *Physical review letters* 45.7 (1980), p. 566.
[296] O. Gunnarsson and R. O. Jones. “Density Functional Calculations for Atoms, Molecules and Clusters”. In: *Physica Scripta* 21.3-4 (1980), p. 394.
[297] A. D Becke. “Perspective: Fifty Years of Density-functional Theory in Chemical Physics”. In: *The Journal of chemical physics* 140.18 (2014).
[298] R. G. Parr and S. K. Ghosh. “Toward Understanding the Exchange-Correlation Energy and Total-Energy Density Functionals”. In: *Physical Review A* 51.5 (1995), p. 3564.
[299] R. O. Jones and O. Gunnarsson. “The Density Functional Formalism, its Applications and Prospects”. In: *Reviews of Modern Physics* 61.3 (1989), p. 689.
[300] J. P. Perdew. “Generalized Gradient Approximation for the Fermion Kinetic Energy as a Functional of the Density”. In: *Physics Letters A* 165.1 (1992), pp. 79–82.
[301] A. D Becke. “Density-functional Exchange-energy Approximation with Correct Asymptotic Behavior”. In: *Physical review A* 38.6 (1988), p. 3098.
[302] D. C. Langreth and M. J. Mehl. “Beyond the Local-density Approximation in Calculations of Ground-state Electronic Properties”. In: *Physical Review B* 28.4 (1983), p. 1809.
[303] J. P. Perdew et al. “Atoms, Molecules, Solids, and Surfaces: Applications of the Generalized Gradient Approximation for Exchange and Correlation”. In: *Physical review B* 46.11 (1992), p. 6671.
[304] AD Becke. “Correlation Energy of an Inhomogeneous Electron Gas: A Coordinate-space Model”. In: *Journal of Chemical Physics* 88.2 (1988), pp. 1053–1062.
[305] C. Lee, W. Yang, and R. G. Parr. “Development of the Colle-Salvetti Correlation-energy Formula into a Functional of the Electron Density”. In: *Physical review B* 37.2 (1988), p. 785.

[306] J. P. Perdew, M. Ernzerhof, and K. Burke. "Rationale for Mixing Exact Exchange with Density Functional Approximations". In: *The Journal of chemical physics* 105.22 (1996), pp. 9982–9985.
[307] A. Savin, F. Colonna, and R. Pollet. "Adiabatic Connection Approach to Density Functional Theory of Electronic Systems". In: *International journal of quantum chemistry* 93.3 (2003), pp. 166–190.
[308] T. Yanai, D. P. Tew, and N. C. Handy. "A New Hybrid Exchange–Correlation Functional Using the Coulomb-Attenuating Method (CAM-B3LYP)". In: *Chemical physics letters* 393.1-3 (2004), pp. 51–57.
[309] E. Runge and E. K. U. Gross. "Density-Functional Theory for Time-dependent Systems". In: *Physical review letters* 52.12 (1984), p. 997.
[310] P. Ehrenfest. "Bemerkung über den Paramagnetismus von Festen Körpern". In: *Zeitschrift für Physik* 5.1 (1921), pp. 35–38.
[311] R. Van Leeuwen. "Key Concepts in Time-dependent Density-functional Theory". In: *International Journal of Modern Physics B* 15.14 (2001), pp. 1969–2023.
[312] R. Van Leeuwen et al. "Introduction to the Keldysh Formalism". In: *Time-dependent density functional theory*. Springer, 2006, pp. 33–59.
[313] R. Van Leeuwen. "Mapping from Densities to Potentials in Time-dependent Density-functional Theory". In: *Physical review letters* 82.19 (1999), p. 3863.
[314] R. Van Leeuwen and E. J. Baerends. "Exchange-Correlation Potential with Correct Asymptotic Behavior". In: *Physical Review A* 49.4 (1994), p. 2421.
[315] J. I. Fuks et al. "Exploring Non-adiabatic Approximations to the Exchange–Correlation Functional of TD-DFT". In: *Physical Chemistry Chemical Physics* 20.41 (2018), pp. 26145–26160.
[316] L. Lacombe and N. T. Maitra. "Non-adiabatic Approximations in Time-dependent Density Functional Theory: Progress and Prospects". In: *npj Computational Materials* 9.1 (2023), p. 124.
[317] C. A. Ullrich and I. V. Tokatly. "Nonadiabatic Electron Dynamics in Time-dependent Density-functional Theory". In: *Physical Review B—Condensed Matter and Materials Physics* 73.23 (2006), p. 235102.
[318] E. K. U. Gross and W. Kohn. "Time-dependent Density-functional Theory". In: *Advances in quantum chemistry*. Vol. 21. Elsevier, 1990, pp. 255–291.
[319] M. A. L. Marques, M. J. T. Oliveira, and T. Burnus. "Libxc: A Library of Exchange and Correlation Functionals for Density Functional Theory". In: *Computer physics communications* 183.10 (2012), pp. 2272–2281.
[320] G. Dahlquist. "Convergence and Stability in the Numerical Integration of Ordinary Differential Equations". In: *Mathematica Scandinavica* (1956), pp. 33–53.
[321] A. Castro, M. A. L. Marques, and A. Rubio. "Propagators for the Time-dependent Kohn–Sham equations". In: *The Journal of chemical physics* 121.8 (2004), pp. 3425–3433.
[322] A. Castro et al. "Octopus: a Tool for the Application of Time-dependent Density Functional Theory". In: *physica status solidi (b)* 243.11 (2006), pp. 2465–2488.
[323] R. Kosloff. "Propagation Methods for Quantum Molecular Dynamics". In: *Annual review of physical chemistry* 45.1 (1994), pp. 145–178.

[324] N. Kovvali. *Theory and Applications of Gaussian Quadrature Methods*. Springer Nature, 2022.
[325] V. I. Lebedev and D. N. Laikov. "A Quadrature Formula for the Sphere of the 131st Algebraic Order of Accuracy". In: *Doklady Mathematics*. Vol. 59. 3. Pleiades Publishing, Ltd. 1999, pp. 477–481.
[326] B. Stevensson and M. Edén. "Efficient Orientational Averaging by the Extension of Lebedev Grids via Regularized Octahedral Symmetry Expansion". In: *Journal of Magnetic Resonance* 181.1 (2006), pp. 162–176.
[327] P. Fischer et al. "Three-wave Mixing in Chiral Liquids". In: *Physical review letters* 85.20 (2000), p. 4253.
[328] P. Fischer et al. "The chiral Specificity of Sum-frequency Generation in Solutions". In: *Chemical physics letters* 352.5-6 (2002), pp. 463–468.
[329] P. Fischer and F. Hache. "Nonlinear optical spectroscopy of chiral molecules". In: *Chirality: The Pharmacological, Biological, and Chemical Consequences of Molecular Asymmetry* 17.8 (2005), pp. 421–437.
[330] M. A. Belkin et al. "Sum-Frequency Vibrational Spectroscopy on Chiral Liquids: A Novel Technique to Probe Molecular Chirality". In: *Physical review letters* 85.21 (2000), p. 4474.
[331] A. J. Moad and G. J. Simpson. "A Unified Treatment of Selection Rules and Symmetry Relations for Sum-Frequency and Second Harmonic Spectroscopies". In: *The Journal of Physical Chemistry B* 108.11 (2004), pp. 3548–3562.
[332] X. Y. Dow et al. "Unified Theory for Polarization Analysis in Second Harmonic and Sum Frequency Microscopy". In: *Biophysical Journal* 111.7 (2016), pp. 1553–1568.
[333] O. Neufeld et al. "Ultrasensitive Chiral Spectroscopy by Dynamical Symmetry Breaking in High Harmonic Generation". In: *Physical Review X* 9.3 (2019), p. 031002.
[334] D. Ayuso. "New Opportunities for Ultrafast and Highly Enantio-sensitive Imaging of Chiral Nuclear Dynamics Enabled by Synthetic Chiral Light". In: *Physical Chemistry Chemical Physics* 24.17 (2022), pp. 10193–10200.
[335] L. Rego and D. Ayuso. "Structuring the Local Handedness of Synthetic Chiral Light: Global Chirality versus Polarization of Chirality". In: *New Journal of Physics* 25.9 (2023), p. 093005.
[336] E. C. Y. Yan et al. "Biological Macromolecules at Interfaces Probed by Chiral Vibrational Sum Frequency Generation Spectroscopy". In: *Chemical reviews* 114.17 (2014), pp. 8471–8498.
[337] L. Wang, T. Ishiyama, and A. Morita. "Theoretical Investigation of C–H Vibrational Spectroscopy. 2. Unified Assignment Method of IR, Raman, and Sum Frequency Generation Spectra of Ethanol". In: *The Journal of Physical Chemistry A* 121.36 (2017), pp. 6701–6712.
[338] B. Zhang et al. "Amide I SFG Spectral Line Width Probes the Lipid–Peptide and Peptide–Peptide Interactions at Cell Membrane in Situ and in Real Time". In: *Langmuir* 34.25 (2018), pp. 7554–7560.
[339] S. Ye et al. "In Situ Molecular Level Studies on Membrane Related Peptides and Proteins in Real Time Using Sum Frequency Generation Vibrational Spectroscopy". In: *Journal of structural biology* 168.1 (2009), pp. 61–77.

[340] S. Ye et al. “Effect of Dehydration on the Interfacial Water Structure at a Charged Polymer Surface: Negligible χ (3) Contribution to Sum Frequency Generation Signal”. In: *Langmuir* 28.2 (2012), pp. 1374–1380.

[341] L. Fu, G. Ma, and E. C. Y. Yan. “In situ Misfolding of Human Islet Amyloid Polypeptide at Interfaces Probed by Vibrational Sum Frequency Generation”. In: *Journal of the American Chemical Society* 132.15 (2010), pp. 5405–5412.

[342] L. Fu, J. Liu, and E. C. Y. Yan. “Chiral Sum Frequency Generation Spectroscopy for Characterizing Protein Secondary Structures at Interfaces”. In: *Journal of the American Chemical Society* 133.21 (2011), pp. 8094–8097.

[343] L. Fu et al. “Chiral Sum Frequency Generation for In Situ Probing Proton Exchange in Antiparallel β-sheets at Interfaces”. In: *Journal of the American Chemical Society* 135.9 (2013), pp. 3592–3598.

[344] Z. Wang et al. “Broad-Bandwidth Chiral Sum Frequency Generation Spectroscopy for Probing the Kinetics of Proteins at Interfaces”. In: *Langmuir* 31.42 (2015), pp. 11384–11398.

[345] K. T. Nguyen. “An Electronically Enhanced Chiral Sum Frequency Generation Vibrational Spectroscopy Study of Lipid-Bound Cytochrome c”. In: *Chemical Communications* 51.1 (2015), pp. 195–197.

[346] J. Tan et al. “Ultrafast Energy Relaxation Dynamics of Amide I Vibrations Coupled with Protein-Bound Water Molecules”. In: *Nature Communications* 10.1 (2019), p. 1010.

[347] G. Y. Stokes et al. “Making “Sense” of DNA”. In: *Journal of the American Chemical Society* 129.24 (2007), pp. 7492–7493.

[348] S. R. Walter and F. M. Geiger. “DNA on Stage: Showcasing Oligonucleotides at Surfaces and Interfaces with Second Harmonic and Vibrational Sum Frequency Generation”. In: *The Journal of Physical Chemistry Letters* 1.1 (2010), pp. 9–15.

[349] E. A. Perets, K. B. Olesen, and E. C. Y. Yan. “Chiral Sum Frequency Generation Spectroscopy Detects Double-Helix DNA at Interfaces”. In: *Langmuir* 38.18 (2022), pp. 5765–5778.

[350] M. Okuno and T. Ishibashi. “Bulk-or-Interface Assignment of Heterodyne-Detected Chiral Vibrational Sum Frequency Generation Signal by its Polarization Dependence”. In: *The Journal of chemical physics* 149.24 (2018).

[351] P. Fischer, F. W. Wise, and A. C. Albrecht. “Chiral and Achiral Contributions to Sum-frequency Generation from Optically Active Solutions of Binaphthol”. In: *The Journal of Physical Chemistry A* 107.40 (2003), pp. 8232–8238.

[352] X. Andrade et al. “Real-space Grids and the Octopus Code as Tools for the Development of New Simulation Approaches for Electronic Systems”. In: *Physical Chemistry Chemical Physics* 17.47 (2015), pp. 31371–31396.

[353] F. Bloch. “Bemerkung zur Elektronentheorie des Ferromagnetismus und der Elektrischen Leitfähigkeit”. In: *Zeitschrift für Physik* 57.7 (1929), pp. 545–555.

[354] C. Legrand, Eric Suraud, and P. G. Reinhard. “Comparison of Self-interaction-corrections for Metalclusters”. In: *Journal of Physics B: Atomic, Molecular and Optical Physics* 35.4 (2002), p. 1115.

[355] G. Galinis et al. “Micrometer-thickness Liquid Sheet Jets Flowing in Vacuum”. In: *Review of Scientific Instruments* 88.8 (2017).
[356] C. Ferchaud et al. “Interaction of an Intense Few-cycle Infrared Laser Pulse with an Ultrathin Transparent Liquid Sheet”. In: *Optics Express* 30.19 (2022), pp. 34684–34692.
[357] J. C. T. Barnard et al. “Delivery of Stable Ultra-thin Liquid Sheets in Vacuum for Biochemical Spectroscopy”. In: *Frontiers in molecular biosciences* 9 (2022), p. 1044610.
[358] M. Oki. “Reactivity of Conformational Isomers”. In: *Accounts of Chemical Research* 17.5 (1984), pp. 154–159.
[359] C. A. Taatjes et al. “Direct Measurements of Conformer-Dependent Reactivity of the Criegee Intermediate CH3CHOO”. In: *Science* 340.6129 (2013), pp. 177–180.
[360] D. B. Boyd. “Conformational Dependence of the Electronic Energy Levels in Disulfides”. In: *Journal of the American Chemical Society* 94.25 (1972), pp. 8799–8804.
[361] C. Brand, W. L. Meerts, and M. Schmitt. “How and Why do Transition Dipole Moment Orientations Depend on Conformer Structure?” In: *The Journal of Physical Chemistry A* 115.34 (2011), pp. 9612–9619.
[362] S. Turchini. “Conformational Effects in Photoelectron Circular Dichroism”. In: *Journal of Physics: Condensed Matter* 29.50 (2017), p. 503001.
[363] R. Hadidi et al. “Conformer-dependent Vacuum Ultraviolet Photodynamics and Chiral Asymmetries in Pure Enantiomers of Gas Phase Proline”. In: *Communications Chemistry* 4.1 (2021), p. 72.
[364] I. Medvedev et al. “The Millimeter-and Submillimeter-wave Spectrum of the Trans–Gauche Conformer of Diethyl Ether”. In: *Journal of Molecular Spectroscopy* 228.2 (2004), pp. 314–328.
[365] W. E. Moerner and G. C. Bjorklund. *Persistent Spectral Hole-Burning: Science and Applications*. Vol. 44. Springer, 1988.
[366] R. S. Ruoff et al. “Relaxation of Conformers and Isomers in Seeded Supersonic Jets of Inert Gases”. In: *The Journal of chemical physics* 93.5 (1990), pp. 3142–3150.
[367] P. Felder and H. H. Günthard. “Conformational Interconversions in Supersonic Jets: Matrix IR Spectroscopy and Model Calculations”. In: *Chemical Physics* 71.1 (1982), pp. 9–25.
[368] J. Lambert, R. N. Compton, and T. Daniel Crawford. “The Optical Activity of Carvone: a Theoretical and Experimental Investigation”. In: *The Journal of Chemical Physics* 136.11 (2012).
[369] M. J. Frisch et al. *Gaussian˜16 Revision C.01*. Gaussian Inc. Wallingford CT. 2016.

Page No.	Type of work	Name of work	Source of work	Copyright holder and contact	Permission equested on	I have permission yes/no	Permission note
51	Figure	K. Midorikawa. "Ultrafast Dynamic Imaging"	Nature Photonics 5 (2011), pp. 640–641	© 2011 journalpermissions @springernature.com	15.02.2026	Yes	6210260824221
61	Figure	A. F. Ordonez and O. Smirnova. "Generalized Perspective on Chiral Measurements without Magnetic Interactions"	Physical Review A 98.6 (2018), p. 063428	© 2018 journalpermissions @springernature.com	8.02.2026	Yes	RNP/26/ FEB/101986
62	Figure	S. Beaulieu et al. "Probing Ultrafast Dynamics of Chiral Molecules Using Time-resolved Photoelectron Circular Dichroism"	Faraday discussions 194 (2016), pp. 325–348.	© 2016 Royal Society of Chemistry	8.02.2026	Yes	1698549-1
66	Figure	D. Ayuso et al. "Synthetic Chiral Light for Efficient Control of Chiral Light Matter Interaction"	Nature Photonics 13.12 (2019), pp. 866–871.	© 2018 journalpermissions @springernature.com	8.02.2026	Yes	6204140799532
69	Figure	S. Beaulieu et al. "Photoexcitation Circular Dichroism in Chiral Molecules"	Nature Physics 14.5 (2018), pp. 484–489	© 2018 journalpermissions @springernature.com	8.02.2026	Yes	6204141009830
130	Figure	J. Lambert, R. N. Compton, and T. Daniel Crawford. "The Optical Activity of Carvone: a Theoretical and Experimental Investigation"	The Journal of Chemical Physics 136.11 (2012).	© 2012 jcp-edoffice @aip.org	16.02.2026	Yes	6210940072169